The role of dimensionality in the glass transition and memory behaviour of amorphous solids

A Thesis

Submitted to the
Jawaharlal Nehru Center for Advanced Scientific Research, Bengaluru
for the Degree of Doctor of Philosophy

by

Monoj Adhikari

Jawaharlal Nehru Center for Advanced Scientific Research, Bengaluru,India.

MAY 2022

I dedicate this thesis to my parents

DECLARATION

This thesis is a presentation of my original research work. Wherever contributions of others are involved, every effort is made to indicate this clearly, with due reference to the literature, and acknowledgement of collaborative research and discussions. The work was done under the guidance of Prof. Srikanth Sastry (Professor at Jawaharlal Nehru Center for Advanced Scientific Research, Bengaluru).

Monoj Adhikari

Monoj Adhikari

CERTIFICATE

I hereby certify that the matter embodied in this thesis entitled "**The role of dimensionality in the glass transition and memory behaviour of amorphous solids**" has been carried out by Mr. Monoj Adhikari at the Theoretical Science Unit, Jawaharlal Nehru Centre for Advanced Scientific Research, Bangalore, India under my supervision and that it has not been submitted elsewhere for the award of any degree or diploma.

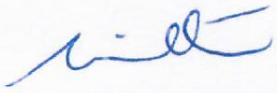

Prof. Srikanth Sastry
(Research Supervisor)

Acknowledgements

"In this silent, serene night of today, the look of the far away deserted homeland reminded me that her every evening, her every afternoon, her every moonlit night, her flowers, her fruits, her pain, her anguish, the tremendous joys of life painted my mind in colors of her diverse beauty. Their inspiration, their melody is at the root of all my literary efforts. Today, after twenty years of faraway life, I would like to congratulate the chirpy, flower-laden shadows of my yard, merely by saying that I have not forgotten. I did not forget. Wherever I have been, I have not forgotten you... Congratulations to all those people I have met in many circumstances and whose misery have painted my book alive. Some of them are alive today; some of them are not. The sorrows, the failures, and the despair of all of them have inspired me... I don't know where they are today. But through the dark-clad peace of this quiet night, I send my congratulations to all. Many of those who would have been happy to see my printed book are not alive today. I'm not sorry about that because I know there's no point in arresting the flow. May their departing path be well. Their words, too, haven't faded from my mind tonight". These are the words of a famous Bengali writer, Bibhutibhusan Bandopadhay, after he finished his great novel – "Pather Panchali". A similar feeling echoes in my mind today, as I complete my thesis – one that has my name on it, but one that would not have been possible without the help of various people. I would like to take this opportunity to thank them.

I would like to express my sincere gratitude to my advisor, Prof. Srikanth Sastry, for his continuous support, guidance, and advice throughout my PhD. He is a great teacher and as W. Arthur Ward said, "*The great teacher inspires*;" Prof. Sastry has always inspired me. In particular, his passion for science, dedication to research, and his ability to work hard inspired me a lot. I thoroughly enjoyed discussing my research problems with him. I will always admire his way of tackling a problem, and hope to inculcate that as much as possible. Beyond science, I also enjoyed my various discussions with him, from politics to poetry... I feel proud to be his student.

I would like to thank Prof. Smarajit Karmakar, my collaborator at TIFR Hyderabad. He

has always made himself available whenever I needed help. His enthusiasm for physics helped me enjoy science and motivated me throughout my Ph.D. Having studied in the same school, he was a source of inspiration to me and my peers, and I consider myself fortunate to be able to work with the person I know and admire from childhood. Thank you very much *Sona Da,* for all your help and support.

I thank my other collaborator Prof. Muhittin Mungan. He gave substantial inputs to the last chapter of my thesis and it was a great learning experience for me. During his visit to Bangalore and my visit to KITP, USA, I had a very good time discussing a variety of topics with him. Thank you Muhittin, for all your help and support.

Thanks to my GSAC committee members Prof. Subir K Das and Prof. Smarajit Karmakar for kindly agreeing to be on my committee and taking time from their schedules for attending different GSAC committee meetings and thesis colloquium. Their comments were really helpful.

I thank all my course instructors, Prof Umesh Waghmare, Prof. Shivaprasad S. M., Prof. Srikanth Sastry, Prof. Kavita Jain, Prof. Meher K. Prakash from JNCASR, and Prof. Chandan Dasgupta, Prof. Vijay Shenoy and Prof. Sumilan Banerjee from IISC for offering different courses which helped me immensely to develop the foundation of my research.

I thank all other TSU faculties, Prof. Swapan K Pati, Prof. Shobhana Narasimhan, Prof. Vidhyadhiraja for helping me in various ways whenever needed.

I was fortunate to come across some wonderful teachers, both at school and university. I thank them all for their great help. Special mention to Jayanta Sir, Tarun Sir, Souvik Sir, Abhigyan Sir, Sisir Sir, Sujit *Da*(Tutor), Partha *Da*, Suchit *Da*, Sunil *Da*, late Aparna *Di*, Manju *Di*, Tapas *Da*, Arani *Da*, Srikantha *Da*, Subhasis *Da*, Manas *Da*, Pijyus *Da*, Bikas *Da* .

I thank Prof. Subi J. George, Prof. Sheeba Vasu, and late Prof. Vijay Kumar Sharma for extending their help during a difficult time.

I acknowledge CCMS, JNCASR for the computational facility. I thank the JNCASR Administration, Doctors, Mess staff, Complab, Security for making my stay at JNCASR wonderful.

I thank all my present and past lab members. I have learnt a lot from my seniors, Anshul, Vinutha, Prem Kumar, Sebastiano, Rajneesh, Himangsu, and Arun. I am really lucky to have my immediate juniors, Yagyik and Pallabi, really talented guys, who helped me a great deal. I am also grateful to Yagyik,Pallbi,Himangsu and Arun for their valuable feedback, and for proofreading my thesis and manuscripts. I also thank Jayathi, Varghese, Ankit, Pushkar, Saurav, Saheli, Dheeraj, Siva, Krishna, Disha. Thanks to you, lab was a fun place. I feel happy to have shared this lab with you guys, and learnt different things from all of you. I also thank Indrajit, Rajsekhar, Bhanu, Kallol, Pappu, Mrinmoy, from TCIS, Hyderabad.

I am truly indebted to Sudenshna *Di*, Dibyojyoti *Da*, Debdipto *Da*, Koushik, Arkamita, Sudip. We had a great time together. I will always remember those days of cooking, chatting over coffee; hostel life was great fun because of you people. I enjoyed the company of Raktim, Subhajit, Manisha, Arindam, Anaranya, and for all the times we went out to dinner. I am grateful to my friend Arun and Jefin for helping me through some difficult times. I also thank Meghna, Sruthi, Arabinda, Saurav, Koyel from TSU. I had a great time discussing various things with them. I thank all my batchmates with whom I started my journey at JNCSAR and other friends at JNCASR; special thanks to Aditya, Aiswariya, Anirudh, Suman, Abhijeet, Badri, Nilaxi, Srikanth, Srimayee, Pavitra, Bharat, Manodeep, Paribesh, Abhiroop, Madhulika, Jiya *Da*, Subhajit *da*, Saikat *da*, Tarak *da*, Rajdeep *da*, Anirban, Sisir, Abhijeet, Sohini, Rajib.

I thank my university friends, specially Sourav, Malay, Sayan, Iman, Bappa. Despite the distance, it helped me immensely to discuss various topics with them over the phone. I also thank my childhood friends Sukla, Olivia, Partyasha, Sayantani, Soumen for all the fun discussions over phone.

I would like to thank Chandrani *boudi*, Sauro and Niladri for their warm hospitality at Hyderabad. I have enjoyed spending time with them. I would also like to thank Bani *Di*, Chandana *Di*, Harsh, and Debu *Da* for helping me to settle down at Hyderabad, outside home for the first time.

Finally, I would like to thank my family members. My father, a very hard working person, always kept his faith in me and gave me the freedom to pursue whatever I wished. He is my hero and I always try to follow him. My hardest day seems to be an easy one when I see the amount of hard work he puts into every aspect of his life. He has taught me great values by example. He will be the happiest to see me successful. My mother, who is very straightforward and unassuming, has always supported me. Even after a tiring day at work, I get rejuvenated when I talk to her. I want to emulate her simplicity, calm and cheerful attitude. Whatever I have achieved so far thanks to them. I thank my brother Manas, and Provas (*Jamaibabu*) who take care of everything in the family, and support me wholeheartedly. I am truly indebted to them. I thank my sister Santana for her sacrifices and Bulti(*Boudi*), who are very warm-hearted, and always fun to talk to. It gives me great happiness and joy when I spend time with my nieces, Rupsa and Riya, and nephew, Adrij. I thank you all for your unconditional love and support. Without you, it would not have been possible for me to pursue this path of science and knowledge.

Synopsis

This is a summary of the work done under the title "**The role of dimensionality in glass transition and memory behaviour of amorphous solids**" The focus of these investigations has been in trying to understand the glass transition, the transformation of a liquid to an amorphous solid when cooled in such a way as to avoid crystallization. A related phenomenon in these solids is that of memory formation; a characterization of this phenomenon and possible connections to the properties of the glassy state are also studied in this thesis.

In order to motivate the discussion contained in this thesis, we begin by describing observed phenomenology, specifically, a change in behaviour of the relaxation time, whose increase with decreasing temperature changes from Arrhenius-like to super-Arrhenius. Concurrently, the microscopic dynamics becomes heterogeneous in that faster (or slower) particles cluster together showing spatially correlated dynamics.The role of such heterogeneities in the complex relaxation dynamics in glass-forming liquids and, as well, the growing length scales governing these relaxation processes have both been widely investigated. Theoretical investigations in the preceding decades have largely focussed on extending the framework of random first order transition theory (RFOT). A lot of effort has been devoted is in the formulation of a mean field description in the infinite dimensional limit. In this limit, the glass transition and the jamming transition (which occurs for athermal systems) is unified in the context of an idealized hard sphere. These developments naturally led to investigations of how results obtained at infinite dimension relate to behaviour at finite dimensions.

In the first part of the thesis, we study glass-forming liquids in spatial dimension $3-8$ using computer simulations and compare our results with the theoretical prediction.

Glasses also display interesting behaviour in the non-equilibrium or driven state. Understanding the mechanical response of glasses to applied deformation is of great interest as it helps to determine material properties such as strength and ductility. Under cyclic shear deformation, glasses show a non-equilibrium phase transition. When the

deformation amplitude is large, configuration of the system keeps changing with increasing number of cycles whereas repeated cycles of low amplitude shear deformation drive the system to so-called absorbing states that encode the amplitude of shear deformation applied – the glass remembers! The mechanical properties of glasses, with a specific focus on memory-formation and the yielding behaviour of amorphous solids under cyclic shear deformation is the focus of the second part of this thesis. The outline of the thesis is the following:

In chapter 1, a brief introduction about the complex phenomenology of glass-forming liquids is presented. The state-of-the-art for problems relevant to this thesis and theoretical attempts to understand this behaviour are then discussed.

In chapter 2, the definitions of different quantities computed in this thesis are presented, along with the details of the models studied and the different methods used.

In chapter 3, the dynamics of a model glass-forming liquid is studied. This liquid consists of soft sphere assemblies interacting with a harmonic potential for spatial dimensions 3−8. At low temperatures, this model shows crossover from a sub-Arrhenius relaxation process at low density to super-Arrhenius behaviour at higher densities in three spatial dimensions. Employing a scaling theory of density-temperature dependent relaxation times, the cross over density, ϕ_0, is identified. This crossover density marks the ideal glass transition density in the hard-sphere limit and is found to be close to the athermal jamming point, ϕ_J in three and four dimensions. We find that ϕ_0 differs from the athermal jamming density, ϕ_J and the difference systematically increases with the increasing dimensions. We compare our results with the theoretical predictions and find a near quantitative agreement between these two.

In chapter 4, the heterogeneity in the dynamics is investigated, with a focus on the breakdown of the Stokes-Einstein relation and on fragility in a model glass-forming liquid. Here too, a binary mixture of soft spheres with a harmonic interaction potential serves as our model glass-former, which we study for spatial dimensions from 3 to 8. Dynamical heterogeneity is quantified through the dynamical susceptibility χ_4, and the non-Gaussian parameter α_2. We find that the fragility, the degree of breakdown of the Stokes-Einstein relation, as well as heterogeneity of dynamics, decrease with increasing spatial dimensionality. We briefly describe the dependence of fragility on density, and use it to resolve an apparent inconsistency with previous results.

In chapter 5, we investigate the relation of diffusivity or relaxation time between different components. We have observed at 3d the diffusivities can be related by a single power law. However, at 4d or higher spatial dimensions, two different power-law regimes are observed with different exponents. For all the dimensions, the exponents in the higher temperature regime are always smaller than the exponents in the lower temperature regime. Both the exponents (high temperature and low-temperature regime) increase with increasing dimensions.We have also investigated

the Adam-Gibbs (AG) relation for spatial dimensions 3 – 8 and found that the AG relation holds for both diffusivity and relaxation time in 3 dimensions for the temperature range considered. However, our initial results suggest that at 4d or beyond, this relation does not hold for either diffusivity or relaxation time. One caveat is that the vibrational entropy has been computed using the harmonic approximation, which needs to be justified to reach any definite conclusions regarding the validity of the AG relation.

In chapter 6, we study memory-formation in a model of amorphous solids. It has previously been demonstrated that the memory of the amplitudes of shear deformation that the system is subjected to are encoded and can be retrieved by subsequent deformation cycles that serve as read operations.Here we consider different read protocols and measurements and show that single and multiple memories can be robustly retrieved through these different protocols. We also show that shear deformation by a larger amplitude always erases the stored memories.Here, we also study low-density sphere assemblies, which serve as models for non-Brownian colloidal suspensions, under athermal deformation. We identify a regime where the signatures of memory encoding are similar to the model glass, even when transitions between local energy minima are absent.

In chapter 7, we study the yielding behaviour of a model glass using an asymmetric cyclic shear deformation protocol, wherein the applied strain is cyclically varied between 0 and a maximum value γ_{max}, and investigate the role of annealing in the yielding transition. Two strikingly different regimes of behaviour similar to symmetric shear deformation emerge depending upon the degree of annealing. However, we find that the yielding behaviour of well-annealed glasses displays striking differences from the case of symmetric shear. In the intermediate strain regime, substantial plasticity emerges before yielding. Though the nature of the deformation is asymmetric, no structural anisotropies are observed.

In chapter 8, we present the conclusions and future outlook of this thesis.

Contents

List of Figures

List of Tables

Chapter 1

Introduction

Glasses are ubiquitous in nature. Window glasses, which are made of silica, are the most common example. However, there exist many different examples, chalcogenide glasses and metallic glasses to name a few, whose properties come to the fore in different contexts. Glasses are one of the oldest artificial materials used by humankind; the oldest glasses known so far were found in the deserts of Egypt [1]. People have been making and using glass for thousands of years and attempts to improve on this process and to produce glasses with desired properties are some of the earliest attempts to better understand this material. The empirical knowledge that glasses are made by cooling liquids quickly begs far more questions than it gives answers. Foremost among these, in the scope of statistical physics, is the question of whether the transformation of liquids to glasses upon cooling is a thermodynamic transition. A considerable amount of effort has been devoted to answering this question – and this question is also the focus of this thesis. Glasses are similar to crystalline solids, in the sense that they are mechanically rigid and capable of supporting load. On the other hand, the microscopic structure of glasses is disordered, similar to that of liquids. This mixed character of glasses makes it difficult to distinguish it from liquids, purely based on structure, and from crystalline solids, based on mechanical response to external forces. Whether the glass is a different state of matter and if so is there any thermodynamic transition involved like other states of matter is a big topic of research till date.

In recent years, this research field has received growing attention from scientists for a variety of reasons. On the one hand, understanding the glass transition has quite broad implications for other systems as well. A hallmark property of glasses is that the relaxation time (the time to reach equilibrium) of the system is much larger than the typical duration of experiments or of numerical simulations. This property is common to a variety of systems, for example, type-II superconductors in the presence of disorder such as high-T_c superconducting materials [2], spin glasses [3, 4], complex

fluids such as colloidal assemblies [5], granular materials [6], emulsions, foams [7], proteins [8], etc. On the other hand, glasses also have applications in developing various technologies [9, 10]. Metallic glasses, alloys of two or more components, enable modern power transmission and are finding increasing use in applications calling for high strength or low shrinkage upon solidification [11]. Chalcogenide glasses have essential applications in optical disc technology and may play a critical role in non-volatile electronic memory [12]. Amorphous silicates for optical fibers are widely used in modern communication technology. Organic glasses are the basis for organic light-emitting diodes and other developments in organic electronics [13].

Glasses can be obtained by cooling a liquid. Typically, a liquid crystallises when cooled below its melting temperature. However, if one can avoid crystallisation somehow (sufficiently rapid cooling or "quenching" is one of the common ways), the liquid will reach a *metastable* or *supercooled* state below its melting temperature [14]. If one decreases the temperature further, viscosity increases rapidly in a small temperature interval. As a result, the dynamics of the liquid becomes too sluggish to explore all possible particle arrangements over an accessible timescale. At this point, the system is said to have fallen out of equilibrium and reached a *glassy state*. This is a key feature, which will be discussed in detail in subsequent sections. The temperature at which the transition occurs is termed as T_g. As the liquid becomes glass without any significant structural change, it is hard to understand the nature of the transition. Understanding the correlation between structure and dynamics has also proved to be challenging. These issues are keenly investigated to this day.

In the following sections, I will describe the basic phenomenology associated with the glass transition, followed by a discussion on the theoretical developments to understand them. At the end of this chapter, I will describe the goal of this thesis.

1.1 Experimental glass transition:

Generally, if we cool a liquid, it will crystallize as the temperature goes below the freezing point. Now, if we can avoid the crystallization somehow, instead of crystal, we will end up with a state called glass. The question therefore becomes about how one might avoid crystallisation. When a liquid is cooled, crystallisation occurs through small fluctuations in the local order of particles, with a small number of them falling into an ordered configuration and forming a nucleus. The growth of these nucleii occurs through the deposition of more particles on the surface. A finite amount of time is needed for the growth of these crystal nucleii which is called the nucleation time ($\tau_{nucleation}$). Similarly, the liquid takes a finite amount of time to reach equilibrium (no memory of the initial state) at each temperature, which is called relaxation time

(τ_α). Now, if the liquid is cooled with a cooling rate such that it relaxes but does not nucleate, it can remain in the liquid phase even below its freezing temperature. This is possible if the amount of time spent at a given temperature is more than τ_α but less than $\tau_{nucleation}$. This is indeed possible for a vast majority of the liquids, starting from molecular liquids to polymer melts [15]. In order to give an idea about the time scales, it is good to mention some typical numbers. Typical values of cooling rate in laboratory experiments are $1 - 100$ Kelvin/min. The typical time scale for τ_α is of the order of 1 pico-second for water near the melting temperature, T_m. The glass transition temperature, T_g, is often defined in experiments as the temperature at which τ_α is of the order of $100s$. The increase of τ_α is associated with the increase in shear viscosity η. These two quantities are related to each other by the Maxwell relation: $\eta = G_\infty \tau$ (τ:stress relaxation time). The viscosity attains values of the order of 10^{13} poise or 10^{12} Pa-s at T_g. To get a sense of how huge this number is, let us calculate the time it will take to empty a cup containing a liquid just above its glass transition. Here, we use the general definition of viscosity which is $F = \eta v A/d$, where F, η, v, A and d are the force, the viscosity, the velocity, the area and the diameter respectively. Now, using $v = l/t$, we find, $t = \frac{\eta l A}{dF}$. We will be substituting the typical values corresponding to the above problem, $F \sim 10$ Newton, $A/d \sim l \sim 0.1m$, $v = l/t$, $\eta = 10^{12}$ we obtain, $t = 10^9$s ($\sim$ 30 years!!) [16]. When a liquid is cooled to a temperature approaching T_g their ability to flow reduces so much so that on the timescale of an experiment, they behave like a solid. In such a state, the substance can support a mechanical load and mechanically behaves like a solid, but the microscopic structure is similar to that of a liquid. This state is known as structural glass and this phenomenon of a liquid transforming into an amorphous solid is known as the glass transition. In the laboratory, T_g is defined by: i) Where viscosity become 10^{13} poise (the corresponding relaxation time is 100s), (Fig. 1.1(a)). ii) The specific heat shows a sharp but continuous drop at a temperature, which is the calorimetric measure of T_g (Fig. 1.1(b)). Note that glasses can also be obtained by controlling the density; however, I will describe all the phenomenology using temperature as the control parameter. The relation between glasses obtained by two different control parameters can be found in [17, 18]. Although the value of T_g is dependent upon a variety of things such as protocol, cooling rate *etc*, T_g is a meaningful concept to characterize the dynamics. The increase in relaxation time is so steep that T_g does not vary significantly even for large changes in the cooling rate. Let us assume that the viscosity or the relaxation time follows Arrhenius behaviour ($\tau_\alpha = \tau_0 \exp \frac{\Delta}{T}$) with temperature. So, at $T = T_g$, the experimental time, t_{exp} will be,

$$t_{exp} = \tau_0 \exp\left(\frac{\Delta}{T_g}\right) \tag{1.1}$$

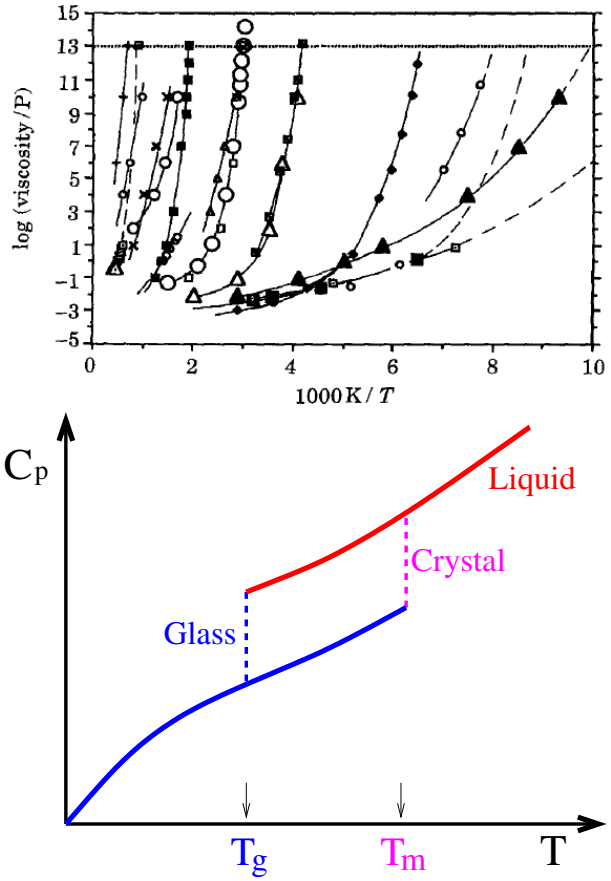

Figure 1.1: Two different metrics are used to define the glass transition temperature, T_g. Left panel: The temperature at which the log of the viscosity divided by P becomes 13 marks the laboratory glass transition, The data is taken from [19]. Right panel: The temperature at which the specific heat of the liquid shows a sharp but continuous drop is the calorimetric measure of T_g.

Here, it deserves to be mentioned that t_{exp} is determined as a multiple of the inverse cooling rate. Differentiating with respect to T_g, we obtain,

$$dT_g = -\left(\frac{\tau_0 \Delta}{T_g^2}\right) \exp\left(-\frac{\Delta}{T_g}\right) dt_{exp} \tag{1.2}$$

This shows that a huge change in t_{exp} causes small shifts in T_g. During supercooling, t_{exp} increases faster with decrease in temperature than predicted by the Arrhenius relation so the change in T_g will be even smaller. Thus we can define T_g meaningfully from an experimental point of view [20].

Our inability to access low enough temperatures to observe an imminent divergence in the relaxation time, while maintaining equilibrium in experiments as well as in simulations, is the main hindrance to understanding the glass transition. In recent times, a lot of emphasis has been given to devising different methods which would enable us to study supercooled liquids at progressively lower temperatures. In the recent past, [21, 22] it has been shown that the vapor deposition method can synthesize organic molecular glasses having a much lower T_g than of any previously synthesized. These glasses are termed as *ultrastable* glasses. In this method, glasses are formed by depositing molecules layer by layer from a vapor onto a substrate. It has been found that the mobility of the molecules at the surface is very large ($\sim 10^8$) compared to the bulk [23, 24]. As a result, at an optimum deposition rate, molecules can sample different configurations and reach equilibrium at the substrate temperature which is kept below the T_g of the bulk material. Glasses synthesized within a few hours with this method are more stable than 20 million year old naturally occurring glasses. The physical properties of these glasses are qualitatively different from ordinary glasses [] and improving our understanding of these properties is an area of intense theoretical investigation [25, 26]. In computer simulations, one cannot access time scales as long as those achievable in experiments. T_g is defined as $10^{-6}s$ in simulations as opposed to $100s$ in experiments. Recently, in the context of simulations as well, different methods have been introduced to obtain stable glasses, the *swap Monte Carlo* method and oscillatory shear deformation to name a few. Swap Monte Carlo method in the context of glass-forming liquids was first introduced in [27]. However, its utility towards producing lower energy glasses has been shown in recent times. In this method, in addition to standard Monte Carlo moves, particle diameters are swapped with a finite probability which enhances thermalization in mixtures and is very efficient when applied to polydisperse systems. These methods enable us to study glass-forming liquids beyond the conventionally defined T_g. Although it was shown that this method works very well in different spatial dimensions [28], its applicability in different systems are limited. How one can use this method in a simple model system is an area of current

research [29].
The glass transition, as described so far, points to a dramatic slow down in the dynamics as being key. In the section to follow, the dynamical properties of glasses are elaborated on.

1.2 Dynamical properties

In this section, we will discuss how the dynamical properties change during the glass transition.

1.2.1 Non-exponential decay of dynamic correlation functions

Dynamic correlation functions describe how any fluctuations in the system relax with time. The real-space, and real-time correlation functions can be directly measured in simulations, whereas Fourier transforms of the real space-time correlation functions are typically computed in experiments. Here, we discuss the nature of the density correlation function where local density is the fluctuating variable for a dense liquid. At high temperatures, the relaxation function, $C(t)$ is relatively featureless; it decays exponentially. At low temperatures, the decay is no longer purely exponential, the decay of $C(t)$ shows a two-step character [14, 16, 30]. This is understood as being a result of two timescales, the first short timescale termed the “ballistic" regime, and the second, longer timescale, the “diffusive" regime. At intermediate time scales between the ballistic and the diffusive region a plateau appears that eventually decays to zero at large times. The length of the plateau increases as T decreases. In Fig. 1.2(a) a typical correlation function is shown schematically. This two-step decay is one of the most prominent features of glass-forming liquids. Conventionally, the time window around the plateau is known as the β relaxation regime and the decay at the longer time scale is known as the α relaxation regime. These two regimes are well separated in time at lower temperatures. In the α regime, the relaxation process can no longer be fitted to an exponential; it is empirically described by a stretched exponential function [31](also known as Kohlrausch-Williams-Watts function) [32]: $C(t) = f_c \exp\left(\frac{-t}{\tau}\right)^{\beta}$. β, which lies between 0 and 1, is a measure of the deviation from the exponential behaviour and is termed as the stretching exponent (also sometimes refereed to as the KWW exponent).

In experiments, the dielectric susceptibility is often used to measure the relaxation dynamics. Dynamic susceptibility, related to the time correlation of polarization fluctuations, can capture the dynamics for a larger range of timescales. In Fig. 1.2(b) the imaginary part of the dielectric susceptibility, $\epsilon''(\omega)$ is shown for various temperatures. We can see that the peak shifts to low frequencies with the lowering of

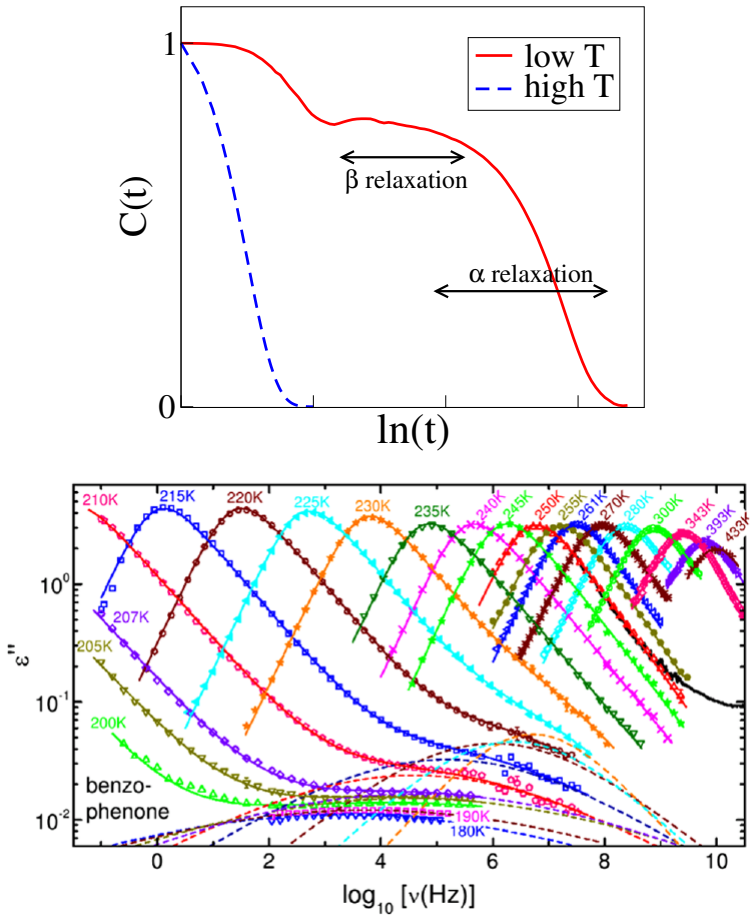

Figure 1.2: Schematic representation of the decay of the density correlation function at high and at low temperatures. Left: At low temperatures the correlation function decays non-exponentially in contrast to high temperatures where the decay is exponential. Right: The imaginary part of the dielectric susceptibility, $\epsilon''(\omega)$ is plotted for different temperatures. The data is taken from [33].

temperature signifying that relaxation time increases with decreasing temperature. At high temperatures, the data follows the Debye law: $\epsilon(\omega) = \epsilon(\infty) + \frac{\Delta\epsilon}{1+i\omega\tau_\alpha}$ (where the real part is $\epsilon' = \epsilon(\infty) + \frac{\Delta\epsilon}{1+\omega^2\tau_\alpha}$ and the imaginary part is $\epsilon'' = \frac{\Delta\omega\tau_\alpha\epsilon}{1+\omega^2\tau_\alpha}$) which corresponds to exponential relaxation. When the dielectric function follows the Debye law, peaks in ϵ'' are symmetric as observed in Fig. 1.2. However, at low temperatures, the relaxation spectra become broader with a long tail at higher frequencyies, i.e., non-Debye, which is the frequency analogue to stretched exponential behaviour of the time correlation function [33]. In the time domain, the correlation function can be fitted with a stretched exponential, $\exp(-(t/\tau)^\beta)$ function. Similarly, in the frequency domain ϵ'' is well-fitted to the Havriliak-Negami form (which generalizes the Debye law): $\epsilon'' = (\frac{\Delta\omega\tau_\alpha\epsilon}{1+(\omega^2\tau_\alpha)^\alpha})^\gamma$. α, γ are the temperature dependent exponents. This form implies that the relaxation becomes increasingly non-exponential with decreasing temperature.

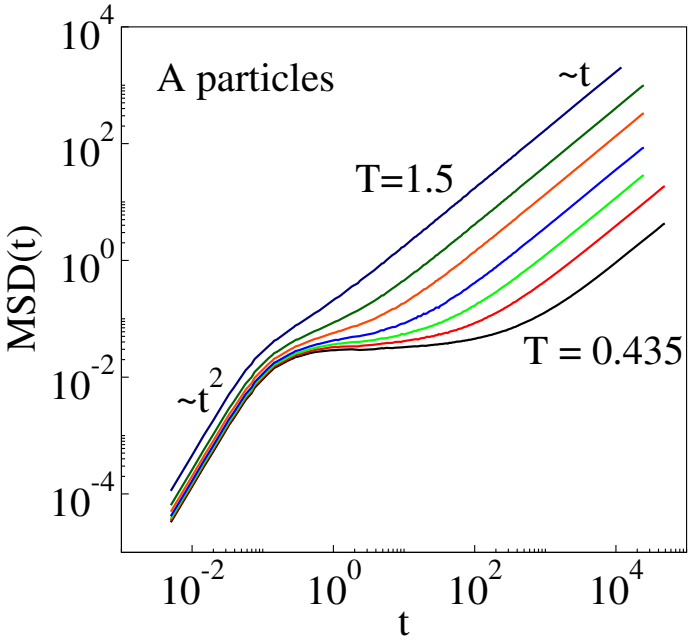

Figure 1.3: MSD is plotted as a function of time for different temperatures for Kob-Anderson model.

The Mean Squared Displacement (MSD), another dynamic observable, also shows a significant change in the supercooled regime. At high temperature, in the early ballistic regime, $MSD \propto t^2$ whereas at long times, i.e., in the diffusive regime $MSD \propto t$ (see Fig. 1.3). However, for supercooled liquids, these two regimes are separated by a plateau, the length of which increases with the decreasing temperatures. Although particles are colliding, MSD does not change much in the plateau regime. On the timescale of the plateau regime, particles are *caged* by their neighbours. After a long time, the particles break the cage and the diffusive regime sets in in the system. The typical MSD behaviour is shown in Fig. 1.3.

1.2.2 Non-Arrhenius temperature dependence of relaxation times

In general, the relaxation time measures the time taken by a system to forget its initial state. Generally, the temperature dependence of relaxation time for a liquid at a high temperature and a low density is Arrhenius. However, the temperature dependence of the α-relaxation time, i.e., τ_α, shows non-Arrhenius behaviour in the supercooled temperature regime. In general, when the dynamics are dominated by overcoming energy barriers by thermal fluctuations, τ_α follows Arrhenius behaviour:

$$\tau_\alpha \propto \exp\left(\frac{\Delta E}{k_B T}\right) \tag{1.3}$$

where ΔE represents the activation energy which is temperature independent and k_B is Boltzmann's constant. The Arrhenius law also holds for other transport coefficients such as diffusivity and viscosity. A large number of glass-forming liquids show a stronger than Arrhenius increase in viscosity, τ_α and diffusivity upon supercooling towards the glass transition. At high temperatures, the dynamics is Arrhenius and at low temperatures, it becomes super-Arrhenius, and this change of behaviour happens gradually over a range of temperatures around a onset temperature. This is a characteristic feature of such liquids [19]. Liquids are categorized into two types on the basis of this change in behaviour: i) Liquids which show this Arrhenius to super-Arrhenius cross-over are called *fragile* glass-formers. Ortho-terphenyl (OTP) is a typical example. ii) Liquids which do not show such a crossover, obeying the Arrhenius law at all temperatures, for example supercooled liquid silica, are termed *strong* glass-formers. We have seen that during supercooling, the relaxation time not only increases by a huge amount but also the rate of increase is remarkably different from what one sees for high temperature low-density liquids. Understanding the super-Arrhenius nature of the dynamics is one of the enduring questions of this field. A universally accepted theory of this crossover in the behaviour of glass-forming liquids has proven elusive. However, several attempts have been made to explain this behaviour. Many different empirical fitting functions with varying degrees of theoretical basis are used to understand the observed behaviour. One of the widely accepted functions which fits the data very well is the Vogel-Fulcher-Tammann-Hesse (VFTH or VFT) fit [34, 35]. The VFT fit is a three parameter fit defined in the following way:

$$\tau = \tau_0 \exp\left(\frac{D T_0}{T - T_0}\right) \tag{1.4}$$

where D is material property. This implies that at a finite temperature, T_0, the relaxation time becomes infinite. Subsequently, this is rationalised by introducing the

concept of the glass transition as a finite temperature thermodynamic transition. However, many other fitting functions have been proposed, implying a zero temperature divergence of the relaxation time/viscosity, one of which is the Zwanzig-Bessler law: $\tau = A\exp\left(\frac{E}{RT^2}\right)$. Between these two disparate scenraios, it is hard to verify which form correctly represents the temperature dependence of the relaxation time, because the system falls out of equilibrium before T_g is reached, making it impossible to measure any equilibrium properties over experimental timescales. Extensive comparisons between different fitting functions have been discussed in the literature [36, 37]. The question of whether there exists a finite temperature divergence of the relaxation time or whether the relaxation time diverges only at zero temperature remains an open question. There are many experimental and simulation studies which indicate that the drastic increase of the relaxation time originates from an underlying thermodynamic transition at finite temperatures. Theoretical analyses predicting a thermodynamic transition are expected to be exact in the infinite dimensional limit. Their validation is possible with studies performed in higher dimensions – a feat only possible with computer simulations. Hence, in this thesis, we too attempt to verify whether there exists an underlying thermodynamic glass transition by studying glass-forming liquids in higher spatial dimensions.

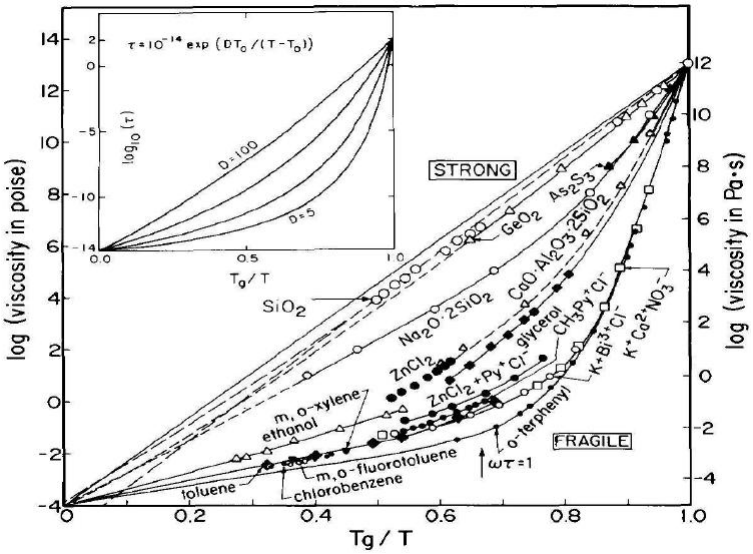

Figure 1.4: Angell plot of the logarithm of viscosity vs the scaled inverse temperature $\frac{T}{T_g}$. Inset: The Angel plot can be generated using the VFT fit. The data is taken from [19].

1.2.2.1 Kinetic fragility

We have discussed the complex behaviour displayed by the relaxation times of supercooled liquids. By plotting the logarithm of the relaxation time or the viscosity as a

function of $\frac{T_g}{T}$, one can distinguish between different supercooled liquids. This kind of plot is called the Angell plot by convention [19, 38]. In Fig. 1.4, we show the original Angell plot where we observe that the temperature dependence of the relaxation time for some systems falls on a straight line. These liquids are categorised as strong glass-formers. Other systems, for which the temperature dependence of the relaxation time deviates from the straight line are categorised as fragile glass-formers. Using this plot, one can quantify how rapidly the relaxation time or the viscosity increases with temperature. This is done by introducing a parameter called *fragility* whose value is system-specific. The fragility, when calculated from the relaxation time or from transport coefficients, is called kinetic fragility. There are many different ways to calculate the fragility of the system. The original definition given by Angell is as follows

$$m = \left(\frac{d log \tau_\alpha}{d\left(\frac{T_g}{T}\right)} \right) \tag{1.5}$$

The kinetic fragility can also be calculated from the VFT formula [39]:

$$\tau(T) = \tau_0 \exp\left(\frac{1}{K_{VFT}\left(\frac{T}{T_{VFT}}\right) - 1} \right) \tag{1.6}$$

K_{VFT} and m are related to each other in the following way: $m = \frac{T_g}{\left[K_{VFT}\left(\frac{T_g}{T_{VFT}}-1\right)\ln 10\right]}$. Due to the simplicity of the second equation, we have used it in the present thesis. The idea of fragility plays an important role in understanding glass-forming liquids as it has been observed that fragility can be related to other thermodynamic and dynamical properties of the system such as configurational entropy [39], specific heat [40] and the elastic constants [41].

1.2.3 Dynamical heterogeneity

One of the most exciting developments in understanding the glass transition is Dynamical Heterogeneity (DH) [42,43]. Dynamical heterogeneity refers to spatio-temporal fluctuations in the dynamics: some clusters of particles move faster than average while some other clusters move slower. As discussed already, relaxation in the supercooled regime follows a stretched exponential with $\beta \leq 1$ being the stretched exponent. It has been observed that β decreases with decreasing temperature. The idea of heterogeneity originated from the search for an explanation for the origin of the stretched exponential decay of the time correlation function. The nature of the decay deviates

further from exponential behaviour with decreasing temperature. Two natural hypotheses are put forward to understand this behaviour. (i) Different regions of the system have different relaxation times, i.e., the dynamics is heterogeneous. The relaxation is exponential for all the different regions. However, the relaxation of the entire system becomes non-exponential upon spatial averaging over the spatial distribution of relaxation times. (ii) The relaxation is non-exponential in all the different regions. The stretched exponential nature of the relaxation is intrinsic to the system and has nothing to do with the heterogeneous spatial averaging. Separate investigations in this regard have suggested one or the other mechanism to be valid but have all come to the conclusion that relaxation is spatially heterogeneous, and have pointed to the coexistence of spatially correlated mobile and immobile particles. If we look at the time evolution of the system, we will find that not only do some particles move faster, while others move slower than the average but also the slower or faster particles are spatially correlated (see Fig. 1.5(left)). The mobility of the particles changes with time, so that a cluster of particles that are slow at some point in time may become faster at some later point in time. Thus, dynamical heterogeneity suggests that there exists a dynamical length scale related to the cluster sizes associated to the growing time scale in the system. There have been many studies [44–47] aimed at understanding how the dynamical length scale grows with temperature and how it is related to the increase in the timescale. A number of definitions have been used to distinguish mobile and immobile particles, nevertheless, the most appropriate definition remains debated. Heterogeneity can be quantified in many different ways such as the van Hove function or the dynamic susceptibility ($\chi_4(t)$). For a homogeneous liquid, the van Hove function is Gaussian. When the dynamics is heterogeneous, it will no longer be Gaussian [48]; it will have a long tail [49]. Correspondingly, the non-Gaussian parameter, $\alpha_2(t)$ will be non-zero for heterogeneous dynamics.

As discussed earlier, the onset of heterogeneity plays a key role in glass-formation; efforts have been made to find a relation between dynamical heterogeneity and other complex dynamical behaviours. In particular the relation between fragility and heterogeneity has been extensively studied. Bohmer *et al.* [50] showed that the fragility index, m (defined earlier) and the stretched exponent, β, are related to each other by compiling the data of around 70 glass-formers. However, in a subsequent study, ref. [51] found that when the data is grouped in a certain way (e.g. simple glass-former, complex glass-former) the correlation between β and m appears weaker. Studies in ref. [52] also claim that no clear relation exists from their experimental study. One important point to remember here is that the stretching exponent does not prove that dynamics are heterogeneous as there is a possibility that the relaxation is intrinsically non-exponential and some current results hint in this dierction. Wang *et al.* [53], studied different glass-formers and showed that heterogeneous liquids are more fragile in

nature: systems having large m have large $\alpha_2(t)$ by implication. Similar observations are also found in a polymer glass when chain stiffness is varied [54]. With the increasing stiffness, fragility increases and the dynamics becomes more heterogeneous.

All these studies involve either observing changes across models or a change of parameter which can affect the structure or other properties of the system. The object of our interest is whether heterogeneity is fundamental to the system as opposed to being incidental to fluctuations in a system of finite size.
Studying glass-forming liquids in different spatial dimensions could be useful in this aspect. The heterogeneity of the dynamics is related to the fluctuation of the relaxation times in the system. If this fluctuation is critical-like, one would expect that the dynamics will become homogeneous with increasing dimension as the number of neighbors increases with increasing dimension and fluctuation in the system become smaller. Now, the pertinent question would be how fragility changes with increasing dimension? In an attempt to understand the relationship between these two, in this thesis, we study glasses in higher spatial dimensions and investigate the behaviour of heterogeneity and fragility.

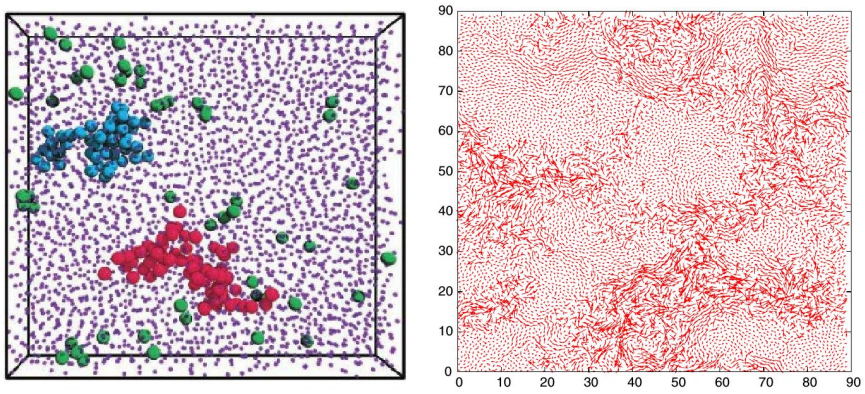

Figure 1.5: Left: Dynamical heterogeneity seen in a three dimensional supercooled colloid using confocal microscopy. The fast particles are represented as large spheres (red and blue) and slow particles as small spheres (violet). The data is taken from [55] Right: Spatial map of single-particle displacements in the simulation of a binary mixture of Lennard-Jones mixture in two dimensions. Arrows show the displacement of each particle in a trajectory of length comparable to the structural relaxation time. The map reveals the existence of particles with different mobilities during relaxation. The data is taken from [56]

1.2.4 Violation of the Stokes-Einstein relation(SER):

Another important feature of glass-forming liquids is a violation of the Stokes-Einstein relation (SER). According to SER, the translational diffusion coefficient (D) of the particles in a liquid is related to η, the shear viscosity of the liquid, in the following way:

$D \propto \eta/T$. According to Einstein, the diffusion coefficient (D) of the Brownian particle and the friction coefficient (ζ) of the liquid at a given temperature, T, are related to each other with the equation $D = \frac{k_B T}{\zeta}$ known as the Einstein relation. Further, the friction coefficient ζ and the viscosity η are related to each other through the Stokes' formula [57], $\zeta = 6\pi\eta R/m$ (The factor 6 is boundary-condition dependent). Combining both the relations we obtain $D = \frac{mk_B T}{6\pi R\eta}$, which is called the Stokes-Einstein relation. This relationship holds at high temperatures for various liquids [58]. As we approach the glass transition by lowering the temperature, the diffusivity, D and the viscosity, η, get decoupled. As discussed earlier, η and τ_α are related to each other, and one can also observe a similar decoupling between D and τ_α. In the supercooled regime, the temperature dependence of D becomes weaker than that predicted for D from the SER [59, 60]: D and η or τ_α are related to each other by fractional SE relations, $D \propto \tau_\alpha^{-1+\omega}$, where $\omega \geq 0$. Various studies [61–64] have shown that SER violations are connected with heterogeneous dynamics. When the dynamics is heterogeneous, diffusion will be dominated by the fast particles as it measures the average displacement of the system at a given time whereas relaxation will be dominated by slower particles as it measures how many particles have moved a certain distance in a given time interval. As a result, relaxation and diffusion will be decoupled, and SER will be violated. In ref [65] the distribution of displacements of particles is calculated for different densities for the hard sphere system. At high densities, the distribution shows bimodality.

Mobile particles and immobile particles are defined using a suitable cut-off and it is shown that the SER is violated for the mobile particles, whereas SER holds for the immobile particles. Similar observations are made when the distribution of diffusivity is considered [66, 67].

At low temperatures, the distribution becomes bimodal which is used to define fast and slow moving particles and SER is violated for fast moving particle however, it holds for slow moving particles. However, other studies [68, 69] show SER is violated for both slow moving and fast moving particles.

These studies fail to clarify whether SER is a direct consequence of dynamical heterogeneity as most of the studies either used an *ad-hoc* threshold to define mobile or immobile particles or did not explicitly consider the implications of clustering. In. [70], it has been argued that violation of SER is a result of combination of local hopping, facilitation and dynamical heterogeneity.
Studying glasses in higher dimensions will help us to understand the role of heterogeneity directly in the violation of SER. As already discussed, one would expect heterogeneity to be less at higher dimension. In this thesis, we attempt to understand this question by investigating the change in the exponent, ω and its possible connection with the degree of heterogeneity.

1.2.5 Timescales and characteristic temperatures of significance

There are many different timescales involved in describing the dynamics of glass-forming liquids. Two different timescales: the α relaxation and the β relaxation time are associated with a two-step relaxation. Whether the two time scales are related is not clearly understood till date. Besides these two time scales, other time scales are those associated with diffusion and shear viscosity.
When a glass-forming liquid is cooled from a high temperature to low temperatures, many distinct changes in dynamics are observed at different temperatures, each of which carries special significance. The melting temp, T_m separates the equilibrium liquid from the supercooled liquid. Below T_m, the change from an Arrhenius to a non-Arrhenius temperature dependence of the relaxation time occurs at a cross-over temperature T_{onset}. At this temperature, a qualitative change occurs in the way the system samples its configuration space which is reflected in many properties of the system, marking the onset of slow dynamics. At even lower temperatures, there exist two characteristic temperatures which come as a consequence of fitting functions, where the relaxation time is found to diverge. The first one is T_c, which is the temperature where Mode Coupling theory (described in detail later) predicts the divergence of relaxation time. In ref [71] it has been shown that T_c is very similar to T_x, the Goldstein temperature. According to Goldstein, T_x acts like a precursor to the glass transition. At T_x, the dynamics of the system can be separated into two regimes: short time vibrations around potential energy minima and long time transitions between these minima. The second one is T_{VFT}, which is below T_c, where VFT predicts a divergence of the relaxation time. The temperature T_{VFT} is physically unattainable in the liquid state as the laboratory glass transition temperature T_g is higher than T_{VFT} for all known systems. For many of glass-formers, T_{VFT} is very similar to T_K, the Kauzmann temperature (described later). Considering all the temperatures one can write the following relations between them: $T_{VFT} \approx T_K < T_g < T_c \approx T_x < T_{onset} < T_m$.

1.3 Static properties

Till now, we have looked at the dynamical properties, i.e., how the system evolves with time. Now we would like to understand how structural, static properties change during the glass transition.

1.3.1 No significant change in structure

There is no obvious structural change when a liquid becomes glass, unlike in the case of other known critical phenomenon. Structural measures like the radial distribution function or the static structure factor show an increase in magnitude in other

well-known critical phenomena. Three phases of matter (gas, liquid, crystal) can be distinguished by looking at the radial distribution function, $g(r)$. While $g(r)$ is always zero at small r due to short range repulsion, at comparatively larger r, $g(r)$ shows a peak corresponding to the first layer (or shell) of particles around the focal one. For liquids, peaks at larger r are lower because correlations are weaker, signifying the lack of long range order in liquids. In contrast, crystals have long range order, the peaks are very sharp, and do not decay with r for ideal crystals, showing slight broadening at finite temperatures. Gasses, which do not have any structure, show no features in $g(r)$, implying that it is equally likely to find a particle at any distance r from a given particle, beyond a short distance where the short range repulsion prevents overlaps. Another measure of structure which is computed in experiments is the static structure factor, $S(q)$, which is the Fourier transform of $g(r)$. These structural quantities, while showing a clear change for the liquid-gas and liquid-crystal transition do not show any significant change near the glass transition. The static structure factor or radial distribution function of the glass is almost indistinguishable from that of a high temperature liquid. In the temperature range for which one observes a significant change in dynamics, one observes an almost insignificant change in structure: a slight modification of the peaks is observed. There have been recent studies which attempt to understand if one can infer a large change in dynamical properties from subtle changes in structural properties [72].

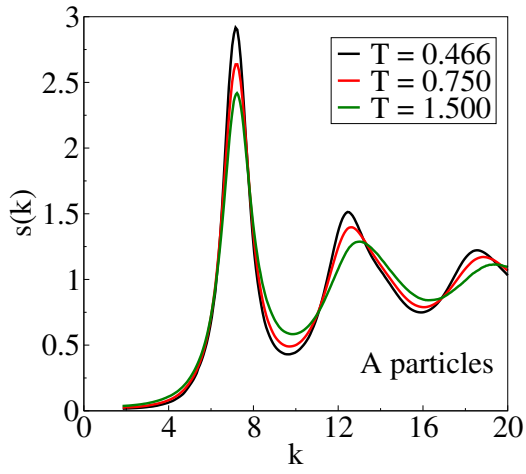

Figure 1.6: Static structure factor of the LJ liquid at three different temperatures does not show any significant change though the dynamics changes considerably over the same range of temperatures.

1.3.2 Kauzmann paradox: Entropy crisis

The entropy of any system at a temperature T can be calculated from the specific heat using the following relation,

$$S(T) = S(T_{ref}) + \int_{T_{ref}}^{T} dT' \frac{C_p}{T'} \tag{1.7}$$

where T_{ref} is the reference temperature. $\Delta S(T) = S_{Liquid}(T) - S_{Crystal}(T)$ is termed as the *excess entropy* of the liquid over the crystal. Let us use melting temperature, T_m, as the reference temperature. Correspondingly, $\Delta C_p(T) = C_{P,Liquid}(T) - C_{P,Crystal}(T)$, $\Delta S(T) = \Delta S(T_m) - \int_T^{T_m} dT' \frac{\Delta C_p}{T'}$. The specific heat for a liquid is higher than that of a crystal. From the above equation, we can see that the excess entropy of a supercooled liquid decreases with temperature. In Fig. 1.7, $\frac{\Delta S(T)}{\Delta S(T_m)}$ is plotted against T/T_m for many different systems for a range of temperature. We can see from this plot that the extrapolated excess entropy will vanish at a finite temperature, conventionally termed the Kauzmann temperature, T_K. For some systems, the liquid entropy is lower than the crystal entropy below T_K. The entropy is zero at zero temperature, which would imply that liquid entropy is negative, violating the third law of thermodynamics. This phenomenon was first pointed out by Kauzmann and is known as the *entropy crisis* or *Kauzmann's paradox* [73] As it is impossible to equilibrate a liquid beyond T_g by

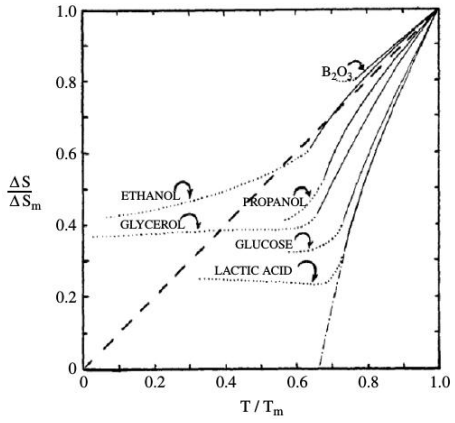

Figure 1.7: Excess entropy as a function of temperatures which becomes zero at T_K. The figure is taken from [73]

conventional methods, whether excess entropy (or the configurational entropy) goes to zero at finite temperature is as yet unknown. However, attempts have been to made to bypass this difficulty by studying a system where a finite fraction of particles are pinned; their positions do not evolve with time. This system is called the random-pinning glass-former. Using theoretical arguments [74] and subsequently in numerical works [75, 76] it has been shown that by increasing the pinning fraction, T_K can be enhanced, and configurational entropy goes to zero at T_K. In a subsequent work,

Ozawa *et. al.* have shown that the entropy in ideal glass may not be purely vibrational; particles can explore more than one inherent structure [77]. However, Chakrabarty *et. al.* [78] have claimed that pinning does not change T_K, rather it changes the fragility of the system. Further study in this direction or the development of new methods to equilibrate the system below T_g may help us to resolve this paradox.

1.4 Theories of glass transition

We see that glass forming liquids show rich phenomenology. However, concrete and complete description which can explain all the phenomenology is still missing. In the following section, I will summaries a few theoretical approaches which can partly capture those phenomenology. Before I do so, it may be important to keep in mind the kind of questions a theoretician seeks to address while constructing a theoretical framework.

- How do we explain the rapid increase of relaxation time as T_g is approached from a higher temperature ?
- What is the origin of super Arrhenius behaviour of relaxation time?
- Is there any relation between the dynamics and thermodynamics and how are they related ?
- Does there exist a finite temperature divergence of the time scale?
- What could be the length scale which can explain the growth of time scale ?

1.4.1 Adam-Gibbs theory

In 1965, G. Adam and H. Gibbs introduced a theory called Adam-Gibbs theory which explains the temperature dependence of the relaxation time in terms of the configurational entropy [79, 80]. The configurational entropy measures the number of independent configurations in configuration space that a system can reside in at a given temperature and density. The configurational entropy, S_c is computed as the difference between the total entropy (S_{tot}) and the vibrational entropy (S_{vib}) of the system [81]. This definition of the configurational entropy is based on the energy landscape picture [71,82,83] where the system vibrates around a potential energy minimum and occasionally jumps from one minimum to another. The Adam-Gibbs theory was the first successful attempt to connect the dynamics and the thermodynamics of glass-forming liquids. According to this theory, the motion of particles in the liquid becomes correlated as the temperature is lowered and the relaxation of the system occurs through

the collective rearrangement of larger and larger regions of correlated particles which are called *Cooperatively Rearranging Regions* (CRR). CRRs define subsystems consisting of a group of particles which can rearrange as a group from one configuration to another independently of their environment. However, individual particles or subsets of CRRs are incapable of rearranging independently. As a result, there are a small number of locally stable states, Ω, that are available for a typical CRR to be found in. This theory assumes Ω is constant, independent of temperature or the size of the CRR. There is a lower limit on Ω which is two since it must have at least two configurations available to it, one of which the region resides in before the transition and the other one to which it may move [79,80]. Another assumption of this theory is that the CRRs are independent, and that they interact weakly with their surroundings. Thus, the number of states that the system can access globally is $\Sigma = \Omega^{(N/n)}$. Here, N is the total number of particles, n is the typical number of particles in each CRR. The configurational entropy, S_c, which is the logarithmic density of the number of stable states,

$$S_c = \frac{1}{N}\log(\Sigma) = \frac{\log(\Omega)}{n} \tag{1.8}$$

$$n(T) = \frac{\log(\Omega)}{S_c(T)} \tag{1.9}$$

where $n(T)$ is the number of particle in a CRR at temperature T. As S_c decreases

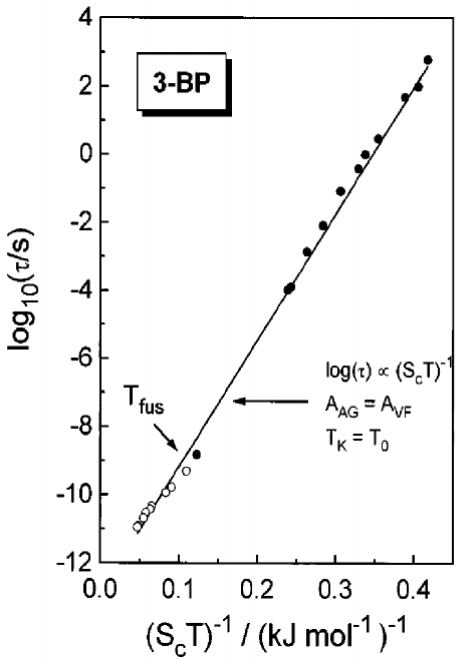

Figure 1.8: Experimental verification of the Adam-Gibbs relation. This figure is taken from [84]

with the lowering of temperature, the size of the CRR, which gives a length scale of the system, increases at lower temperature. Thus, the above relation explains how

the length scale increases with the decrease of configurational entropy. The further assumption of this theory is that energy barrier for a rearrangement is proportional to the size of the CRR, $n(T)$. If we use this assumption in the Arrhenius formula, we obtain the Adam-Gibbs relation:

$$\tau(T) = \tau_0 \exp\left(\frac{n(T)}{T}\right) \tag{1.10}$$

$$\tau(T) = \tau_0 \exp\left(\frac{C}{TS_c(T)}\right) \tag{1.11}$$

C is a constant. Adam-Gibbs theory has been tested for a wide variety of model systems in simulations as well as in experiments, and it has been shown that this relation is valid for an accessible range of temperatures. In Fig. 1.8 we showed one such example from experiments. Using the linear temperature dependence of TS_c (which comes from fitting experimental data), $TS_c(T) = K/T_K(T - T_K)$, the AG relation becomes

$$\tau(T) = \tau_0 \exp\left(\frac{D}{T - T_K}\right) \tag{1.12}$$

The above equation is the same as the VFT relation for $T_K = T_0$, the Kauzmann temperature where S_c goes to zero. It has been observed that $T_K \sim T_0$ [84] for a large number of systems with a few exceptions.
Even though the AG relation holds for different systems, this theory has many limitations [85]. i) The main ingredient of the AG relation is the presence of CRRs. However, the method to determine the size and shape of CRRs is not clearly defined. ii) The assumption that Ω is constant has no theoretical or experimental basis. Despite these limitations, the AG relation is used extensively to explain the relaxation dynamics of glass-forming liquids. In this thesis, we investigate the AG relation at higher spatial dimensions and check whether it holds for higher spatial dimensions as well.

1.4.2 Mode Coupling Theory

One of the most successful theories which can explain this complex phenomenology is Mode Coupling Theory (MCT). This theory, based on the exact microscopic description of a correlated liquid, was first introduced by Gotze and coworkers in the 1980s. It takes the static property of a liquid such as structure factor as input and aims to predict the dynamical properties of that liquid. It distinguishes different liquids via structure factor only. In the Zwanzig-Mori formalism of MCT, the whole universe is divided into two mutually orthogonal sub spaces: One consisting of the variables of interest, and other one containing “everything else". Now, the aim is to describe the dynamics of the variable of interest in the presence of other “non interesting variable". Our variable

of interest is the density function $\rho(r,t)$.

Using the projection operator formalism, time evolution of any correlation function C cab written as:

$$\frac{d\mathbf{C}(t)}{dt} = i\Omega.\mathbf{C(t)} - \int_0^t ds\mathbf{K}(s).A(t-s) + \mathbf{f(t)} \tag{1.13}$$

where, Ω is the frequency matrix, $f(t)$ is the fast fluctuating force, defined by, $f_t = e^{i(1-P_A)Lt}i(1-P_A)LA(0)$ and $\mathbf{K}(s)$ is the time dependent memory function given by the auto correlation function of the fluctuating force. The above equation, eq. 1.13 is called generalized Langevin equation which is an exact equation. However, there is no rigorous solution to the equation and approximation is used to solve this. Two such approximation is made: (i) Approximate the memory function as a four point density correlation function,

$$\mathbf{K}(t) \sim \sum_{k_1,k_2,k_3,k_4} \langle \rho^*(k_1,0)\rho^*(k_2,0)e^{i(1-P_A)Lt}\rho(k_3,0)\rho(k_4,0)\rangle \tag{1.14}$$

and (ii) Four point correlation function can be factorized into two two point correlation functions. Note that sometimes MCT is considered a mean field theory because of this approximation. Now, using these approximations full MCT equation can be obtained,

$$\frac{d^2F(k,t)}{dt^2} + \frac{K_BTK^2}{mS(k)}F(k,t) + \int_0^t dsK_{MCT}(k,s)\frac{dF(k,t-s)}{st} = 0 \tag{1.15}$$

with the memory function given by

$$K_{MCT}(k,t) = \frac{\rho k_BT}{16\pi^3 m}\int d\mathbf{q}|V_{\mathbf{q},\mathbf{k}-\mathbf{q}}|^2F(q,t)F(|\mathbf{k}-\mathbf{q},t) \tag{1.16}$$

,where k_B is the Boltzmann constant, m is the particle mass, ρ is the bulk density and the factors

$$V_{\mathbf{q},\mathbf{k}-\mathbf{q}} = k^{-1}[\mathbf{k}.\mathbf{q}c(q) + \mathbf{k}.(\mathbf{k}-\mathbf{q})c(|\mathbf{k}-\mathbf{q}|) \tag{1.17}$$

are referred to as vertices with $c(k) = \rho^{-1}[1 - \frac{1}{S(k)}]$ denoting the direct correlation function. For any glass forming liquid, at any given ρ and T if $S(k)$ is known then using the above equation one can predict the full microscopic dynamics. The transition from liquid to glass can be described by solving separate MCT equations for the range of temperature and density.

Although MCT uses many approximations and it only takes $S(k)$ as an input which does not change much with temperature, it can make some remarkable predictions. Of course, MCT can correctly predict scaling properties in the β relaxation regime. MCT predicts the cage formation is the key mechanism for the vitrification. MCT predicts

a glass transition at T_c, the relaxation time diverges at T_c which implies $F(k,t)$ does not decay to zero. The corresponding non-ergodicity parameter is also often in good agreement with experiments. However, the MCT predicted T_c is much larger than actual T_g. The power law divergence also holds for the small range of relaxation time about $2-3$ decades, which implies that it fails to explain the dynamics in the deeply supercooled regime. Also, MCT fails to describe the heterogeneity of the dynamics. Subsequently, there have many attempts to improve the prediction of standard MCT. Extended MCT, generalized MCT and inhomogeneous MCT, to name a few. However, all these are approximate theory and unable to predict all the aspects of the glass transition.

Although MCT has been described as a mean field theory because of the factorisation of the four point correlation function it has been discussed in [86, 87] and subsequent works that MCT in the standard form is not the correct mean field theory in the sense that it is not the right description in the limit of large dimensions (it has pathological behavior for large d as discussed in [86]). Subsequently, attempts have been made to construct a mean field theory that could be exact at infinite dimensions. Below, I will describe one of the recent developments.

1.4.3 Mean field phase diagram of amorphous systems

In the previous sections, we have observed that systems undergo a phase transition from liquid to glass at a finite temperature (or finite density for hard sphere systems). It is possible to cool or compress glasses within the glass phase, motivating the question of how the property of glasses change as they are compressed/cooled further. This question has been investigated in the framework of a mean field theory of glasses [88–92]. We introduce this theory, beginning with a brief discussion of some techniques relevant to the discussion.

1.4.3.1 Quenched disorder

Let us consider a disordered system which can be characterized by the following generic Hamiltonian $\mathcal{H}(\{a_T\},\{a_D\})$. Here, $\{a_T\}$ denotes the thermal variable and $\{a_D\}$ denotes the disorder variable. The thermal variables obey Hamilton's equations of motion. The disorder variables $\{a_D\}$ are random which are drawn from a given probability distribution. If these variables do not change during the course of an experiment, the disorder is said to be *quenched*.

1.4.3.2 Replica Method

The free energy of such a system is given by

$$[F]_D = -k_B T[\ln Z(\{a_D\})]_D = -k_B T \int \mathcal{D}\{a_D\} P(\{a_D\}) \ln Z(\{a_D\}) \tag{1.18}$$

$P\{a_D\}$ is the probability distribution from which $\{a_D\}$ is drawn. Solving the partition function for a Hamiltonian without disorder is in itself difficult. In the presence of the disorder, it is even more difficult. The averaging over disorder can be computed using a method called replica method. This method involves the use of the following identity

$$\langle \ln z \rangle = \langle \lim_{n \to 0} \frac{z^n - 1}{n} \rangle \tag{1.19}$$

$$[\ln Z]_D = \lim_{n \to 0} \frac{[Z^n]_D - [1]_D}{n} = \lim_{n \to 0} \frac{[Z^n]}{n} - \frac{1}{n} \tag{1.20}$$

Where n is the index of *replicas* which are different copies of the system, with the same disorder. For a system of n replicas the partition function can be written as,

$$Z^n(\{a_D\}) = Tr_{\{a_T^\alpha\}} \exp[-\beta \sum_{\alpha=1}^{n} \mathcal{H}[(\{a_D\}, \{a_T^\alpha\})] \tag{1.21}$$

We observe that it is easier to take the disorder average of the above function.
We next discuss the mean field theory of glasses for a hard sphere glass-former.
In the infinite dimensional limit, the glass forming liquid is confined to a single free energy minimum at the dynamical transition density, ϕ_d (Mode Coupling transition density). Correspondingly, the diffusion constant strictly vanishes beyond ϕ_d. The system remains confined to a restricted region of phase space for an infinite time. Below, we will discuss the behaviour of the system at a density, $\hat{\phi} > \hat{\phi}_d$. Let us consider an equilibrium configuration, $Y = \{y_i\}$ at a density $\hat{\phi}_g$ which is larger than ϕ_d and another configuration, $X(t) = \{x_i(t)\}$ which evolves according to the Langevin equation of motion with the initial condition $X(0) = Y$. As the diffusion constant is zero in this regime, the MSD, Δ between $X(t)$ and Y remains finite even in the long-time limit.

$$\lim_{t \to \infty} \Delta[X(t), Y] = \Delta_r \tag{1.22}$$

The dynamics of $X(t)$ will be stationary as $X(0) = Y$ and Y is sampled from the equilibrium distribution. Thus, we can write,

$$\Delta[X(t+\tau), X(t)] = X(\tau) \to \lim_{\tau \to \infty} X(\tau) = \Delta_r \tag{1.23}$$

$X(0)$ is compressed to another density $\hat{\phi} \neq \hat{\phi}_g$ and the system is allowed to evolve at this new density $\hat{\phi}_g$. If the diffusion constant remains zero at the new density, it is expected that the equation 1.22 will also hold. Correspondingly $X(0), X(t), X(t+\tau)$ will all be close to each other and at log time limit it will follow:

$$\Delta[X(t+\tau), X(t)] = X(\tau) \rightarrow \lim_{\tau \to \infty} X(\tau) = \Delta_1 \tag{1.24}$$

Δ_r is the relative long time distance between $X(t)$ and Y, whereas Δ_1 is the displacement between different configurations which are separated by time τ. In general, Δ_1 and Δ_r are different except when both X and Y are at the same density.
One can next consider the thermodynamics of the system. We assume that X follows Boltzmann distribution, however, a constraint on the distance between Y and X is maintained. With this assumption, we can write the partition function as,

$$Z[\Delta_r, \hat{\phi}|Y, \hat{\phi}_g] = \int dX \exp(-\beta H(X; \hat{\phi}))\delta[\Delta_r - \Delta(X, Y)] \tag{1.25}$$

where $H(X)$ is the energy of the configuration X, and the restricted average is accounted for with the delta function. The free energy of the glass can be obtained by taking an average over the initial configuration Y. Y plays the role of quenched disorder in the system and free energy can be computed by using replica method. The free energy obtain in this method is called Franz-Parisi constrained free energy or potential,

$$V_{FP}[\Delta_r, \hat{\phi}|\hat{\phi}_g] = \overline{f(\Delta_r, \hat{\phi}|Y, \hat{\phi}_g)}^Y \tag{1.26}$$

where

$$f(\Delta_r, \hat{\phi}|Y, \hat{\phi}_g) = -\frac{1}{N\beta} \ln(Z[\Delta_r, \hat{\phi}|Y, \hat{\phi}_g]) \tag{1.27}$$

$$V_{FP}[\Delta_r, \hat{\phi}|\hat{\phi}_g] = -\frac{1}{N\beta} \int \frac{dY}{Z[\hat{\phi}_g]} \exp(-\beta H(Y; \hat{\phi}_g)) \ln(Z[\Delta_r, \hat{\phi}|\hat{\phi}_g]) \tag{1.28}$$

where $Z[\hat{\phi}_g] = \int \exp(-\beta H(Y; \hat{\phi}_g))$ is the equilibrium partition function at $\hat{\phi}_g$.
At the infinite dimensional limit, the equation. 1.28 could be solved using the replica method [88] and V_{FP} is expressed as a function of the order parameters, Δ_r and Δ_1.
Using the above formalism, the mean field phase diagram (Fig. 1.9) of the amorphous system can be obtained. The reduced pressure is obtained from the equation of state which can be derived from the equation. 1.28 using virial expansion [90]. Now starting from the equilibrated configuration at $\hat{\phi}_g$ if the system is decompressed, the glass undergoes a melting transition; it melts into a liquid. However, upon compression the glass explores lower energy, stabler glassy states and remains dynamically arrested. Upon further compression, the glas undergoes the Gardner transition at ϕ_G. Beyond ϕ_G, the relation between Δ_r and Δ_1 breaks down and a complex free energy landscape

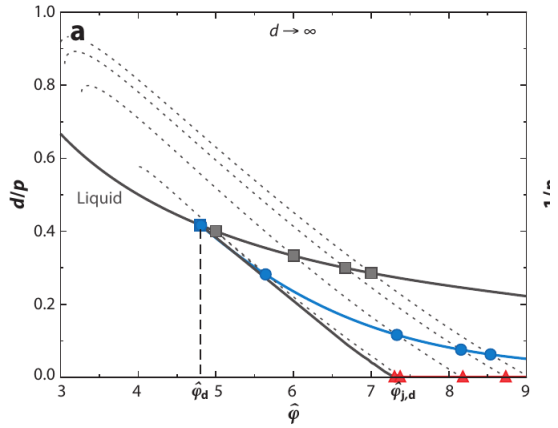

Figure 1.9: The mean field phase diagram of the hard sphere fluid. The inverse reduced pressure is plotted against the scaled volume fraction. The black line corresponds to the equilibrium equation of state. The blue squares correspond to the dynamical transition point. Blue dots represent the Gardner transition point. Red dots denote the jamming point. The figure is taken from [92].

emerges [93]. Compressing further within this phase, the pressure eventually diverges and the system reaches the jamming density ϕ_J.
Subsequently, these developments have led to investigations of how the infinite spatial dimensional results relate to behaviour in finite dimensions. Mangeat and Zamponi [94] have proposed an approximate scheme that not only provides the same qualitative phase diagram of infinite dimension and critical exponents are same but also offers concrete numbers for various quantities such as transition density. This scheme takes the equation of state and correlation function as inputs and provides the replicated free energy as an output from which physical observables can be derived. By construction, this scheme becomes exact at infinite dimensions. For the hard sphere interaction potential, different transition densities such as the dynamical transition density,ϕ_d, the Kauzmann density ϕ_K is measured infinite dimensions (upto dimension=60) following this scheme. It has been found that the scaled ϕ_k $(2^d\phi_K)$ asymptotically goes to $\log d$, whereas the scaled $\phi_d(2^d\phi_d)$ becomes constant ($\sim 4.8067..$) at a limit large dimension (shown in Fig. 1.10). Following the same scheme the largest jamming density, ϕ_{th} is also computed; in the infinite dimensional limit, the scaled ϕ_{th} $(2^d\phi_{th})$ becomes constant 6.25818 (shown in Fig. 1.10).

In this thesis, using computer simulations, we have computed ϕ_J and ϕ_K and we compare our results to theoretical predictions.

1.5 Jamming transition

In the above sections, we have discussed how a liquid becomes a glass by lowering the temperature. In these systems, thermal fluctuations are very important for the

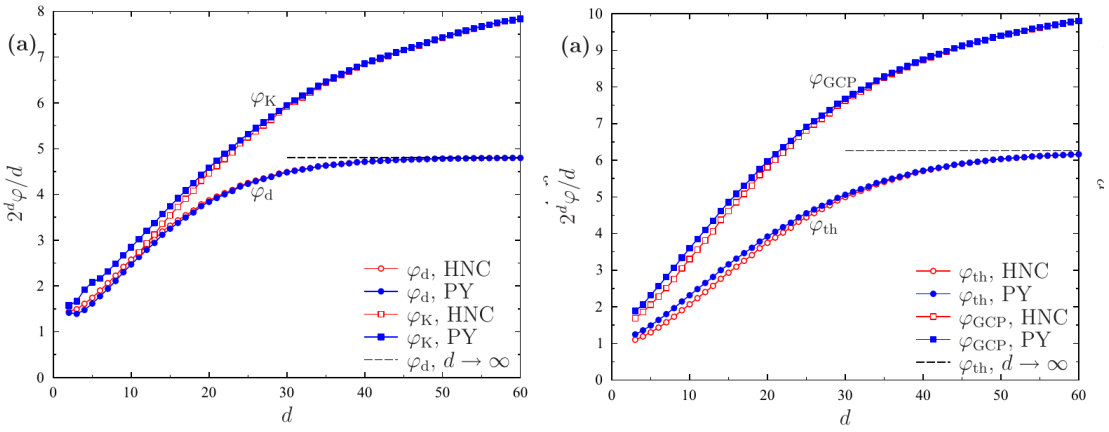

Figure 1.10: Left: ϕ_d and ϕ_K is shown against dimension using different approximate scheme. Right: The largest glass density ϕ_{GCP} and ϕ_{th} is shown as a function of dimension using different approximate scheme. The data is taken from [94].

stability of the system. However, a class of materials such as foams, where the constituent particles' sizes are large. As a result, thermal fluctuation plays a negligible role in that system. When we compress these athermal systems, after some point they lose their ability to flow; this non-equilibrium transition from the flowing state to jammed system is called the *jamming transition*, with the jamming transition point ϕ_J [95, 96]. This point is not a unique point [97]. Depending on the initial conditions and on the protocol, it may vary from $0.639 - 0.642$ for mono-disperse systems and is between $0.648 - 0.662$ for bidisperse systems. Even though the microscopic origin of the glass transition and the jamming transition are very different, they share some interesting similar phenomenology in particular when assemblies of soft particles are considered. Below the critical density/temperature, both the systems flows. Above the critical density/temperature the system behaves like a solid; it yields on application of a critical stress [98]. The dynamics near the transition is heterogeneous in both the systems [43]. The natural questions that arises naturally is whether there is any relation between the two transitions. Using a theoretical model it has been shown that the jamming transition occurs well inside the glassy phase [99, 100]. The flow curves of thermal and athermal systems reveal jamming and glass transitions share universal exponents [101]. Considering an infinite dimensional model system of hard spheres, Charbonneau *et al.* [91] showed that although the jamming occurs well inside the glassy phase, the two transitions are different. On the other hand, rheological experiments [102, 103] and recent simulations [104] in a 3d system support the idea that these two transitions are different. It has been claimed that the glass transition density will be above the jamming transition density [104]. Theoretical studies which consider varying spatial dimension [105–108] show that the relationship between these two transitions depends on the dimensionality.

In this thesis, we study the glass and jamming transition in different spatial dimensions and try to understand the relation between them.

1.6 Aging

In the above sections, we have discussed the interesting phenomena of super cooled liquids when in equilibrium below T_g. However, we can ask what happens when the temperature is lowered below the glass transition temperature, T_g. As we discussed earlier, the relaxation time becomes astronomically large below T_g, as a result the physical properties of the system evolve slowly with time. This phenomenon is called 'aging'.

The simplest way one can understand aging is the following: after equilibrating a liquid at a high temperature, it is subsequently quenched to a lower temperature below T_g. At this lower temperature, the system evolves for a time t_w. Liquids that are evolved for different periods, t_w, have different properties; those evolved for longer t_w are found to be "aged" in comparison to those evolved for shorter t_w.
Aging implies that the system will remember the waiting time, t_w, its 'age'; the properties of the system depend on the t_w. On the time scale of observation, quantities such as the volume or the potential energy, which are calculated from instantaneous snapshots of the liquid, do not show good evidence of aging, while, the two-time quantities (as density-density correlation function) depend explicitly on both times, rather than on their difference. In Fig. 1.11, a typical behavior of the self-intermediate scattering function is shown for the Lennard-Jones molecular liquid quenched below T_g. In an aging system, the relaxation time increases with waiting time, t_w. This implies that t_w is the relevant timescale in an aging system as the equilibration timescale is diverging.
One could ask whether it is possible to find a way to erase the history of the system. Investigations into whether imparting energy to the system through deformations such as shear would "reverse" the apparent aging led to interesting findings. On the one hand, shear of sufficiently high amplitude did in fact erase the effects of aging, in fact leading to a transition to the flowing state – yielding. On the other hand, repeated cycles of low amplitude shear deformation drive the system to so-called absorbing states that encode the amplitude of shear deformation applied – the glass remembers! In the second part of thesis, we have investigated memory behaviour and the response, under cyclic shear deformation, of amorphous solids. Below, we will give a brief introduction to memory effects.

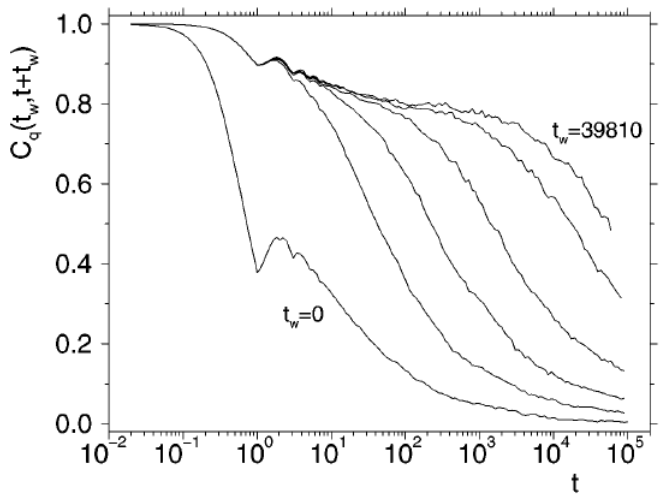

Figure 1.11: Time correlation function is plotted against time for different waiting times for the BMLJ system. The image is taken from [109]

1.7 Memory effects:

The term memory most often refers to the ability to recall a specific piece of information. If we consider the human mind as a device then we can think that it can encode some information, then the stored information will be read out at some later time and sometimes the information can be erased from that device also. In our daily life, we commonly see such a device in the form of computer memory. In fact, memory, the ability to remember something, arises in different forms in a large variety of systems [110]. Systems which are not in equilibrium are capable of retaining a memory of their past history. Examples include a broad range of systems, magnetic memory, super fluid helium in capillaries [111], shape memory [112], artificial spin ice [113], many particle vortex assemblies, [114] crumpled thin sheets and elastic foams [115] etc. In these systems, when a field is applied to the system, it gets stuck to one of its local energy minimum states and as a result, ergodicity is broken. Simple systems, like magnetic system, have a finite number of local energy minimum structures. In these systems, there is a one-to-one correspondence between the state that the system is trapped in and the field with which it was driven. As a result, it is easy to read out the stored information. However, complex systems have a large number of minima. The existence of such multiple minima opens up a path for the system to be trapped into one of these when driven by an external field. As a result, it is difficult to find a simple relation between the state where the system will be trapped and the applied field. Correspondingly reading out the stored information is not trivial.
In the following section, we will briefly discuss different kinds of memory with increasing complexity and discuss the different protocols of reading.

1.7.1 Memory of a direction and magnitude

One of the simplest forms of memory is the memory of direction; a material can remember the latest direction in which it was driven. A common example of such memory is magnetic storage. The magnetic system has two well-defined states. When it is driven by an external field, individual magnetic ions are all aligned in the same direction, whereas the ions will be aligned in the opposite direction if we reverse the direction of the external field. This one-to-one correspondence between the driven field and the final state is used in digital storage. The memory of direction is also observed in the materials displaying 'pulse sign memory' [116, 117]. When an electric pulse is applied to the system, the response of the system, the voltage pulse, becomes slow or fast depending on the direction of the preceding pulse. This simple form of memory of direction can occur in vastly different systems: from simple systems like coupled gears to more disordered systems such as a suspension of non-Brownian particles and dry granular matter. Thus, understanding the memory behaviour in these systems may help us to identify the underlying connections between these largely different systems.
Another example of memory where a single input is stored is *Kovacs effect* [118, 119]. This effect is observed when a glass former is cooled from a high temperature, T_0 to a low temperature, T_1, and allowed to relax for some time but not fully, following which, the temperature of the system raised again, $T_2 (T_1 < T_2)$. When the evolution of the system is monitored by investigating volume, a non-monotonic behavior of the volume is observed. It shows a peak at a time which depends on the duration of time spent at T_2, the lower temperature. The system has memory of the time duration.

1.7.2 Hysteresis and return point memory

In the previous sections, we describe memory of a direction. Depending on the recent direction the system can be trapped in either of the two states. Now, we can think of a slightly complex system where the system will be in state "+1" or "−1" when it is driven by an external field H. The system will be in the +1 state when the applied field $H \geq H^+$ or it will be in −1 state when $H \leq H^-$ ($H^+ \neq H^-$). However, when the field is in between H^+ and H^-, the state will depend on the history of the driving field. Thus, this simple system can give rise to hysteresis and is often called as hysteron. There are many real systems which can be modelled as a system consisting of a large number of hysterons. These systems show important memory effects called return point memory (RPM). Below, we will discuss the hysteresis and return point memory effects in a magnetic system.

When a ferromagnetic material is driven by a magnetic field, and one varies the magnetic field adiabatically between a large positive (H_{sat}) and negative field ($-H_{sat}$), the magnetization forms a closed loop; termed as hysteresis loop. This hysteretic system shows Return Point Memory(RPM) [120]. If we apply the field in the following way, we will see RPM (Fig. 1.12).

- Step 1: The applied field is lowered from H_{sat} to some magnetic field (H_{min}).
- Step 2: Field is increased to some another field H_{max}, which is also lower than H_{sat}.
- Step 3: It is lowered again to H_{min}.

The final state of the system is the same as the initial state when it first reaches to H_{min}, which implies the system can remember the initial state. This same memory behaviour can be extended to sub-cycles within cycles and so on. One important thing to notice here, while increasing H, if we continue past H_{max}, we will erase the memory. Under some specific conditions, an anti-ferromagnetic system also shows RPM [121].

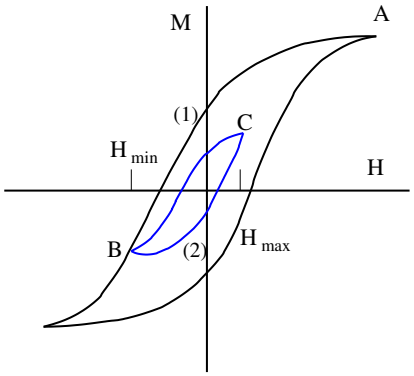

Figure 1.12: Schematic of hysteresis loop for a ferromagnet, showing RPM

RPM makes a read protocol possible, but it depends on a special property called the "No Passing rule" [122] which is described below.
A state $S = (s_1, s_2, s_3..s_n) \geq R = (r_1, r_2, r_3..r_n)$ if and only if for all i, $s_i \geq r_i$. This ordering of states is called *partial ordering*. However, it is not easy to differentiate between any arbitrary pairs of state using this relation, as most of them will not have any relation. Now let us consider a system, where such an ordering exists and the state $S(t)$ is evolving under the field $H_S(t)$ and R(t) is evolving under the field $H_R(t)$. If we assume that initially $S(0) \geq R(0)$, and the fields $H_S(t) \geq H_R(t)$, then according to "No-passing" theorem the system will remain $S(t) \geq R(t)$.

1.7.3 Memory in sheared suspensions

So far, we have discussed memory effects where memory can be encoded just by a single cycle of driving. However, in many cases, one needs multiple cycles of driving to encode a memory. Memory effects in sheared suspension is one such case where we need multiple cycles of shear deformation to encode a memory.
When this system is deformed periodically for a large number of cycles, it shows a non-equilibrium phase transition from a diffusing to non-diffusing state as we change the amplitude of shear deformation. Depending on the amplitude of shear deformation, the system reaches either to a diffusing state or to a non-diffusing, absorbing state. These two states are marked by a critical value (depends on the volume fraction) called γ_c. In absorbing states, particles cease to move when it is viewed stroboscopically, i.e., zero strain after each cycle. After n number of cycles with a fixed amplitude γ_1, the system reaches to an absorbing state. This behaviour can be reproduced successfully in the random organization model [123]. It has been observed that when the training process of repeatedly shearing by γ_1 is complete, a shear deformation with all $\gamma < \gamma_1$ results in no rearrangements of particles since a larger amplitude shear encloses a smaller value en route. As a result, this procedure encodes a memory, which can be read by performing a single cycle of shear deformation with variable amplitude and measuring the fraction of particles that are moved. As soon as γ_i crosses γ_1, the irreversibility occurs. As a result, there occurs a sharp change of slope in the plot of the fraction of particles that are moved vs the deformation amplitude γ. This kink characterises the memory (Fig. 1.13) (results are shown here for random organization model). The system has remembered the amplitude of shear deformation. Interestingly, when each shear cycle contains more than one amplitude, the system can encode multiple memories transiently. However, when the system reaches a steady state for the highest γ, the system loses all but the highest amplitude memory [124–126].

1.7.4 Memory behavior of amorphous solids

Amorphous solids are another example where one needs multiple cycles of driving to encode a memory. However, unlike the sheared suspension, this system can remember multiple memories persistently. Below we will discuss the memory effects of amorphous solids.
Upon application of small strains, glasses or amorphous materials respond elastically. However, they display plastic deformation when the strain is larger than a specific yield strain, which is a material dependent property. Although this broad mechanical behaviour is similar to that of crystalline solids, a lack of translational order and consequently not having well-defined defects makes amorphous material distinct from its

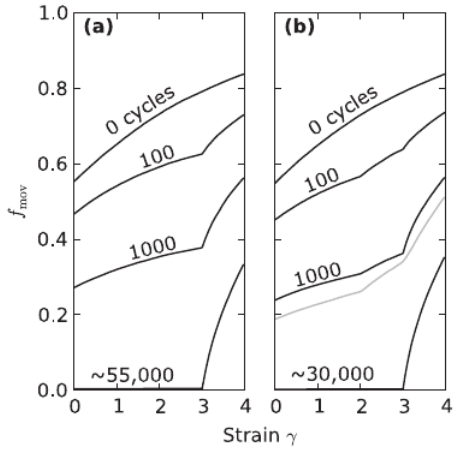

Figure 1.13: (a): Fraction of particles moved (f_{mov}) is plotted as a function of reading amplitude for the system, trained at $\gamma_1 = 3$. Different lines correspond to different numbers of training cycles. f_{mov} shows a kink when the reading amplitude is the same as the training amplitude. (b): The system can remember multiple memories transiently. After a large number of cycles only the largest amplitude is remembered. The figure is taken from [124]

crystalline counterpart. Various studies on amorphous materials have focused on understanding the yielding behaviour of this system [98, 127, 128]. Recently, it has been observed that the yielding transition is associated with a non-equilibrium absorbing to diffusing transition [129, 130]. Upon application of shear deformation periodically, after a transient, the amorphous material either reaches an absorbing state or a diffusing state. When the amplitude of shear deformation is smaller than a threshold, the system reaches the absorbing state where the configuration remained unchanged after the end of the cycles, whereas if the amplitude of the deformation is larger than the threshold, the system reaches a diffusing state where configurations change from cycle to cycle. The threshold amplitude of strain corresponds to the yielding point. This transition is very similar to what was observed in sheared suspensions, discussed earlier. Now the question is, does the absorbing state of a glass-forming liquid also show memory behaviour similar to that of a sheared suspension. Fiocco *et al.* [131] have studied the memory behaviour of amorphous solids, and the answer to the above question is in the affirmative. Fiocco *et al.* [131] have shown that this system can remember not only a single amplitude of shear deformation, but also multiple memories persisitently when driven with multiple amplitudes.
The protocols of reading used by Fiocco *et al.* [131] can not be used in experiment easily. In this thesis, we have employed different protocols of training or reading. We also focus on understanding the nature of this memory by studying different systems.

Subsequently, the memory effects in amorphous solids are also observed in experiments [132, 133]. Recently a lot of efforts have been made to understand the nature

of the memory in amorphous solids. Keim *et al.* [133] has claimed that the memory in amorphous solids is RPM in nature. When the system is driven by alternating cycles of two different amplitudes, the system can remember both the amplitudes. Keim *et al.* [133] showed that the system could encode multiple memories only when the smallest amplitude is applied last. This similar behaviour is also observed in the system where RPM is observed. Specifically, they show *Presiach* model which is a classic model for RPM behavior [134], can similarly encode multiple memory. Using this analogy, it has been shown that memory in amorphous solids is RPM in nature. Subsequently, Mungan *et al.* [135], using a novel method called the transition network method [136], showed that the memory effects in a two dimensional model glass are nearly RPM. In a system with RPM, for example, the magnetic system, a memory is read by comparing the state at the maximum amplitude of the driving field between cycles [137]. However, the memory in an amorphous system is studied using the stroboscopic configurations (shear deformation, $\gamma = 0$). Following the analogy of the magnetic system, we should be studying states at maximum deformation. In a practical sense, the states at maximum deformation can also not be used to study memory behavior. However, one can think of a modified protocol where the strain is applied in one-sided manner ($0 \rightarrow \gamma_{max} \rightarrow 0$) and ask is this a better protocol for encoding and reading out the memory? As mentioned earlier, memory behaviour is observed when the system is deformed with amplitudes which are below yielding. However, so far yielding behavior is studied either by uniform shear deformation or symmetric cyclic shear deformation. In this thesis, we explore an asymmetric shear deformation protocol to understand the yielding behavior of amorphous solids.

1.8 Scope of the thesis

A consensus theory of the glass transition is still lacking. Computer simulations play a crucial role in understanding the phenomenology and in verifying theoretical predictions, since one can probe the microscopic behaviour directly. In this thesis, we study different model glasses using computer simulations. In the first part, we study glass-forming liquids in higher spatial dimensions. In the second part of the thesis, we have studied the mechanical properties, specifically yielding and memory effects of amorphous solids. The outline of the thesis is the following:

In chapter 2, the definition of the different quantities computed in this thesis, the details of the models and of the methods are presented.

In chapter 3, we study the dynamics of the glass-forming liquids for soft sphere

assemblies interacting with a harmonic potential in higher spatial dimensions. This question we ask how the jamming point and glass transition point are related to each other in this system.

In chapter 4, we study different measures of dynamical heterogeneity and fragility by varying spatial dimensions. Our aim is to understand the possible relation between heterogeneity and fragility.

In chapter 5, we study Adam-Gibbs relation in higher spatial dimensions and attempt to understand the power law relation of diffusivity and relaxation time between the two different type of particles. We ask does Adam -Gibbs relation is valid in spatial dimensions larger than three.

In chapter 6, we study memory effects in cyclically deformed amorphous solids and sphere assemblies. We ask what could be experimentally relevant protocols of reading, how memory can be erased, criteria to have persistent multiple memories.

In chapter 7, we study yielding and memory behavior using an asymmetric shear deformation protocol. We attempt to understand the role of plastic deformation for differently annealed systems and how does the protocol of shear deformation change the yielding amplitude

In chapter 8, we present the conclusions and future outlook of this thesis.

Chapter 2

Definitions, models and methods

In this chapter, I will describe the relevant definitions and formulae used to compute the different quantities of interest. I will also discuss the details of the model and the methods that I will be using in the subsequent chapters.

2.1 Definitions:

2.1.1 Two point correlation functions

For a system of N point particles, local density is defined as

$$\rho(\mathbf{r},t) = \sum_{i=1}^{N} \delta(\mathbf{r} - \mathbf{r}_i(t)) \tag{2.1}$$

The simplest possible correlation function is the two point correlation; the van-Hove function is one of them:

$$\begin{aligned} G(\mathbf{r},t) &= \frac{1}{\rho}\langle \rho(\mathbf{r},t)\rho(0,0)\rangle & (2.2)\\ &= \left\langle \frac{1}{N}\int d\mathbf{r}\prime \rho(\mathbf{r}'+\mathbf{r},t)(\rho(\mathbf{r}',0)\right\rangle \\ &= \left\langle \sum_i \sum_j \frac{1}{N}\int d\mathbf{r}\prime \delta(\mathbf{r}'+\mathbf{r}-\mathbf{r}_j(t),t)\delta(\mathbf{r}'-\mathbf{r}_i(0),0)\right\rangle \\ &= \frac{1}{N}\left\langle \sum_j \sum_i \delta(\mathbf{r}-\mathbf{r}_j(t)+\mathbf{r}_i(0))\right\rangle & (2.3) \end{aligned}$$

where ρ is the average number density, the angular bracket corresponds to the ensemble average. It gives the probability density of finding a particle j in the vicinity of r at time t given that the particle i was in the vicinity of the origin at time $t = 0$. $G(\mathbf{r},t)$ can be divided into two parts:

(i) The self part $G_s(\mathbf{r},t)$, which gives the probability density of finding a particle i in the vicinity of r at time t given that this particle was at origin at time $t=0$, and
(ii) The distinct part $G_d(\mathbf{r},t)$, which gives the probability density of finding a particle $j \neq i$, given particle i was at the origin at time $t=0$.
This gives:

$$\begin{aligned} G(\mathbf{r},t) &= G_s(\mathbf{r},t) + G_d(\mathbf{r},t) \\ G_s(\mathbf{r},t) &= \frac{1}{N}\left\langle \sum_i \delta(\mathbf{r} - \mathbf{r}_i(t) + \mathbf{r}_i(0)) \right\rangle \\ G_d(\mathbf{r},t) &= \frac{1}{N}\left\langle \sum_i \sum_{j\neq i} \delta(\mathbf{r} - \mathbf{r}_j(t) + \mathbf{r}_i(0)) \right\rangle \end{aligned} \tag{2.4}$$

The Fourier transform of $G(\mathbf{r},t)$ from real to k space gives the intermediate scattering function $F(\mathbf{k},t)$

$$\begin{aligned} F(\mathbf{k},t) &= \int d\mathbf{r} G(\mathbf{r},t)\exp(-i\mathbf{k}.\mathbf{r}) \\ &= \frac{1}{N}\langle \rho(\mathbf{k},t)\rho(-\mathbf{k},0)\rangle, \end{aligned} \tag{2.5}$$

where

$$\rho(\mathbf{k},t) = \int d\mathbf{r}\rho(\mathbf{r},t)\exp(-i\mathbf{k}.\mathbf{r}) \tag{2.6}$$

This implies that $F(\mathbf{k},t)$ measures the correlation of the local density in the Fourier space. Again, $F(\mathbf{k},t)$ can be divided into the self and distinct parts:

$$\begin{aligned} F(\mathbf{k},t) &= F_s(\mathbf{k},t) + F_d(\mathbf{k},t) \\ F_s(\mathbf{k},t) &= \int d\mathbf{r} G_s(\mathbf{r},t)\exp(-i\mathbf{k}.\mathbf{r}) \\ F_d(\mathbf{k},t) &= \int d\mathbf{r} G_d(\mathbf{r},t)\exp(-i\mathbf{k}.\mathbf{r}) \end{aligned} \tag{2.7}$$

$F_s(\mathbf{k},t)$ can be directly compared to experimental measure of intermediate inelastic neutron scattering function, $I_{inc}(k,t)$. In this thesis, we compute $F_s(\mathbf{k},t)$ at $\mathbf{k} = k_{max}$ which corresponds to the first peak of the structure factor which we shall define later. Fourier transforming $F(\mathbf{k},t)$ further into the frequency domain, we obtain the dynamic structure factor,

$$S(\mathbf{k},\omega) = \int F(\mathbf{k},t)\exp(-i\omega t)dt \tag{2.8}$$

The dynamics is also studied by another two-point time correlation function of local

density, the overlap function ($q(t)$), which is defined by,

$$\begin{aligned} q(t) &= \int d\mathbf{r}\rho(\mathbf{r},t_0)\rho(\mathbf{r},t+t_0) \\ &= \sum_i \sum_j \delta(\mathbf{r}_j(t_0)-\mathbf{r}_i(t+t_0)) \end{aligned} \tag{2.9}$$

Here, t_0 is the time origin over which averaging is performed. Again, $q(t)$ can be divided into the self part and distinct part:

$$q(t) = \sum_i \delta(\mathbf{r}_i(t_0)-\mathbf{r}_i(t+t_0)) + \sum_i \sum_{i\neq j} \delta(\mathbf{r}_i(t_0)-\mathbf{r}_j(t+t_0)) \tag{2.10}$$

Further, in numerical computation, the δ function is approximated by a window function $w(x)$ which defines the condition of "overlap" between two particle positions separated by a time interval t, and self part of the $q(t)$ can be written as:

$$q(t) = \frac{1}{N}\sum_{i=1}^{N} w(|\mathbf{r}_i(t_0)-\mathbf{r}_i(t+t_0)|) \quad \text{where} \quad w(x) = \begin{cases} 1.0 & \text{if } x \leq a \\ 0 & \text{otherwise.} \end{cases}$$

We introduce $1/N$ factor here so that it normalizes to 1 when all the particles are correlated and goes to zero when there is no correlation between them.

2.1.1.1 Choice of the cutoff a for the overlap function:

Equation. 2.11 implies that in simulations, the value of the overlap function depends on the choice of the cutoff parameter a. The parameter a is chosen so that particles separated due to vibrational motion are considered overlapping. This implies that a^2 lies in the plateau region of the mean squared displacement (MSD) curve as shown in Fig. 2.1

2.1.1.2 Estimation of relaxation time

The structural relaxation time can be computed from the self intermediate scattering function or overlap function. At high temperatures, correlation function decays exponentially: $C(t) = C(0,T)\exp\left(-\frac{t}{\tau}\right)$. As discussed in the introduction, with the lowering of temperature, $C(t)$ develops a plateau and relaxation occurs in two-steps. Then, the relaxation time can be estimated by fitting $C(t)$ to the stretched exponential form:

$$C(t) = C(0,T)\exp\left(-\left(\frac{t}{\tau}\right)^{\beta}\right) \tag{2.11}$$

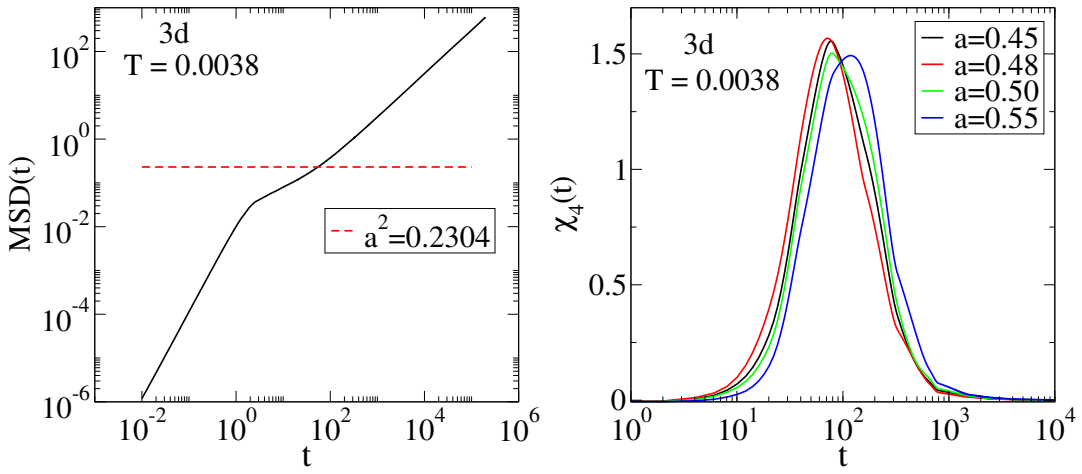

Figure 2.1: Left Panel: The MSD (3d soft sphere system) is plotted against time and the value of "a" is chosen such that it is above the plateau of the MSD curve. Right Panel: $\chi_4(t)$ is plotted as a function of time for different values of a. The value of "a" for which χ_4 is maximum is chosen as the parameter for overlap function.

Alternatively, the relaxation time can be estimated by measuring the time at which $C(t)$ decays to $1/e$. Below, we discuss whether this definition is meaningful or not. When a system is in the diffusive region, the $G_s(\mathbf{r},t)$ becomes Gaussian,

$$G_s(\mathbf{r},t) = \frac{1}{\sqrt{2\pi\sigma^2}} \exp\left(-\frac{r^2}{2\sigma^2(t)}\right) \quad \text{(in 3d)} \tag{2.12}$$

Then, $F_s(\mathbf{k},t)$ becomes

$$\begin{aligned} F_s(\mathbf{k},t) &= \int d\mathbf{r} G_s(\mathbf{r},t) \exp(-i\mathbf{k}.\mathbf{r}) \\ F_s(\mathbf{k},t) &= \exp\left(-\frac{k^2\sigma^2(t)}{2}\right) \end{aligned} \tag{2.13}$$

In the diffusive region, $\sigma^2(t) = 2Dt$, then,

$$F_s(\mathbf{k},t) = \exp\left(-k^2 Dt\right) \tag{2.14}$$

Thus, we can write $F_s(\mathbf{k},t) = \exp(-\frac{t}{\tau})$ which implies that the time at which $F_s(k,t)$ or any time correlation function becomes $1/e$, gives a measure of structural relaxation time.

2.1.2 Four point correlation function

We have also studied the variance, $\chi_4(t)$ of the fluctuation of the overlap function ($\chi_4(t)$ is also called the dynamic susceptibility) which is defined as follows

$$\chi_4(t) = N\left(\langle q(t)^2\rangle - \langle q(t)\rangle^2\right) \tag{2.15}$$

The quantity, $\chi_4(t)$ can be written as an integral to a higher order four point correlation function $g_4(\mathbf{r},t)$ [62, 138] commonly used in the context of dynamical heterogeneity.

$$\begin{aligned} g_4(\mathbf{r},t) &= \frac{1}{N}\langle\rho(0,0)\rho(0,t)\rho(\mathbf{r},0)\rho(\mathbf{r},t)\rangle - \langle\rho(0,0)\rho(0,t)\rangle\langle\rho(\mathbf{r},0)\rho(\mathbf{r},t)\rangle \\ \chi_4(t) &= \int d\mathbf{r} g_4(\mathbf{r},t) \end{aligned} \tag{2.16}$$

In Fig. 2.2, we show $q(t)$ and $\chi_4(t)$ and relevant timescales for 3d soft sphere system.

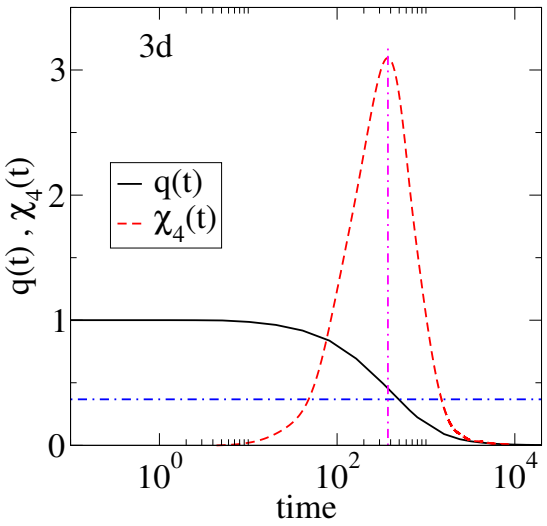

Figure 2.2: $q(t)$ and $\chi_4(t)$ (3d soft sphere system) is plotted as a function of time in the semi-log scale. The dashed magenta line represents τ_α, which is the time at which $\chi_4(t)$ is maximum.

2.1.3 Mean squared displacement and diffusivity

The mean squared displacement (MSD) characterizes the particle-averaged translational motion in the system. The translational diffusion coefficient (D) is a transport coefficient which can be computed from the MSD. The MSD is also a useful quantity to check if the runs are sufficiently long – for a sufficiently long run the MSD is well

into the diffusive (linear t dependence) regime. The MSD is defined as

$$\mathrm{MSD}(t) = \frac{1}{N}\sum_i \langle (r_i(t) - r_i(0))^2 \rangle \tag{2.17}$$

D is computed by fitting the asymptotic behaviour of MSD to the form $\lim_{t\to\infty} \mathrm{MSD}(t) = 2dDt$, where d is the spatial dimension. In Fig. 2.3, we show an example of how we compute diffusivity.

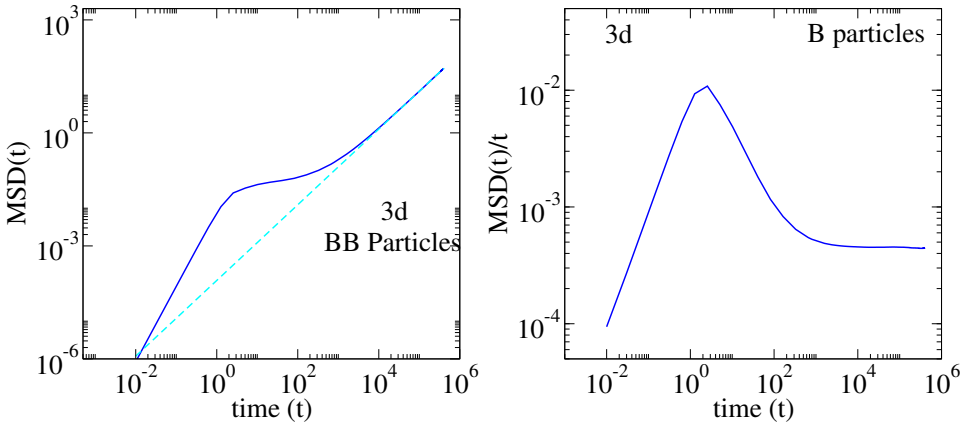

Figure 2.3: Left panel: MSD (3d soft sphere system) is plotted as a function time. By fitting the MSD at large times, we can obtain D. Right Panel: $\frac{MSD}{t}$ is plotted against time. At large t, we see $\frac{MSD}{t}$ is constant which indicates that the system is in diffusive regime (MSD $\sim 2dDt$). The plateau value gives a measure of D.

2.1.4 Non-Gaussian parameter

The non-Gaussian parameter $\alpha_2(t)$ is defined as:

$$\begin{aligned} \alpha_2(t) &= C_D \frac{\langle r^4(t) \rangle}{\langle r^2(t) \rangle^2} \quad , \\ \langle r^{2n} \rangle &= \frac{1}{N} \left\langle (r_i(t) - r_i(0))^{2n} \right\rangle \end{aligned} \tag{2.18}$$

n=1,2; C_D is a spatial dimension dependent coefficient to ensure that $\alpha_2(t) = 0$ when the distribution of displacements is a Gaussian, $C_D = \frac{d}{d+2}$. The time, t^* at which the non-Gaussian parameter $\alpha_2(t)$ is maximum, is a measure of the time scale of heterogeneity in the system.

2.2 Computational Methods

2.2.1 The Brown and Clarke algorithm

We have performed constant number, constant volume and constant temperature (NVT) molecular dynamics simulations. We kept the temperature constant using the Brown and Clarke algorithm, which we describe below.

Hoover's equation of motion

In MD simulations, particles evolve following Newton's equation of motion. The temperature is kept constant by adding a velocity dependent damping force to the interacting forces. Each particle i follows the so called Hoover's equations of motion [139].

$$\begin{aligned} \dot{\mathbf{r}}_i &= \mathbf{v}_i(t) = \frac{p_i}{m} \\ \dot{\mathbf{v}}_i &= \frac{\mathbf{F}_i(t) - \alpha \mathbf{v}_i(t)}{m} \end{aligned} \tag{2.19}$$

The constant α is chosen in such way that the kinetic temperature is a constant of motion. The kinetic temperature is related to velocity by:

$$\frac{fT}{2} = \frac{m}{2} \sum_i^N \mathbf{v}_i . \mathbf{v}_i \tag{2.20}$$

where f is the number of degrees of freedom, equal to $N \times d - (d+1)$, where N is the total number of particles and d is the spatial dimension. Now, to keep the temperature constant, we set

$$\frac{dT}{dt} = 0 \implies \alpha = \frac{\sum_i \mathbf{F}_i . \mathbf{v}_i}{\sum_i \mathbf{v}_i . \mathbf{v}_i} = -\frac{\dot{U}}{2K} \tag{2.21}$$

U is the total potential energy and K is the total kinetic energy of the system. According to the Brown and Clarke algorithm [140], if the equations of motion are integrated using the Leap-frog scheme [141], we do not need to solve Eqn. 2.21. Rather, the velocity would be simply rescaled.
In the Leap-frog scheme, the equations of motion can be written as,

$$\begin{aligned} \mathbf{v}_i(t + \frac{\Delta t}{2}) &= \mathbf{v}_i(t - \frac{\Delta t}{2}) + \frac{\mathbf{F}_i(t)}{m} \Delta t + O(\Delta t^2) \\ \mathbf{r}_i(t + \Delta t) &= \mathbf{r}_i(t) + \mathbf{v}_i(t + \frac{\Delta t}{2}) \Delta t + O(\Delta t^2) \end{aligned} \tag{2.22}$$

Note that in this scheme, the initial position and velocity are not in the same instant of time, there is an offset of $\Delta t/2$. The velocity at the same time step can written as

$$\mathbf{v}_i \approx \frac{1}{2}\left[\mathbf{v}_i(t-\frac{\Delta t}{2}) + \mathbf{v}_i(t+\frac{\Delta t}{2})\right] \tag{2.23}$$

Now, using Hoover's equations of motion, Eqn. 2.19, Eqn. 2.22 will become,

$$\begin{aligned} \mathbf{v}_i(t+\frac{\Delta t}{2}) &= \mathbf{v}_i(t-\frac{\Delta t}{2}) + \alpha_i(t)\Delta t - \frac{\alpha \mathbf{v}_i(t)}{m}\Delta t \\ \mathbf{r}_i(t+\Delta t) &= \mathbf{r}_i + \mathbf{v}_i(t+\frac{\Delta t}{2})\Delta t \end{aligned} \tag{2.24}$$

We can define an intermediate velocity update,

$$\mathbf{v}_i'(t) = \mathbf{v}_i(t-\frac{\Delta t}{2}) + \alpha_i(t)\frac{\Delta t}{2} \tag{2.25}$$

Using Eqn. 2.24 and Eqn. 2.25, we obtain

$$\mathbf{v}_i(t) = \mathbf{v}_i(t-\frac{\Delta t}{2}) + \alpha_i(t)\frac{\Delta t}{2} - \frac{\alpha \mathbf{v}_i(t)}{2m}\Delta t \tag{2.26}$$

$$\mathbf{v}_i(t)\left[1+\frac{\alpha\Delta t}{2m}\right] = \mathbf{v}_i(t-\frac{\Delta t}{2}) + \alpha_i(t)\frac{\Delta t}{2} \tag{2.27}$$

$$\mathbf{v}_i(t) = \beta \mathbf{v}_i'(t) \tag{2.28}$$

where,

$$\beta = \frac{1}{1+\frac{\alpha\Delta t}{2m}} \tag{2.29}$$

Now, we replace α in Eqn. 2.24 by β,

$$\mathbf{v}_i(t+\frac{\Delta t}{2}) = (2\beta-1)\mathbf{v}_i(t-\frac{\Delta t}{2}) + \beta\alpha_i(t)\Delta t \tag{2.30}$$

β can be obtained from

$$T(t) = \frac{m}{f}\sum_{i=1}^{N} v_i^2(t) \tag{2.31}$$

$$= \frac{m}{f}\left(\sum_{i=1}^{N} v_i^2(t)\right)\beta^2 \tag{2.32}$$

$T(t)$ is the instantaneous kinetic temperature. $T(t)$ will be the same as the simulation temperature $T(r)$ when

$$\beta^2 = \frac{f T_r}{m\sum_{i=1}^{N} v_i^2(t)} \tag{2.33}$$

Finally, using the Brown and Clarke algorithm, Hoover's equations become,

$$\mathbf{v}_i(t+\frac{\Delta t}{2}) = (2\beta - 1)\mathbf{v}_i(t-\frac{\Delta t}{2}) + \beta\alpha_i(t)\Delta t \tag{2.34}$$

$$\mathbf{r}_i(t)(t+\frac{\Delta t}{2}) = \mathbf{r}_i(t) + \mathbf{v}_i(t+\frac{\Delta t}{2})\Delta t \tag{2.35}$$

2.2.2 Calculation of free energy and entropy

2.2.2.1 Total free energy and entropy

Calculation of entropy in general is not a trivial task in a simulation or experiment. Entropy is related to the free energy in the following way:

$$S = -\frac{\partial A}{\partial T} \tag{2.36}$$

Where A is the Helmotz free energy. Thus, we first need to compute the free energy. the Helmholtz free energy is defined as

$$A = -k_B T \ln Z \tag{2.37}$$

$$Z = \frac{1}{N!}\int \exp(-\beta H(\mathbf{R},\mathbf{P}) d\mathbf{R} d\mathbf{P} \tag{2.38}$$

We see that the free energy is not a direct function of phase space coordinates; rather, it is a function of phase space volume. So, absolute free energy can not be calculated directly from the simulation. Different methods are employed to obtain free energy in simulations. One such method is thermodynamic integration [142]. In this method, first we need to find a reference state where the free energy is known exactly either analytically or numerically. Then we need to find a reversible path from this reference state to the state of our interest, the target state. By integrating thermodynamic variables like pressure, energy or some perturbed Hamiltonian along this path, one obtains the free energy of the target state with respect to the reference state. Below, we will describe how we calculate the free energy for our system [81].

- The reference state for our system is the ideal gas, which is the high temperature and low density limit of the liquid. The Hamiltonian of our system can be written as $H = K(\mathbf{P}) + U(\mathbf{R})$, where K is the kinetic part and U is the interacting part. Kinetic part of the Hamiltonian will give the ideal gas part of the free energy. So the total free energy can be written as $A_{total} = A_{id} + A_{ex}$. As our system is a binary mixture, we also need to add the contribution due to the mixing entropy. So at the reference state, at zero density and and high temperature (T_{ref}), the

partition function will be:

$$Z(0, T_{ref}) = \frac{N!}{N_A! N_B!} Z_{id}(0, T_{ref}) \tag{2.39}$$

correspondingly the free energy will become,

$$A(0, T_{ref}) = A_{id} + A_{ex} \tag{2.40}$$

$$A_{ex} = -T_{ref} \ln \frac{N!}{N_A! N_B!} \tag{2.41}$$

- Now, we will compute the excess free energy at the reference temperature, T_r and at density, ρ by integrating the excess pressure along the isotherm at T_r. The integration is performed using 10-point Gauss-quadrature method.

$$P_{ex} = \rho^2 \left(\frac{\partial (A_{ex}/N)}{\partial \rho} \right)_{N,T} = P - P_{id} \tag{2.42}$$

$$A_{ex}(\rho, T_{ref}) - A_{ex}(0, T_{ref}) = N T_{ref} \int_0^{\rho} \partial \rho \left(\frac{\beta_{ref} P}{\rho^2} - \frac{1}{\rho} \right) \tag{2.43}$$

- Next, we obtain the excess free energy at the target temperature T by integrating the potential energy along the isochore at ρ from T_r to T. The temperature dependence of potential energy is obtained by fitting to an empirical from, $U(\rho, T) = a + bT^c$ [143].

$$U(N) = \left(\frac{\partial (\beta A_{ex})}{\partial \beta} \right)_{N,\rho} \tag{2.44}$$

-

$$\beta A_{ex}(\rho, T) - \beta_{ref} A_{ex}(\rho, T_{ref}) = \int_{\beta_{ref}}^{\beta} (U(\rho, \beta') \partial \beta') \tag{2.45}$$

- Next, we obtain the total free energy by adding the ideal gas free energy at the target free energy to the excess part obtained by thermodynamic integration.

$$A(\rho, T) = A_{ex}(\rho, T) + A_{id}(\rho, T) \tag{2.46}$$

$$A_{id}(\rho, T) = N T (d \ln(\Lambda) + \ln(\rho) - 1) \tag{2.47}$$

Where Λ is the de-Broglie wavelength, $\Lambda = \frac{h}{\sqrt{(2\pi T)}}$

- Finally, we obtain total entropy $S = -\frac{\partial A}{\partial t}$.

$$S = A(\rho, T)/T - E/T - Nd/2 \tag{2.48}$$

2.2.2.2 Vibrational entropy

Vibrational entropy or basin entropy is defined as the entropy due to vibration around the energy minimum of the system. This entropy can be calculated by assuming the energy basins to be harmonic wells. This approximation works well in the low temperature regime. At high temperatures, one needs to incorporate an-harmonic contributions of the basin. First, we will discuss the method to estimate harmonic vibrational entropy [81,144,145]. We consider the state of the system that weakly vibrates around an energy minimum structure, inherent structure (IS). If δr_i is the displacement of the ith particle from its position in the IS, the potential energy can be approximated as

$$U = U_{IS} + \frac{1}{2}\sum_{ij}\frac{d^2U}{dr_i dr_j}\delta r_i \delta r_j \tag{2.49}$$

The second term of the equation is called the Hessian matrix, which is of dimensions $3N \times 3N$. We can write, using harmonic approximation, the canonical partition function of a single basin (Z_{basin}) as the product of the partition functions ($Z_{h.o}$) of $3N$ one dimensional harmonic oscillators (h.o.) with frequencies (ω_i) (The Hamiltonian of the harmonic oscillators can be written as $\frac{1}{2m}p^2 + \frac{1}{2}m\omega^2 q^2$, p and q are the generalized coordinates, and m is the mass which is set to unity). These ω_is are the square root of the of the eigenvalues (ω_i^2) of the Hessian matrix. We obtain $3N$ independent eigenvalues, out of which $3N - 3$ are non-zero, by diagonializing the Hessian matrix. The canonical partition functions of a one dimensional harmonic oscillator with a non-zero frequency ω is

$$\begin{aligned} Z_{h.o.}(\omega) &= \int \frac{dqdp}{h}\exp\left[-\frac{\beta p^2}{2} - \frac{\beta\omega^2 q^2}{2}\right] \\ &= \frac{2\pi}{\beta h\omega} \end{aligned} \tag{2.50}$$

and with zero frequency,

$$\begin{aligned} Z_{h.o}(0) &= \frac{1}{h}\sqrt{(\frac{2\pi}{\beta})}V^{\frac{1}{3}} \\ &= z_0 \end{aligned} \tag{2.51}$$

Thus, the basin partition function can be written as :

$$\begin{aligned} Z_{basin} &= \exp(-\beta U_{IS})\left[\prod_{i=1}^{3N-3}\frac{2\pi}{\beta h\omega_i}\right]z_0^3 \\ &= \exp(-\beta U_{IS})\exp(-\beta f_{basin}) \end{aligned} \tag{2.52}$$

where $f_{basin} = \left(\prod_{i=1}^{3N-3}\frac{2\pi}{\beta h\omega}\right)z_0^3$. Finally,

$$\beta U_{IS} + \beta f_{basin} = -\ln Z_{basin} \tag{2.53}$$

$$\beta f_{basin} = \ln\sum_{i=1}^{3N-3}\frac{\beta h\omega_i}{2\pi} - \ln z_0^3$$

$$S_{basin} = -\frac{\delta f_{basin}}{\delta T} \tag{2.54}$$

2.2.3 Configurational entropy

The configurational entropy is defined as following: $S_c = \frac{1}{N}\log\Omega$, (where Ω is the number of amorphous minima visited by the system) which is a measure of the number of uncorrelated configurations that a system can sample in the configuration space at a given density and temperature. Goldstein [82] proposed a description of the dynamics of glass forming liquids in terms of high dimensional configuration space, called as potential energy landscape (PEL). The PEL is a hyper-surface representing the interaction potential as a function of coordinates of all particles in a $Nd+1$ dimensional space for an N particle liquid in d dimensions. A configuration as a whole is represented by a single point on this hyper-surface. The evolution of the system can be described as the movement of the point in the hyper-surface. The PEL has a large number of local minimum structures which is known as *inherent structures*. These minima are separated by energy barriers. At high temperatures, the system can sample all possible energy configurations without needing to overcome the barriers as the thermal energy, k_BT is much larger than the energy barriers. However, at low temperatures, as the thermal energy is less, the system spends most of the time at some local minima and occasionally jumps to other minima. From the above discussion, we can see that the configuration space can be divided into *basins* such that each basin has exactly one local minimum or inherent structure and each configuration in that basin can be mapped to that inherent structure. In this picture, the partition function of the whole system can be written as the integral of the partition function of single basin over inherent structure energies, e_{IS}:

$$Z = \int_{e_{IS}} Z_{basin}(e_{IS}, N)\Omega(e_{IS}, N)de_{IS}, \tag{2.55}$$

where Z is the canonical partition function of the whole system and $Z_{basin}(e_{IS}, N)$ is the partition function of the basin and $\Omega(e_{IS}, N)de_{IS}$ denotes the number of inherent structure in the energy range, e_{IS} and $e_{IS} + de_{IS}$. The above equation can further be written as

$$Z = \int_{e_{IS}} \exp[-\beta(e_{IS} + f_{vib})] \exp[S_c(e_{IS}, N)/k_B] de_{IS} \tag{2.56}$$

Where $S_c(e_{IS}, N)$ is the configurational entropy density, which is independent of temperature. The configurational entropy, $S_c(e_{IS}, N, T)$ can be obtained by averaging configurational entropy density sampled at a given temperature:

$$S_c(e_{IS}, N, T) = \int de_{IS} S_c(e_{IS}, N) P(S_c, N, T) \tag{2.57}$$

Where $P(S_c, N, T)$ is the probability density of sampling inherent structures of energy between e_{IS} and $e_{IS} + de_{IS}$. Using Equation. 2.56, the S_c can be written as $S_{Liquid} = S_{vib} + S_c$. The total entropy S_{Liquid}, which measures the total number of configurations participating in the liquid state, has been decomposed into a sum of the vibrational entropy S_{vib}, which counts how many configurations there are within each minimum, plus the configurational entropy S_c, counting the number of minima. As we already discussed the method to calculate total entropy, S_{Liquid} and vibrational entropy, we can obtain S_c, subtracting these two.

$$S_c = S_{tot} - S_{vib} \tag{2.58}$$

2.3 Jamming protocol

Here, we describe the protocol to obtain the jamming point ϕ_J. We follow the procedure described in Ref. [97]. In this work, the initial configurations were chosen from the equilibrium fluid at low density. It was shown that the jamming point depends on the density at which the configuration was equilibrated; the jamming point moves to higher densities with increase in the initial density. However, if we use random initial configurations as was done in Ref. [146], we could obtain the lowest jamming point. As we are interested in finding the lowest jamming point, we use random initial configurations. The protocol is illustrated in Fig. 2.4, which we describe below.

- We compress the system by uniformly inflating all the particle diameters.
- After each step of compression the potential energy of the system is minimized using the conjugate gradient method.
- We continue this process until the system reaches an energy of the order of 10^{-5}.

- To locate the jamming density, we slowly (10 times lower than the compression) decompress the system and at each step of decompression, the energy is minimized.
- We continue decompression until the energy of the system becomes less than 10^{-16}. The density at which the energy reaches 10^{-16} is the estimate of the jamming density.
- The above procedure is repeated for 1000 independent configurations, to obtain the average jamming density and the corresponding distribution.

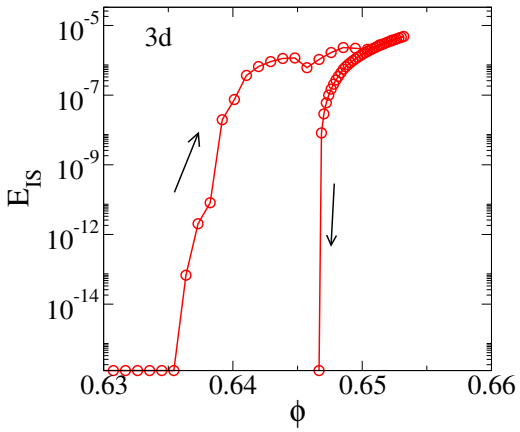

Figure 2.4: The jamming protocol is described here for 3d soft sphere system. The energy of the minimized configuration is plotted as function of ϕ during a compression-decompression cycle.

2.4 Athermal quasi static (AQS) shear

In this thesis, we have studied the yielding and memory behaviour of amorphous solids using athermal quasi static (AQS) shear protocol. Before, we discuss the AQS protocol, we will discuss affine transformations and the Lees-Edwards boundary condition which are used to implement the AQS.

2.4.1 Affine transformation

Any transformation which has the following property is called an affine transformation:

- Collinearity of points: three or more points which lie on the same line (called collinear points) continue to be collinear after the transformation.
- Parallelism: two or more lines which are parallel, continue to be parallel after the transformation.

- The ratios of lengths along a line is preserved.

- The distance between points, angles between points and the origin is not preserved.

Examples in 3D

- Scale

$$A = \begin{bmatrix} a & 0 & 0 \\ 0 & b & 0 \\ 0 & 0 & c \end{bmatrix}$$

- Shear

$$A = \begin{bmatrix} 1 & b & c \\ d & 1 & e \\ f & g & 1 \end{bmatrix}$$

- Rotation along z

$$A = \begin{bmatrix} cos\theta_z & -sin\theta_z & 0 \\ sin\theta_z & cos\theta_z & 0 \\ 0 & 0 & 1 \end{bmatrix}$$

2.4.2 Lees-Edwards periodic boundary conditions

When the simulation box is tilted, instead of periodic boundary conditions, Lees-Edward boundary conditions are used. In Fig. 2.5, we have schematically shown the concept of this boundary condition. The images of the simulation box are shifted in the direction perpendicular to the displacement gradient. When the particles pass through the simulation box from the surface normal to the x-axis, they re-enter through the opposite surface using normal periodic boundary conditions (PBC). If the particles are passing through the surface normal to the z-axis, x-coordinate of those particles will be modified to $x - \Delta x$ and then the standard PBC will be applied to the modified x-coordinate. We now describe the AQS protocol. The AQS shear protocol has two steps:

- Particles are displaced by applying an affine transformation $x' = x + d\gamma\, z$, where $d\gamma$ is the strain increment in the xz plane, with y and z coordinates unaltered. Shear strain γ is incremented by small strain steps.

- The energy of the deformed configuration is minimized using the conjugate gradient method, subject to Lees- Edwards periodic boundary conditions.

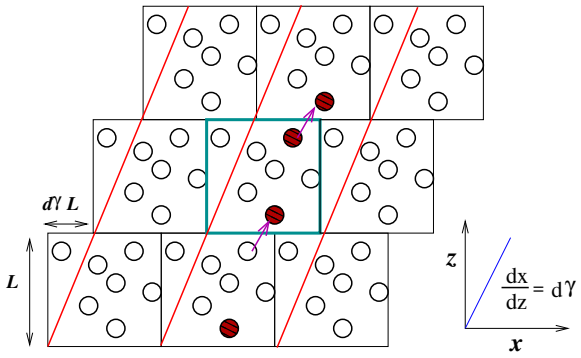

Figure 2.5: Two-dimensional representation of the Lees-Edwards boundary condition. When the principal simulation box (center) is sheared, its periodic image cells are also sheared and displaced simultaneously to provide homogeneous shear conditions. The spatial arrangement of the particles can be interpreted as particles in square boxes displaced by $d\gamma L$

Two dimensional pair correlation function: In order to assess the structural change resulting from cyclic deformation, we compute a two dimensional directional pair correlation function $g(x,z)$ in the shear plane xz, which is defined as:

$$g(x,z) = \frac{1}{2N\rho a} \times \left\langle \sum_{i=1}^{N-1} \sum_{j \neq i}^{N} \delta(x-(x_i-x_j))\delta(z-(z_i-z_j))\theta(a-|y_i-y_j|) \right\rangle \tag{2.59}$$

where $\langle .. \rangle$ implies averaging over independent samples. x_i, y_i, z_i are the particle coordinates. Since we compute a two dimensional correlation function in a three dimensional system, we consider pairs of particles with are in the same (shear) plane, by demanding that their vertical (y) separations do not exceed a specified value, $a = 0.04\sigma_{AA}$. This is enforced by the Heaviside function $\theta(a-|y_i-y_j|)$. In practice, we divide the simulation box into slabs of fixed width a along the y direction and compute $g(x,z)$ for pairs of particles within each slab, averaging over all the slabs. The data shown are averaged over 30 independent samples.

2.5 Details of the models studied

We describe below the two model systems that we have studied in this thesis.

2.5.1 The Kob-Andersen model

The Kob-Andersen Binary mixture ($A_{80}B_{20}$) with Lennard-Jones interactions between particles (BMLJ) [147] is a model glass former that has been extensively investigated.

The interaction potential, with a quadratic cut-off, is given by

$$\begin{aligned} V_{\alpha\beta}(r) &= 4\epsilon_{\alpha\beta}\left(\left(\frac{\sigma_{\alpha\beta}}{r}\right)^{12} - \left(\frac{\sigma_{\alpha\beta}}{r}\right)^{6}\right) \\ &\quad -4\epsilon_{\alpha\beta}\left(c_0 + c_2\left(\frac{r}{\sigma_{\alpha\beta}}\right)^{2}\right), r_{\alpha\beta} \leq r_{c,\alpha\beta} \\ &= 0, \qquad\qquad r_{\alpha\beta} > r_{c,\alpha\beta} \end{aligned} \tag{2.60}$$

where $\alpha, \beta \in$ (A,B), $\epsilon_{AB}/\epsilon_{AA} = \epsilon_{BA}/\epsilon_{AA} = 1.5$, $\epsilon_{BB}/\ \epsilon_{AA} = 0.5$, and $\sigma_{AB}/\sigma_{AA} = \sigma_{BA}/\sigma_{AA} = 0.8$, $\sigma_{BB}/\sigma_{AA} = 0.88$. The interaction potential has cut off, $r_{c,\alpha\beta} = 2.5\sigma_{\alpha\beta}$. We report results in reduced units, with units of length, energy and time scales being σ_{AA}, ϵ_{AA} and $\sqrt{\frac{\sigma_{AA}^2 m_{AA}}{\epsilon_{AA}}}$ respectively.

2.5.2 Soft sphere binary mixture

This model is also used as a model glass former and in studies of jamming [148]. The interaction potential is given by:

$$\begin{aligned} V_{\alpha\beta}(r) &= \epsilon_{\alpha\beta}\left(1 - \frac{r}{\sigma_{\alpha\beta}}\right)^{2}, \qquad r_{\alpha\beta} \leq \sigma_{\alpha\beta} \\ &= 0, \qquad\qquad r_{\alpha\beta} > \sigma_{\alpha\beta} \end{aligned} \tag{2.61}$$

where $\alpha,\ \beta \in$ (A,B), indicates the type of particle. The two types of particle differ in their sizes, with $\sigma_{BB} = 1.4\sigma_{AA}$, but with the interaction strengths being the same for all pairs. In reporting results for this system, we use reduced units, with units of length, energy and time scales being σ_{AA}, ϵ_{AA} and $\sqrt{\frac{\sigma_{AA}^2 m_{AA}}{\epsilon_{AA}}}$ respectively.

Chapter 3

Relationship between glass point and jamming point of sphere assemblies in higher spatial dimensions

3.1 Introduction

Fluid states of matter can transform to rigid, amorphous solids through the glass transition or the jamming transition. The glass transition describes the transition to disordered solid states typically in molecular systems upon a decrease in temperature, whose nature has been intensely investigated over several decades [30, 47, 56, 149, 150]. The jamming transition has likewise been been widely investigated in *athermal* systems, typified by granular matter [96, 151, 152]. Their relationship has also been the subject of considerable research [92]. Whereas molecular glass formers and granular matter represent cases which exhibit one or the other of these phenomena, several systems, such as colloidal suspensions, in principle exhibit both phenomena, and their interplay is important, *e.g.* in their rheology [102]. An idealised system in which both phenomena have been investigated in detail is the hard sphere system. Theoretical investigations over the last decade, extending the framework of the random first order transition (RFOT) theory [61, 153, 154], have focused on the hard sphere system, and a unified mean field description of both these phenomena have been developed in the limit of infinite dimensions [92, 94, 155]. These developments have naturally led to investigations of how the infinite dimensional results relate to behaviour in finite dimensions. An appealing and systematic approach to addressing questions in this regard is to study the effect of spatial dimensionality on the glass transition and jamming phenomenology, which have been pursued for hard particle systems extensively [70, 92, 94, 156–159]. In particular, the relationship between the glass transition and jamming transition has been investigated [94, 156]. In addition to systems of hard

spheres, a small number of other studies have investigated the role of dimensionality in determining aspects of glassy dynamics [64, 160–163], such as dynamical heterogeneity in a binary mixture of the Lennard-Jones particles as a function of temperature. A more extensive investigation of the dependence on spatial dimensionality in systems where both thermal and density effects play a role are thus of great interest. In the present work, we would like to understand the relationship between ideal glass transition density and jamming point by varying spatial dimensions for a model system where temperature and density both are controlled parameters. We study soft sphere assemblies interacting with a harmonic potential by investigating the dynamics at different densities and temperatures. In the zero-temperature limit, the behavior of this system approaches the density-controlled hard sphere model, while it is similar to thermally driven fluids at high density and finite temperature. In the hard sphere limit, the system *jams*, losing the ability to flow, at a critical density, ϕ_J, *via* the non-equilibrium jamming transition [97, 146]. Several works [97, 99, 105, 164–168] have considered and demonstrated the scenario that the jamming density is not unique, but can occur over a range of densities. The jammed state can be obtained by compressing an equilibrated liquid. The system jams at larger and larger densities as the initial density of equilibrated liquid increases. In turn, the range of jamming densities is associated with a line of glass transition densities (kinetically determined or otherwise, as in mean-field results [92, 155]). This line of kinetically defined glass transition density ends with a *Kauzmann* density ϕ_0, which may be expected to be the relevant density for the divergence of relaxation times. The relationship between the jamming and Kauzmann densities have been investigated, with varying conclusions regarding the relative values of ϕ_J and ϕ_0 [104, 108, 156, 169, 170]. Several studies [92, 94, 105–108] also indicate that the relationship between these two transition densities depends on dimensionality. In [169, 170], the relaxation times were studied for the same model we consider, in three dimensions. With increasing density, relaxation times exhibit a cross over from sub-Arrhenius to super-Arrhenius temperature dependence. Relaxation times were analysed through a scaling function that assumes a divergence for the hard sphere systems at a density ϕ_0, and by defining an effective hard sphere diameter at finite temperatures [171], to obtain two distinct scaling collapses across ϕ_0. The estimate of ϕ_0 thus obtained if found to be very close to ϕ_J, the jamming point, although the meaning of the two densities was clearly distinguished. In the present work, we perform extensive molecular dynamics simulations for a wide range of ϕ, T values in different spatial dimensions ranging from $d = 3$ to 8. We perform a scaling analysis similar to [169, 170] but with a newly proposed scaling function, to obtain ϕ_0 as a function of d. We obtain jamming densities following the analysis in [97, 146]. Our results clearly demonstrate that $\phi_0 > \phi_J$ for $d > 4$, with ϕ_0/ϕ_J increasing with d, as may be expected from mean field results [92, 94, 155].

3.2 Simulations details

We use sphere assemblies interacting with harmonic potential as a model glass former [172] (defined in the chapter 2). We study glasses in the spatial dimension from $3-8$. We have worked with the system size varying from $1000-5000$ which is a binary mixture (50:50). We have investigated the dynamics at $10-14$ densities around the jamming density. The number density, ρ, is related to the volume fraction, ϕ: $\phi = \rho V_d$, where V_d is the volume element in d dimension.

$$\phi = \rho V_d = \rho 2^{-d} \frac{\pi^{d/2}}{\Gamma(1+\frac{d}{2})}((0.5\sigma_{AA}^d + 0.5\sigma_{BB}^d) \tag{3.1}$$

, where $\rho = N/V$, with V expressed in units of the small particle diameter. We use ϵ_{AA} as the energy unit, and $\sqrt{\frac{\sigma_{AA}^2 m_{AA}}{\epsilon_{AA}}}$ as time unit, where m_{AA} is the mass which is set to unity. Molecular dynamics (MD) simulations are performed in a cubic box with the periodic boundary conditions in the constant number, volume, and temperature (NVT) ensemble. The integration time step is $dt = 0.01$. Temperatures were kept constant using an algorithm due to Brown and Clarke [140]. The data, presented here, have run length more than $100\tau_\alpha$ (τ_α = relaxation time).

3.3 Results

3.3.1 Sub-Arrhenius to super-Arrhenius transition

We study the dynamics by measuring a two point correlation function, the overlap function, $q(t)$ (for the B particles):

$$q(t) = \frac{1}{N_B}\sum_i^{N_B} w(|\mathbf{r}_i(t_0) - \mathbf{r}_i(t+t_0)|) \quad \text{where} \quad w(x) = \begin{cases} 1.0 & \text{if } x \le a \\ 0 & \text{otherwise.} \end{cases}$$

We choose the parameter values $a = 0.48, 0.50, 0.55, 0.60, 0.75$,and 0.80 for 3d, 4d, 5d, 6d, 7d, and 8d, respectively. (Details are given in chapter 2). Relaxation time, τ_α is estimated as the time where $q(t) = 1/e$. In Fig. 3.1, the relaxation time is plotted as a function of temperature for various densities for $3-8$ spatial dimensions. The relaxation behaviour is Arrhenius at high temperature for all the densities in each dimension. However, at low temperature, the dynamics changes from sub-Arrhenius to

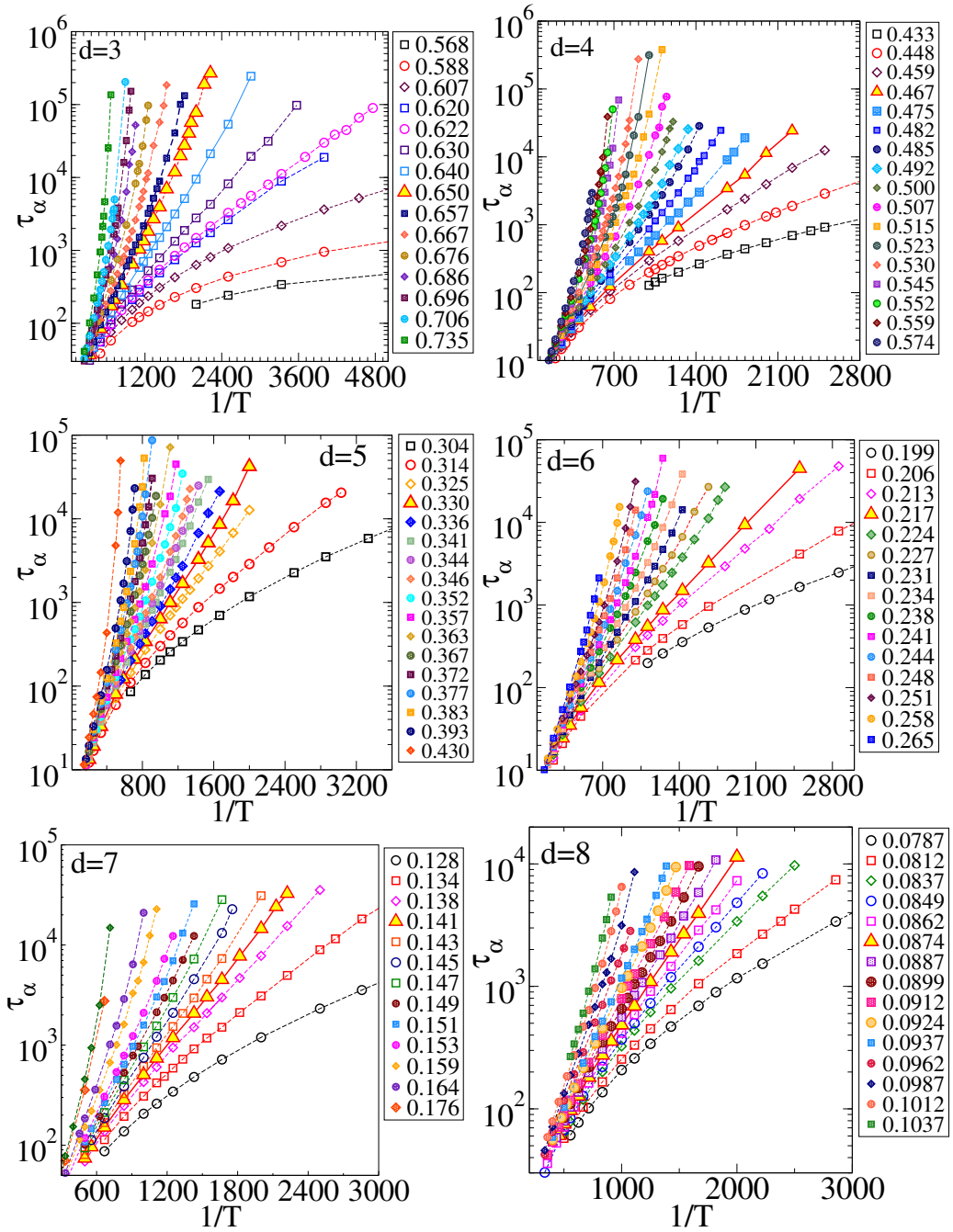

Figure 3.1: Relaxation time as a function of inverse temperature is plotted in a semi-log scale for several densities in different dimensions. The data with filled symbol represents the density beyond which one expects the cross over from sub-Arrhenius to super-Arrhenius behaviour.

super-Arrhenius with the increasing density. In Fig. 3.1, we have highlighted the density at which the cross over occurs. In order to locate the cross-over density between sub-Arrhenius to super-Arrhenius temperature dependence, we consider a subset of densities in the vicinity of that density in each dimension. We fit the τ_α at high temperatures to an Arrhenius form

$$\tau_\alpha = \tau_0 \exp\left(\frac{A}{k_B T}\right) \tag{3.2}$$

In Fig. 3.2, we show the Arrhenius fits in each dimension, which demonstrates that the change from sub-Arrhenius to super-Arrhenius temperature dependence of the relaxation times. Previous studies have shown that the dynamics shows scaling behaviour around the cross over density of sub Arrhenius to super Arrhenius.

3.3.2 Berthier and Witten (BW) scaling

Considering an expression for relaxation times for hard sphere fluids of the form $\sqrt{T}\tau_\alpha^{hs} \sim \exp\left[\frac{A}{(\phi_0-\phi)^\delta}\right]$, Berthier and Witten [169] analysed relaxation times for soft spheres by defining a temperature dependent effective volume fraction of the form $\phi_{eff} = \phi - aT^{\mu/2}$, which leads to the scaling form

$$\sqrt{T}\tau_\alpha(\phi, T) \sim \exp\left[\left(\frac{A}{|\phi_0 - \phi|^\delta}\right) F_\pm\left(\frac{|\phi_0 - \phi|^{\frac{2}{\mu}}}{T}\right)\right], \tag{3.3}$$

where $F_\pm(x)$ refers to the scaling function for the super-Arrhenius and the sub-Arrhenius branch and μ, δ and ϕ_0 are adjustable parameters. Plotting $|\phi_0 - \phi|^\delta \log(\tau_\alpha)$ against $|\phi_0-\phi|^{\frac{2}{\mu}}/T$, with suitable choices of the parameters, a data collapse on to two branches above and below ϕ_0 is obtained. The values of $\phi_0 = 0.635$ and $\delta = 2.2$ were determined from such a procedure, with the δ value being in close agreement with experimental and simulation results for colloidal hard spheres and theoretical results [173–175]. The estimated ϕ_0 is close to but distinct from the jamming density of $\phi_J = 0.648$ estimated for the binary mixture studied in [97, 146, 169] and here. We have used the same scaling formula for spatial dimension, $3 - 8$. The continuity of τ_α at finite temperature and $\phi = \phi_0$ demands for some unknown exponent y, the following equation must be satisfied,

$$\ln(\sqrt{T}\tau_\alpha) = \frac{A}{|\phi - \phi_0|^\delta}\left[\frac{|\phi - \phi_0|^{\mu/2}}{T}\right]^y \tag{3.4}$$

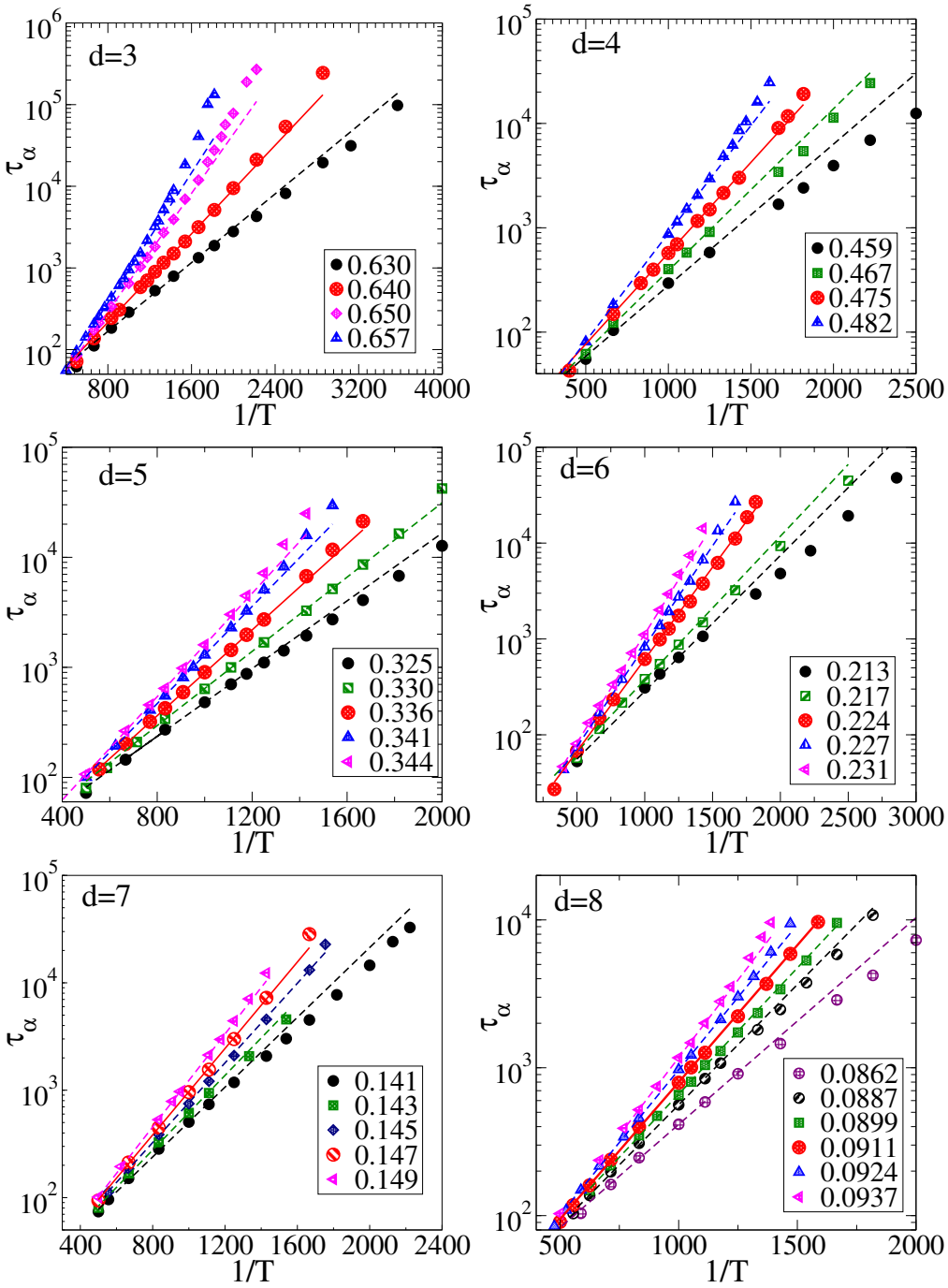

Figure 3.2: Relaxation time is plotted as a function of inverse temperature and fitted with the Arrhenius form at high temperatures. The points correspond to simulation data. Lines are fits to Arrhenius form.

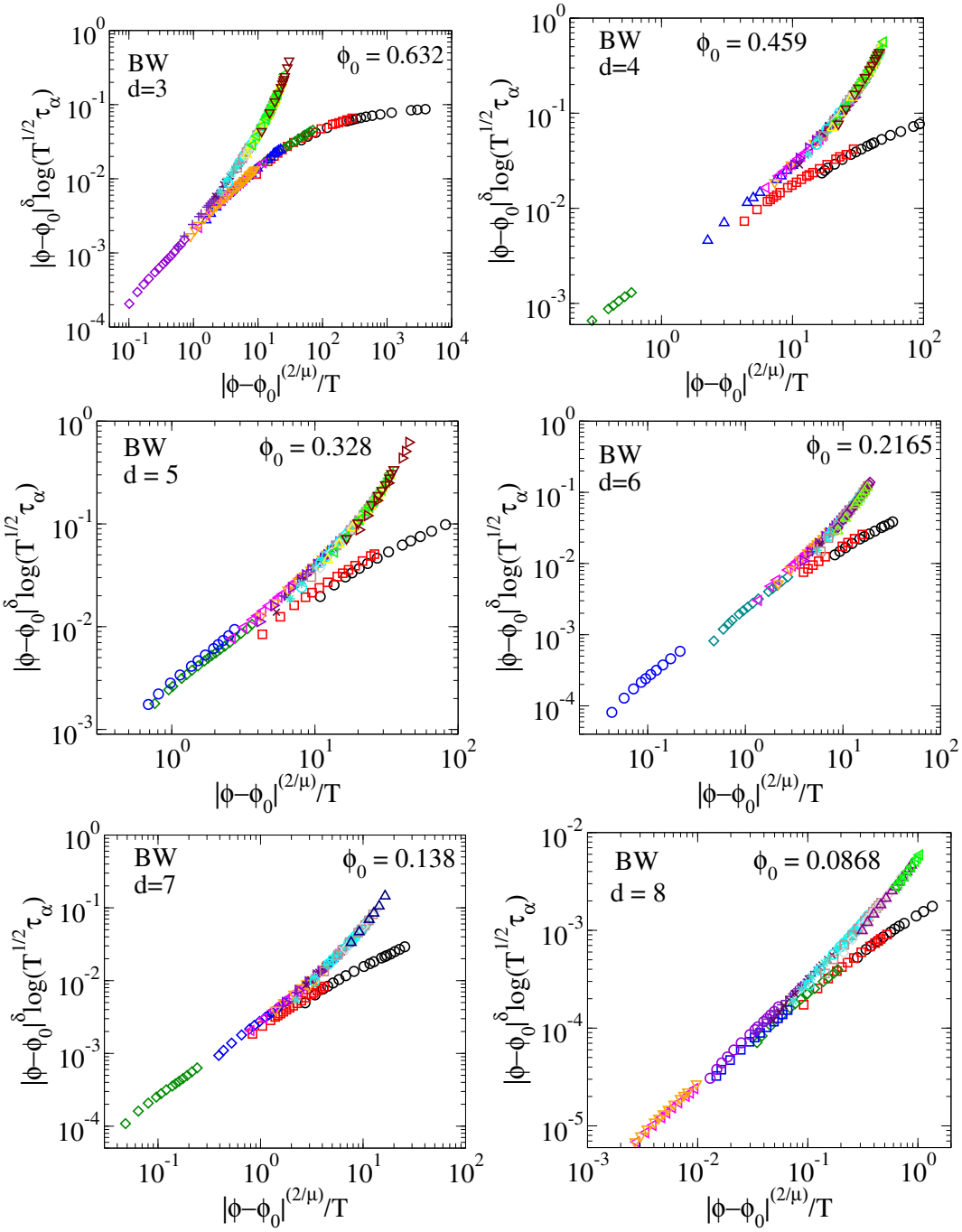

Figure 3.3: Data collapse of relaxation times using the Berthier-Witten scaling function. The estimated ϕ_0 values are shown in the legends.

and y has to be,

$$\frac{\mu y}{2} = \delta \tag{3.5}$$

$$y = \frac{\delta\mu}{2} \tag{3.6}$$

$$\ln(\sqrt{T}\tau_\alpha) = \frac{A}{T^{\mu\delta/2}} \tag{3.7}$$

This implies that

$$F_+(x \to 0) \sim F_-(x \to 0) \sim x^{\mu\delta/2} \tag{3.8}$$

This should correspond to purely Arrhenius behaviour at ϕ_0 for all temperatures which means μ, δ will be such that $\tau_\alpha \sim \exp(A/T)$. In Fig. 3.3, we show the scaling plots of relaxation times (BW scaling) for $3-8$ spatial dimensions. In performing the data collapse, we consider the densities within the bounding ranges identified above and we impose the condition $\mu\delta/2 = 1$ so that the scaling form in Eq. 3.3 leads to an Arrhenius form at ϕ_0. We compute a quantification of the error, χ^2_τ, as detailed below for a range of ϕ_0 and δ values, and identify the ϕ_0 and δ values that minimize χ^2_τ. The values of χ^2_τ *vs.* ϕ_0 and δ are not smooth, for reasons we describe below. Thus, after we identify the ϕ_0 and δ values that minimize χ^2_τ, we consider small variations around such values in order to improve the quality of the data collapse of τ_α into two branches across ϕ_0. The best estimates of ϕ_0 are shown in the legends in Fig. 3.3, and error bars, obtained by considering an increase in χ^2_τ by 20% of the lowest value, are shown in the Table below. Recently, in [176] the same scaling analysis has been revisited with the conclusion that if one considers ϕ_0, δ and μ as free parameters, a good scaling collapse of comparable quality to [169] could be obtained for significantly different sets of parameter values. It is thus desirable to explore alternate scaling functions, which we do in this work based on the evaluation of an effective diameter following the prescription in [177].

3.3.3 New scaling formula

The observations in [176] raise serious concerns about the reliability of the estimates of ϕ_0 obtained. We address this issue by proposing an alternate scaling function based on the evaluation of an effective diameter following the prescription in [177]. We do not consider other improvements to the Barker-Henderson expression commonly used in liquid-state theory, as we wish to analyse the dynamical data with a minimal set of parameters, which nevertheless will be accurate in capturing low temperature behavior. Following [177], the expression for the effective diameter with only temperature

dependent corrections can be written as

$$\sigma_{eff} = \int_0^{r_0} [1 - \exp(-\beta u(r))]\, dr \tag{3.9}$$

where $\beta = 1/T$, and $u(r)$ is the pair potential, r_0 is the cutoff of the potential. For the harmonic pair potential, Equation. 3.9 will become,

$$\sigma_{eff} \quad = \quad \int_0^{\sigma} \left[1 - \exp\left(-\beta\left(1 - \frac{r}{\sigma}\right)^2\right)\right] dr. \tag{3.10}$$

Integrating the above equation, one can obtain,

$$\sigma_{eff} = \sigma\left[1 - \frac{1}{2}\sqrt{\frac{\pi}{\beta}}\, erf(\sqrt{\beta})\right] \tag{3.11}$$

Now, we know,

$$erf(\beta) \approx 1 - \frac{1}{(1 + a_1\beta + a_2\beta^2 + a_3\beta^3 + a_4\beta^4)^4} \qquad \beta \geq 0 \tag{3.12}$$

Where, $a_1 = 0.278393, a_2 = 0.230389, a_3 = 0.000972, a_4 = 0.078108$. The leading order term of the error function will be $T^{5/2}$. Also, the temperature range in our case is around 10^{-2} to 10^{-5}. In this range, $erf(\sqrt{\beta}) \approx 1$. The equation 3.11 becomes,

$$\sigma_{eff} = \sigma\left[1 - \frac{1}{2}\sqrt{\frac{\pi}{\beta}}\right] \tag{3.13}$$

For any general dimension, d, one can write

$$\sigma_{eff}^d = \sigma^d\left[1 - \frac{d\sqrt{\pi}}{2}\sqrt{T} + \frac{d(d-1)\pi}{8}T - \mathcal{O}\left(T^{3/2}\right)\right]. \tag{3.14}$$

Thus, we can approximate the expansion with the following form in general dimensions,

$$\sigma_{eff}^d = \sigma^d(1 - a\sqrt{T} + bT^{\beta}), \tag{3.15}$$

where a, b and β are constant. β has to be larger than 0.5. The effective volume fraction for general dimension will then be

$$\phi_{eff} \sim \phi\left(1 - a\sqrt{T} + bT^{\beta}\right). \tag{3.16}$$

Assuming that relaxation times for the hard sphere fluid follow

$$\sqrt{T}\tau_\alpha^{hs} \sim \exp\left[\frac{A}{(\phi_0-\phi)^\delta}\right], \tag{3.17}$$

and employing Eq. 3.16 for the effective diameter, we have

$$\sqrt{T}\tau_\alpha(\phi,T) \sim \exp\left[\frac{A}{(\phi_0-\phi)^\delta\left(1-\frac{\phi(a\sqrt{T}-bT^\beta)}{\phi_0-\phi}\right)^\delta}\right] \tag{3.18}$$

based on which, we write a scaling form

$$\sqrt{T}\tau_\alpha(\phi,T) \sim \exp\left[\left(\frac{A}{|\phi_0-\phi|^\delta}\right)F_\pm\left(\frac{|\frac{\phi_0}{\phi}-1|}{a\sqrt{T}-bT^\beta}\right)\right] \tag{3.19}$$

where $F_\pm(x)$ refer to the scaling functions for the super-Arrhenius and the sub-Arrhenius branches.

An Arrhenius form of the relaxation times at finite T and $\phi=\phi_0$ requires δ to be 2, which we employ. a is kept fixed in the following to expressions in Eq. 3.14, and we allow b and β to be fitting parameters, with $\beta > 0.5$. This introduces an additional parameter as compared to BW scaling. However, rather than estimating b, β and ϕ_0 through a scaling analysis of τ_α, we first require that $P/\rho T$ where P is the pressure is a unique function of ϕ_{eff} and estimate b and β from the data collapse of $P/\rho T$.

The pressure P is evaluated at each state point, in each dimension, as a function of ϕ and T, *i.e.* $P = f(T,\phi)$. For a suitable choice of the effective volume fraction $\phi_{eff}(\phi,T)$, we may expect P to be a unique function of ϕ_{eff}.

we require that $Z \equiv P/\rho T$, plotted as a function of ϕ_{eff} should exhibit a data collapse for the full set of densities and temperatures in each dimension, and use this to obtain the best fit values of b and β, keeping the choice of a fixed to values given in Eq. 3.14. We compute the error of the pressure collapse as follows. The range of x (or ϕ_{eff}) values is divided into bins of width δx (we choose $\delta x = 0.05$), and each bin is indexed by i, with n_i data points, from different density, temperature data sets. For each bin, we compute a mean y value $\langle y_i\rangle = \frac{1}{n_i}\sum_{j=1}^{n_i} y_j$. We then define

$$\chi^2 = \frac{1}{tot_{bin}(n_i>1)}\sum_{i(n_i>1)}\frac{1}{n_i}\sum_{j=1}^{n_i}[y_i(j)-\langle y_i\rangle]^2 \tag{3.20}$$

where $tot_{bin}(n_i>1)$ is the total number of bins with more than one data point. We observe that in each dimension the best estimate of β is close to 0.7. Thus, we employ

$\beta = 0.7$ for all dimensions, and estimate b values that minimize χ^2. Scaling collapse of τ_α through Eq. 3.19 is used to estimate the remaining parameter ϕ_0. In Fig. 3.4 and 3.5, we show pressure collapse and corresponding collapse of dynamics.

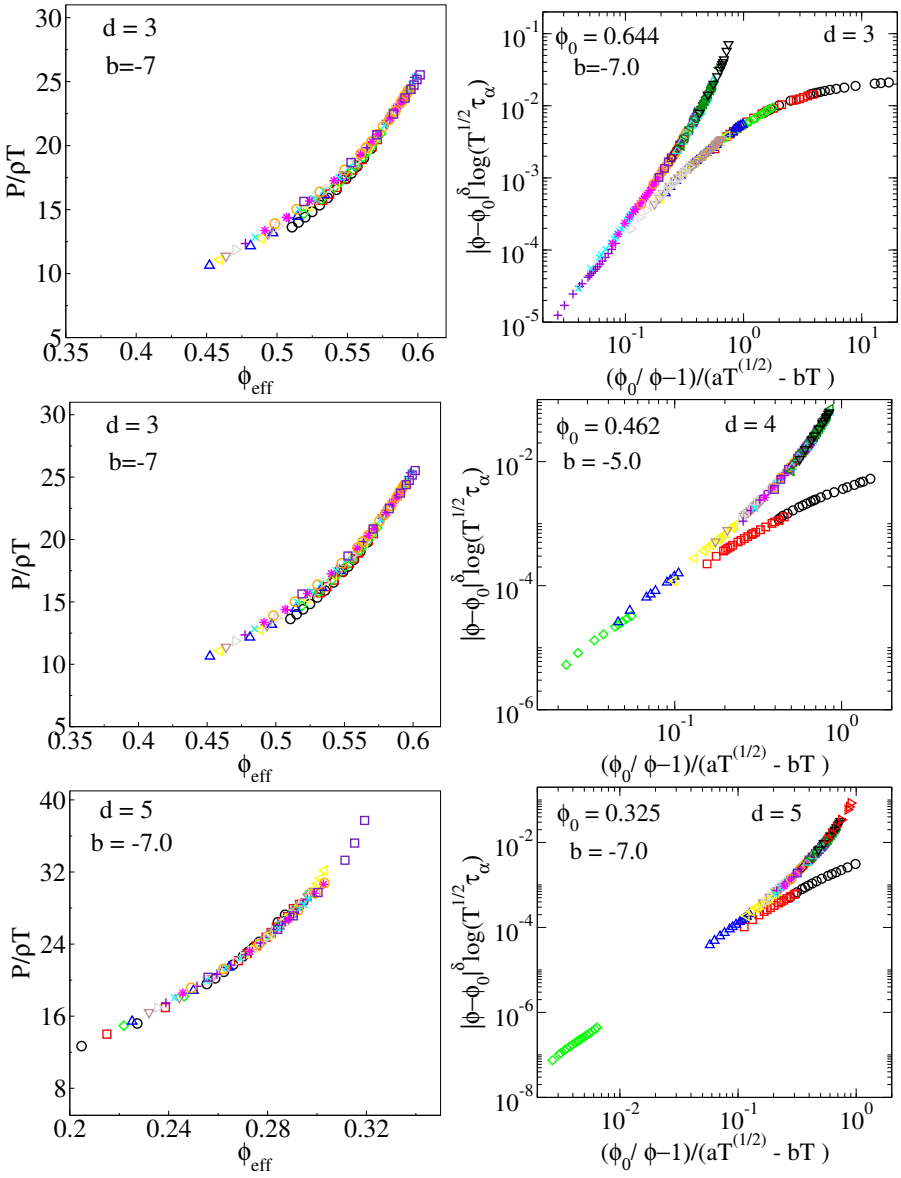

Figure 3.4: Left: Reduced pressure is plotted as a function of ϕ_{eff}. Different colour points represent different initial volume fraction. We choose c and α in such a way that pressure collapses into each other (Top: 3d, Middle: 4d, bottom: 5d). Right: The same parameters obtained from pressure collapse are used for the dynamical scaling. (Top:3d, Middle: 4d, bottom: 5d)

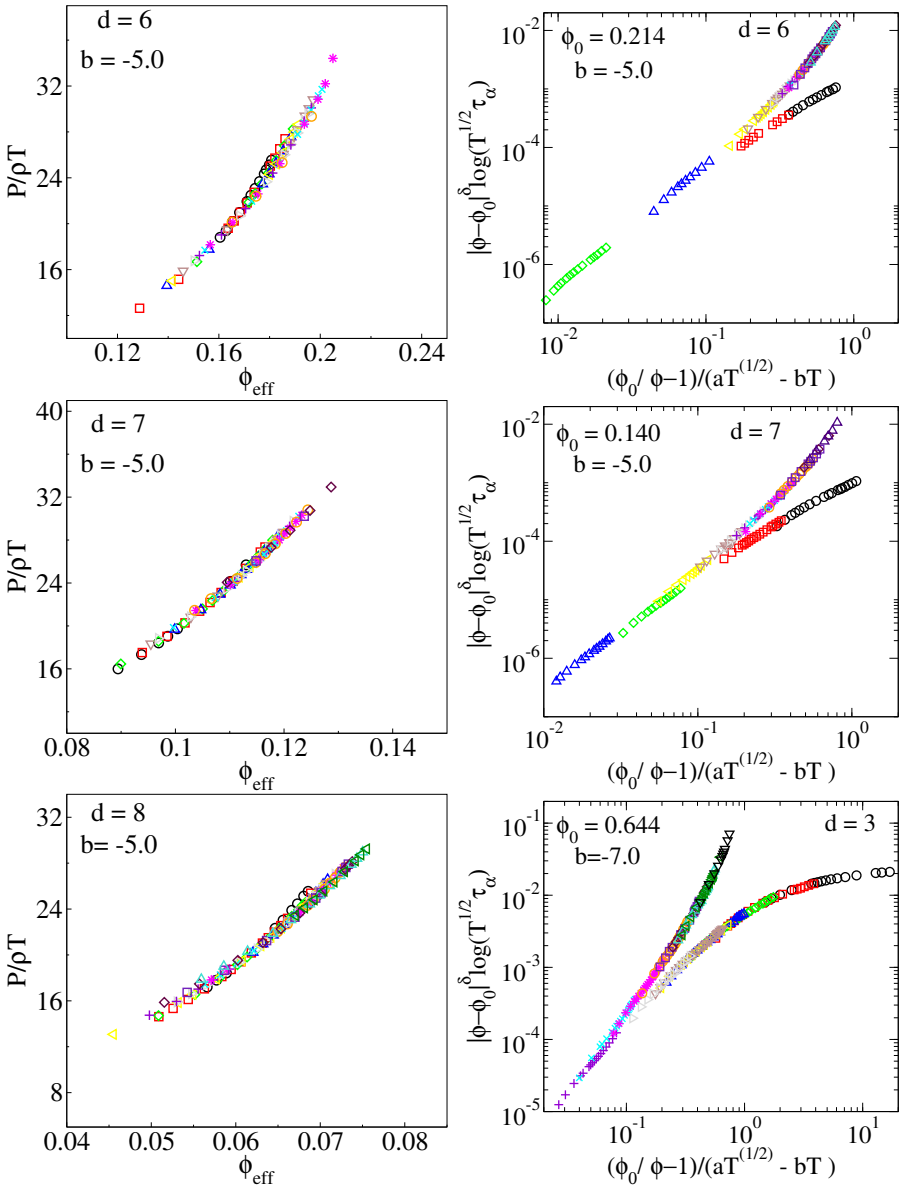

Figure 3.5: Left: Reduced pressure is plotted as a function of ϕ_{eff}. Different colour points represent different initial volume fraction. We choose c and α in such a way that pressure collapses into each other (Top: 6d, Middle: 7d, bottom: 8d). Right: The same parameters obtained from pressure collapse are used for the dynamical scaling. (Top:6d, Middle: 7d, bottom: 8d)

3.4 Error analysis for the scaling of relaxation times

We describe here the estimation of parameters that lead to scaling collapse of the relaxation times into two scaling functions above and below the density ϕ_0, with explicit reference to the new scaling form shown in Eq. 3.19 wherein the parameters describing the effective packing fraction ϕ_{eff} have been determined through the equation of state. In this case, only the parameters ϕ_0 and δ need to be determined. We follow a similar procedure for the case of the Berthier-Witten scaling form in Eq. 3.3. For each choice of the fitting parameters, we define an error χ^2_τ as follows: For each choice of ϕ_0, the range of densities is divided into a subset with $\phi > \phi_0$ and $\phi < \phi_0$, for each of which we define $\chi^{\pm 2}_\tau$, and define $\chi^2_\tau = \chi^{+2}_\tau + \chi^{-2}_\tau$ where + corresponds to the set $\phi > \phi_0$ and − corresponds to the set with $\phi < \phi_0$. For each subset of data, for each data point, we define an x value and a y value, with $x = \log\left(\frac{|\frac{\phi_0}{\phi}-1|}{a\sqrt{T}-bT^\beta}\right)$ and $y = \log\left[|\phi_0-\phi|^\delta \log\left(\sqrt{T}\tau_\alpha(\phi,T)\right)\right]$. The range of x values is divided into bins of width δx (we choose $\delta x = 0.05$), and each bin is indexed by i, with $n_i^\pm$ data points for the two subsets. For each bin, and for each subset, we compute a mean y value $\langle y_i^\pm\rangle = \frac{1}{n_i^\pm}\sum_{j=1}^{n_i^\pm} y_j^\pm$ (for bins with $n_i^\pm \neq 0$, $\langle y_i^\pm\rangle = 0$ otherwise). We then define

$$\chi^{\pm 2}_\tau = \frac{1}{tot_{bin}(n_i>1)} \sum_{i(n_i^\pm>1)} \frac{1}{n_i^\pm} \sum_{j=1}^{n_i^\pm} \left[y_i^\pm(j) - \langle y_i^\pm\rangle\right]^2 \tag{3.21}$$

from which the total error χ^2_τ is computed, and minimized with respect to the parameters sought to be estimated (ϕ_0 and δ). We note that the quantity χ^2_τ is not a smooth function of the parameters ϕ_0 and δ, since the number of points n_i in each bin can change discontinuously with a variation of ϕ_0 and δ. Further, for some choices of ϕ_0 and δ, low values of χ^2_τ can be obtained for relatively poor scaling collapse, arising from the fact that several bins of x values contain a single data set and hence does not contribute to the error. Thus, (only in the case of BW scaling) after we obtain estimates of ϕ_0 and δ that minimize χ^2_τ, we consider small variations around these values that improve upon the scaling collapse. Finally, for the scaling function Eq. 3.19, we fix the value of δ to be $\delta = 2$, which we justify below.

3.4.1 Justification of the choice $\delta = 2$

Based on the scaling function Eq. 3.19 we propose, a natural choice for the value of δ is 2, which leads to an Arrhenius form at low temperatures at the crossover density ϕ_0. The value $\delta = 2$ is also what has been argued to be valid in 3 dimensions [174], and close to the value found in [169, 170]. Nevertheless, the value of δ in higher dimensional hard sphere fluids is not available, and therefore, we consider initially the

variation of δ, along with ϕ_0, in Eq. 3.19, after fixing b and β using equation of state data. We compute the error as described above for a range of choices of ϕ_0 and δ, which is shown in Fig. 3.6 for $d = 3$. We note that a range of ϕ_0 values and corresponding δ values exhibit comparable errors. In Fig. 3.7 we show the minimum of χ^2_τ for each ϕ_0 and plot it as a function of ϕ_0 (left) and equivalently, the corresponding δ. Though the errors are comparable for the range of ϕ_0 and δ we consider, minimum errors are obtained for δ values close to $\delta = 2$. Similar results are also obtained for all other dimensions. On this basis, we conclude that the choice $\delta = 2$ is reasonable, which we fix in subsequent analysis, and estimate ϕ_0 based on minimizing χ^2_τ, as shown in Fig. 3.8.

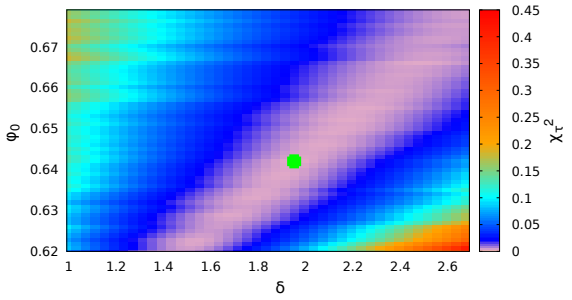

Figure 3.6: Heat map of error χ^2_τ as a function of ϕ_0 and δ for a big range of δ and ϕ_0. The green dot indicates the values of ϕ_0 and δ for which χ^2_τ is minimum.

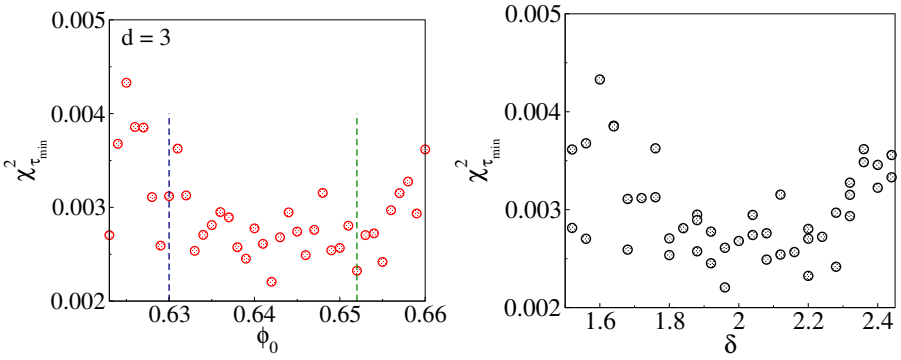

Figure 3.7: For each ϕ_0, we obtain the value of δ for which χ^2_τ is minimum. The minimum χ^2_τ so obtained is plotted as a function of ϕ_0 (left) and alternately, the corresponding δ (right). The vertical lines indicate the range of ϕ_0 within which we estimate the best fit value, as described in Sec. S1.

Thus we obtain ϕ_0, the ideal glass transition density of hard sphere using different scaling formulas; the different estimates of ϕ_0, are reported on Table 3.1

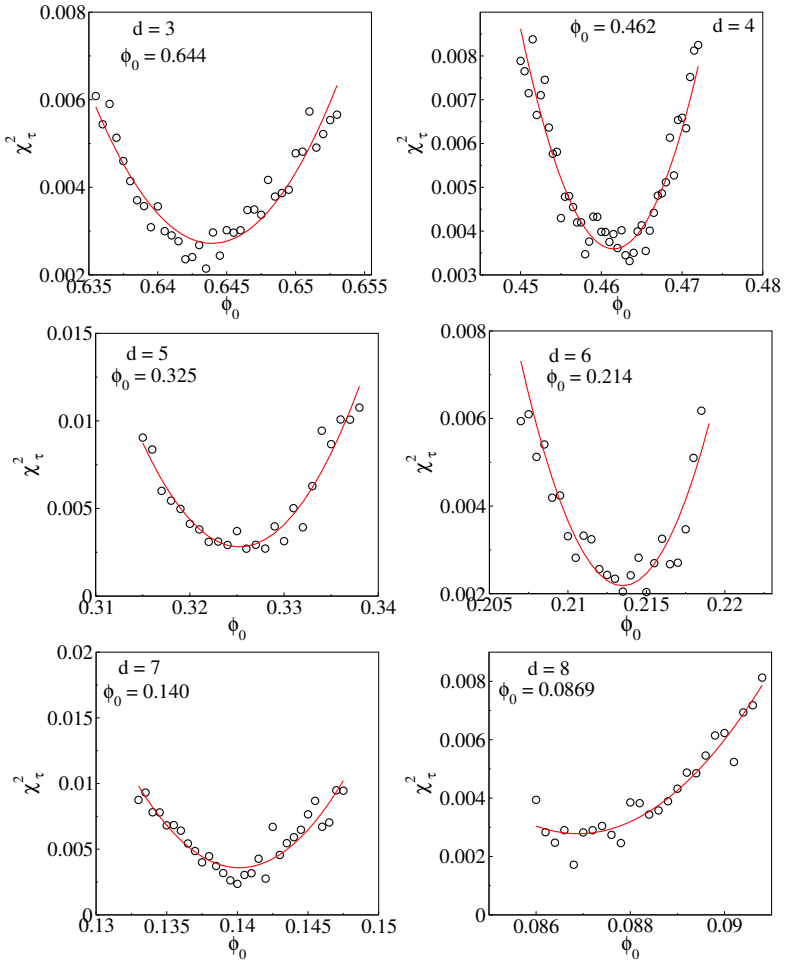

Figure 3.8: χ^2_τ as a function of ϕ_0, with $\delta = 2.0$.

Dimension	BW	AKS	MZ [94]
3	0.632 ± 0.001	0.644 ± 0.003	0.624414
4	0.459 ± 0.001	0.462 ± 0.004	0.480302
5	0.328 ± 0.001	0.325 ± 0.003	0.325298
6	0.214 ± 0.0005	0.214 ± 0.002	0.203008
7	0.138 ± 0.0005	0.140 ± 0.002	0.126974
8	0.0868 ± 0.0002	0.0870 ± 0.001	0.0777626

Table 3.1: Densities ϕ_0 obtained from different scaling procedures, and from theoretical estimates in [94], shown for 3 – 8 spatial dimensions.

3.4.2 Jamming density of soft sphere

We next estimate the jamming densities following the protocol employed in [97]. However, initial configurations are random, as was done in Ref. [146]. Use of initial configurations as random configurations makes sure, the jamming densities we show here are the low density limit over which jamming can occurs. We choose 1000 configurations from the range of densities in each dimension (as jamming point has no dependency of initial densities). These initial configurations are compressed till the energy reaches 10^{-5} with the compression step 0.0001 for $d = 3$ and 4; 0.00005 for $d = 5, 6$; 0.00001 for $d = 7$ and 8×10^{-5} for $d = 8$), and decompressed (10 times lower than the compression step) till the energy decreases below 10^{-16}, at the jamming density (details of the procedure is given in chapter 2). Fig. 3.9 illustrates the protocol for $d = 3 - 8$. Based on the initial densities used, the ϕ_J we estimate corresponds to the low density limit of the range over which jamming can take place. The procedure is applied to 1000 independent initial configurations, and the histogram of jamming densities obtained is shown in Fig. 3.10.

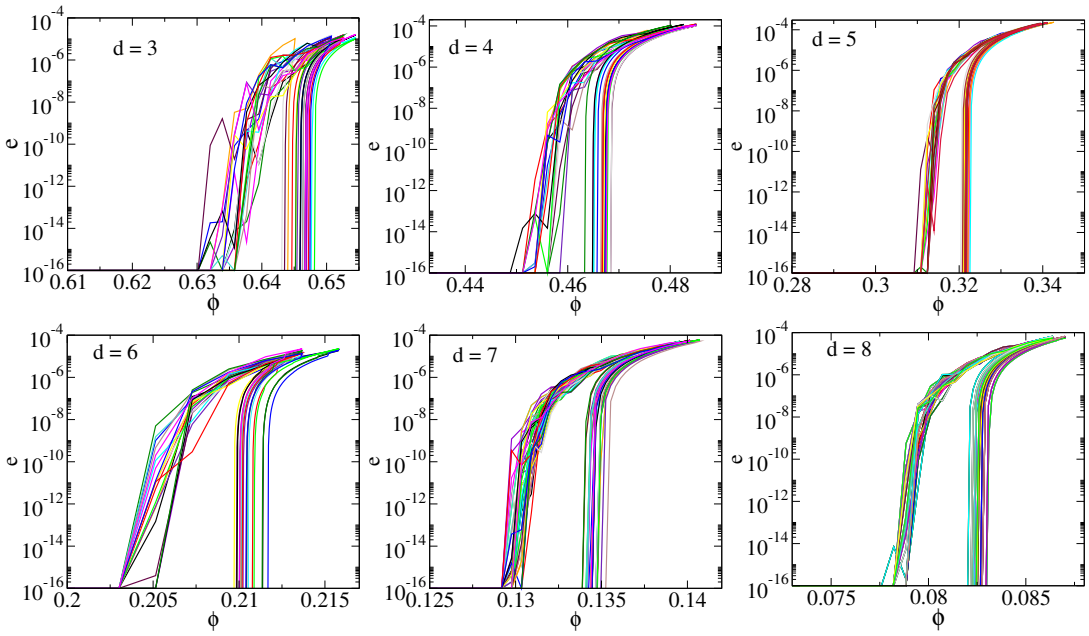

Figure 3.9: Energy as a function of density ϕ during the compression and decompression cycles. Different lines correspond to different initial conditions (We show here 50 samples).

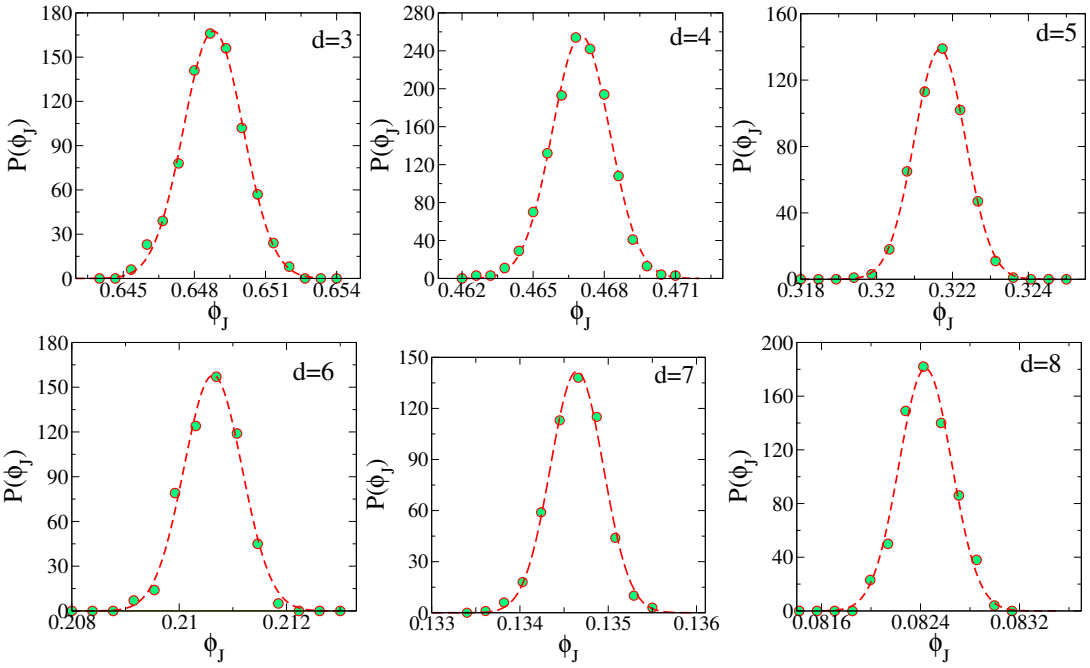

Figure 3.10: Histogram of the jamming densities ϕ_J obtained from 1000 samples are shown for 3 – 8d

Comparison of densities The average jamming density ϕ_J is shown in Fig. 3.11(also tabulated in Table 3.2), along with estimates of ϕ_0 obtained above. The ratio ϕ_0/ϕ_J, shown in the inset, increases with d, with $\phi_0 > \phi_J$ for $d > 4$, whereas for $d = 3$ and 4, ϕ_0, ϕ_J with the two values being very close. The jamming densities ϕ_J we obtain are very similar to, but slightly larger than, those obtained for monodisperse spheres in [159, 178]. In Fig. 3.11, we compare the scaled jamming densities we obtain, with those in [178]. We also show the recent theoretical calculations in [94] for the corresponding quantity ϕ_{th}, which shows the same trend as our ϕ_J data, but are smaller. We further show the ϕ_0 values we obtain, along with the corresponding calculated values in [94]. As discussed in [94, 155], $2^d\phi_0/d$ is expected in increase as $\log d$, whereas $2^d\phi_J/d \to 6.2581$ as $d \to \infty$. We are not able to quantitatively comment on either prediction, but we note that the values of ϕ_0 calculated in [94] are in near quantitative agreement with our results, whereas the ϕ_J values in [94] underestimate our results as well as those in [159, 178].

3.4.3 Fraction of rattlers as a function of density

In order to understand the physical meaning of ϕ_0, we have calculated another density where the fraction of rattler becomes zero. We have computed the fraction of rattlers as a function of density in 3 – 8 spatial dimensions. First, the system is equilibrated at some fixed temperatures (where $\tau_\alpha \sim 10$). Then, the equilibrated liquid is quenched at zero temperature following the conjugate gradient minimization method.

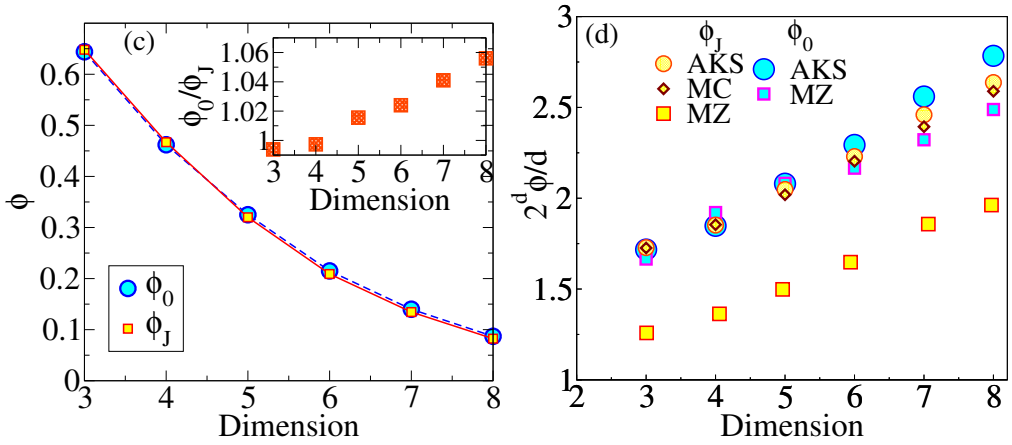

Figure 3.11: Left Panel: The jamming density, ϕ_J and the glass transition density, ϕ_0, plotted as a function of spatial dimension. Inset: Ratio of ϕ_0 and ϕ_J, plotted as a function of spatial dimension. Right Panel: Comparison of ϕ_0 and ϕ_J values from the present work (AKS) with previous simulation [178] (MC) and theoretical calculations [94] (MZ) using the Percus-Yevick closure.

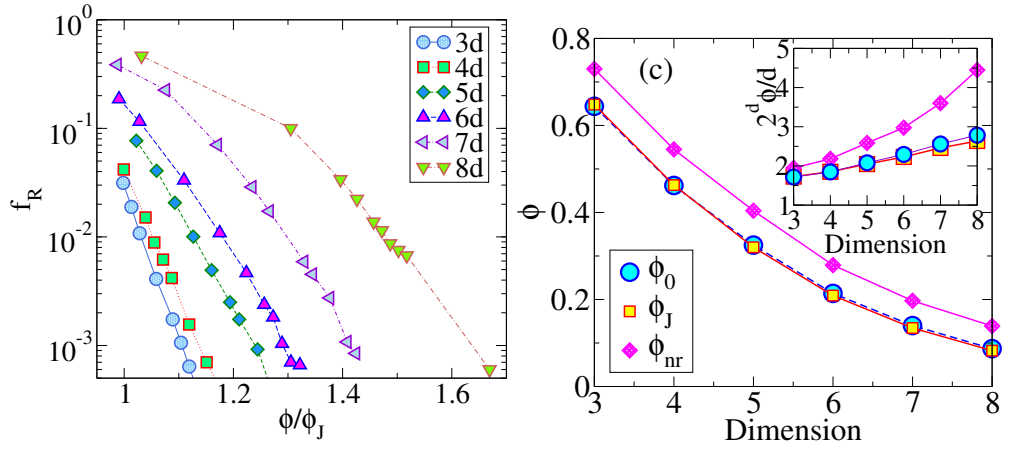

Figure 3.12: Left: Fraction of rattlers as a function of densities (scaled with the jamming density, ϕ_J) in $3-8$ spatial dimensions. Right: ϕ_{nr} along with ϕ_J and ϕ_0 is plotted against dimension. Inset: Same data with Y axis is scaled as $2^d\phi/d$

d	ϕ_J	ϕ_0
3	0.648 ± 0.0014	0.644 ± 0.003
4	0.467 ± 0.0015	0.462 ± 0.004
5	0.320 ± 0.0008	0.325 ± 0.003
6	0.209 ± 0.0006	0.214 ± 0.002
7	0.1345 ± 0.0004	0.140 ± 0.002
8	0.0824 ± 0.0003	0.0870 ± 0.001

Table 3.2: Jamming and glass transition densities ϕ_J and ϕ_0 for dimensions d from 3 to 8. Error bars for ϕ_0 are obtained by considering an increase in the error χ^2_τ (defined in SM) by 20% of the lowest value. The error bars of ϕ_J is computed from half width at half maximum of the distribution of ϕ_J (shown Fig. 3(b) and the SM).

.

The structure obtained after the minimization is called the inherent structure (IS). We have computed the Hessian matrix at this IS and computed the eigenvalues of the Hessian matrix. The Hessian matrix is defined as

$$\mathcal{H}_{ij}^{\alpha\beta} = \frac{\partial^2 U}{\partial r_i^\alpha \partial r_j^\beta}, \tag{3.22}$$

where, i and j refer to particle i and j. α and β correspond to different spatial directions and α, β varies from 1 to d. U is the total potential energy of the system and r_i^α is the αth component of the position vector of particle i. For a system of N particle, the Hessian matrix will be of size $Nd \times Nd$. In the “d" dimension, there will be at least “d" eigenvalues which are zero (for translational symmetry). If there are more than “d" eigenvalues which are zero, we have termed them as rattlers. The fraction of ratters, f_R is the total number of rattlers divided by the total number of eigenvalues. In Fig. 3.12, we have shown the fraction of rattlers, f_R, as a function of density (scaled with jamming density, ϕ_J) for $3-8$ spatial dimension. The density at which f_R goes to zero (as, at large density, f_R decays almost exponentially, we have used a tolerance of 10^{-5}) is termed as ϕ_{nr}. We see that this density is neither corresponds to ϕ_J nor ϕ_0. This density turns out to be always larger than ϕ_0 at each dimension.

3.4.4 Density-temperature diagram

Finally, we compute the temperature at which the relaxation times show an apparent divergence by fitting the data at each density above ϕ_0, for each dimension, to the Vogel-Fulcher-Tammann (VFT) form, $\tau_\alpha = \tau_0 \exp\left[\frac{1}{K_{VFT}\left(\frac{T}{T_{VFT}}-1\right)}\right]$. In Fig. 3.13, we show the density-temperature diagram for $3d$ and $5d$ (results for other dimensions is shown in the SM) which shows ϕ_0 (red diamond) and ϕ_J (navy blue square), along with the density dependent T_{VFT} (orange circles), and the state points at which simulations

have been performed (blue cirles). The results shown illustrate the manner in which the relationship between ϕ_0 and ϕ_J changes with spatial dimension. The T_{VFT} values shown clearly extrapolate to zero at $\phi \to \phi_0$, illustrating clearly that the ϕ_0 is the relevant limit density for the density dependent glass transition.

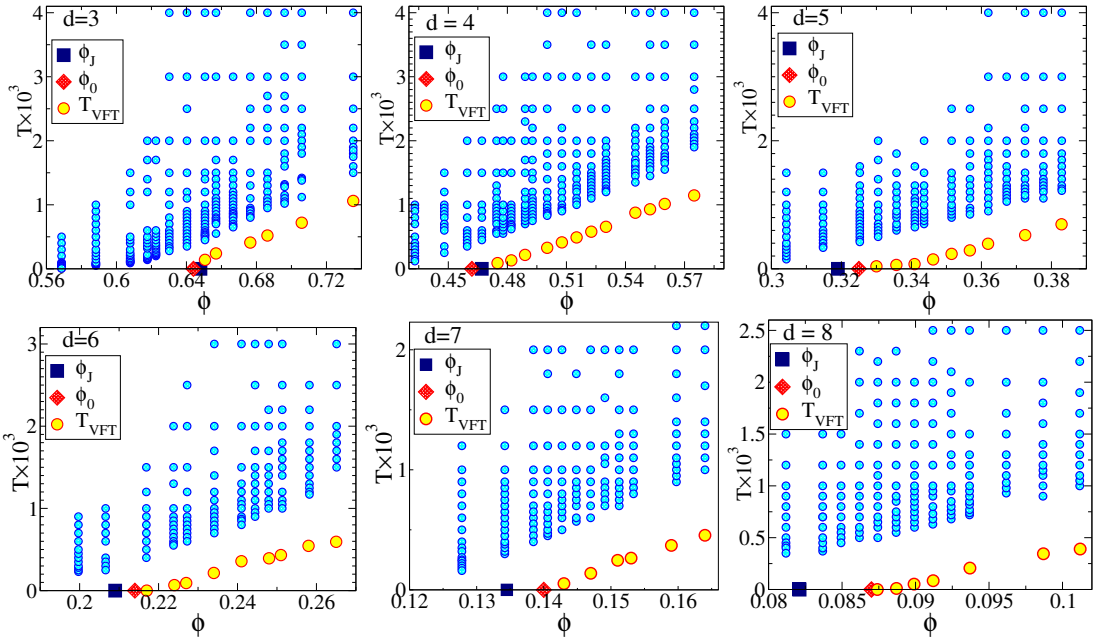

Figure 3.13: All the data points simulated in 3 – 8d along with ϕ_J and ϕ_0 for that dimension is plotted in a single plot for different dimensions. The red dots correspond to the T_{VFT} at that density.

3.5 Conclusion

To summarize, we have studied the dynamics of model glass forming liquids consisting of soft (harmonic) spheres by measuring relaxation times as a function of temperature for several densities for spatial dimensions 3−8. The temperature dependence exhibits a crossover from sub-Arrhenius to super-Arrhenius behavior as density increases. We perform a new scaling analysis of the relaxation times to identify a density ϕ_0 which corresponds to the ideal glass transition density for the hard sphere (or zero temperature) limit. We also estimate the (lowest) jamming density ϕ_J, and show that for $d > 4$, $\phi_0 > \phi_J$ and thus confirms that the glass transition and the jamming transition are fundamentally independent. Theoretical calculations of jamming density and glass transition density in finite dimensions have not been verified before in numerical simulations. We find near quantitative agreement of our estimated ϕ_0 values with the theoretical results [94] (albeit with a steeper d dependence for the ϕ_0 we obtain), whereas the ϕ_J values we obtain are underestimated in [94]. However subsequent theoretical analysis [179] shows that ϕ_J values computed in [94] can not produce correct values and our numerical results confirm that observation. Our results thus provide a useful benchmark for future efforts in developing quantitative theories of the glass and jamming transitions.

Chapter 4

Heterogeneity and fragility of glass forming liquids in Higher Dimensions

4.1 Introduction

When a glass-forming liquid is cooled to low temperatures, its dynamics becomes heterogeneous; spatially correlated clusters of particles move faster or slower than the average. The growth of dynamic heterogeneity (DH) and its associated dynamic length scales with the lowering of temperature have been considered a hallmark of relaxation dynamics in glass forming liquids [42, 43, 48, 138, 180–183]. The role of such heterogeneities in the complex relaxation dynamics in glass forming liquids, and growing length scales governing these relaxation processes have been widely investigated [47, 184]. An extensively studied phenomenon, which has been analysed in the context of dynamical heterogeneity is the breakdown of the Stokes-Einstein relation (SER) $\frac{D\eta}{T} = constant$ (or equivalently, $D\tau_\alpha = constant$) where D is the diffusion coefficient, η is the shear viscosity, T is the temperature, and τ_α is the structural relaxation time [59, 64, 66, 68, 70, 185–198]. Although the origin of such a breakdown in hopping dynamics have also been investigated [195, 197, 198], significant evidence links the breakdown of the Stokes-Einstein relation with length scales over which dynamics is heterogeneous [195, 198, 199]. It has also been suggested that fragility, which quantifies the degree of non-Arrhenius increase of relaxation times upon lowering temperature, is also related to heterogeneous dynamics. Böhmer *et al.* [50] investigated the correlation between the fragility and heterogeneity of dynamics, by compiling data for a large number of glass formers. Fragility was quantified by the fragility index m which measures the steepness of rise of relaxation times at the glass transition, in an Angell plot [200], wherein the logarithm of the relaxation time is plotted against inverse temperature scaled to the glass transition temperature (T_g/T). The KWW exponent, β, which characterises stretched exponential relaxation of density fluctuations, was

considered as a measure of the heterogeneity of dynamics. Large values of fragility index were found to correspond to small values of β. Such a correlation between heterogeneity and fragility have been probed in several works (and also contested [201]), typically through consideration of the relationship between configurational entropy, fragility and cooperative length scales of dynamics [202–205]. Some of the issues involved have been addressed within the framework of the random first order transition (RFOT) theory [61, 153, 154], extensions of mode coupling theory [206], recent exact results in the limit of infinite spatial dimensions [92] and corresponding investigations of dynamics in variable dimensions [207]. In particular, analyses of static and dynamic behaviour that may be expected in finite dimensions have led to identification of an upper critical dimension of $d_u = 8$ above which mean-field theories provide the correct description [208, 209]. Within the framework of the generalised entropy theory as well [162], $d = 8$ arises as a special dimension, above which an entropy vanishing transition does not exist at finite temperature. In this context, it is of interest to understand how aspects of heterogeneous dynamics, the breakdown of the SER, and fragility depend on spatial dimensionality. Indeed, some studies have addressed such dependence [64, 70, 160]. In particular, Charbonneau *et al.* [70] considered hard sphere fluids up to 10 dimensions and showed evidence that the exponent ω in the relation $D \sim \tau_\alpha^{-1+\omega}$ that quantifies the break down of the SER vanishes within numerical uncertainty above spatial dimension $d = 8$. However, this remains the only study that has explored the dimension dependence above $d = 4$. A similar study, for a model system with an interaction potential other than hard core interaction, which permits the study of both temperature and density dependent behaviour, is therefore desirable. We undertake such a study in the present work.

We investigate a model glass forming liquid consisting of a binary mixture of spheres interacting with a harmonic potential, in 3–8 spatial dimensions. In the zero-temperature limit, this model has the limiting behaviour of the hard sphere model whose behaviour is controlled by density alone, while it exhibits behaviour of dense glass formers at high densities, at finite temperature. We perform computer simulations and investigate various measures of dynamical heterogeneity (DH) such as the non-Gaussian parameter, $\alpha_2(t)$, the dynamical susceptibility, χ_4 as a function of time for a wide range of temperatures. We compute the fragilities from the temperature dependence of the relaxation times, and further investigate the breakdown of the SER from a comparison of diffusion coefficients and relaxation times. We find a consistent variation of behaviour as the spatial dimension increases, wherein the fragility, extent of heterogeneity, and the degree of breakdown of the SER decrease with increasing spatial dimensionality, consistent with the approach to mean-field behaviour at $d = 8$. We briefly discuss the dependence on density of fragility and resolve an apparent inconsistency with previously published results which suggested an increase of fragility with increasing

dimension while the degree of heterogeneity decreased.

4.2 Simulations details

We investigate a 50 : 50 binary mixture of particles that interact with a harmonic potential given by [169, 172]. The details of the model are given in chapter 2.

We present results for $3d$ - $8d$ fixing the density at $1.3\phi_J$, where ϕ_J is the jamming density. We have used ϕ_J=0.645(3d), 0.467(4d), 0.319(5d), 0.209(6d), 0.133(7d), 0.0821(8d), using estimates by Charbonneau *et al.* [156]. Our estimates of ϕ_J are close to the values used here to a high degree of accuracy. Thus, the volume fraction we use in our simulations are as follows: 0.8384 (3d), 0.6071 (4d), 0.4147 (5d), 0.2717 (6d),0.1729 (7d), 0.1067 (8d). The number density, ρ is related to the volume fraction ϕ for the binary mixture in the following way

$$\phi = \rho 2^{-d} \frac{\pi^{d/2}}{\Gamma(1+\frac{d}{2})}((c_A\sigma_{AA}^d + c_B\sigma_{BB}^d) \tag{4.1}$$

where $\rho = N/V$, with N being the number of particles, and V the volume, and the fractions $c_A = c_B = 1/2$. The corresponding number densities are following: 0.8556 (3d),0.8132 (4d), 0.7904 (5d), 0.7891 (6d), 0.8114 (7d), 0.8554 (8d). The system size is fixed at 5000 particles, which is large enough that the linear dimension L is $> 2\sigma_{BB}$ in all dimensions. Molecular dynamics (MD) simulations are performed in a cubic box with periodic boundary conditions in the constant number, volume, and temperature (NVT) ensemble. The integration time step was fixed at $dt = 0.01$. Temperatures are kept constant using the Brown and Clarke [140] algorithm. The data, presented here, have run lengths of around 100τ (where τ is the relaxation time, defined below). We present results that are averaged over five independent samples. For results over a range of densities which we discuss in section IV, results are from 1-2 independent samples at densities other than those mentioned above.

4.3 Results

4.3.1 Fragility in different dimensions

We quantify the microscopic dynamics by computing the overlap function (for the B particles) We quantify the microscopic dynamics by computing the overlap function,

which is defined (for the B particles) by:

$$q(t) = \frac{1}{N_B}\sum_{i}^{N_B} w(|\mathbf{r}_i(t_0) - \mathbf{r}_i(t+t_0)|) \quad \text{where} \quad w(x) = \begin{cases} 1.0 & \text{if } x \le a \\ 0 & \text{otherwise.} \end{cases}$$

We choose the parameter values $a = 0.48, 0.50, 0.55, 0.60, 0.75$,and 0.80 for 3d, 4d, 5d, 6d, 7d, and 8d, respectively. (details are given in chapter 2) We calculate the relaxation times by considering the overlap function for the B particles. The relaxation time, τ_α is computed as the time at which $\langle q(t)\rangle = 1/e$, where $\langle\cdots\rangle$ refers to an ensemble average (we average over initial times and over samples). We compute the relaxation times for a wide range of temperatures in each dimension. The relaxation times exhibit super-Arrhenius temperature dependence, the strength of which is quantified by the kinetic fragility. Here, we estimate the kinetic fragility from Vogel-Fulcher-Tammann (VFT) fits to the temperature dependence of the α relaxation times:

$$\tau_\alpha = \tau_0 \exp\left[\frac{1}{K_{VFT}\left(\frac{T}{T_{VFT}} - 1\right)}\right], \tag{4.2}$$

where K_{VFT} is the kinetic fragility of the system and T_{VFT} is the temperature at which the relaxation time diverges by extrapolation. In Fig. 4.1, we show relaxation time as a

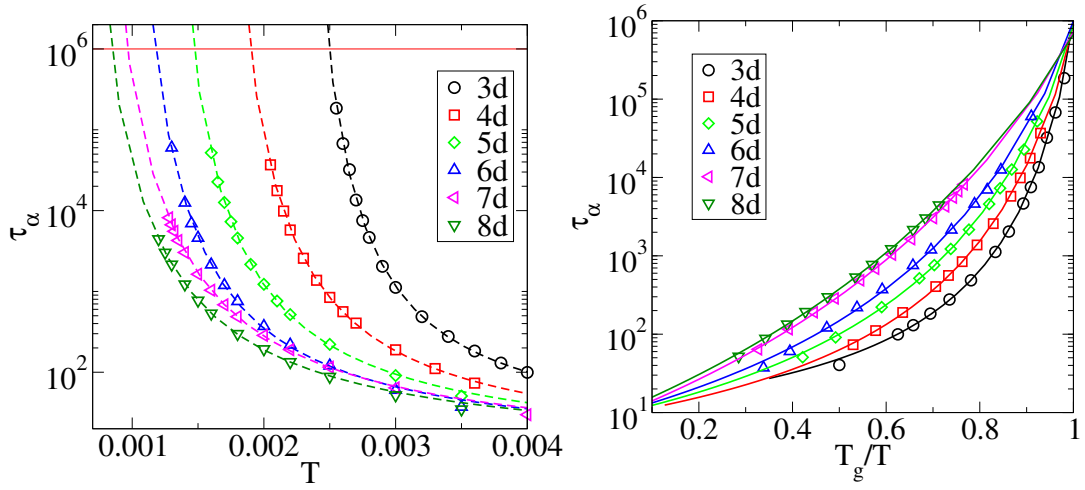

Figure 4.1: Relaxation time as a function of temperature for various dimensions. Left: Points (dot) represent simulation data along with fits (lines) to the VFT form. Right: Angell plot, of logarithm of the relaxation times, plotted against T/T_g where the glass transition temperature T_g is chosen to be the temperature at which the relaxation time reaches the value 10^6. The fragility is highest for $3d$, with the fragility decreasing with increasing spatial dimensionality.

function of temperature in a semi-log plot for each dimension, against temperature, as well as against scaled inverse temperature T_g/T, in an Angell plot. The *glass transition* temperature T_g is defined as the temperature where relaxation time becomes 10^6. The

pre-factor in Eq. 4.2, $\tau_0 \approx 10$ in all dimensions, and thus its inclusion or otherwise in defining T_g does not alter the observed behavior. From the Angell plot, it is apparent that the liquid becomes more fragile as the spatial dimension increases. The kinetic fragility K_{VFT} and the divergence temperature T_{VFT} are plotted as a function of dimension in Fig. 4.2, which shows that both K_{VFT} and T_{VFT} are decreasing functions of spatial dimensionality.

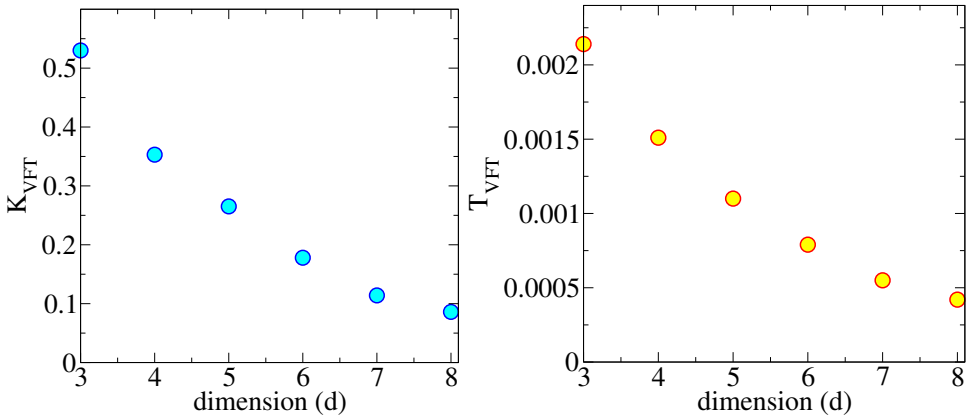

Figure 4.2: Left: Kinetic fragility is plotted as a function of spatial dimensionality at fixed density $\phi = 1.3\phi_J$, which decreases with increasing dimensionality. Right: The divergence temperature T_{VFT} is plotted as a function of spatial dimensionality at fixed density $\phi = 1.3\phi_J$ which also decreases with increasing dimensionality.

4.3.2 Heterogeneity in dynamics

We next investigate the heterogeneity in dynamics by two different measures of heterogeneity: 1. The dynamical susceptibility, χ_4, and 2. The non-Gaussian parameter, α_2.

4.3.2.1 Dynamical susceptibility, χ_4

Dynamical susceptibility, χ_4, which measures the fluctuations in the overlap function $q(t)$, is defined by:

$$\chi_4(t) = N_B\left[\langle q(t)^2\rangle - \langle q(t)\rangle^2\right] \tag{4.3}$$

where the average is over initial configurations and the independent samples.

As it has been demonstrated extensively, the time dependence of $\chi_4(t)$ is non-monotonic, and exhibits a peak value, (χ_4^{peak}), at a time that is proportional to the alpha relaxation time. In Fig. 4.3, we show $\chi_4(t)$ against time for different temperatures in each dimension. The peak value of χ_4^{peak} as well as the time at which it occurs, $t_{\chi_4}^{max}$, increase strongly upon a decrease in temperature, indicating that the heterogeneity of dynamics increases with a decrease in temperature, and is maximum at a time scale

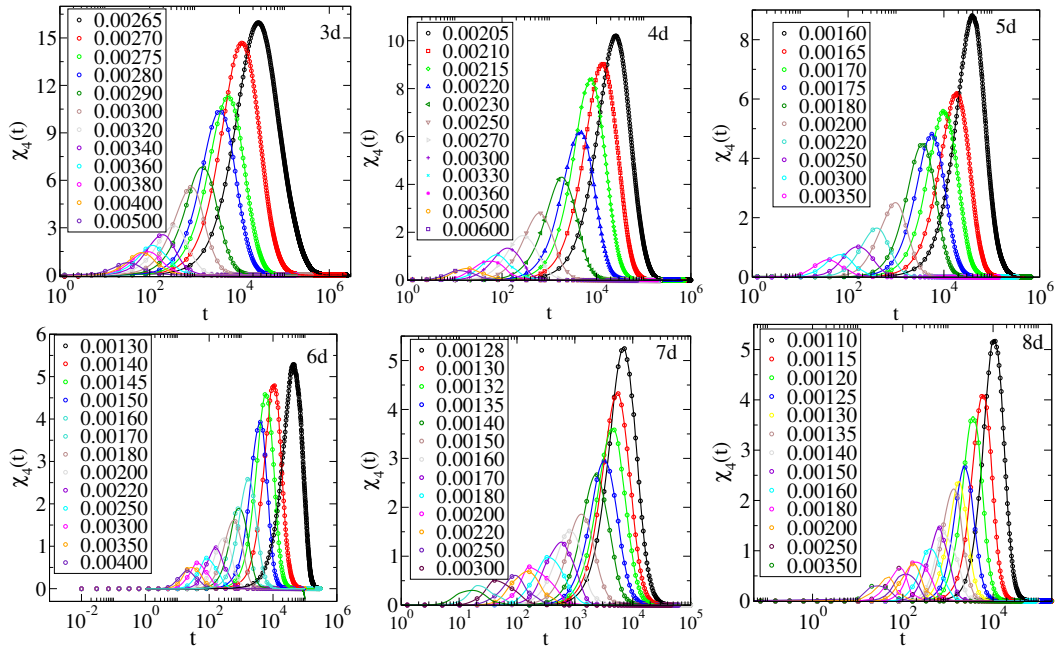

Figure 4.3: The dynamical susceptibility $\chi_4(t)$ is plotted as a function of time for different temperatures for spatial dimensions 3 – 8.

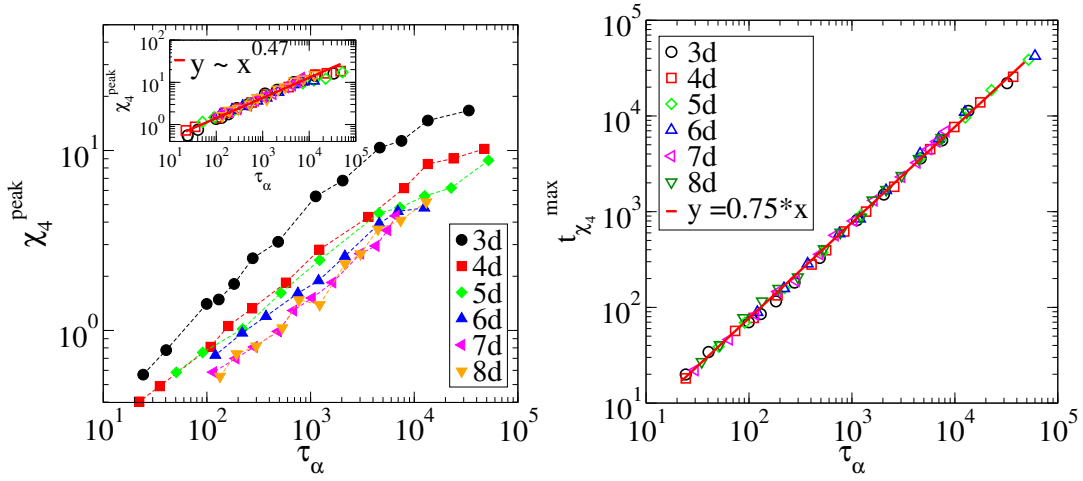

Figure 4.4: Left: The peak value of $\chi_4(t)$, χ_4^{peak}, is shown as a function of relaxation time, τ_α. Inset: By scaling χ_4^{peak} values, the data for different dimensions are collapsed onto a master curve. A power law fit (red line) provides a reasonable description for most of the temperature (τ_α) range, with exponent 0.47. Right: The time at which $\chi_4(t)$ is maximum, $t_{\chi_4}^{max}$ is plotted as a function of τ_α for different dimensions. The data for different dimensions overlap, and demonstrate that $t_{\chi_4}^{max} \sim \tau_\alpha$.

that increases in proportion to τ_α. To compare the degree of heterogeneity for different spatial dimensions, we show, in Fig. 4.4 (Left panel), χ_4^{peak} as a function of τ_α for each dimension. For a given τ_α, χ_4^{peak} decreases with increasing spatial dimension implying that heterogeneity decreases with increasing spatial dimensionality. We also observe that χ_4^{peak} shows a power law dependence on τ_α at higher temperatures as $\chi_4^{peak} \sim \tau_\alpha^z$, with z being the power-law exponent. Deviations from power law behaviour is mostly observed at lower temperatures. This behaviour is consistent with previous observations in three dimensions [46,183,210,211], including polymeric glass formers [212] and exponent z is found to be close to 0.62 for binary hard sphere fluids [183, 210] whereas $z = 0.51$ has recently been found for a model liquid that aims to tune the degree of mean field character [213]. Our estimate is on the lower side of these values, but close to that reported in [213]. Since the power law regime is limited in extent, there is room for error in the exact determination of the exponent. Remarkably, however, we find that the exponent of the power law, z, is the same in all dimensions for our studied model, as evidenced by the data collapse, regardless of the precise value. The expectation of a power law dependence arises, for example, from inhomogeneous mode coupling theory [206], and the deviations from the power law are understood to be a consequence of the role played by activated processes at low temperatures. Thus, the observation of a common exponent describing the power law dependence of χ_4^{peak} on τ_α should perhaps be seen as mean-field behaviour that does not depend on spatial dimensions and thus not surprising. Nevertheless, to our knowledge, such a universal behaviour has not previously been reported across the range of spatial dimensions that we investigate.

4.3.2.2 Non-Gaussian parameter, $\alpha_2(t)$

Next, we investigate another measure of heterogeneity, the non-Gaussian parameter, $\alpha_2(t)$, for different dimensions. As previously discussed in detail [204, 212, 214], $\alpha_2(t)$ and χ_4 correspond to distinct aspects of heterogeneity, associated with correlated clusters of mobile, and immobile, particles respectively. The non-Gaussian parameter, $\alpha_2(t)$ measures the deviation of the van Hove distribution of displacements of the particle in time t from Gaussian form, expected for spatially homogeneous dynamics, and is given by

$$\alpha_2(t) = C_d \frac{\langle r^4(t)\rangle}{\langle r^2(t)\rangle^2} - 1 \tag{4.4}$$

$$\langle r^{2n}\rangle = \frac{1}{N}\langle(\vec{r}_i(t) - \vec{r}_i(0))^{2n}\rangle \tag{4.5}$$

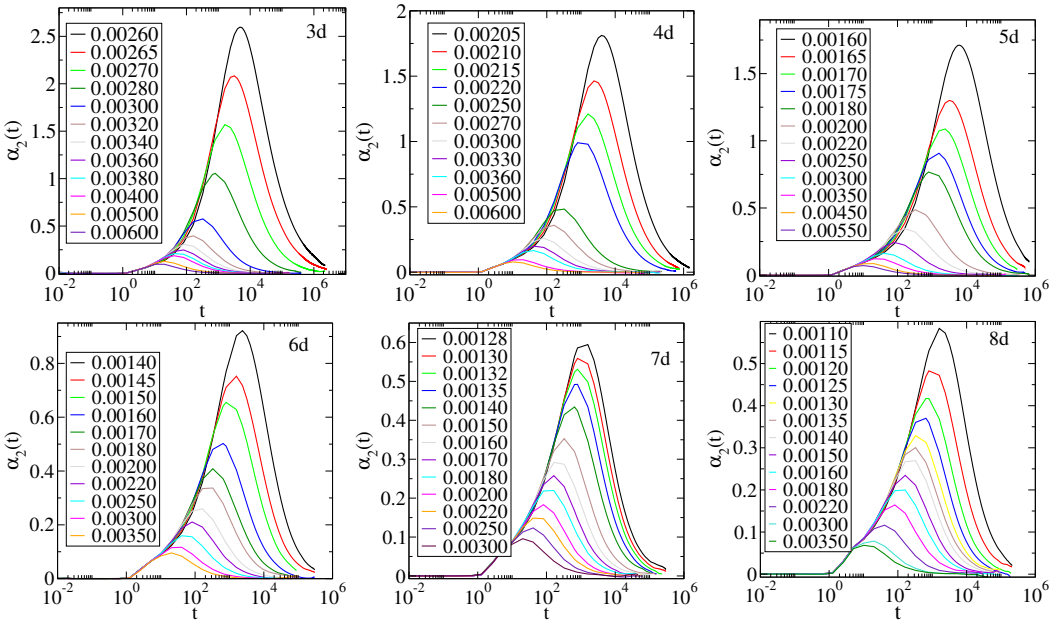

Figure 4.5: The non-Gaussian parameter α_2 is plotted against time for different temperatures and spatial dimensions 3 – 8.

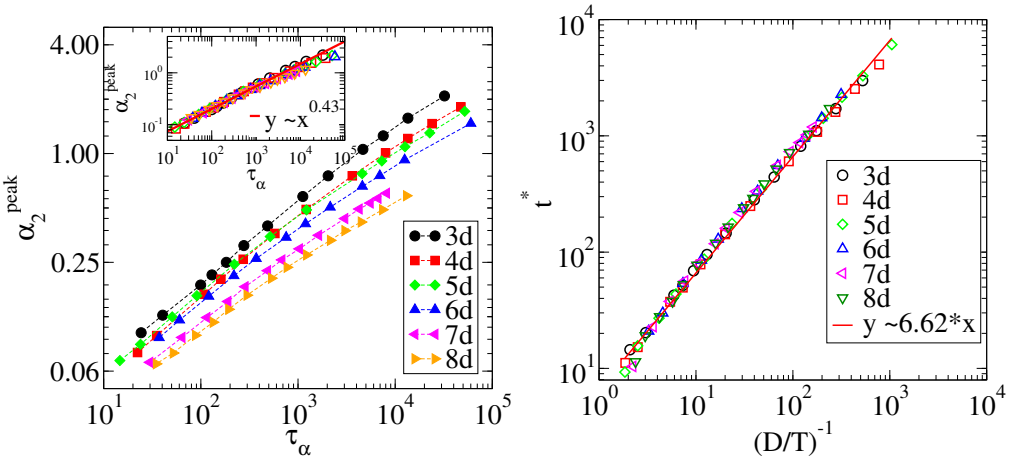

Figure 4.6: Left: The peak value of $\alpha_2(t)$, α_2^{peak}, is shown as a function of relaxation time, τ_α for different dimensions. Inset: By scaling α_2^{peak} values, the data for different dimensions are collapsed onto a master curve. A power law fit (red line) provides a reasonable description for most of the temperature (τ_α) range, with exponent 0.43. Right: The time at which $\alpha_2(t)$ is maximum, t^* is plotted as a function of $(D/T)^{-1}$ for different dimensions. The data for different dimensions overlap, and demonstrate that $t^* \sim (D/T)^{-1}$, albeit with small deviations apparent at low temperatures.

where C_d is a spatial dimension dependent coefficient to ensure that $\alpha_2(t) = 0$ when the distribution of displacements is a Gaussian. Similar to χ_4, α_2 also shows non-monotonic behaviour with respect to time. However, the characteristic time t^* at which $\alpha_2(t)$ is maximum is smaller than τ_α, and has been demonstrated to be proportional to a time scale determined by the diffusion coefficient, $(D/T)^{-1}$ [204]. In Fig. 4.5, we show $\alpha_2(t)$ against time for different temperatures and spatial dimensions $3-8$. We see that α_2^{peak} increases with a decrease in temperature for all spatial dimensions. Similarly to χ_4, we report α_2^{peak} against τ_α for spatial dimension $3-8$ in Fig. 4.6 (Left panel). We see that for a given τ_α, α_2^{peak} also decreases with increasing dimensionality. This again implies that heterogeneity decreases with increasing spatial dimensionality. Similar to χ_4^{peak}, α_2^{peak} also displays a power law dependence on τ_α at higher dimensions, with deviations at lower temperatures. The inset of Fig. 4.6 (Left panel) demonstrates that for α_2^{peak}, the exponent of the power law is 0.43 and is a good description of the data for all dimensions. In [53] the behaviour of α_2^{peak} *vs.* τ_α was fitted to two power laws, with exponents 0.8 (high temperatures) and 0.3 (low temperatures). While we find the exponent to be 0.43 convincingly over two decades of (high to moderate temperature) relaxation times, we do find that an exponent of 0.3 is a good description of low temperature data. In Fig. 4.6 (Right panel), we show the time t^* against $(D/T)^{-1}$, where D is diffusivity, for different spatial dimensions, confirming the validity of the relation $t^* \sim (D/T)^{-1}$ beyond three dimensions [204].The observed relationship between t^* and D/T has been found to be valid in many different glass formers as well as other materials [64,204,215,216], and our results show that it is valid in different dimensions as well. We note, however, that an exponent other than -1 has been reported recently for a metallic glass former [217].

4.3.3 The Breakdown of the Stokes-Einstein Relation

A much studied phenomenon associated with glassy behavoiur is the violation or breakdown of the Stokes-Einstein relation (SER), which relates the translational diffusion coefficient (D) of a Brownian particle to the shear viscosity η of the surrounding liquid at a temperature T: $D = mk_BT/c\pi R\eta$, where m is the mass and R is the radius of the particle, T is the temperature of the liquid, and the factor c is a constant which depends on the boundary condition at the surface of the Brownian particle. It is been observed in several investigations that the SER is also satisfied when one considers the self-diffusion of particles in a liquid at relatively high temperatures (The caveats and the extent to which such a statement is valid have also been discussed, *e. g.* [70]). However, as temperature is decreased towards the glass transition, the SER is observed to break down. As mentioned in the introduction, violations of the SER, which can be expressed as $\frac{D\eta}{T} = constant$, have been investigated considering

τ_α in place of $\frac{\eta}{T}$, expressing the SER as $D\tau_\alpha = constant$ [64, 70, 198]. This equivalence has been validated by computing the viscosity η and comparing with τ_α, at the wave vector corresponding to the peak of the structure factor. Further, several works have considered relaxation behavior as a function of the wave vector k [64,70,193,198], either through the k dependent viscosity [193] or relaxation times computed as a function of k. In [198], it was shown that for a given k, violation of the SER arise when k^{-1} falls below a length scale characterising dynamical heterogeneity. In the preent work, we do not investigate the k dependence of the violation of SER, but consider only the τ_α defined above. The breakdown of SER is characterized by an exponent ω that describes a scaling $D \sim \tau_\alpha^{-1+\omega}$. As mentioned above, a limited number of previous studies [64, 70, 160] have considered SER and the breakdown thereof as a function of spatial dimension. Charbonneau *et al.* [70] have performed a hydrodynamic analysis of SER for varying spatial dimension, as well as numerical investigations up to $d = 10$ for hard sphere liquids. Here, we examine validity or breakdown of the SER employing the self diffusion coefficients D and the τ_α described above, as a function of spatial dimensionality.

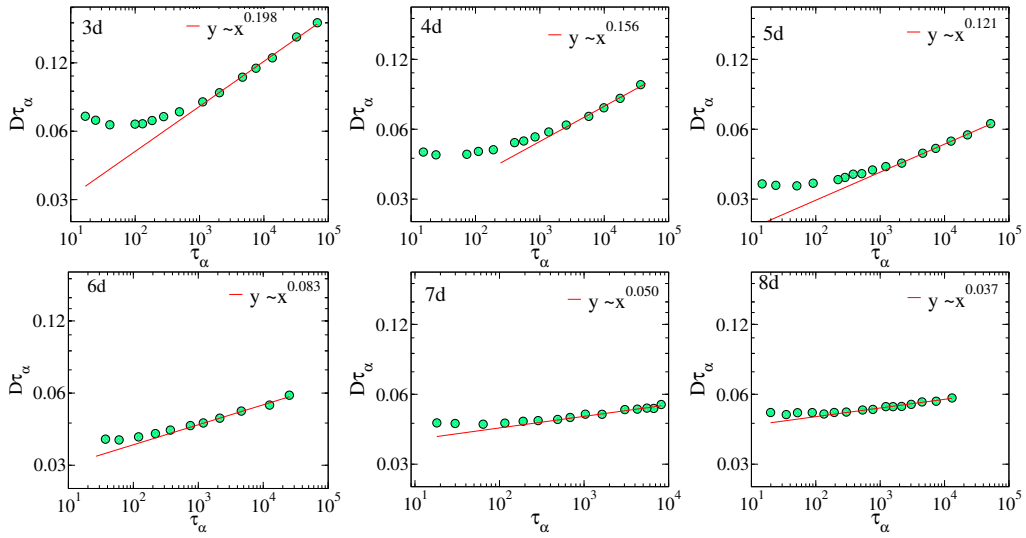

Figure 4.7: $D\tau_\alpha$ is plotted against τ_α in a log-log plot. The low temperature data is fitted with the form: $D\tau_\alpha \sim \tau_\alpha^\omega$. From the fit, we obtain ω for each spatial dimension.

In Fig. 4.7, we show the diffusivity, D multiplied by the relaxation time, τ_α, against τ_α in log-log plot. We observe that $D\tau_\alpha$ is roughly constant for small τ_α (high temperature), at least for $3d, 4d$ and $5d$, but display power law behaviour with a finite ω for large τ_α. We obtain the exponent ω by power-law fits of the form $D\tau_\alpha \sim \tau_\alpha^\omega$ for the data in the low temperature regime. In Fig. 4.9 (Left panel), we show ω as a function of spatial dimension. We find that ω is large for 3d, and decreases with increasing spatial dimensionality following a relation, $\omega \sim (d - d_c)$. We see ω becomes zero by

extrapolation of the linear form at d= 8, consistently with the idea that the upper critical dimension $d_u = 8$, and consistently with results for the hard sphere fluid [157]. The numerical values of ω show a deviation from the linear fit for $d = 7, 8$ and do not vanish for $d = 8$, as also seen in [157]. With the results available, we cannot further probe this issue. Improved numerical results and performing simulations at higher dimensions than 8 will permit more precise statements in this regard. Next, we compute the break down temperature for SER relation. Considering $D\tau_\alpha$ as a function of temperature, one finds a near constant value at high temperature, and an increase upon lowering temperature, which indicates the breakdown of SER. Since such a deviation is continuous, one needs to use a threshold, as has routinely been done in previous work. We use a threshold of 7.5% of the high temperature value to determine T_{SEB}, as shown in Fig. 4.8 below. In determining the exponent ω, we consider values of $D\tau_\alpha$ (plotted against τ_α) below T_{SEB}.

In Fig. 4.9 (Right panel), we show the breakdown temperature for SER relation, T_{SEB}, as a function of spatial dimension.

4.3.4 Density Dependence and Comparison with Previous Results

We next briefly consider the dependence of the fragility on the density at which the liquids are studied, and address an apparent inconsistency with previous results. In Fig. 4.10, we show the kinetic fragility K_{VFT} and the divergence temperature T_{VFT} against density, scaled with ϕ_J. We note that the kinetic agility K_{VFT} decreases and nearly vanishes as the density is decreased towards ϕ_J (Indeed, for higher spatial dimensions, such vanishing appears to occur for densities higher than ϕ_J, whose significance is discussed elsewhere), while at any fixed density, the fragility is a decreasing function of spatial dimensionality, consistently with the results discussed already for $\phi = 1.3\phi_J$. Similarly to K_{VFT}, T_{VFT} also decreases as the density is lowered, while being smaller for higher dimensions at fixed density. Thus, in comparing behaviour as a function of dimensionality, care must be exercised to compare results at the same scaled densities.

The observed dependence on density and spatial dimensionality helps explain an apparent inconsistency with results discussed by Sengupta *et al.* [64]. In [64], simulation results were shown for the Kob-Andersen (KA) binary Lennard-Jones mixture, and it was observed that liquids in $4d$ were less heterogeneous than in $3d$ (consistently with results here), but had larger fragility than in $3d$, which is not consistent with the present observations that the fragility too decreases with increasing spatial dimensionality.

As noted above, the fragility as well as the heterogeneity depends upon the density for a given spatial dimension, and thus, to compare results in different dimensions, one

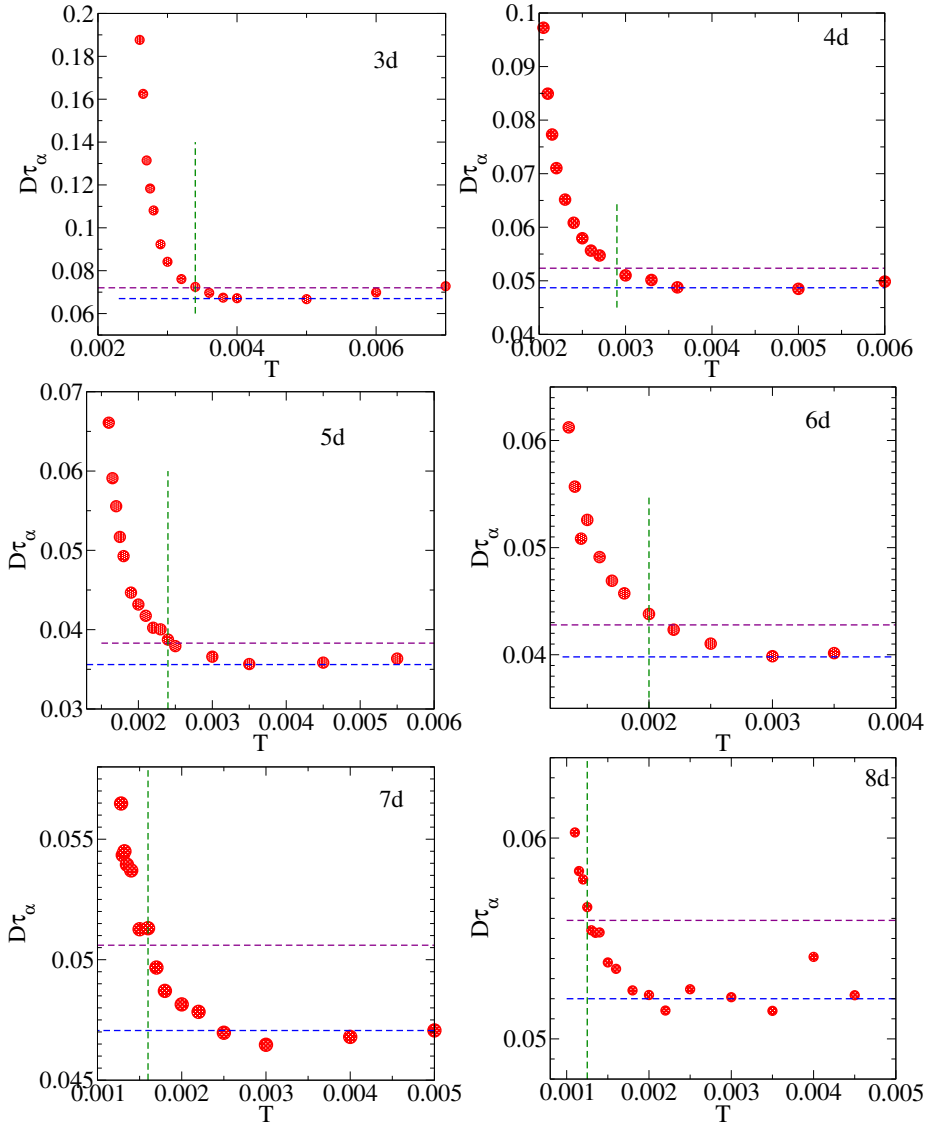

Figure 4.8: $D\tau_\alpha$ is plotted against temperature for $3-8$ spatial dimensions. We define T_{SEB} as the temperature below which $D\tau_\alpha$ exceeds the high temperature value by 7.5%. The green dotted line represents T_{SEB}.

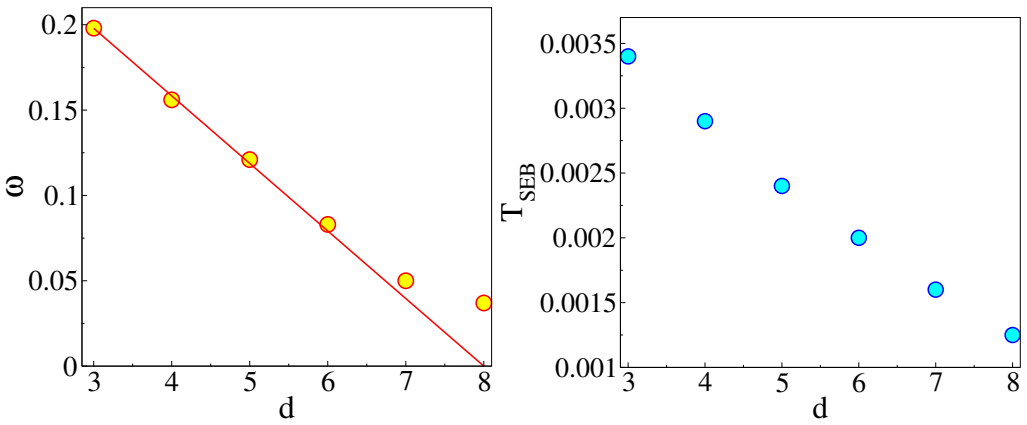

Figure 4.9: Left panel: The exponent ω is plotted against the spatial dimensions. The exponent ω decreases with increasing spatial dimensionality. Right panel: T_{SEB}, the temperature where SER breaks down is plotted against spatial dimension. T_{SEB} also decreases with increasing spatial dimensionality.

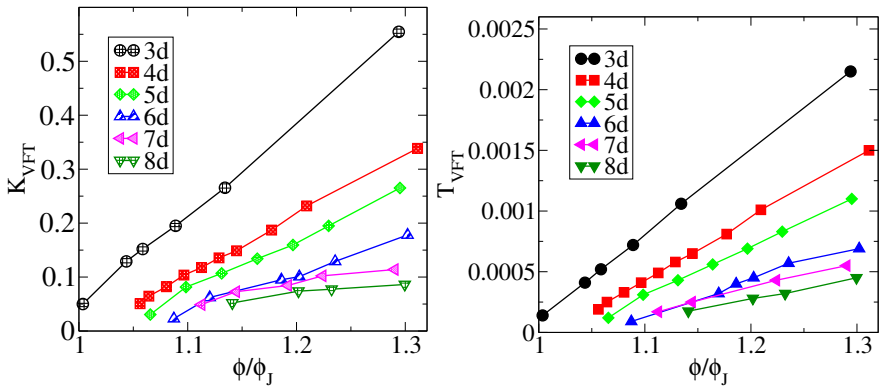

Figure 4.10: Left panel: The kinetic fragility K_{VFT} is shown as a function of scaled density ϕ/ϕ_J for spatial dimensions 3 – 8. Right panel: T_{VFT} is shown as a function of scaled density ϕ/ϕ_J for spatial dimensions 3 – 8.

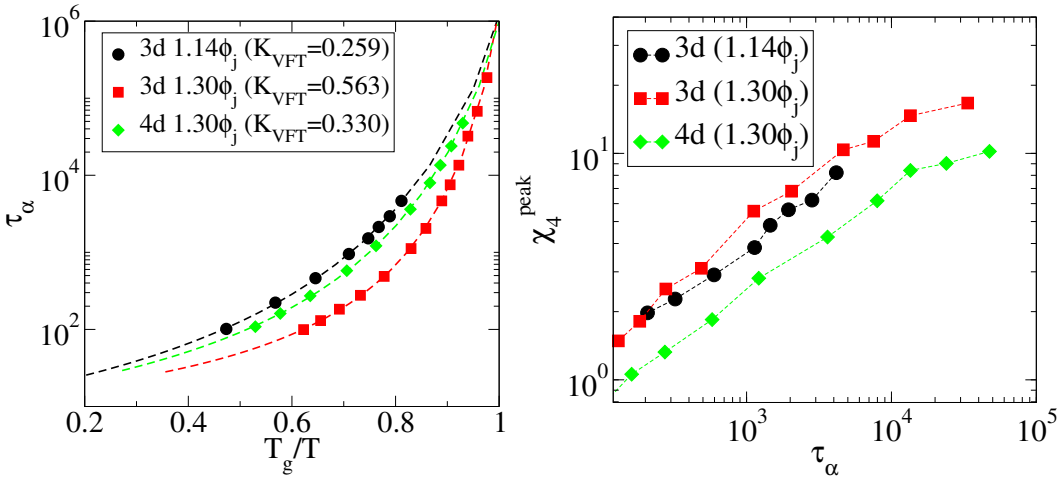

Figure 4.11: Left panel: Relaxation times are shown in an Angell plot for (a) 3d at two different densities, $1.14\phi_J$, $1.3\phi_J$ and (b) for 4d at density $1.3\phi_J$. The kinetic fragility at $1.14\phi_J$ (3d) is lower than the $3d$ and $4d$ systems at density $1.3\phi_J$. Right panel: χ_4^{peak} is plotted against τ_α for 3d at two different densities, $1.14\phi_J$ and $1.3\phi_J$ and for 4d at $1.3\phi_J$. χ_4^{peak} values for 4d at $1.3\phi_J$ are lower than for the $3d$ systems at both $1.14\phi_J$ and $1.3\phi_J$.

must consider appropriate densities. For the KA system, we do not have a jamming density to provide an appropriate scale, and instead, we use the zero temperature limit of the spinodal density for reference [218]. The spinodal density for the KA system is ~ 1.1 for 3d whereas it is ~ 1.4 for 4d. The simulations in [64] were performed at higher densities, 1.2 for 3d which is 1.09 times the spinodal density whereas for 4d the density of 1.6 was employed, which is 1.14 times the spinodal density. Thus, the scaled density in $4d$ is higher than the scaled density in $3d$, which leads to a higher fragility in the higher dimension. To illustrate this possibility, we consider for the soft sphere system a lower density of $1.14\phi_J$ in $3d$, in addition to $1.3\phi_J$, and compare with results in $4d$ at $1.3\phi_J$.

In Fig. 4.11 (Left panel), we show an Angell plot for three different cases: $1.14\phi_J$ and $1.30\phi_J$ at 3d and $1.30\phi_J$ at 4d. We note that the $3d$ system at $1.14\phi_J$ has a lower fragility (as confirmed by calculating K_{VFT}) than the $4d$ system at $1.3\phi_J$. Plotting χ_4^{peak} against τ_α for the same three cases (Right panel, Fig. 4.11), we see that the $4d$ system has the lowest heterogeneity. Thus, comparing the $3d$ system at $1.14\phi_J$ with the $4d$ system at $1.3\phi_J$ would lead to the conclusion that the heterogeneity in $3d$ is higher than in $4d$ while the fragility is higher in $4d$, whereas comparison at the same scaled density would lead to the conclusion that both the fragility and heterogeneity would decrease with increasing spatial dimensionality. We therefore conclude that the results in [64] can be understood consistently with our present results by noting the choice of densities in [64].

4.3.5 MCT exponent and temperature at higher dimensions

In Figure. 4.12(Left panel), we show the MCT fit of the relaxation time against temperature. The results show that indeed a regime exists in each dimension where relaxation times obey a power law as would be expected by MCT, but with these results, we cannot comment on the range of validity *vs.* dimensionality. We also show the exponent γ_c and the transition temperature, T_c as a function of the spatial dimension in Fig. 4.12(Right panel).

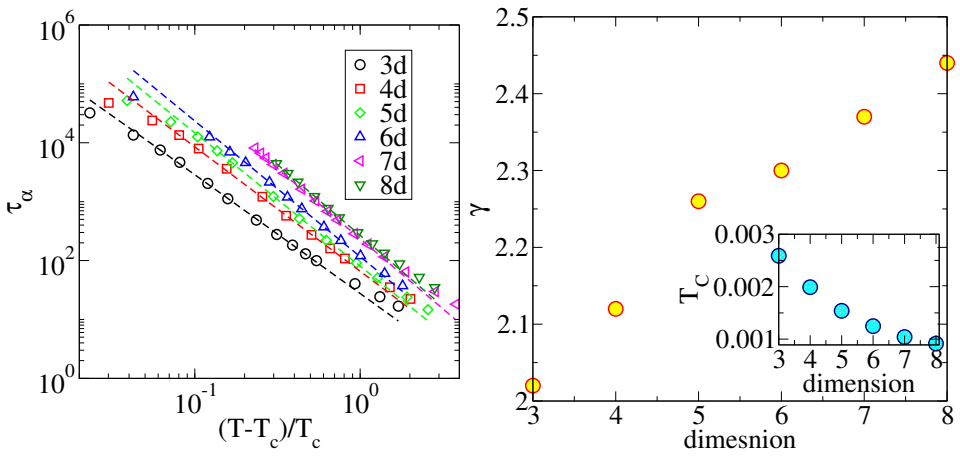

Figure 4.12: Left: Relaxation time is plotted as a function of temperature for $3-8$ spatial dimensions. We show log-log plot of τ_α vs $\frac{T-T_c}{T_c}$. Lines are the MCT fit of the data. Right: MCT exponent, γ_c as a function of dimension. Inset: MCT temperature,T_c as a function of dimension. T_c decreases with increasing dimensions

4.4 Summary and Conclusions

In conclusion, we have investigated the relationship between fragility, heterogeneity and the breakdown of the Stokes-Einstein relation in different spatial dimensions. Our results show that at fixed density, the fragility, the degree of heterogeneity and the degree of violation of the Stokes-Einstein relation decrease with increasing spatial dimensionality. The heterogeneity measures χ_4^{peak} and α_2^{peak} depend on the relaxation time τ_α at high and moderate temperatures in a power law fashion, with power law exponents that do not depend on spatial dimensionality. The exponent ω that characterises the breakdown of the Stokes-Einstein relationship displays a nearly linear relationship with spatial dimensions that corresponds to a vanishing of ω at $d = 8$, consistently with the idea that $d = 8$ represents the upper critical dimension. The ω values in $d = 7, 8$ display small deviations from such linear behaviour with d, which requires further investigation including studies in dimensions above 8. We show that

fragilities decrease with density at all spatial dimensions, approaching Arrhenius behaviour close to the jamming density. The observed density dependence helps rationalise earlier results that suggested that fragility and heterogeneity may vary in opposite ways as a function of spatial dimensionality.

Chapter 5

Power law relationship between diffusivities and Adam-Gibbs relation in higher dimensions

5.1 Introduction

Understanding the rapid increase of relaxation time of the glass-forming liquids when it is cooled below the melting temperature is one of the important themes in the study of glasses [42, 43]. Different theories have attempted to find a possible connection between thermodynamics and dynamics to understand the underlying reason for this dynamical behaviour. The celebrated Adam-Gibbs relation [79, 80] hypothesizes such a connection between a dynamic and a thermodynamics quantity of the system. It suggests that the increase in relaxation time is associated with the decrease in configurational entropy, a measure of the number of independent configurations that a system can sample in the configuration space at a given density and temperature. According to this theory:

$$X = X_0 \exp\left(\frac{A_X}{T S_c}\right) \tag{5.1}$$

Where X is a characteristic relaxation time scale such as α relaxation time, τ_α or inverse diffusivity, D^{-1}, X_0 is a pre-factor, A_X is a constant and S_c is the configurational entropy. Even though AG relation is purely phenomenological, it is mostly obeyed in numerical simulations as well as in various experiments [39, 84, 219–224] except some violations at very low temperatures reported recently [225, 226]. Further, this phenomenological theory has been rationalized by the random first order transition (RFOT) theory [61, 153, 154] considering activated relaxation dynamics due to growing length scales [45–47, 227–229] associated with the glass transition. Different dynamical quantities like relaxation time (τ_α) or diffusivity (D) or viscosity (η) are related

by the Stokes-Einstein Relation (SER) that states $D\eta/T$ = constant, or equivalently $D\tau$ = constant. Even though Adam-Gibbs relation describes a generalized form of the dynamic quantities like structural relation or diffusivity, we have shown in the previous chapter that a hallmark property of glass-forming liquids is the breakdown of the Stokes-Einstein relation (SER). It is shown that SER holds at a higher temperature, but as the temperature is decreased below a characteristic temperature, the SER breaks down. [59, 64, 66, 68, 70, 185–192, 194–198]. Thus, the diffusivity, D and the relaxation time, τ_α is no longer inversely proportional as the glass transition is approached; it obeys a fractional power law: $D\ \tau_\alpha^{-1+\omega}$. Naturally, the question arises if AG relation holds equally well for all such dynamic quantities. In a recent work, this question has been addressed, and it has been shown that the diffusivity obeys AG relation for a more extensive range of temperature [198] in comparison to the structural relaxation time. Again, as most of the glass formers are binary or multi-component, it has been argued in previous work that the AG relation to be valid, the diffusivity of different components has to follow power law dependence [230]. Though Parmer *et al.* [230] have shown that the power law behaviour between diffusivity of different components holds for a large number of numerical simulations as well as experiments, whether it also holds at higher spatial dimensions or not are yet to be explored. Parmar *et. al.* have shown a single power law relation between diffusivity of different components is necessary for the AG relation to be valid or violated consistently for the individual components. The same argument holds for the structural relaxation time also. In this study, we have investigated the power law relationship between diffusivity and the structural relaxation time of different components in 3 to 8 spatial dimensions. Having checked that, we have examined further the validity of the AG relation across the spatial dimensions.

5.2 Simulation details

We use sphere assemblies interacting with harmonic potential as a model glass former [172]. Details of the model have been discussed in chapter 2. We study glasses in the spatial dimension from $3-8$ at a packing fraction $1.3\phi_J$.(To check density dependence we show results at $1.14\phi_J$ also). We have performed MD simulation in an NVT ensemble of a binary mixture (50:50) of 5000 particles. The integration time step is $dt = 0.01$. Temperature is kept constant using Brown and Clarke [140] algorithm. All the MD trajectories are of length of $100\tau_\alpha$ where τ_α is the relaxation time. Results shown here averaged over 5 independent samples.

5.3 Results

We quantify the microscopic dynamics by computing the overlap function, which is defined (for the B particles) by:

$$q(t) = \frac{1}{N_B}\sum_{i}^{N_B} w(|\mathbf{r}_i(t_0) - \mathbf{r}_i(t+t_0)|) \quad \text{where} \quad w(x) = \begin{cases} 1.0 & \text{if } x \leq a \\ 0 & \text{otherwise.} \end{cases}$$

Here a is the cut-off within which particle positions are treated as indistinguishable [211]. We choose $a = 0.48, 0.50, 0.55, 0.60, 0.75, 0.80$ for 3d, 4d, 5d, 6d, 7d, 8d respectively. The details of this choice are discussed in chapter 2. The relaxation time is estimated as the time at which $q(t) = 1/e$. The dynamics is also examined by measuring another quantity MSD as follows.

$$\text{MSD}(t) = \frac{1}{N}\sum_{i}\langle (r_i(t) - r_i(0))^2 \rangle \tag{5.2}$$

$\lim_{t\to\infty} \text{MSD}(t) = 2dDt$ (d= spatial dimension)
The diffusivity, D is obtained by fitting the MSD at a long time limit. We have computed diffusivity and relaxation time for a wide range of temperatures in each dimension. As our system is a binary mixture, we compute diffusivity and relaxation time for both species. We denote diffusivity and relaxation time for small particle, A as D^A, τ_α^A. Similarly, D^B, τ_α^B represent the diffusivity and relaxation time of the large particle, B.

5.3.1 Power law relationship of diffusivity and relaxation time for different components

In Fig. 5.1 we show MSD for B particle for different dimensions. We can clearly see the system reaches a diffusive state for all the temperature range we considered. The diffusivity, D is obtained by fitting the MSD at a long time limit. We have computed diffusivity for a wide range of temperatures in each dimension. As our system is the binary mixture, we compute diffusivity for both species.

In Fig. 5.2, we show D^B against D^A for $3-8$ spatial dimensions. The vertical line indicates the temperature at which SER breaks down. The temperature is denoted as T_{SEB} for each dimension. We have found that at 3d, the diffusivity of different components shows a fractional power law dependence across the temperature, both below and above the T_{SEB} temperature. However, starting from 4d, at higher spatial dimensions, D^A and D^B does not follow any single power law behaviour; rather, two different power law behaviour exists at two different temperature regime. At the lower

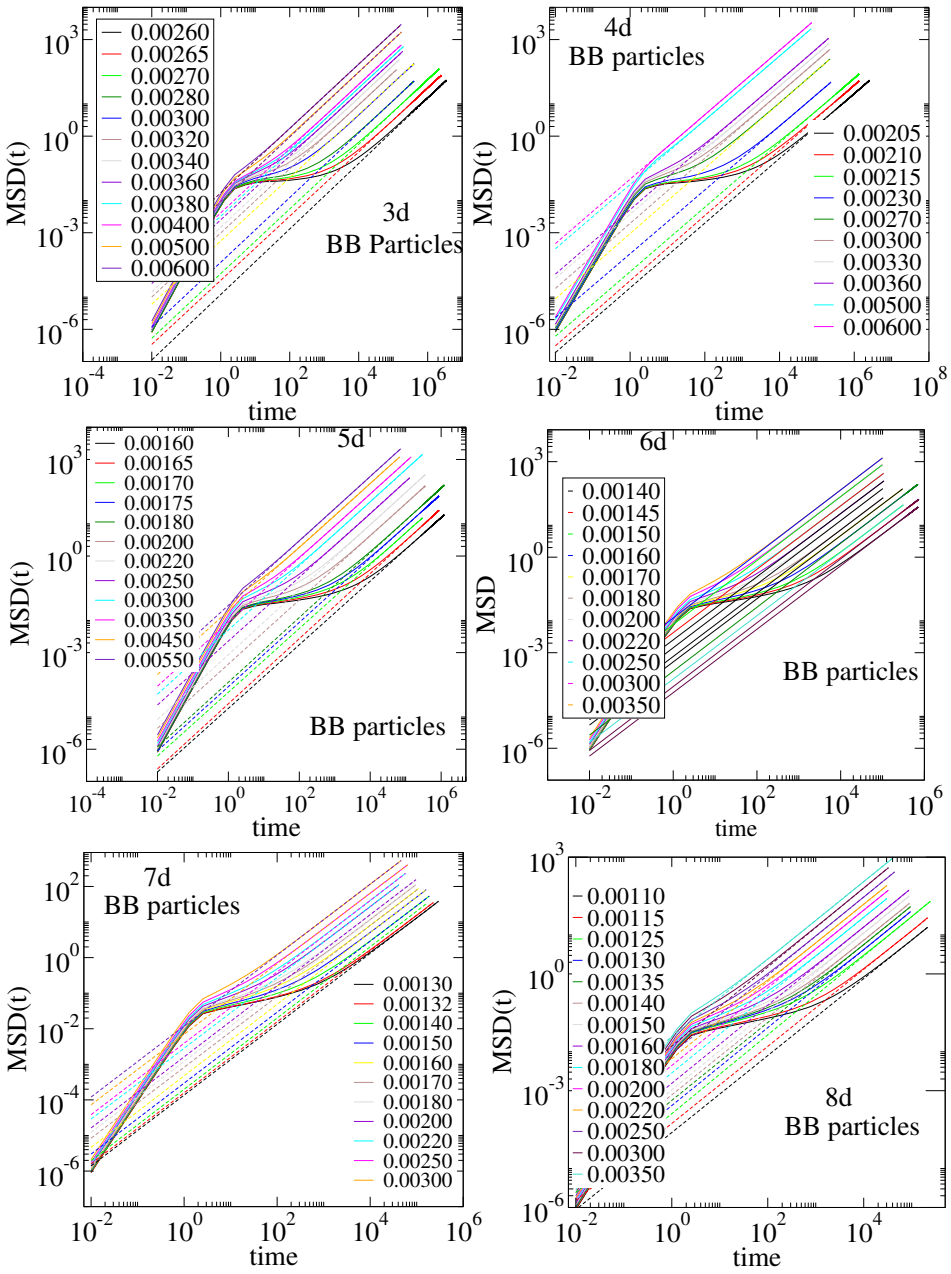

Figure 5.1: MSD computed for considering B particle again is plotted against time for spatial dimension 3 – 8

temperature regime, exponents are larger compared to the exponents of the higher temperature regime.

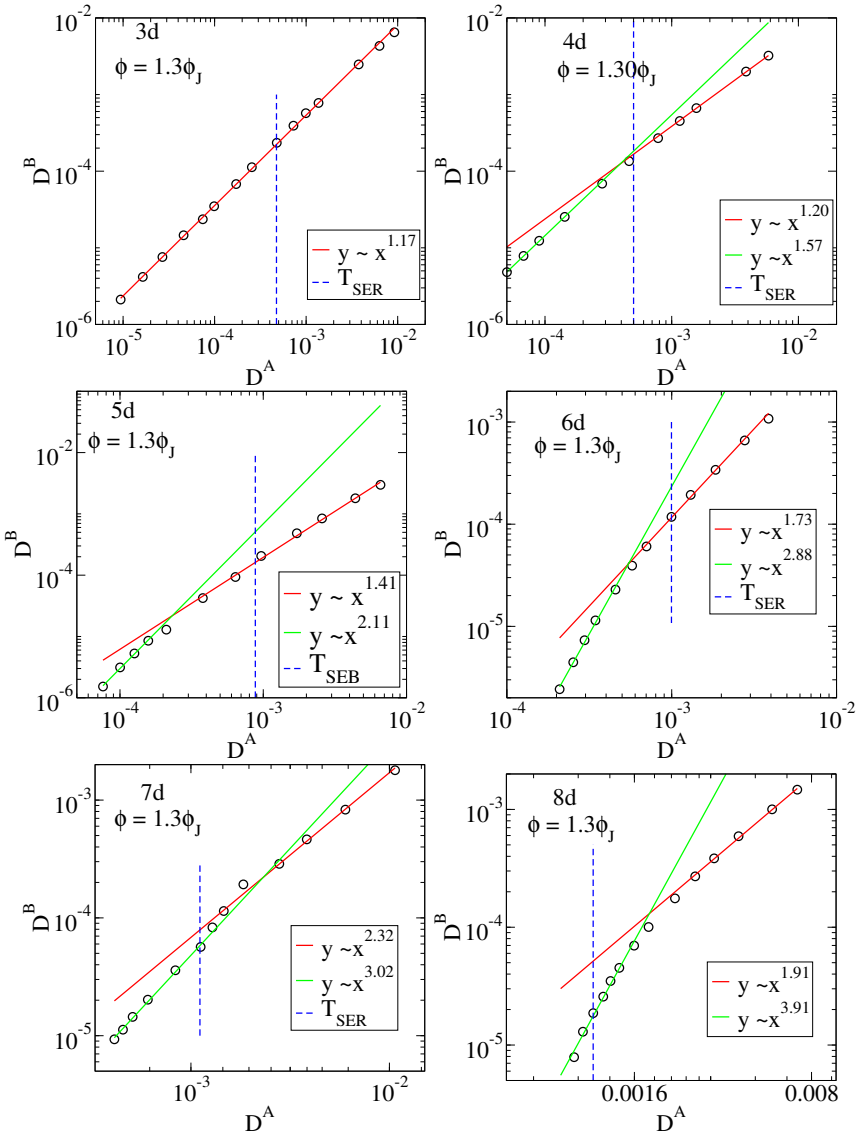

Figure 5.2: D^B is plotted against D^A for $3-8$ spatial dimensions at a fixed density, $1.3\phi_J$. At 3d, it shows a single power law. However, for all other dimensions, we observe two different power law regime between D_B and D_A. The exponents are different in different dimensions. The SER break down temperature is also shown as a blue dotted vertical line in each dimension.

We have already discussed, SER does not hold for glass-forming liquids. As a result, diffusivity and relaxation time is no longer inversely proportional at low temperature. Hence we investigated the power law relationship for relaxation time of different components as well. In Fig. 5.3, we show τ_α^B as a function of τ_α^A for a wide range of temperatures (at a fixed density, $1.3\phi_J$) for $3-8$ spatial dimension. This observation is similar to what we have found for diffusivity. At 3d, τ_α^B and τ_α^A shows a single power law. However, for dimensions higher than three, the relationship between τ_α^A and τ_α^B can not be explained with a single power law For the whole temperature regime. Two different power law regimes are found. The exponents in two different regimes are different. In, Fig. 5.4, we show the exponents for different dimensions. The exponents for power law of τ_α are denoted as α_τ^{highT} and α_τ^{lowT} for high temperature and low temperature respectively. Similarly α_D^{highT} and α_D^{lowT} represent the exponents of diffusivity for high temperatures and low temperature respectively. We found that the exponents α_τ^{highT} and α_D^{highT} both increases with increasing dimensions. However their values at a fixed dimension are very similar. Similar observations are found for α_τ^{lowT} and α_D^{lowT}. In each dimension, α_τ^{lowT} or α_D^{lowT} is always higher than the α_τ^{highT} or α_D^{highT}. Next, we attempted to understand the effect of density in the existence of different power law relations at different temperature regimes among the diffusivity or the relaxation time of the different components. Hence we have investigated the power law behaviour of diffusivity and relaxation time of different components at a comparatively lower density, $1.14\phi_J$. In Fig. 5.5 we show D^B against D^A and in Fig.5.6, we show τ_α^B as a function of τ_α^A for a wide range of temperatures at $1.14\phi_J$. At this density, we have similar observation as in higher density. At 3d, we observe single power law for both diffusivity and relaxation time and at $4-8$ dimensions, it shows existence of two different power law. In Fig. 5.7, we summarize the different exponents at density $1.14\phi_J$.

At this stage, we are not able to give any explanations for why there exists a single power law for diffusivity/relaxation time of different components at dimensions three, and it violates with dimensions larger than three. However, we focus on the consequences of this violation and investigate the AG relation for different dimensions.

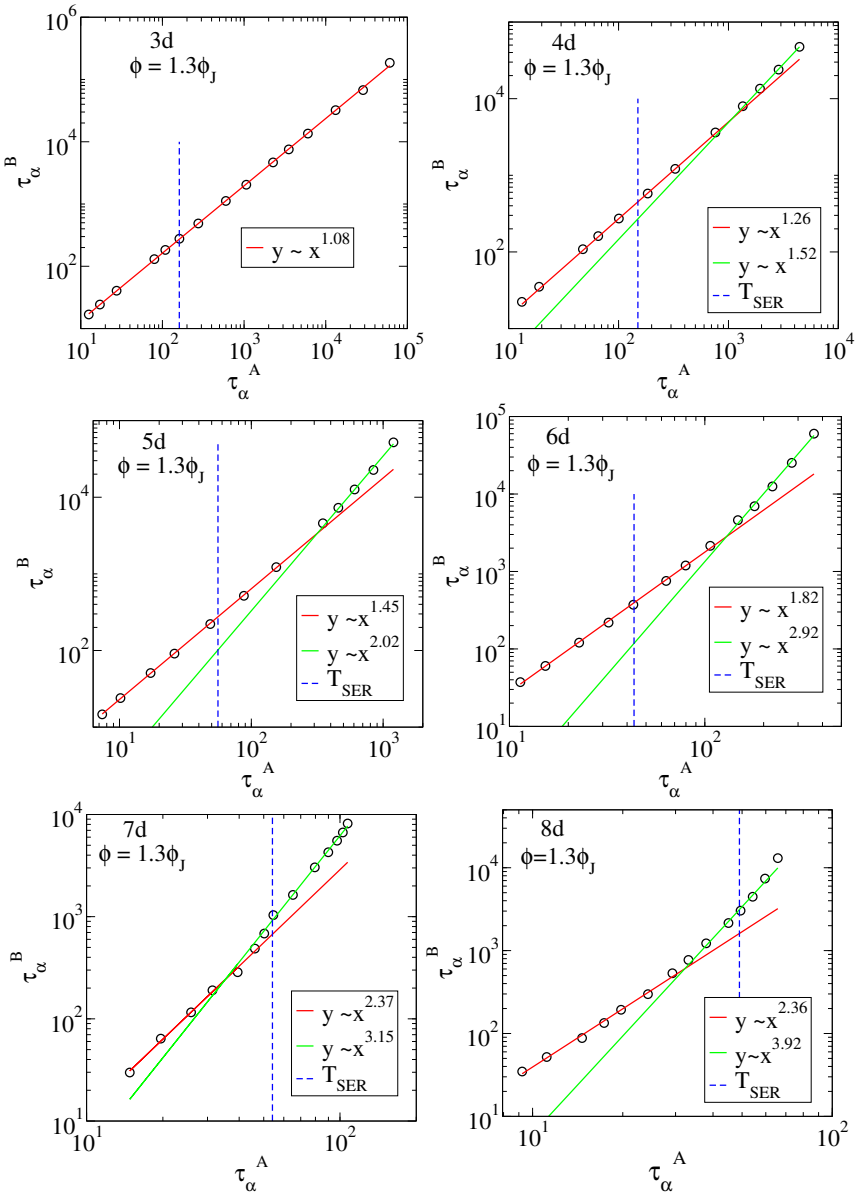

Figure 5.3: τ_α^B is plotted against τ_α^A for 3−8 spatial dimensions at a fixed density, $1.3\phi_J$. At 3d, it shows a single power law. However, for all other dimensions, we observe two different power law regime between τ_α^B and τ_α^A. The exponents are different in different dimensions. The SER break down temperature is shown as a blue dotted vertical line in each dimension.

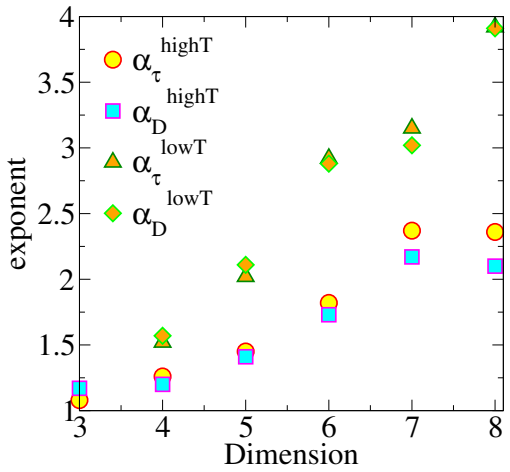

Figure 5.4: The exponents of power law at high temperatures are termed as α_τ^{highT} and α_D^{highT} for τ_α and diffusivity respectively. Similarly The exponents of power law at low temperatures are termed as α_{tau}^{lowT} and α_D^{lowT} for τ_α and diffusivity respectively. All the exponents at different dimensions are plotted here. We see exponents of both kinds are increasing as we increase the dimension. Exponents at low temperatures are always higher compared to the exponents at high temperatures in each dimension.

5.3.2 AG relation in different dimensions

The previous result suggests that the diffusivity of different components shows a single power law for the system where AG relation holds. In this study, we find that the diffusivity of different components does not follow a single power law for the whole range of temperature under investigation for four and the dimensions above. Does this mean that at higher spatial dimension, AG relation does not hold? To answer this question, we have investigated the AG relation for $3-8$ spatial dimensions.

We have computed the configurational entropy, S_c for different temperatures for $3-8$ spatial dimensions. S_c is estimated as the difference between the total entropy and the vibrational entropy, $S_c = S_{tot} - S_{vib}$. We have discussed in detail the procedure to compute the total entropy, S_{tot} in chapter 2. Total entropy is calculated using thermodynamic integration [81] by constructing a reversible path from a reference state, the ideal gas state, to the target state. The vibrational entropy is calculated using the harmonic approximation of a basin [81, 144, 145] discussed in detail in chapter 2. We note here harmonic approximation to compute basin entropy is extensively used for 3d glass formers. As a first step, we have followed the same procedure to compute vibrational entropy at higher dimensions. However, we did not validate how well this approximation can be extended for the higher dimensions. In Fig. 5.8 -5.13, we have shown the S_{tot}, S_{vib} and S_c as a function of temperature for the spatial dimensions, $3-8$d. We have observed that S_{tot}, S_{vib} and S_c decreases with decreasing temperature. Extrapolation of the simulated data points shows that S_c goes to zero at a finite

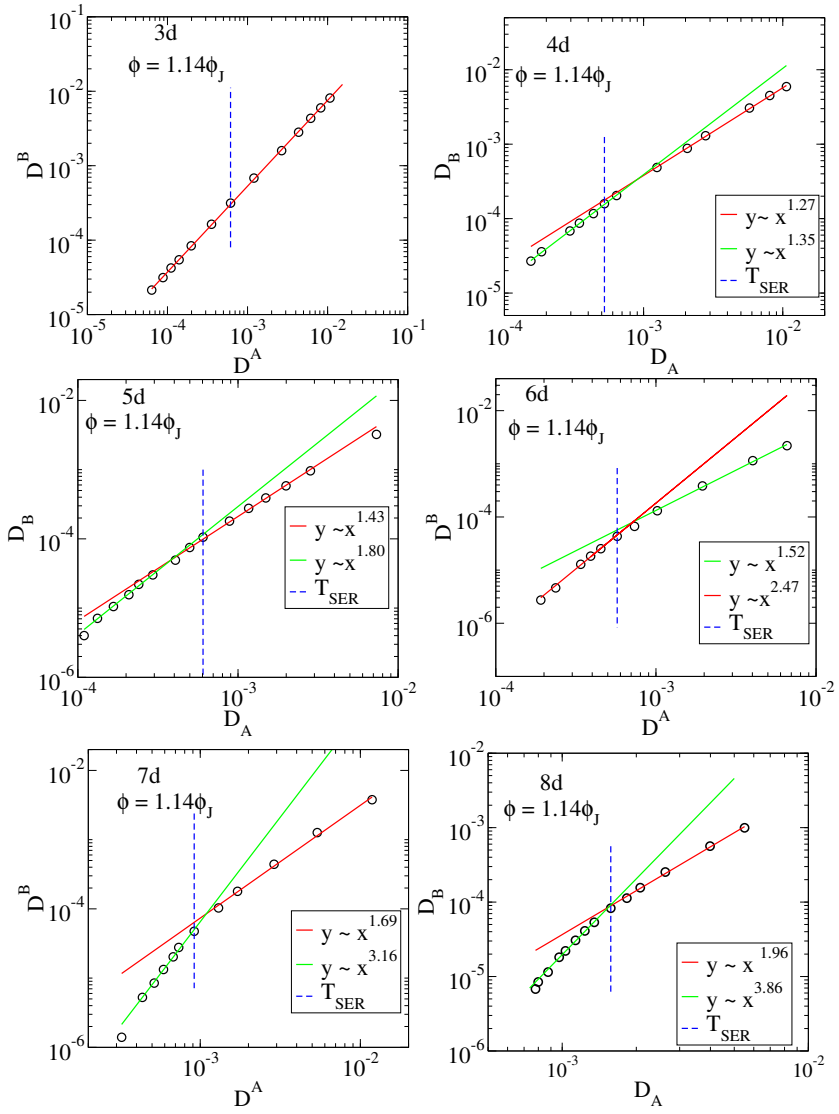

Figure 5.5: D^B is plotted against D^A_α for $3-8$ spatial dimensions at fixed density, $1.14\phi_J$. At 3d. It shows a single power law. However, for all other dimensions, we observe two different power law regime between D_B and D_A. The exponents are different in different dimensions. The SER break down temperature is also shown as a blue dotted vertical line in each dimension.

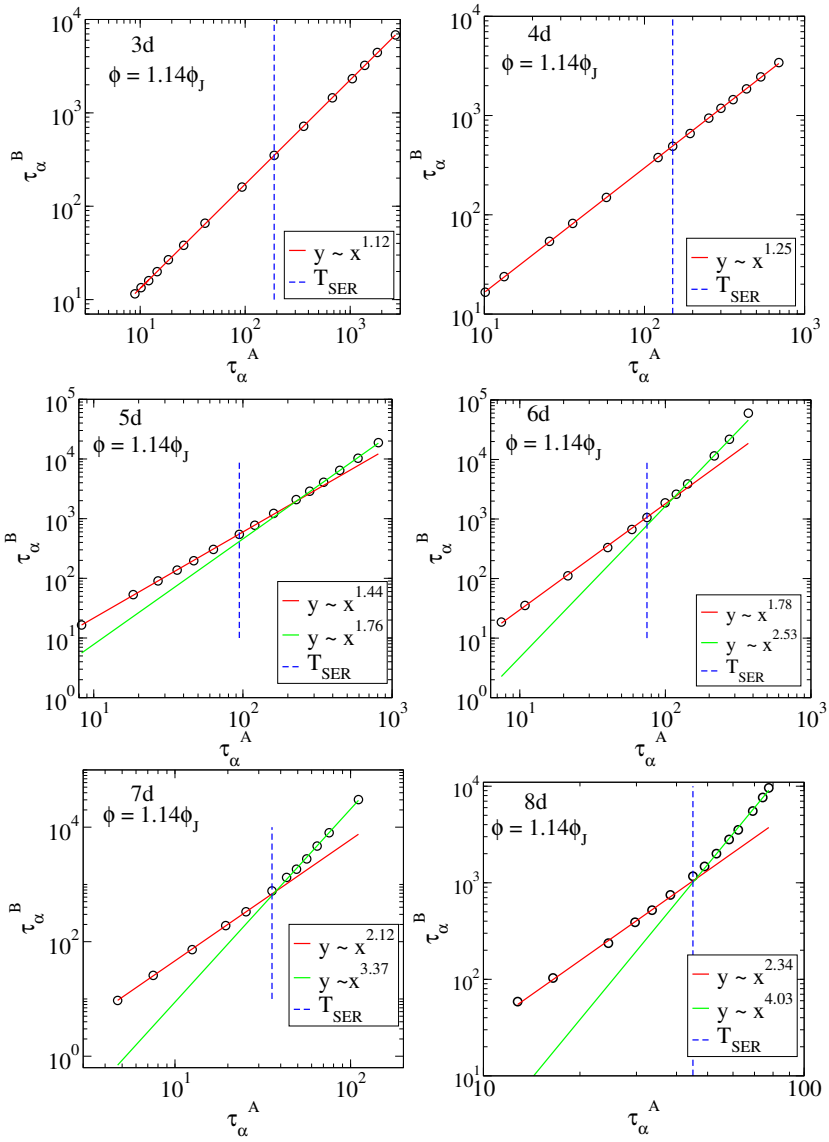

Figure 5.6: τ_α^B is plotted against τ_α^A for $3-8$ spatial dimensions at a fixed density, $1.14\phi_J$. At 3d, it shows a single power law. However, for all other dimensions, we observe two different power law regime between τ_α^B and τ_α^A. The exponents are different in different dimensions. The SER break down temperature is shown as a blue dotted vertical line in each dimension.

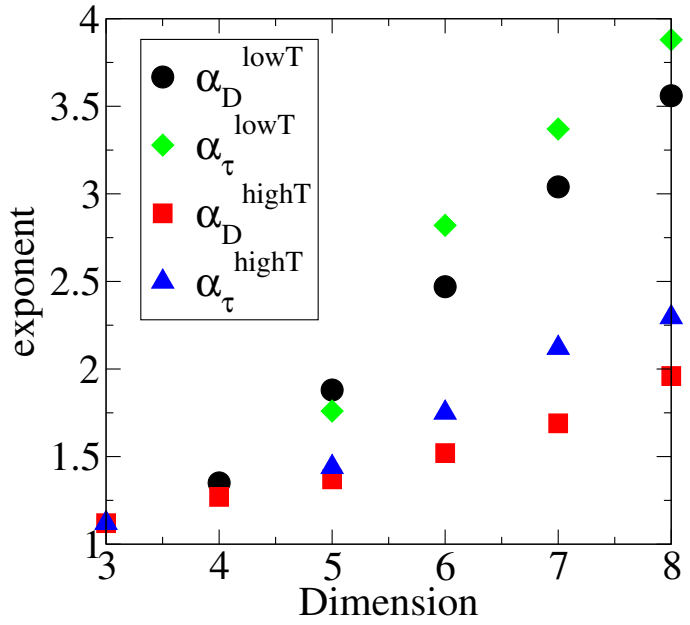

Figure 5.7: All the exponents at different dimensions are plotted here (at density $1.14\phi_J$). We see both kinds of exponents are increasing as we increase the dimension. Exponents at low temperatures are always higher compared to the exponents at high temperatures in each dimension.

temperature. This suggests a finite temperature divergence of relaxation time.

In Fig. 5.14-5.19, we have shown the AG relation for spatial dimensions $3-8$. We show $(D^B)^{-1}$ and τ_α^B against the inverse of the TS_c in the semi-log scale. In 3d, we have seen that AG relation hold for both diffusivity and relaxation time. As a result of which we see a straight line when $(D_B)^{-1}$ or τ_α^B is plotted against $1/TS_c$. This result is consistent with the previous studies. However, our initial results suggest that at dimension 4 or larger, the AG relation is not valid either for relaxation time or for diffusivity. Thus, our observations are consistent with the previous result of Parmer *et al.* [230] which shows AG relation to be valid; there should be a power law between diffusivity of different components. We also observed that when there exists a power law between the diffusivity of different components (which is the case at 3d), the AG relation also holds for the whole temperature range; otherwise, the AG relation does not hold (which is the case for dimensions larger than 3). However, based on this initial result, we can not make any decisive comments on whether this will always be the case or there will be a different explanation to understand these results.

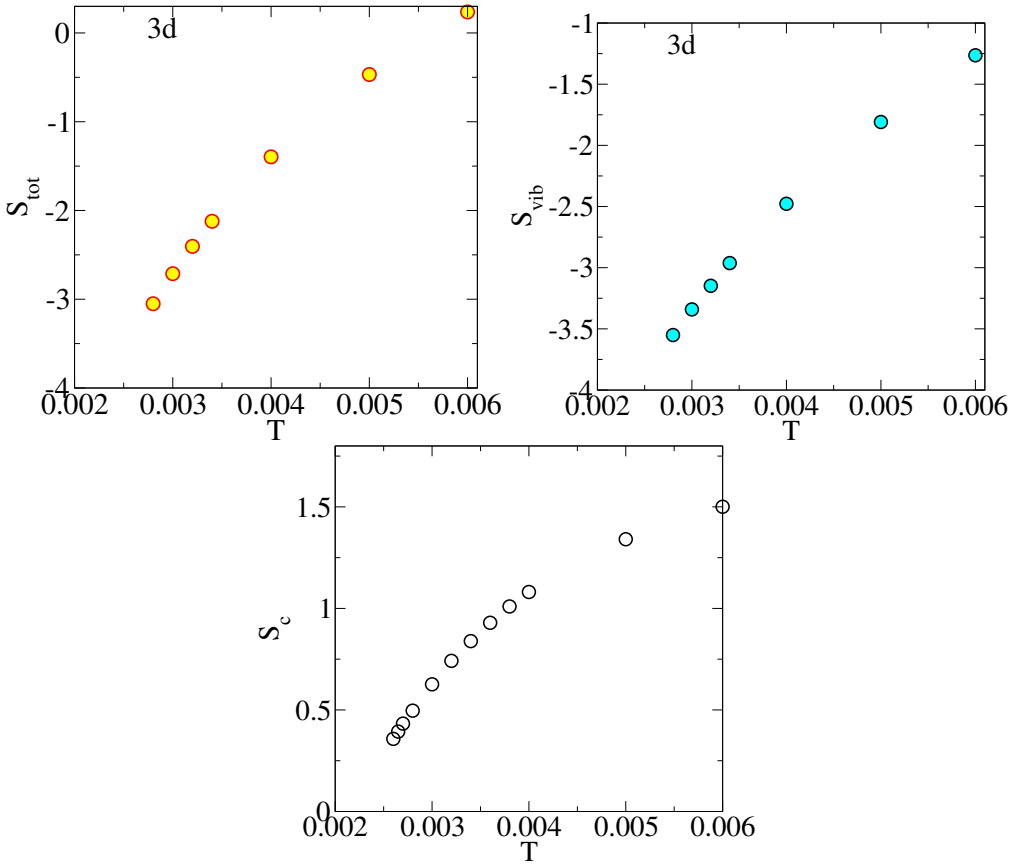

Figure 5.8: The total entropy, S_{tot} (Top Left), vibrational entropy S_{vib} (Top Right), configurational entropy, S_c (Bottom) is plotted as a function of temperature in three dimension..

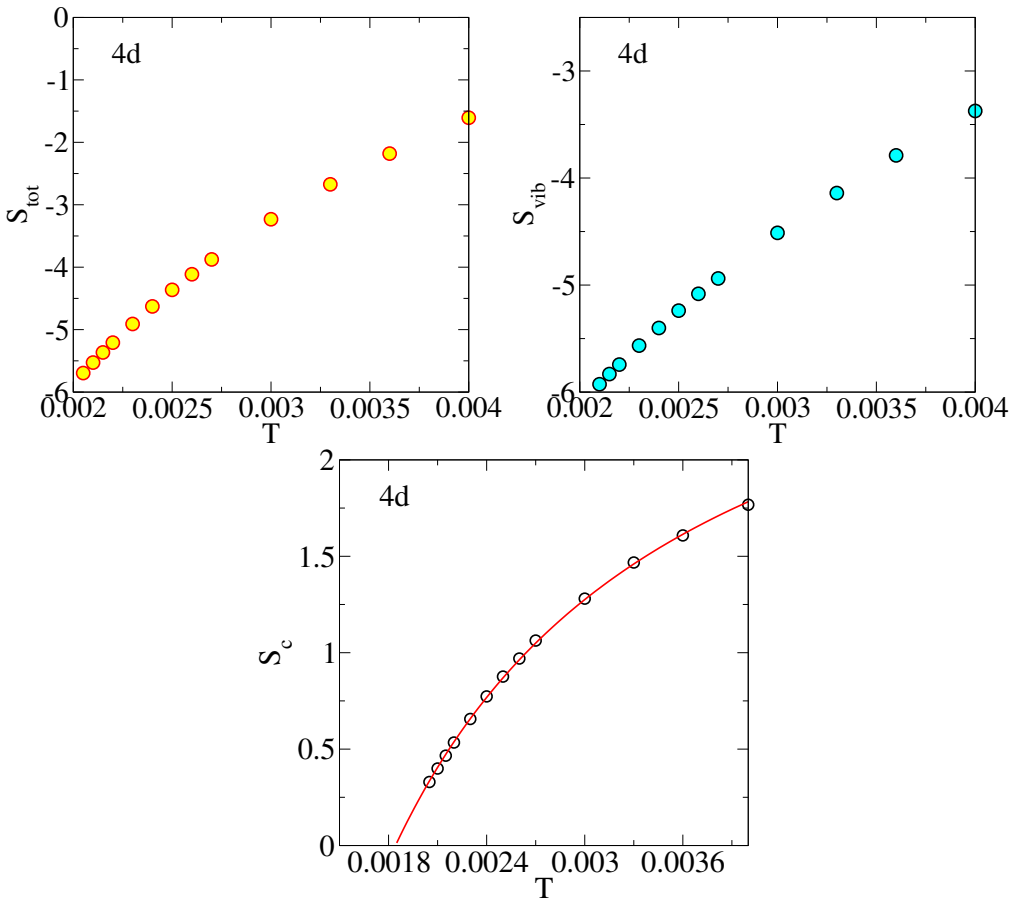

Figure 5.9: The total entropy, S_{tot} (Top Left), vibrational entropy S_{vib} (Top Right), configurational entropy, S_c (Bottom) is plotted as a function of temperature in four dimension.

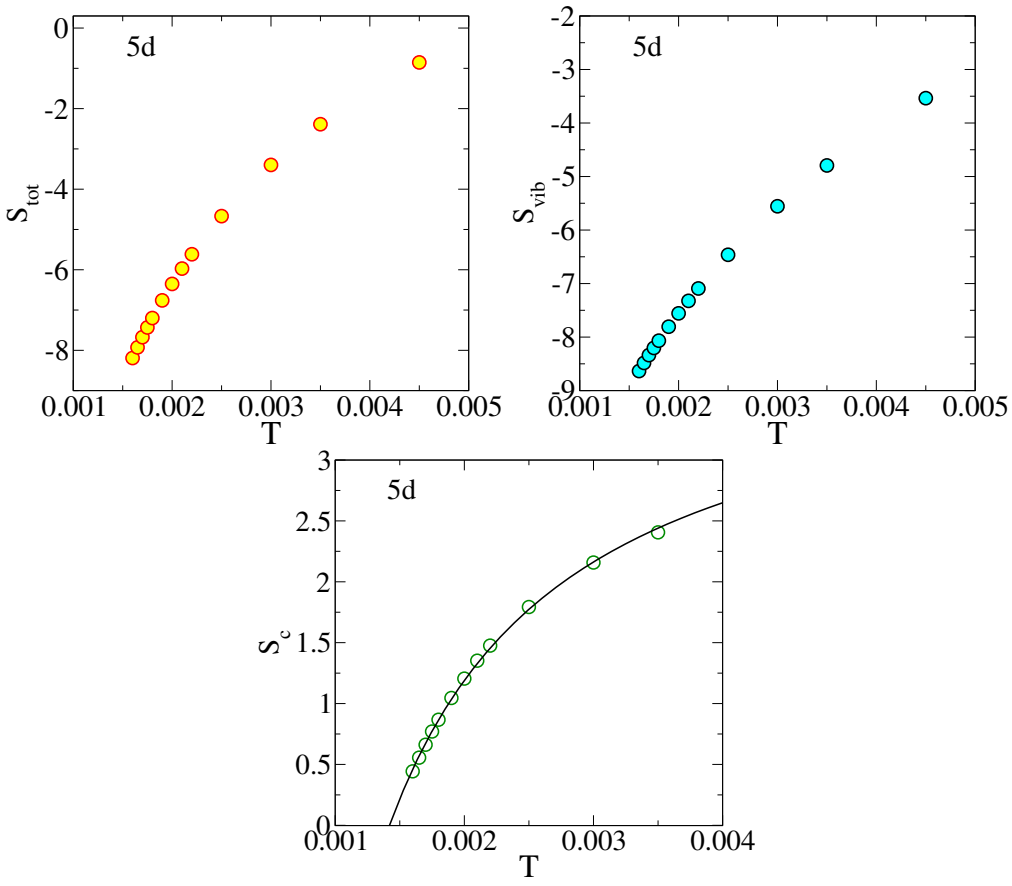

Figure 5.10: The total entropy, S_{tot} (Top Left), vibrational entropy S_{vib} (Top Right), configurational entropy, S_c (Bottom) is plotted as a function of temperature in five dimension.

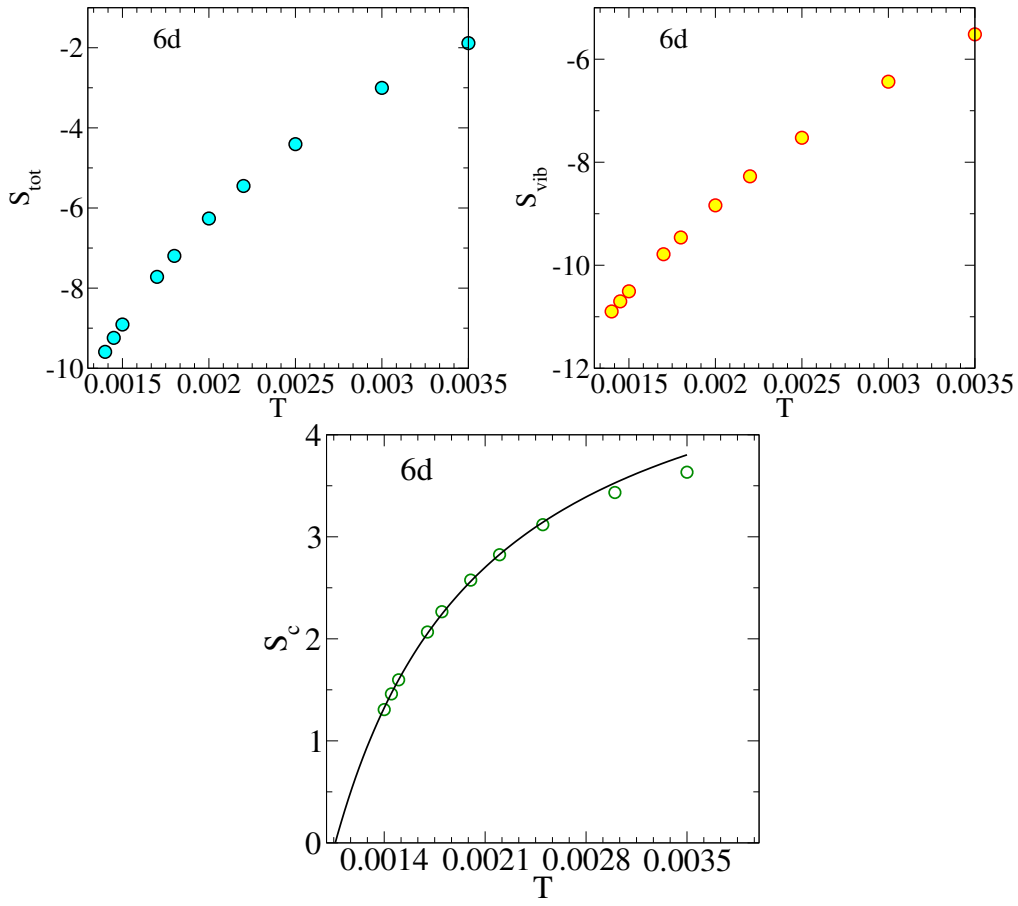

Figure 5.11: The total entropy, S_{tot} (Top Left), vibrational entropy S_{vib} (Top Right), configurational entropy, S_c (Bottom) is plotted as a function of temperature in six dimension.

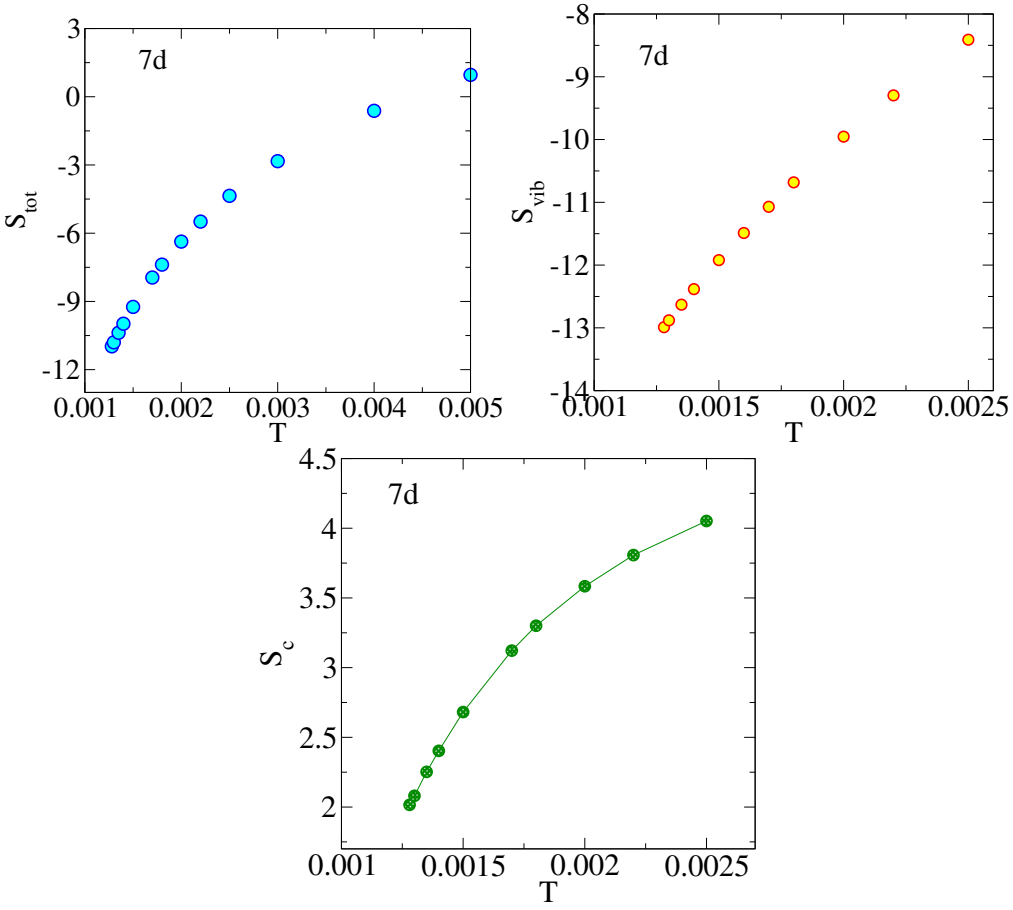

Figure 5.12: The total entropy, S_{tot} (Top Left), vibrational entropy S_{vib} (Top Right), configurational entropy, S_c (Bottom) is plotted as a function of temperature in seven dimension.

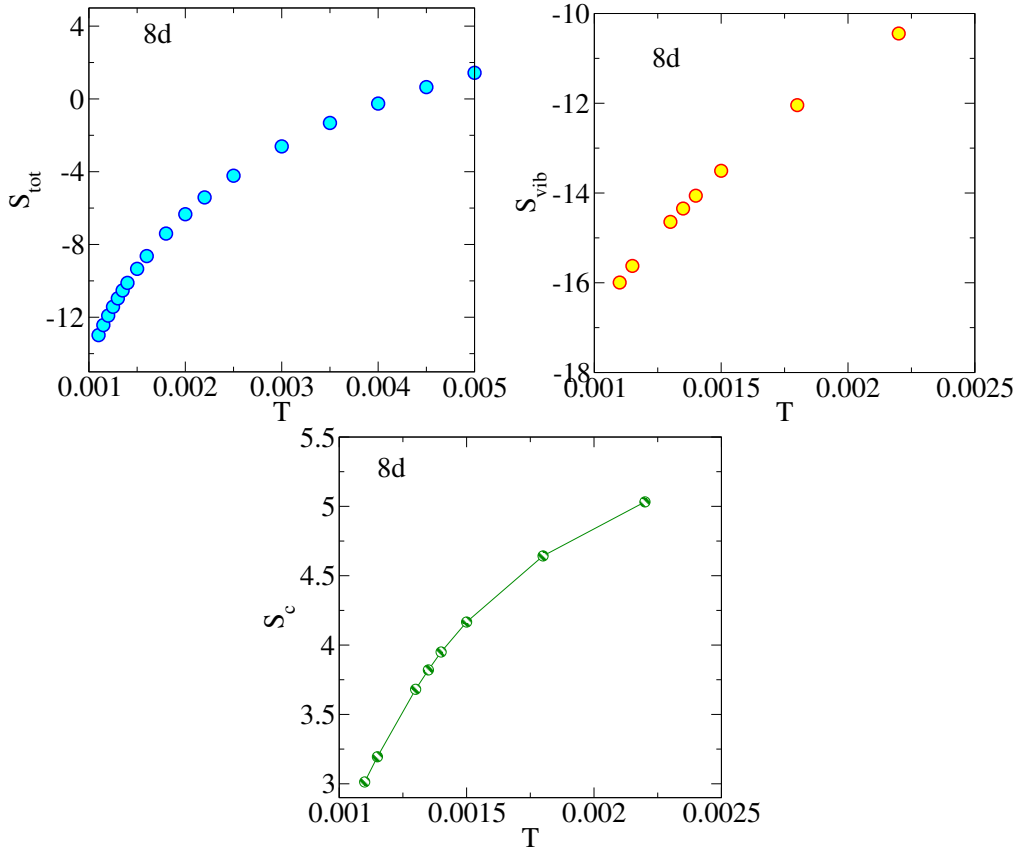

Figure 5.13: The total entropy, S_{tot} (Top Left), vibrational entropy S_{vib} (Top Right), configurational entropy, S_c (Bottom) is plotted as a function of temperature in eight dimension.

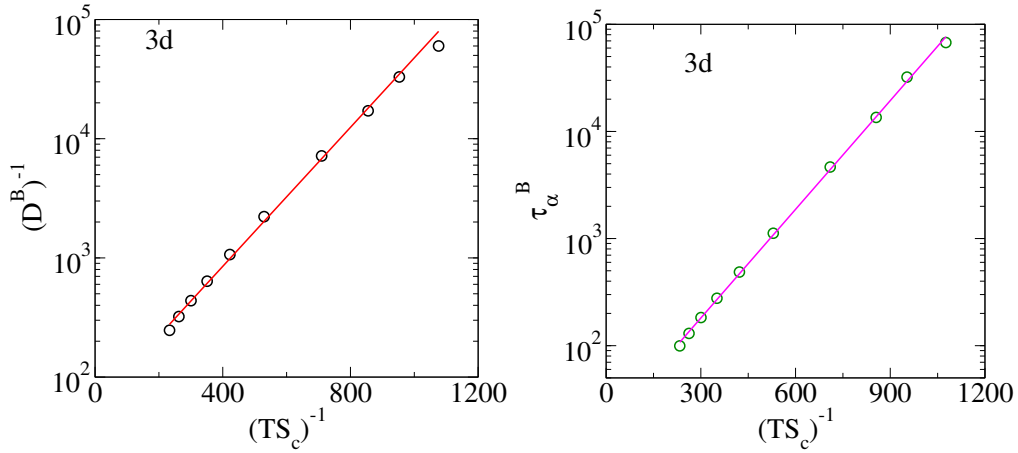

Figure 5.14: Left: $(D^B)^{-1}$ is plotted as function of inverse of TS_c in a semi-log plot. Right: τ_α^B is plotted as function of inverse of TS_c in a semi-log plot. AG relation is valid at 3d both for diffusivity as well as for relaxation times.

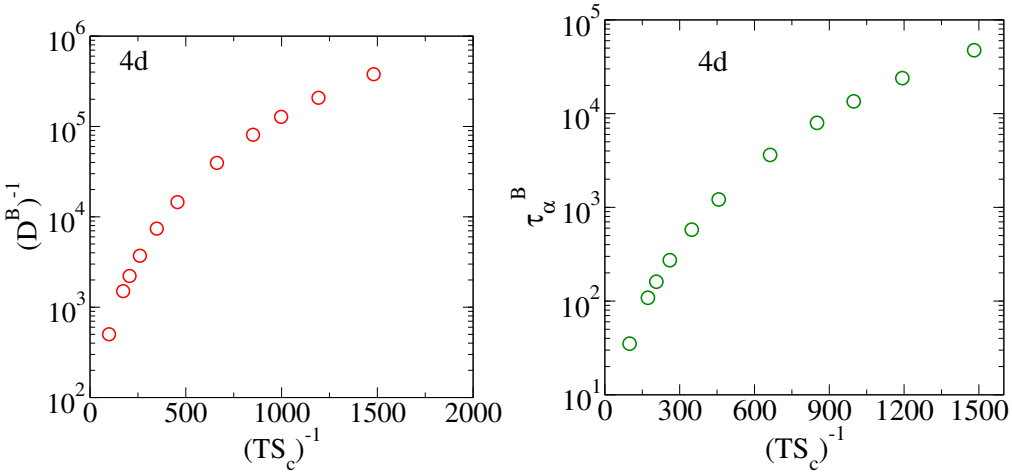

Figure 5.15: Left: $(D^B)^{-1}$ is plotted as function of inverse of TS_c in a semi-log plot. Right: τ_α^B is plotted as function of inverse of TS_c in a semi-log plot. We see that AG relation is not valid at 4d for this system.

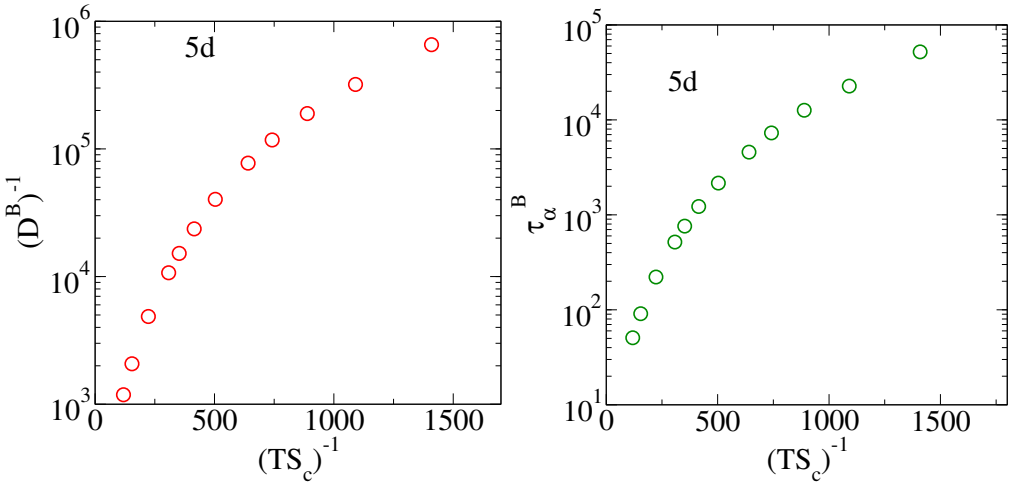

Figure 5.16: Left: $(D^B)^{-1}$ is plotted as function of inverse of TS_c in a semi-log plot. Right: τ_α^B is plotted as function of inverse of TS_c in a semi-log plot. We see that AG relation is not valid at 5d for this system.

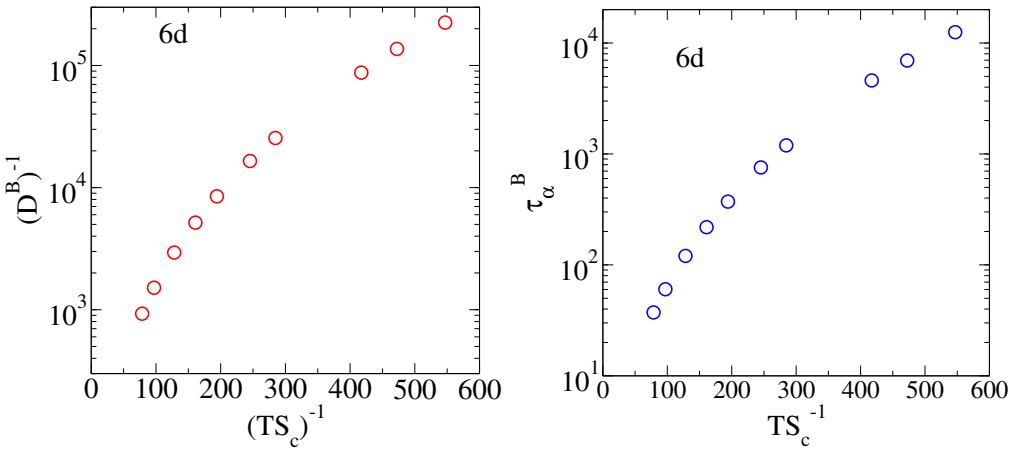

Figure 5.17: Left: $(D^B)^{-1}$ is plotted as function of inverse of TS_c in a semi-log plot. Right: τ_α^B is plotted as function of inverse of TS_c in a semi-log plot. We see that AG relation is not valid at 6d for this system.

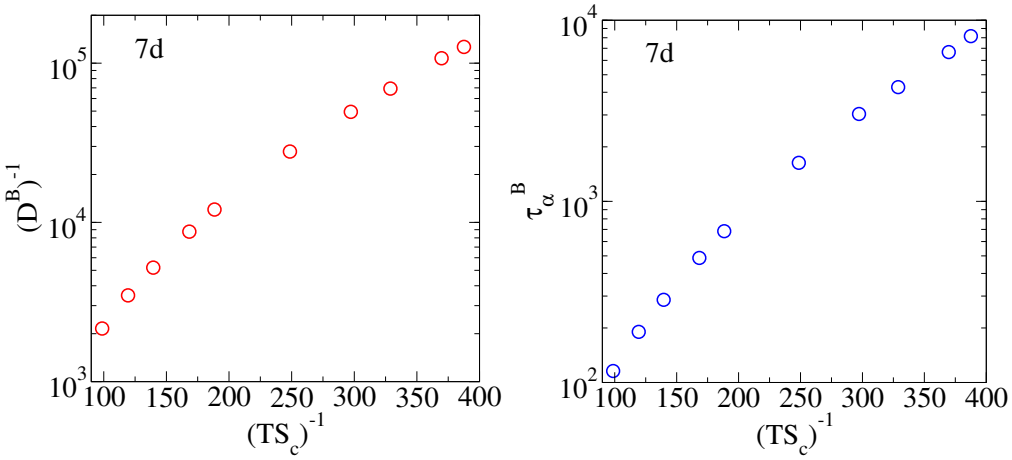

Figure 5.18: Left: $(D^B)^{-1}$ is plotted as function of inverse of TS_c in a semi-log plot. Right: τ_α^B is plotted as function of inverse of TS_c in a semi-log plot. We see that AG relation is not valid at 7d for this system.

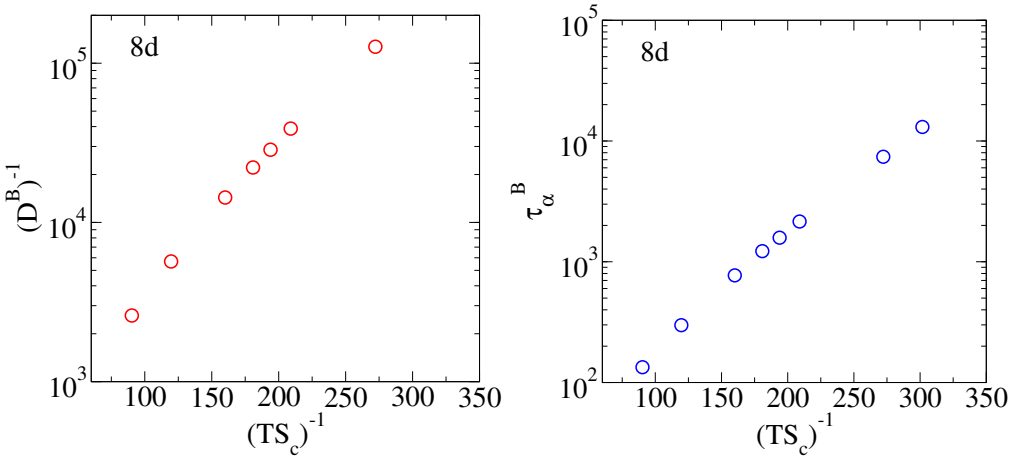

Figure 5.19: Left: $(D^B)^{-1}$ is plotted as function of inverse of TS_c in a semi-log plot. Right: τ_α^B is plotted as function of inverse of TS_c in a semi-log plot. We see that AG relation is not valid at 8d for this system.

5.4 Discussion

In this study, we have investigated the relation of diffusivity or relaxation time between different components. We have observed that at $3d$ it shows a single power law relation. However, at 4d or higher spatial dimensions, two different power law regimes are observed with different exponents for different temperature regions. The exponents at a higher temperature regime are always smaller than the exponents at a lower temperature regime for all the dimensions. Both the exponents (high temperature and low-temperature regime) increases with increasing dimensions. Similar observations are found at a lower density, suggesting the density does not play any role in the emergence of the different power law regimes. We have also investigated the Adam-Gibbs relation for spatial dimension $3-8$. We found AG relation holds for both diffusivity and relaxation time at 3 dimension for the whole temperature range we have studied. However, our initial results suggest that at 4d or above, AG relation does not hold for either diffusivity or relaxation time. Though this observation confirms the previous result of Parmar *et. al.* [230] that diffusivity of different components should be related by a single power-law for the AG relation to be valid, there are other checks that must be done before reaching any definite conclusion.
We have computed vibrational entropy using harmonic approximation, which needs to be justified to reach any definite conclusions regarding the validity of AG relation. As the recent results by Das *et. al.* [231] show AG relation at very low temperature does not hold when vibrational entropy is calculated considering only the harmonic part. However, after adding the anharmonic contribution, they can show AG relation is valid for the entire range of temperature. In the future, we would like to compute vibrational entropy employing different methods and check whether this initial observation of AG relation not being valid at dimensions larger than three is correct or not.

Chapter 6

Memory formation in cyclically deformed amorphous solids and sphere assemblies

[1]

6.1 Introduction

Retention of memory of past history arises ubiquitously in describing the properties of condensed matter, ranging from near equilibrium conditions to far from equilibrium conditions, including in the presence of external driving. Simple examples may merely involve a dependence on history that breaks a symmetry or leads a system to reside in a metastable state. Indeed such history dependence forms the basis of conventional memory devices, such as magnetic or phase change memory devices. Other popular memory devices, such as shape memory materials, rely on the presence of phase transformations, but also on the ability of a material to reside in one among a large number of possible structures, in order to accommodate externally applied deformation. The presence of multiple distinct internal structures or states in which a material can exist for long times is a generic condition for the presence of memory effects, seen particularly in systems that exhibit some form of disorder. The range of examples is vast, and includes structural glasses and spin glasses , magnetic systems with disorder that exhibit return point memory, and charge density waves systems that exhibit return point memory and pulse duration memory, crumpled thin sheets and elastic foams , systems exhibiting echoes, sheared colloidal suspensions, glasses and related model systems, and shaken granular systems, to name a few examples.

[1] chapter is based on publication in Eur. Phys. J. E (2018) 41: 105

This list of largely condensed matter examples does not include the large array of biological contexts in which memory formation is important and interesting, such as neuronal, genetic, epigenetic, immunological *etc.* memories, but some approaches to modeling such memories have been developed with input from theories of disordered spin models, and in turn, such approaches inform some recent work on self assembly and design of functional materials.

In this chapter, we address memory effects in two broadly related systems, namely athermally sheared glasses and non-Brownian colloidal suspensions. Non-Brownian suspensions, when subjected to large amplitude oscillatory shear show a transition from an *absorbing state* at low amplitudes of shear (wherein, particles cease to move when observed stroboscopically, *i. e.* at the end of each cycle, after a transient) to a diffusing state at large amplitudes. The threshold or critical amplitude γ_c displays features akin to a continuous phase transition, with diverging time scales to reach steady states, and a continuous rise of the fraction of active particles (defined as particles that move during a cycle, which serves as an order parameter). These features are realised through a simple model in which pairs of particles that overlap when subjected to shear deformation are given random displacements or *kicks* after they are returned to their undeformed positions, and the process is repeated for each cycle. Memory effects were studied in this model by Keim *et al.* After a number of cycles of shear deformation with a fixed amplitude $\gamma_1 < \gamma_c$, the system reaches an absorbing state. When this *training* process of repeatedly shearing by γ_1 is complete (*i. e.* when particles cease to move), a shear cycle with any $\gamma < \gamma_1$ results in no rearrangements of particles since a larger amplitude shear includes smaller amplitudes within its cycle. On the other hand, a deformation by an amplitude bigger than γ_1 will result in particle rearrangements. As a result, this procedure encodes a memory, which can be read by performing shear deformation cycles with increasing amplitude and measuring the fraction of particles which are displaced as a function of amplitude. The fraction of particles that move is zero below the training amplitude, and becomes finite for amplitudes beyond γ_1. When the training phase involves cycles of more than one amplitude, the system can encode multiple memories transiently, but when the number of cycles increases and the system reaches a steady state, memory of all but the highest amplitude are lost. Interestingly, addition of noise during the training cycles induces the memories of multiple training amplitudes to be retained. Subjecting the system to deformation by an amplitude larger than the largest training erases the memories, but gradually. These features of memory have also been realised experimentally in sheared non-Brownian suspensions.

Cyclically sheared amorphous solids (glasses) under athermal conditions reveal a transition, associated with yielding behaviour, that bears resemblance to the absorbing to diffusive transition in athermal suspensions. At amplitudes of shearing below

a threshold value, the model amorphous solids studied computationally reach stroboscopically invariant states, whereas they reach diffusive states above the threshold. The threshold strain amplitude is characterised by diverging times to reach the steady state. Despite such similarity with athermal suspensions, there are significant differences, since a sheared amorphous solid never reaches a state where the particles do not interact with each other. It is thus interesting to consider the nature of memory effects in amorphous solids, which was addressed in before. It was found that cyclically deformed amorphous solids also show memory similar to athermal suspensions, but with key differences. In deformed glasses, a read cycle leaves the system unperturbed only at the training amplitude in the case of single memory, and the lowest amplitude of shear in the case of multiple memories. The origin of this behaviour was analysed in the case of single memories. It was shown that in the steady state reached after training, the system reaches the same configuration at the end of each cycle, but it does so at the end of a sequence of transitions between local energy minima, or *inherent structures*. A read cycle of any amplitude other than the training amplitude will disrupt this cycle of transitions, and will lead to a measurable signature. In the work described, the mean squared displacement with respect to the trained configuration was used as the measurement.

6.2 Our goal

The work of Fiocco *et. al.* raises a number of obvious questions which we address in this chapter. Fiocco *et. al.* studied memory effects in the absorbing state at a single training amplitude (or a single pair of amplitudes). We study memory effects in absorbing state with many different amplitudes and address how the memory effects (*e. g.* their strength) depend upon the amplitude of deformation below γ_c, and we study whether memory effects are possible above γ_c. Fiocco *et. al.* used the simplest possible way to read off the memory – since the investigation was *in silico*, copies of the trained system were made, and each copy was independently subjected to a different, single, read cycle with a different strain amplitude. We refer to this protocol as a *parallel read*. Such a procedure is, of course, not available for experimental investigation, wherein the read cycles must be applied sequentially. We thus address whether the memory effects seen earlier are reproduced also with a *sequential read* protocol. We consider different measurements, namely, measuring mean squared displacements with respect to the final configuration from the previous read cycle instead of the trained configuration, and also the computation of the fraction of active particles. We consider whether the previous results concerning multiple memories can be extended beyond two memories, and investigate further whether such memories are persistent or transient. We also consider the conditions under which memories are erased. Finally, we consider

structural signatures of training by considering x, z dependent pair correlations, following previous work on athermal suspensions.

As mentioned before, the differences in the memory signatures in athermal suspensions and glasses has been rationalised by the presence in the latter case of a non-trivial energy landscape, and transitions of the trained system between energy minima during a cycle of shear, even after reaching a stroboscopically invariant state. In the case of athermal suspensions and models thereof, in the steady state after full training, the system undergoes cyclic shear without any of the particles colliding (or interacting) with the other particles, whereas in a glass, particles always have finite interactions among them, leading to a non-trivial energy landscape that is traversed by the system. In probing this distinction further, we consider a different model of sheared athermal assemblies of particles, namely, soft sphere assemblies at densities below the jamming density, that are subjected to cyclic deformation under athermal conditions. In such systems, in addition to the absorbing state wherein spheres do not interact with each other any longer and the diffusive or active regime wherein they do, a third, intermediate state has been identified, where the sphere coordinates are stroboscopically invariant, but spheres undergo collisions during the strain cycling. This state has been termed *loop reversible*. We investigate how the memory effects may be different in the loop reversible state as compared to the absorbing state (also referred to as point reversible) and the diffusive states. We show that in the loop reversible state, memory effects very similar to those in glasses are observed, thereby indicating that the distinction between the earlier studied cases of suspensions and glasses lies in the presence or absence of non-trivial displacements during cyclic deformation, rather than the presence or absence of a non-trivial landscape.

6.3 Models and definitions

We simulate KA-BMLJ samples consisting of $N = 4000$ particles in three dimensions. The system, at fixed number density (N/V, V being the volume) $\rho = 1.2$ is equilibrated at reduced temperature $T = 0.466$ *via* a constant temperature molecular dynamics simulation. All the simulations reported here are performed in LAMMPS. We simulate $50:50$ soft sphere mixtures consisting of 2000 particles, at packing fraction $\phi = 0.61$ (where ϕ for the binary mixture considered is related to the number density, ρ by $\phi = \frac{\pi}{6}(x_A\sigma_{AA}^3 + x_B\sigma_{BB}^3)\rho$ where x_A, x_B are the fractions of A,B type of particles, each equal to 0.5 in this case) in three dimensions. The initial configurations are obtained from Monte Carlo simulations of hard sphere mixtures of the same size ratio, equilibrated at packing fraction $\phi = 0.363$. The higher density configurations are obtained starting from these initial configurations by performing a fast initial compression of the hard sphere system using a Monte Carlo simulation till the desired density is reached.

Training Protocols: Configurations taken from the equilibrated liquid are subjected to energy minimization using the conjugate-gradient algorithm to obtain sets of local energy minimum structures which are termed as *inherent structures*. The inherent structures are then subjected to cyclic shear deformation using the Athermal Quasi-Static (AQS) procedure as described in chapter 2. Shear strain γ is incremented by small strain steps ($d\gamma = 2 \times 10^{-4}$ for the BMLJ system and $d\gamma = 10^{-3}$ for soft sphere system). Samples are subjected to oscillatory shear deformation following the sequence: $0 \rightarrow \gamma_1 \rightarrow 0 \rightarrow -\gamma_1 \rightarrow 0$ where γ_1 is the amplitude of deformation. This sequence is referred as a single "cycle". We apply this sequence repeatedly till they reach a steady state. This procedure is referred to as *training* the samples. The BMLJ system is trained at different amplitudes, $\gamma_{train} = 0.02, 0.03, 0.04, 0.05, 0.06, 0.07$ (which are below γ_c, the yielding strain γ_c) and $\gamma_{trained} = 0.09, 0.11$ (which are above γ_c). When a single training amplitude is applied, the results shown are averaged over 30 independent samples. When multiple training strain amplitudes are applied, the data shown are averaged over 50 independent samples. The soft sphere system is trained at two different amplitudes $\gamma_1 = 0.03$, 0.12 (below yielding) and 0.1 and 0.12 above yielding. For both single memory and multiple memory cases, the data shown here are averaged over 10 independent samples.

Reading Protocols: After training, in the read procedure we refer to as “Parallel read", identical copies of the samples are subjected to a single cycle of shear ($0 \rightarrow \gamma_{read} \rightarrow 0 \rightarrow -\gamma_{read} \rightarrow 0$, where γ_{read} is the amplitude of deformation of reading) deformation each, with such amplitudes covering the range of strain amplitudes from 0 to 0.13. We also consider a second read protocol which we refer to as “Sequential read". In this case, after training, we apply single cycles of shear for an increasing sequence of amplitudes, using the final configuration after a cycle at one amplitude as the starting configuration for the cycle at the next (higher) amplitude. As the measurement that is used to reveal the presence or absence of memory of the training, we use the mean squared displacement (MSD) of particles in configurations at the end of a full cycle of deformation, with respect to the reference configuration. We compute the MSD either with respect to the final configuration of the training phase (or the initial configuration for the read protocol), which we denote by MSD_0, or compute the MSD with respect to the final configuration of the previous read cycle, in which case (for the i^{th} cycle) we denote it as MSD_{i-1}. MSD_0 is defined as

$$MSD_0 = \frac{1}{N} \sum_k (\mathbf{r}_k(read) - \mathbf{r}_k(trained))^2 \tag{6.1}$$

where $\mathbf{r}_k(trained)$ is the position of particle k in the trained configuration, and $\mathbf{r}_k(read)$ is the position of particle k after the relevant read cycle. MSD_{i-1} is defined as

$$MSD_{i-1} = \frac{1}{N}\sum_k (\mathbf{r}_k(i) - r_k(i-1))^2\rangle \tag{6.2}$$

where i and $i-1$ are cycle indices.

We also compute the fraction of active particles (f_{active}) to characterize the memory. We define f_{active} as the fraction of particles that move larger than $0.1\sigma_{AA}$ during a read cycle. We use the notation N_{cycles} for the number of training cycles.

6.4 Results: The BMLJ system

6.4.1 Single Memory

First, we study memory effects in the absorbing states ($\gamma < \gamma_c = 0.08$) prepared with different amplitudes of cyclic shear deformation. The samples are trained at γ_1 = 0.02, 0.03 and 0.06. After training, parallel reading is performed on the trained samples.

6.4.1.1 Parallel read

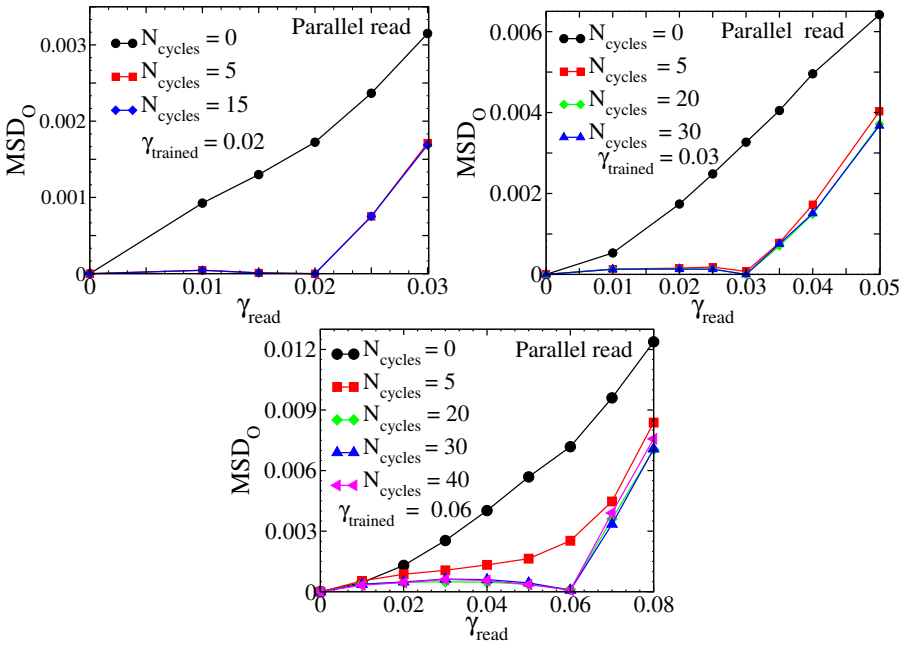

Figure 6.1: The mean squared displacement (MSD) for different training cycles during parallel reading. The system is trained at $\gamma_{trained} = 0.02$ (top) and 0.03 (middle) and 0.06 (bottom). In each case, the MSD at $\gamma_{trained}$ is either lower than other γ values (partially trained) or zero (fully trained), constituting a memory of the training amplitude.

In Fig.6.1, the MSD is plotted against γ_{read} for different numbers of training cycles. In the untrained system ($N_{cycles} = 0$), with the application of shear deformation in the read cycles, particles move by larger amounts for larger strain values. As a result, the MSD increases with γ_{read} monotonically for the untrained system. However, as the number of the training cycles is increased, the system evolves towards the absorbing state. Correspondingly, the MSD for γ_{read} close to $\gamma_{trained}$ is seen to decrease. After a significant number of training cycles, when the system has reached the absorbing state, the MSD becomes zero at $\gamma_{read} = \gamma_{trained}$ since one more cycle of shear deformation with amplitude $\gamma_{trained}$ leaves the system unchanged. The MSD vs. γ_{read} curve thus displays a clear signature or memory of the training deformation amplitude. If we increase the number of training cycles further, the nature of the MSD vs. γ_{read} curve does not change, which is expected as the system already is in the absorbing state. As previously noted, the MSD is finite not only for read amplitudes bigger than the training amplitude, but also for smaller read amplitudes, which is significantly different from the case of sheared suspensions. This can be rationalised by the differences in the nature of reversibility in the two cases.

To illustrate the reasons for the memory signatures observed, we consider the changes in the energy and particle positions during a read cycle.

6.4.1.1.1 Energy changes during a read cycle: The evolution of the system is investigated by measuring energy during the read cycles as a function of strain. When the system is subjected to oscillatory shear deformations, the energy will be proportional to γ^2 if the system deforms elastically. The observed energies *vs.* strain for each read amplitude are fitted to a quadratic function and the difference ΔE of the data from the quadratic fits, which highlight relevant details, are studied. The ΔE curves are shown for three different read amplitudes in Fig. 6.2. It is observed that the ΔE curves display discontinuous jumps which correspond to plastic rearrangements of particles and correspondingly, transitions between energy minima. When $\gamma_{read} = \gamma_{trained}$, such jumps in energy are nevertheless organized such that the energy (and ΔE) returns to the initial value at the end of a cycle. When $\gamma_{read} \neq \gamma_{trained}$, however, the sequence of transitions that take place do not lead to the final state being the same as the initial state, which leads to finite signatures in the energy (and the MSD) during the read cycles.

6.4.1.1.2 Position changes during a read cycle: Next, we consider how the position of a particle evolves during the reading cycle, for $\gamma_{trained} = 0.03$ and $N_{cycles} = 30$. The Y coordinate of a single particle is plotted as a function of strain γ for different read amplitudes γ_{read} in Fig. 6.3. Although the particle position changes discontinuously in all cases (corresponding to jumps between local energy minima), for

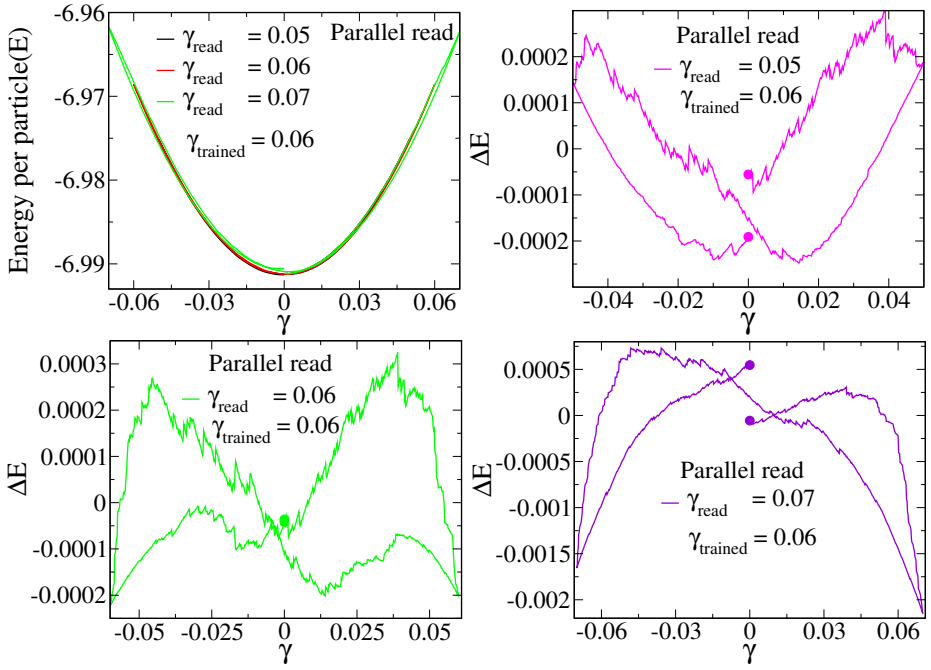

Figure 6.2: Potential energy is plotted as a function of strain γ during the reading cycle. The potential energy curve is fitted to a quadratic function (top panel), and the difference ΔE obtained by subtracting the quadratic fit from the data is shown (bottom three panels) to clearly display relevant details. The system is trained at $\gamma_{trained} = 0.06$. ΔE are shown for read cycles for different amplitudes, which are indicated in the legends. While the energy values return to the initial value when $\gamma_{read} = \gamma_{trained}$, they do not do so for other read amplitudes.

$\gamma_{read} = \gamma_{trained} = 0.03$, the particle position during the read cycle clearly retraces the same cycle as the last training cycle. In contrast, for $\gamma_{read} = 0.02, 0.04$ the trajectory of the particle as indicated by its Y coordinate departs strongly from that during the final reading cycle, and the particle does not return to the initial position at the end of the read cycle.

6.4.1.1.3 Strength of the memory: We have studied memory effects with various amplitudes below the yielding strain amplitude to understand the dependence of memory behaviour on the amplitudes of training. We define and measure the *strength of the memory* as a function of the training amplitude as follows. We have observed earlier that there is a non-monotonic increase in the MSD as we increase the amplitude of γ_{read} for all γ_{read} which is less than or equal to $\gamma_{trained}$. In this regime, the MSD increases initially, but goes through a maximum and becomes zero at $\gamma_{read} = \gamma_{trained}$. If the system is partially trained, the MSD at $\gamma_{trained}$ may be lower than neighbouring strain values but finite. We thus subtract the MSD at $\gamma_{read} = \gamma_{trained}$ from the maximum of the MSD below $\gamma_{trained}$, and use it as a measure of the strength of the memory. The result is presented in Fig. 6.4.

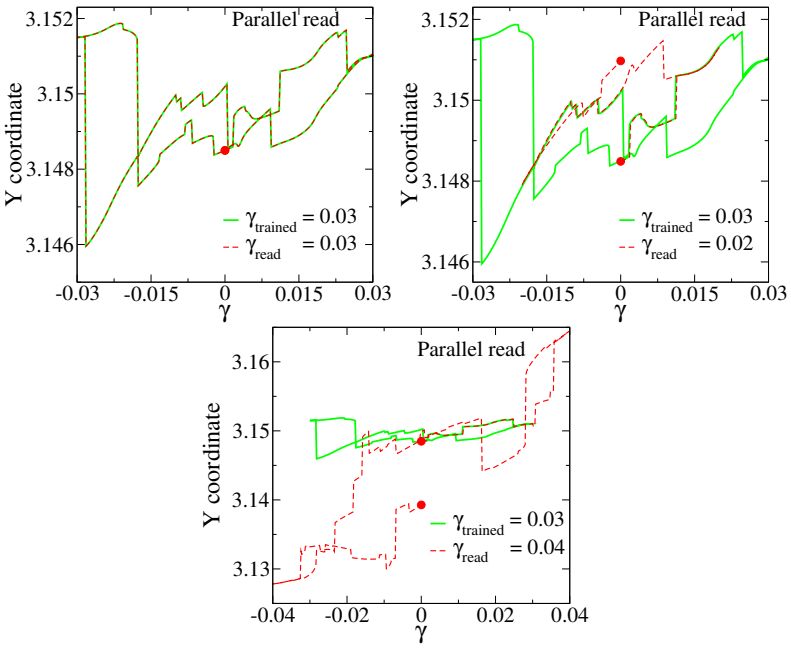

Figure 6.3: The Y coordinate of a single particle is plotted as a function of strain γ for $\gamma_{trained} = 0.03$, $N_{cycles} = 30$. Top: The particle follows the same path during the last training cycle (Cycle = 30), and the read cycle at the same amplitude, $\gamma_{read} = \gamma_{trained} = 0.03$. Middle and bottom panel: When the trained sample is read at different amplitudes $\gamma_{read} = 0.02$ and 0.04 the particle does not retrace the same path.

6.4.1.1.4 Structural signatures of memory: In order to assess if the encoding of memory involves clear structural signatures, we compute the two dimensional pair correlation function $g(x,z)$ defined earlier. In Fig:6.5, we show the result for a system trained at $\gamma_{trained} = 0.06$, along with the $g(x,z)$ for an inherent structure quenched from the liquid (*i. e.* not subjected to any shear deformation). We do not see any significant difference between the liquid inherent structure and the trained system, surprisingly, and the correlation function of the trained system does not show any significant anisotropy. Although we cannot exclude effects too weak for our numerical estimation to detect, or other subtle effects that require alternate measures, the lack of a clearer structural signature in the case of a model glass is puzzling.

6.4.1.1.5 Application of cyclic shear deformation with a different amplitude to a trained system: In the preceding sections, cyclic shear deformation with an amplitude $\gamma_{trained} (< \gamma_c)$ is applied to an equilibrated samples repeatedly. After a large number of training cycles, the system remembers the amplitude of deformation by which it is trained. We now ask what the effect of applying shear deformation at a second "retraining" amplitude. We ask if such retraining will lead to the system "forgetting" the earlier training, or, in other words, whether the memory will be erased. We consider two cases: (1) The retraining amplitude $\gamma_{retrained}$ is greater than $\gamma_{trained}$. (2) The retraining amplitude $\gamma_{retrained}$ is smaller than $\gamma_{trained}$.

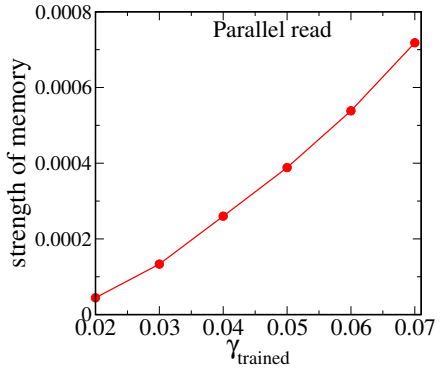

Figure 6.4: The strength of memory is plotted as a function of $\gamma_{trained}$. The strength of memory increases with the increase in amplitude of training below yielding amplitude.

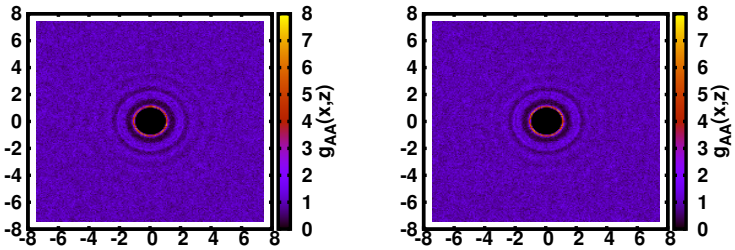

Figure 6.5: Two dimensional pair correlation function, $g_{AA}(x,z)$ for an inherent structure quenched from the liquid (top) and a trained sample with $\gamma_{trained} = 0.06$ (bottom) of the BMLJ system. The data shown here is averaged over 30 different samples.

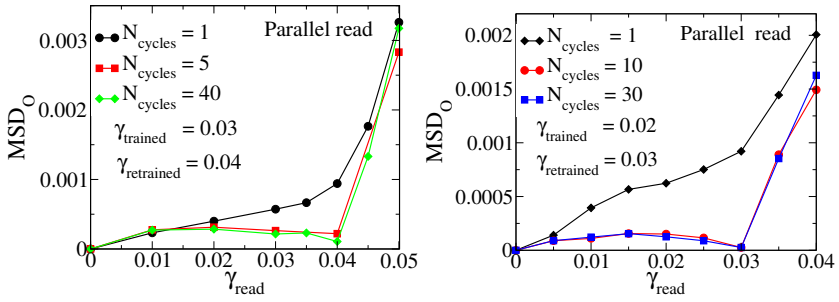

Figure 6.6: The MSD for the system which is retrained at a larger amplitude than the training amplitude during parallel reading. Top: The system is first trained at $\gamma_{trained} = 0.03$ fully (30 cycles) and then cycles of shear deformation with amplitude $\gamma_{retrained} = 0.04$ are applied to that trained system. The MSD, even after a single cycle, does not show a memory of the training at $\gamma_{trained} = 0.03$. Instead, a change of slope in the MSD is visible at $\gamma = 0.04$ (black curve). After a large number of retraining cycles (40 cycles) with $\gamma_{retrained} = 0.04$ the system shows the usual signature of memory at $\gamma = 0.04$, namely a depression/vanishing of the MSD at the retrained amplitude. Bottom: The system is first trained at $\gamma_{trained} = 0.02$ fully (15 cycles) and then cycles of shear deformation with amplitude $\gamma_{retrained} = 0.03$ are applied to that trained system. The plot does not show a vanishing of the MSD at $\gamma_{read} = 0.02$ even after one cycle at the new amplitude (black curve). After a large number of retraining cycles (30 cycles) with $\gamma_{retrained} = 0.03$, the system displays a vanishing MSD at $\gamma = 0.03$.

(1). Retraining amplitude is larger than the training amplitude. Erasure of memory: We consider a sample which is trained at $\gamma_{trained}$ over a large number of cycles. The trained sample is then deformed cyclically for varying numbers of cycles at $\gamma_{retrained} > \gamma_{trained}$. We show two such cases in Fig. 6.6, in which we consider a configuration trained at $\gamma_{trained} = 0.03$ trained for 30 cycles, and $\gamma_{trained} = 0.02$ trained for 15 cycles. In the first case (Fig. 6.6, top panel), we see that even after a single cycle at $\gamma_{retrained} = .04$, the memory at $\gamma_{trained} = 0.03$ is erased, in that no signature of trained at that amplitude is present. Further, after a single cycle, a depression of the MSD at $\gamma_{retrained} = .04$ is visible, which evolves with further cycles to a vanishing MSD at $\gamma_{retrained} = .04$. Thus we conclude that retraining a system at a higher amplitude erases the memory, which is consistent with previous observations for models of colloidal suspensions. A second example with $\gamma_{trained} = .02$ and $\gamma_{retrained} = .03$ displays the same features.

(2). Retraining amplitude is smaller than the training amplitude: Here we consider once again a configuration trained at $\gamma_{trained} = 0.03$ trained for 30 cycles, but apply retraining deformations at $\gamma_{retrained} = 0.02$. The results shown in Fig. 6.7, indicate that the memory of the new (retraining) amplitude forms even after one cycle, with a vanishing of the MSD at that amplitude but the memory of $\gamma_{trained} = 0.03$ is not erased. If there is no information of training at all (at $\gamma = 0.03$), the MSD should be increasing rapidly as soon as it crosses 0.02 similar to Fig. 6.1 (Top panel). However,

we observe MSD increases slowly until 0.03. Thus the MSD at $\gamma_{trained} = 0.03$ is not any longer zero, but is depressed and it shows a change in slope at $\gamma_{read} = \gamma_{trained}$ in a manner that is similar to the signature of multiple memories which we discuss later.

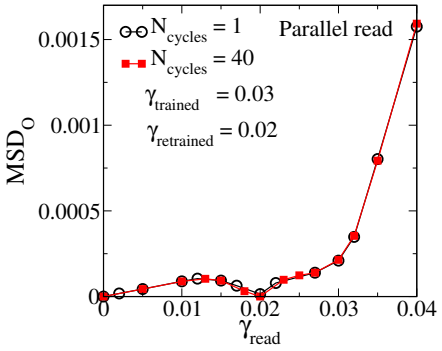

Figure 6.7: The MSD for the system which is retrained at a smaller amplitude than the training amplitude during parallel reading. The system is first trained at $\gamma_{trained} = 0.03$ fully (30 cycles) and then cycles of shear deformation with amplitude $\gamma_{retrained} = 0.02$ are applied to that trained system. The MSD, even after a single cycle, is close to zero at $\gamma_{read} = \gamma_{retrained}$. However, instead of increasing monotonically for larger γ_{read}, a depression of the MSD is apparent around $\gamma_{trained} = 0.03$ indicating persistence of memory of that amplitude.

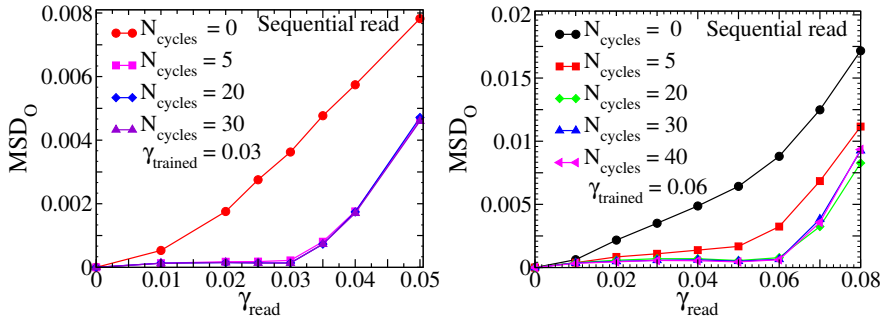

Figure 6.8: The MSD for the single trained system during sequential reading. Different lines correspond to different number of training cycles. The MSD is measured with respect to the original configuration. The system is trained at $\gamma = 0.03$ (top) $\gamma = 0.06$ (bottom). When γ_{read} is same as $\gamma_{trained}$, there is a change in slope of the MSD vs. γ_{read} curve.

6.4.1.2 Sequential read

So far, we have shown results using the parallel read protocol wherein multiple copies of the trained system are subjected to read cycles at different amplitudes. Such a procedure is not available if a measurement is made experimentally, where the same trained system has to be subjected sequentially to read cycles of deformation. We thus consider the analogous sequential read protocol next, wherein after training, the trained configuration is subjected sequentially to a set of read deformations with increasing

amplitude. The MSD data, with respect to the starting, trained, configuration are shown in Fig. 6.8, for different numbers of training cycles. It is observed that the non-monotonicity of the MSD is greatly diminished and the MSD values at the training amplitude are not strictly zero. Nevertheless, the MSD data reveal a clear memory of the training amplitude, in that the MSD remain small up to the training amplitude and increase rapidly thereafter. In Fig. 6.9, we show the corresponding results for MSD computed at each amplitude with respect to the configuration at the end of the previous read cycle, for a fully trained system. In this case too, the MSD data reveal a clear memory of the training amplitude, once again with a significantly reduced non-monotonicity of the MSD data.

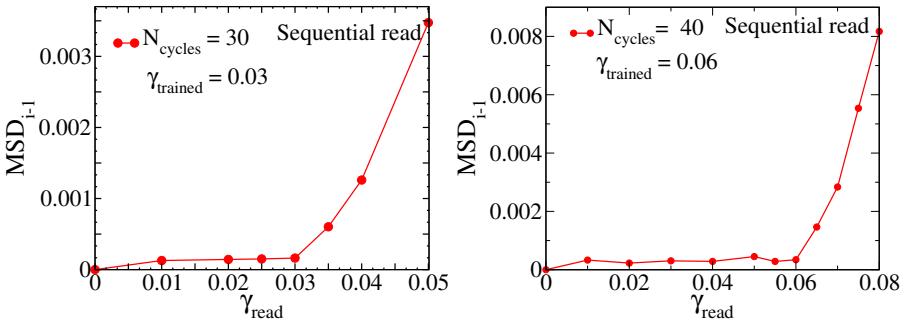

Figure 6.9: The MSD, measured with respect to the configuration after the previous read cycle, is plotted for fully trained system during sequential reading. The system is trained at $\gamma = 0.03$ (top) and $\gamma = 0.06$ (bottom).

6.4.1.3 The fraction of active particles:

In previous related studies, instead of MSD, the fraction of active particles, f_{active}, has been considered as the measurement. Here, we perform the analogous measurement, by defining an active particle as one that has moved by a distance greater than $0.1\sigma_{AA}$ during a read cycle. In Fig. 6.10 (top panel), we show the fraction of active particles (with distances measured with respect to the original trained sample), for different numbers of training cycles. After sufficient training, the f_{active} data show a clear signature of memory of the training amplitude, and a non-monotonicity similar to the MSD data. In Fig. 6.10 (bottom panel), we show the corresponding data wherein displacements are measured with respect to the configuration at the end of the previous read cycle, for the fully trained system. Here too, the memory of the training amplitude is clearly revealed.

6.4.1.4 Memory effects in the diffusing state

We have so far analysed memory effects for the trained system prepared with different amplitudes in the absorbing state, $\gamma_{trained} < \gamma_c$. As already discussed, for

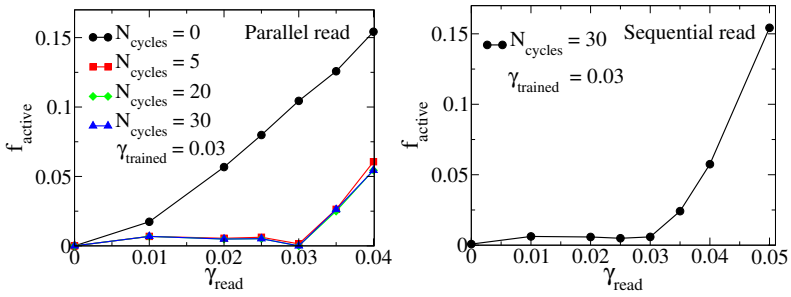

Figure 6.10: The fraction of active particles (f_{active}) is plotted as a function of γ_{read} for a system trained at $\gamma_{trained} = 0.03$. Different lines in the top panel correspond to different numbers of training cycles. Top: (Parallel reading) After a large number of training cycles, when the system reaches the steady state, f_{active} becomes zero at $\gamma_{read} = \gamma_{trained}$. Bottom: (Sequential reading) f_{active} increases rapidly as γ_{read} crosses $\gamma_{trained}$ for the completely trained system.

$\gamma_{trained} > \gamma_c$, the system reaches a diffusing state and does not return to the same configuration at the end of successive cycles. Thus, we do not expect that the system will retain any memory of the training amplitude. We test this expectation by performing measurements for two training amplitudes above γ_c, namely $\gamma_{trained} = 0.09$, and $\gamma_{trained} = 0.11$. Results of MSD_0 shown in Fig. 6.11 reveal indeed that there are no signatures of memory of the training amplitude in these cases.

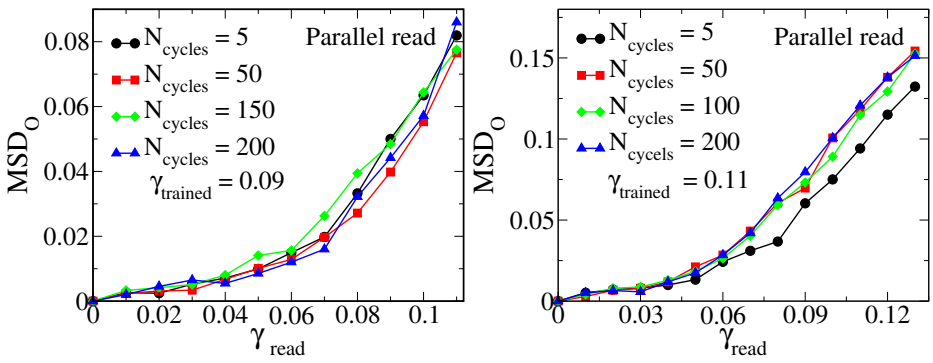

Figure 6.11: The MSD for the system which is trained at the amplitude larger than γ_c. The system is trained at $\gamma_{trained} = 0.09$ (top) $\gamma_{trained} = 0.11$ (bottom) for a different numbers of the training cycles. The MSD increases with increasing γ_{read}, and shows no memory of the training amplitude.

As shown in a recent study, however, one may expect shear banding in the diffusing regime. The system size we have used here is too small (4000 particles) for shear banding to be clearly present. Hence, we consider next a larger system of $N = 64000$, and perform the same study. The results are presented in Fig. 6.12 for $\gamma_{trained} = 0.09$, and $\gamma_{trained} = 0.12$, which do not show any signatures of memory of the training amplitude, confirming the results for the smaller system studied earlier.

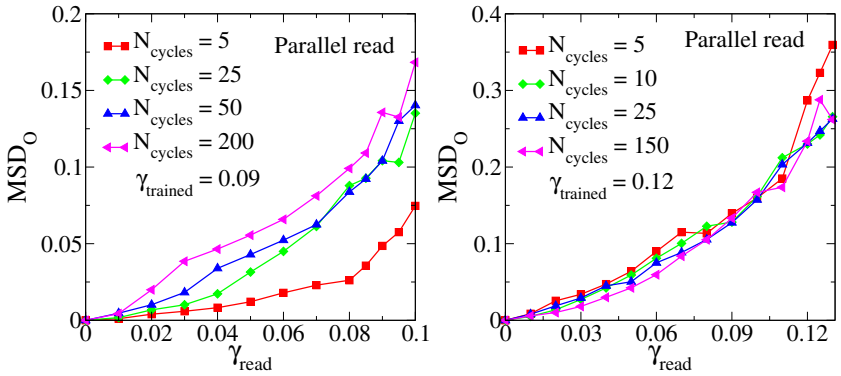

Figure 6.12: The MSD for the system which is trained at the amplitude larger than γ_c for $N = 64000$. The system is trained at $\gamma_{trained} = 0.09$ (top panel) and $\gamma_{trained} = 0.12$ (bottom panel). The different lines correspond to the different numbers of training cycles. No memory effects are observed for these amplitudes, which are larger than the yielding strain.

6.4.2 Multiple memories

We next consider the case of multiple memories. Here, we train the system by subjecting it to repeated cycles of deformation at two different amplitudes γ_1 and γ_2 ($0 \to \gamma_1 \to 0 \to -\gamma_1 \to 0 \to \gamma_2 \to 0 \to -\gamma_2 \to 0$) and perform reading as in the case of single memories. We consider training amplitudes $\gamma_1 = 0.02$ and $\gamma_2 = 0.01$. Note that we have only considered $\gamma_1 > \gamma_2$. We find that a reversal of the order does affect the memory effects, but we do not elaborate on this feature further. To assess the dependence of multiple memories on the deformation training amplitudes, we also consider $\gamma_1 = 0.06$ and $\gamma_2 = 0.04$. We then consider also the case of encoding three memories as described below.

6.4.2.1 Parallel read

In Fig. 6.13, we show results using parallel read for the two sets of training amplitudes, for two different numbers of training cycles. As seen clearly, the data reveal signatures of memory of both amplitudes, although they are different for the two amplitudes. For the smaller amplitude, the MSD goes to zero, whereas it remains finite at the larger amplitude. At the larger amplitude, however, a sharp change in the MSD values is seen, which serves as a clear signature of memory of that training amplitude. As previously discussed, both these memories are persistent, and do not diminish in strength with increased number of training cycles. We note that this training protocol with repeated cycles of alternating strain amplitudes and the protocol we discussed earlier, where we train a system completely and then apply a retraining cycle with a smaller amplitude than the training amplitude, produce very similar results. This result is in agreement with the work of Keim *et al.* [133] where they show that the system could encode both

the memories only when the smallest amplitude is applied last.

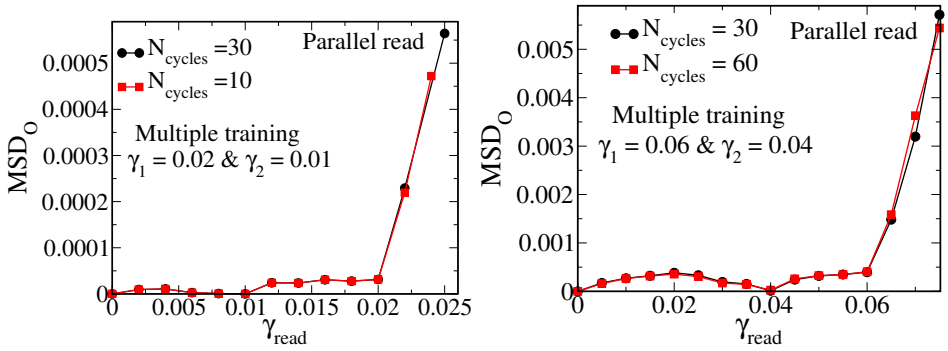

Figure 6.13: The MSD for the system which is trained at multiple amplitudes (top: $\gamma_1 = 0.02$ and $\gamma_2 = 0.01$, bottom: $\gamma_1 = 0.06$ and $\gamma_2 = 0.04$). Two kinks are observed at $\gamma_1 = 0.06$ and $\gamma_2 = 0.04$ (for other set it is at $\gamma_1 = 0.02$ and $\gamma_2 = 0.01$). The different lines correspond to the different numbers of training cycles. Both the memories are present after a large number of training cycles persistently.

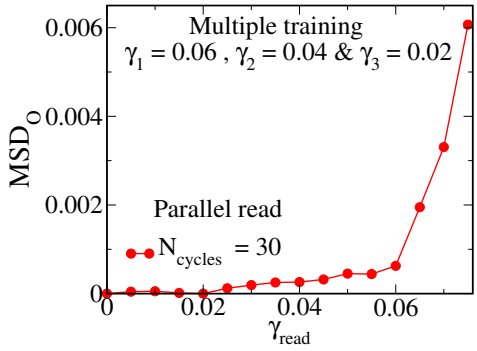

Figure 6.14: The MSD for the system trained with three different amplitudes. The system is trained at $\gamma_1 = 0.06$, $\gamma_2 = 0.04$, $\gamma_3 = 0.02$. The memory is observed at $\gamma = 0.06$ and $\gamma = 0.02$

We next consider whether a larger number of memories can be encoded. To this end, we train configurations with three different amplitudes ($0 \rightarrow \gamma_1 \rightarrow 0 \rightarrow -\gamma_1 \rightarrow 0 \rightarrow \gamma_2 \rightarrow 0 \rightarrow -\gamma_2 \rightarrow 0 \rightarrow \gamma_3 \rightarrow 0 \rightarrow -\gamma_3 \rightarrow 0.$), with $\gamma_1 = 0.06$, $\gamma_2 = 0.04$ and $\gamma_3 = 0.02$. When subjected to read cycles, we find (as shown in Fig. 6.14) signatures of memory only at the smallest and largest of the amplitudes, namely $\gamma_3 = 0.02$ and $\gamma_1 = 0.06$. In order to assess the role of training protocol, we consider a different sequence of training deformations, with a repetition of the pattern $\gamma_1\gamma_2\gamma_2\gamma_2\gamma_3$. In this case, as shown in Fig. 6.15, all three training amplitudes have corresponding dips in the MSD revealing that all these memories are encoded in the trained system.

6.4.2.2 Sequential reading

We next employ sequential reading as done before for single memories for the case of multiple memories, with two different training amplitudes with $\gamma_1 = 0.06$, $\gamma_2 =$

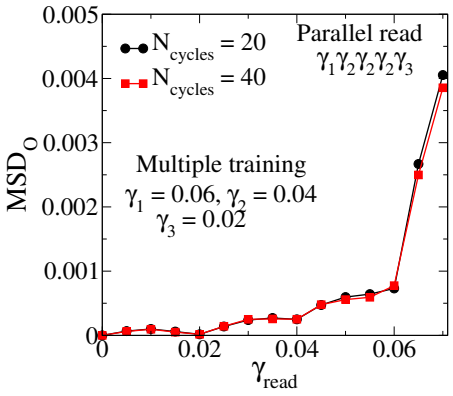

Figure 6.15: The MSD for the system which is trained at three different amplitudes during parallel reading. The system is trained for training cycles where a single cycle has three different shear deformation amplitude (sub)cycle repeated according to the pattern: $\gamma_1\gamma_2\gamma_2\gamma_2\gamma_3$. Here $\gamma_1 = 0.06$ $\gamma_2 = 0.04$ and $\gamma_3 = 0.02$. After a large number of training cycles, signatures of all three memories are clearly seen and these memories are persistent.

0.04. As shown in Fig.6.16, when the MSD is measured with respect to the trained configuration, sequential read generates data which capture the encoding of multiple memories as clearly as the parallel read, but when the MSD is measured with respect to the final configuration of the previous read cycle, a less distinct signature is seen at the smaller of the training amplitudes, $\gamma_2 = 0.04$. While there may be variations of the procedure used here that will generate a clear signature of multiple memories even in this case, we do not pursue this investigation further in that direction.

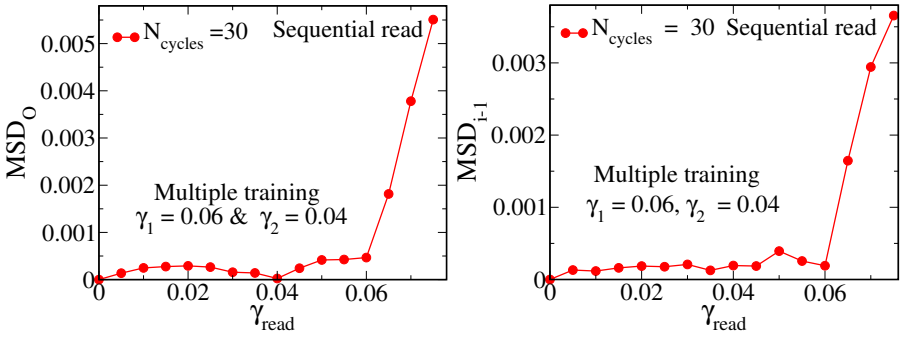

Figure 6.16: The MSD for the system, trained at multiple amplitudes during sequential reading. Top: The MSD is measured with respect to the original configurations. Bottom: The MSD is measured with respect to the final configuration of the previous read cycle.

6.4.2.3 Application of cyclic shear deformation with different amplitudes to a trained (at multiple amplitudes) system

Similar to the case of single memory, we wish to investigate the effect of applying cyclic deformation at a new amplitude in a multiply trained system. The system is

trained at two different amplitudes $\gamma_1 = 0.06$ and $\gamma_2 = 0.04$, and is then subjected to a single cycle of shear deformation with γ_3 repeatedly. We have three cases (1). γ_3 is smaller than both γ_1 and γ_2. (2). γ_3 is less than γ_1 but greater than γ_2 and (3). γ_3 is larger than both γ_2 and γ_1. We consider these cases in turn.

6.4.2.3.1 Retraining amplitude is smaller than both the training amplitudes:

We consider configurations trained at $\gamma_1 = 0.06$ and $\gamma_2 = 0.04$. We then apply cyclic shear deformation with $\gamma_3 = 0.02$. The results are shown in Fig.6.17. Kinks in the MSD curves at $\gamma_1 = 0.06$ (largest γ) and $\gamma_3 = 0.02$ indicate that the memory of these amplitudes is encoded, and remain even after a large number of cycles at $\gamma_3 = 0.02$. No clear signature is visible at $\gamma_2 = 0.04$. As in the case of triple memories, it may be possible that this signature will remain if a different training protocol is used, but we do not investigate it further.

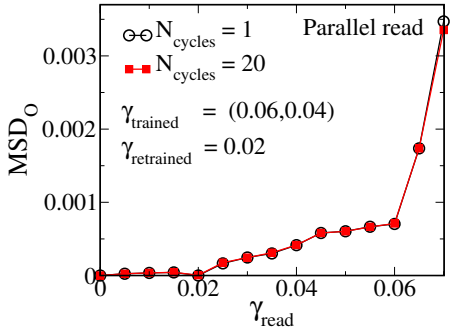

Figure 6.17: The MSD for the system which is retrained at an amplitude which is smaller than both the training amplitudes. Different lines correspond to numbers of retraining cycles. A single cycle of shear deformation with amplitude $\gamma_3 = 0.02$ is applied to the system trained at $\gamma_1 = 0.06$ and $\gamma_2 = 0.04$. The new configuration has memory at $\gamma_3 = 0.02$ and $\gamma_1 = 0.06$ but no distinct memory of $\gamma_2 = 0.04$. Memory signatures at $\gamma_1 = 0.06$ remains robustly even after a large number of retraining cycles at $\gamma_3 = 0.02$.

6.4.2.3.2 Retraining amplitude is smaller than one of the training amplitudes but larger than the other:

We consider configurations trained at $\gamma_1 = 0.06$ and $\gamma_2 = 0.04$. We then apply cyclic shear deformation with $\gamma_3 = 0.05$. The results are shown in Fig.6.18. Even after a single deformation at $\gamma_3 = 0.05$, the memory at $\gamma_2 = 0.04$ is erased, while the memory at $\gamma_1 = 0.06$ is weak but present. In addition, a strong signature of memory at $\gamma_3 = 0.05$ appears after a single cycle.

6.4.2.3.3 Retraining amplitude is larger than both the training amplitudes:

We consider configurations trained at $\gamma_1 = 0.06$ and $\gamma_2 = 0.04$. We then apply cyclic shear deformation with $\gamma_3 = 0.07$. As shown in Fig. 6.19, a single cycle of shear deformation with $\gamma_3 = 0.07$ erases both the memories. This is consistent with the

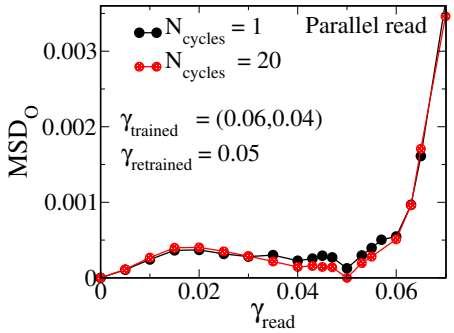

Figure 6.18: The MSD for the system which is retrained at an amplitude which is smaller than one training amplitude but larger than other. A single cycle shear deformation with amplitude $\gamma_3 = 0.05$ is applied to the system which is trained at two different amplitudes, $\gamma_1 = 0.06$ and $\gamma_2 = 0.04$. The new system does not have a clear signature of memory at $\gamma_2 = 0.04$ but has features revealing memory at $\gamma_1 = 0.06$ and at $\gamma_3 = 0.05$, which remain after a large number of retraining cycles at $\gamma_3 = 0.05$.

observation for the case of single memory that deformation by a larger amplitude erases stored memories.

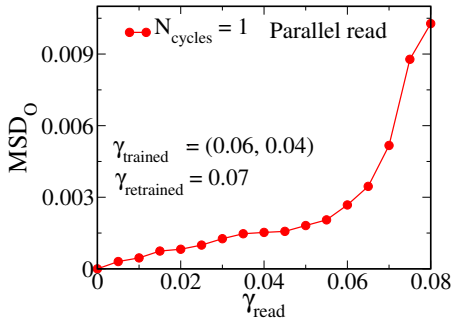

Figure 6.19: The MSD for the system which is retrained at an amplitude larger than both the training amplitudes. A single cycle of shear deformation with amplitude $\gamma = 0.07$ is applied to the system which is trained at multiple γ, $\gamma_1 = 0.06$ and $\gamma_2 = 0.04$, which erases memories of both these amplitudes.

6.5 Results: Soft Sphere binary mixture system

The differences in memory effects in the BMLJ glass former described above and the model considered in have previously been rationalised in terms of the observation that trained configurations of BMLJ that reach an absorbing state nevertheless traverse a non-trivial energy landscape during a read cycle, which involve multiple transitions between energy minima. Thus, even though the configurations reach the same configuration at the end of a cycle, their trajectories during the cycle are non-trivial. This is in contrast with the model of a sheared colloidal suspension studied wherein, upon reaching an absorbing state, sheared configurations return to the same configuration

at the end of each shear cycle. More importantly, the particles merely undergo affine deformations during the cycle and do not interact with other particles. They thus experience a trival, flat, landscape during the read cycles. It is thus interesting to ask if there are cases that deviate from both these scenarios. Such a case is presented in the study of sheared soft spheres. The soft sphere system at densities below the jamming point, under AQS deformation, traverses a trivial landscape, in the sense that the energies of the inherent structures always remain zero. However, this system displays different regimes in applied strain, for which the nature of the absorbing states are different. For small applied strain, the system reaches absorbing states which are similar to those of the model studied in wherein during a shear cycle, particles do not interact with other particles and show smooth affine displacements. These are termed *point reversible* states. At higher amplitudes, a new regime is encountered wherein particles return to their original positions at the end of a shear cycle, but during the cycle, they may collide or interact with other particles that they come into contact with. These states are referred to as *loop reversible* states. It is thus interesting to consider the nature of memory in point reversible and loop reversible states. For the volume fraction $\phi = 0.61$, the transition from point to loop reversible states occurs around $\gamma_c^{pl} = 0.07$. Accordingly, we consider $\gamma_{trained} = 0.03$ (which belongs to the point reversible regime) and $\gamma_{trained} = 0.12$ (which belongs to the loop reversible range) to study the nature of memory effects in the case of training at a single amplitude. We will subsequently consider multiple memories, which are described later.

6.5.1 Single memory

6.5.1.1 Parallel reading

We start with an equilibrated system and then train it for a sufficient number of cycles with a single amplitude. The number of training cycles needed for the soft sphere system to reach the absorbing state is much larger than for the BMLJ configurations. The trained system is subjected to read cycles using parallel reading. We have a system which is trained at $\gamma = 0.03$, (where the system is point reversible) and another system which is trained at $\gamma = 0.12$ (where the system is loop reversible). The results are shown in Fig. 6.20. We observe that when the training amplitude belongs to the point reversible regime, the MSD is zero for all the amplitudes below the training amplitude, similarly to the model discussed before. When the amplitude is in the loop reversible range, the memory behaviour is similar to the BMLJ system discussed earlier, in that the MSD is finite both above and below the training amplitude.

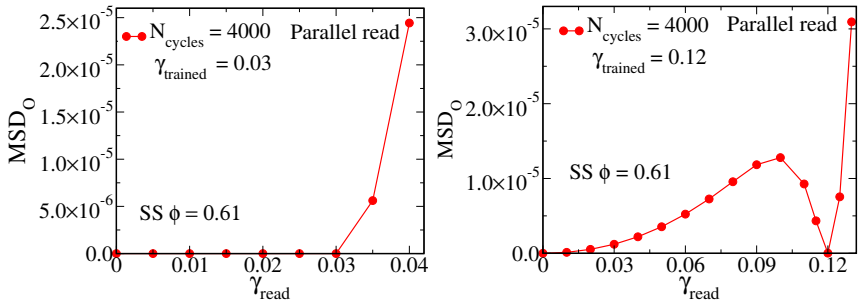

Figure 6.20: The MSD for the single trained system during parallel read. Top: The system is trained at $\gamma_{trained} = 0.03$. At this amplitude, system is point reversible. We find that the MSD is zero for all $\gamma_{read} \leq \gamma_{trained}$. Then there is a change of slope. Bottom: The system is trained at $\gamma_{trained} = 0.12$. At this amplitude, the system is loop reversible. We find that the MSD is zero only when $\gamma_{read} = \gamma_{trained}$

6.5.1.2 Sequential reading

We also perform sequential reading for the cases considered above, and present the results in Fig. 6.21. We observe that when the amplitude is in the point reversible range, the memory behaviour is the same as for parallel reading. The MSD is zero at all γ_{read} below $\gamma_{trained}$ and it increases with increasing read amplitude above. This behaviour is expected since the application of γ_{read} ($< \gamma_{trained}$) does not change the system in any way. When the training amplitude is in the loop reversible range, the system is not reversible at $\gamma_{read} = \gamma_{trained}$ (MSD is not zero, although very small) but a sharp change in MSD occurs across $\gamma_{trained}$ and the resulting MSD behaves very similarly to the parallel read case.

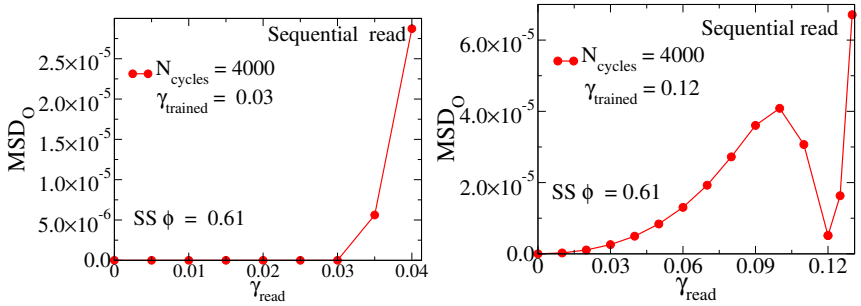

Figure 6.21: The MSD for the single trained system during sequential reading. Top: The system is trained at $\gamma = 0.03$. At this amplitude, the system is point reversible. We find that the MSD is zero for all $\gamma_{read} \leq \gamma_{trained}$, and increases rapidly thereafter. Bottom: The system is trained at $\gamma = 0.12$. At this amplitude, the system is loop reversible. We observe that the MSD decreases sharply around and is very small at $\gamma_{read} = \gamma_{trained}$ This memory behaviour is different from parallel reading, since the system is not fully reversible at $\gamma_{read} = \gamma_{trained}$, although it displays a very clear memory signature.

6.5.1.2.1 Structural signature of memory: We study the nature of structural change due to training by computing the two dimensional pair correlation function

$g(x,z)$ for a training amplitude in the point reversible regime. We choose $\phi = 0.54$ (in order to have better clarity) at which density the system is point reversible at $\gamma = 0.23$. The results are presented in Fig. 6.22 indicating that $g(x,z)$ for the trained system shows significant anisotropy and significantly different from $g(x,z)$ that of the fluid (not shown) which is isotropic. This behaviour is analogous to the observations in non Brownian suspension although the observed anisotropy is different owing to the differences in the shearing protocol. Other partial pair correlation functions display similar behaviour (not shown).

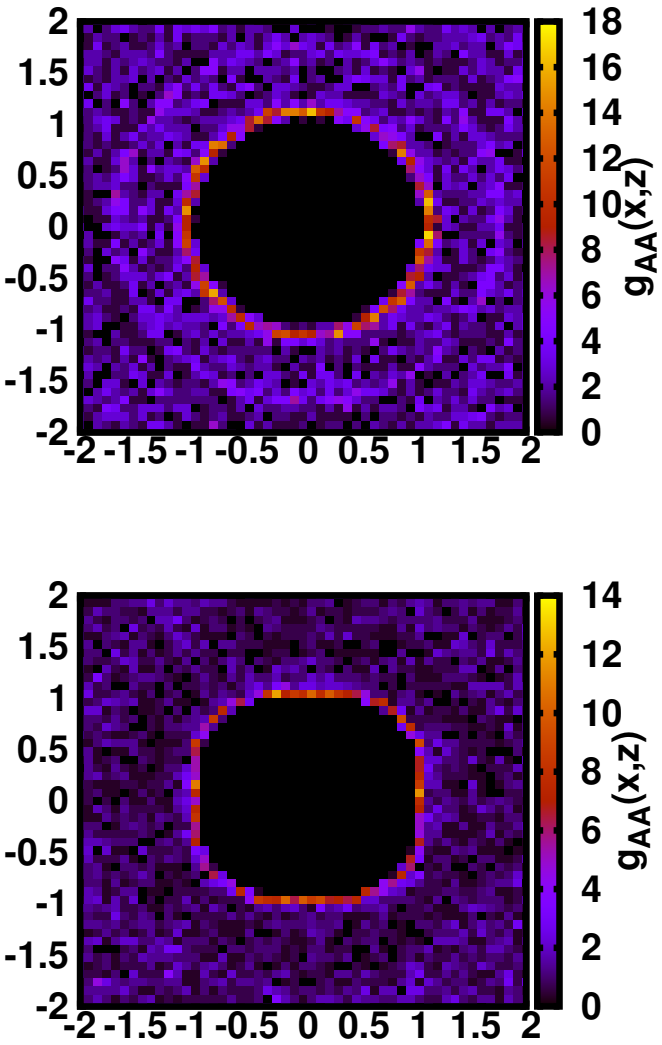

Figure 6.22: Two dimensional pair correlation function, $g_{AA}(x,z)$ for an inherent structure quenched from the liquid (top) and for the trained system (bottom) in the shear plane xz. The system is trained at $\gamma_{trained} = 0.23$. The data are averaged over 40 different samples.

6.5.2 Memory effects in the diffusing states

At very large amplitude of shearing the soft sphere system shows diffusive behaviour, like the BMLJ. The MSD increases with increasing accumulated strain linearly. We consider whether any memory effects are present in this regime, by analysing configurations trained at $\gamma_{trained} = 1.0$ and $\gamma_{trained} = 0.8$, at packing fraction $\phi = 0.61$. The results are presented in Fig. 6.23. As before, the system is trained over a large number of training cycles and after training, the system is read using parallel reading. It is observed that the MSD increases smoothly as γ_{read} increases and there are no signatures of memory of the training amplitudes.

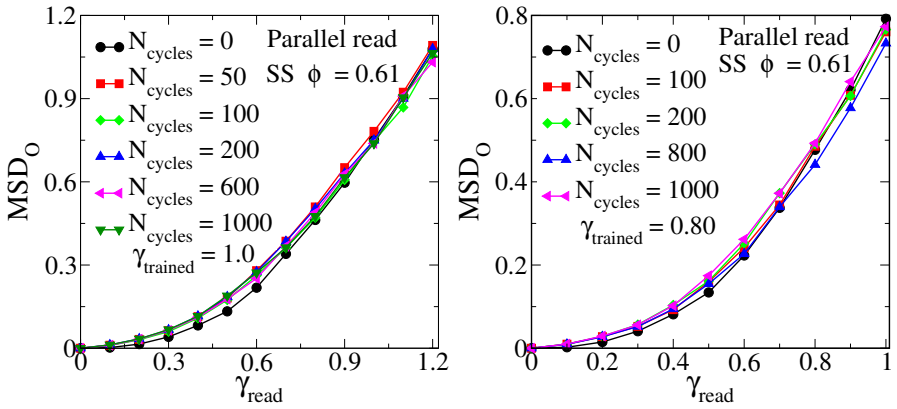

Figure 6.23: The MSD for the configurations trained at $\gamma = 1.0$ (top) $\gamma = 0.8$ (bottom). Both these amplitudes belong to diffusive regime. The different lines correspond to different numbers of training cycles. We do not observe any memory signatures in these cases.

6.5.3 Multiple memories

We consider three cases in studying multiple memories in the soft sphere system: (i) Both the training amplitudes are below γ_c, (ii) Both the training amplitudes are above γ_c, and (iii) One training amplitude is below γ_c, and the other is above γ_c. Here, γ_c refers to the strain at which a transition is observed from the point reversible to loop reversible states. We consider each of these cases employing both parallel and sequential read protocols.

6.5.3.1 Parallel reading

We perform parallel reading to the trained samples. The results are shown in Fig. 6.24. We first consider configurations trained at amplitudes $\gamma_1 = 0.05$ and $\gamma_2 = 0.03$. The system is point reversible at both the amplitudes. We train the system for 3000 cycles. After training, the system is read using the parallel reading protocol. Below the higher training amplitude, the MSD is zero for all amplitudes. This implies that the

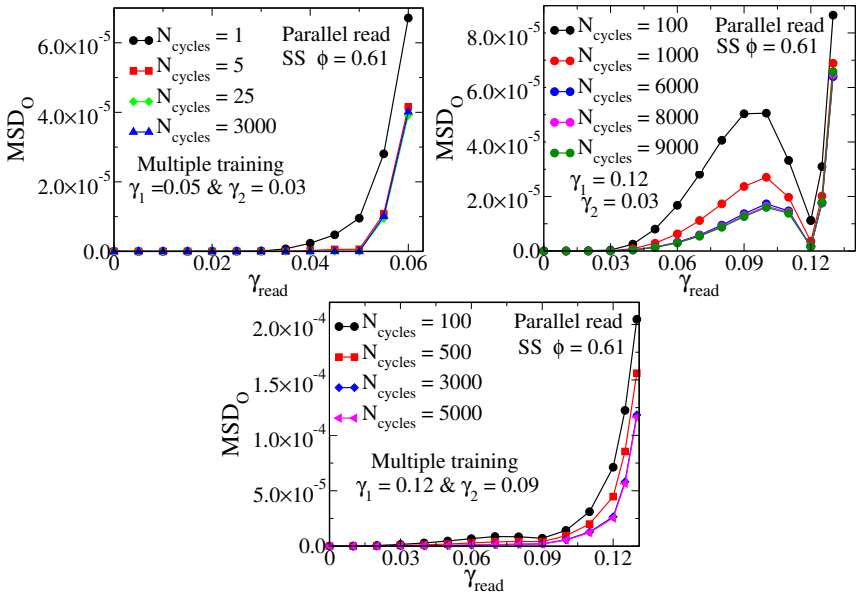

Figure 6.24: The MSD for the multiple trained system during parallel reading. Different lines correspond to different numbers of training cycles. Top panel: The system is trained $\gamma_1 = 0.05$ and $\gamma_2 = 0.03$. At these amplitudes, the system is point reversible. After one training cycle, the MSD is zero below $\gamma_2 = 0.03$ and finite above, but with more training cycles, the MSD becomes zero for all $\gamma_{read} < \gamma_1 = 0.05$. Thus, only the memory of the largest amplitude remains. Middle panel: The system is trained $\gamma_1 = 0.12$ and $\gamma_2 = 0.03$. At the amplitude $\gamma = 0.12$, the system is in loop reversible at $\gamma = 0.03$, the system is point reversible. The MSD remains zero below $\gamma_{read} = \gamma_2$ and exhibits a minimum value approaching zero at $\gamma_{read} = \gamma_1$, each being a clear signature of memory in the respective regimes. Bottom panel: The system is trained $\gamma_1 = 0.12$ and $\gamma_2 = 0.09$. At both these amplitudes, the system is loop reversible. While the MSD is close to zero below $\gamma_{read} = \gamma_2$, no clear signature of memory is present near $\gamma_{read} = \gamma_1$. The presence of multiple memories in this case cannot be concluded from these observations. The results may be compared with those in Fig. 6.20 for single memories.

multiple memories are transient when both the amplitudes are in the point reversible range, consistently with previous observations. We next consider training amplitudes $\gamma_1 = 0.12$ (at which the system is loop reversible) and $\gamma_2 = 0.03$ (at which the system is point reversible). After training for 9000 cycles the system is read using the parallel reading protocol. We observe that below $\gamma_{read} = \gamma_2$, the MSD remains zero, and at $\gamma_{read} = \gamma_1$ the MSD exhibits a minimum, approaching zero for large enough training cycles. Thus, both these memories are retained with expected signatures. Finally we consider training amplitudes $\gamma_1 = 0.12$ and $\gamma_2 = 0.09$. The system is loop reversible at both the amplitudes. We train the system for 5000 cycles. After training, the system is read using the parallel reading protocol. We observe that the MSD approaches zero for all amplitudes below $\gamma_{read} = \gamma_1$ but no distinct signature of memory is found at $\gamma_{read} = \gamma_1$. These observations are both surprising, since neither conforms to the expected memory behaviour in analogy with the BMLJ glass. The case of multiple

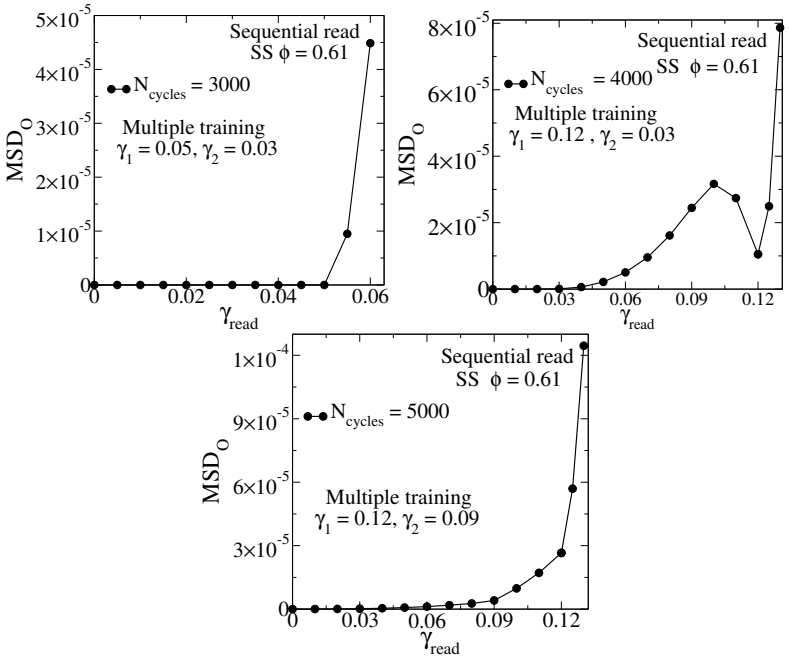

Figure 6.25: The MSD for the multiple trained system during sequential reading. Different lines correspond to different numbers of training cycles. Top panel: The system is trained $\gamma_1 = 0.05$ and $\gamma_2 = 0.03$. At these amplitudes, the system is point reversible. After one training cycle, the MSD is zero below $\gamma_2 = 0.03$ and finite above, but with more training cycles, the MSD becomes zero for all $\gamma_{read} < \gamma_1 = 0.05$. Thus, only the memory of the largest amplitude remains. Middle panel: The system is trained $\gamma_1 = 0.12$ and $\gamma_2 = 0.03$. At the amplitude $\gamma = 0.12$, the system is in loop reversible at $\gamma = 0.03$, the system is point reversible. The MSD remains zero below $\gamma_{read} = \gamma_2$ and exhibits a minimum value at $\gamma_{read} = \gamma_1$, each being a clear signature of memory in the respective regimes. Bottom panel: The system is trained $\gamma_1 = 0.12$ and $\gamma_2 = 0.09$. At both these amplitudes, the system is loop reversible. While the MSD is close to zero below $\gamma_{read} = \gamma_2$, no clear signature of memory is present near $\gamma_{read} = \gamma_1$. The presence of multiple memories in this case cannot be concluded from these observations. The results may be compared with those in Fig. 6.21 for single memories

memories in the loop reversible regime thus require further investigation.

6.5.3.2 Sequential reading

We perform sequential reading for each of the cases considered above, and show the results in Fig. 6.25. We observe that the memory behaviour is the same as in the case of the parallel reading protocol.

6.6 Summary and Conclusions

We have performed numerical investigations of memory effects in two model systems, the Kob-Andersen binary mixture (BMLJ) and a soft sphere mixture. In the former case, our results extend and elaborate on the results and observations from earlier work, in particular in the form of considering different protocols for reading the encoded memories. The latter case offers an interesting extension of previous studies, in that it offers an example displaying features that are distinct from the earlier studied cases of a model glass and a model of colloidal suspensions, exhibiting features found in both these earlier examples. In the loop reversible regime of this model, the memory effects seen are, to a large extent, similar to the case of the model glass, even while the system samples a trivial energy landscape. In considering structural signatures of memory, we find that the model glass studied does not reveal the features seen previously for the model of colloidal suspensions, and thus prompting further investigations on the manner in which the memory is encoded in this system. On the other hand, the soft sphere system in the point reversible regime does exhibit the expected structural signatures. These results taken together offer a detailed characterisation of memory effects in the studied model systems.

While reading multiple memories, the MSD becomes zero at the smaller amplitude, and it shows a change of slope at the larger amplitude, but MSD is no longer zero at that amplitude. Thus, in the future study, it would be interesting to find a protocol where MSD becomes zero at all the amplitudes so that reading becomes cleaner. The robustness of this memory at finite temperature and finite shear rate needs to be investigated in future. It would also be interesting to develop a mesoscopic model for memory behaviour to better understand how the system finds a limit cycle and under what condition this limit cycle can be destroyed.

Chapter 7

Yielding behavior of glasses with one sided shear

7.1 Introduction

The response to applied mechanical stresses is a fundamental characteristic of solids that is relevant in the context of material science. For large applied stresses or deformations, *plastic* deformations contribute significantly to such response, leading eventually to yielding and flow. In the case of amorphous solids, ranging from hard glasses such as oxide glasses to soft solids, these plastic deformations are relevant for understanding their yielding behaviour and rheology [98,232]. Recent years have witnessed significant activity in developing a statistical mechanical description of these phenomena [127, 128, 233]. Yielding behaviour in model amorphous solids has been investigated experimentally [234–236], through computer simulations [129, 130, 237–246], and theoretical investigations including the study of elastoplastic models [233, 239, 247, 248]. These investigations have largely focused on the response to uniform shear, but several investigations have explored yielding behaviour under cyclic deformation [26,130,245,249]. A specific issue that has received considerable attention recently is the role of annealing of the glasses that are subjected to deformation, in determining the nature of yielding. Indeed, under both uniform shear and cyclic shear, it has been demonstrated that a qualitative change occurs in the yielding behaviour when the degree of annealing of the glasses considered increases. Under cyclic deformation, poorly annealed glasses display significant mechanically induced annealing, and converge to a common threshold energy, before yielding takes place. In contrast, well annealed glasses (with energies below the threshold energy), do not display any change in properties with increasing amplitude of shear until the yielding amplitude is reached, where yielding is accompanied by a discontinuous change in energy and stress, the amount

of which depends on the degree of annealing [26]. Under uniform shear a similar response is observed [250]. Apart from the context of yielding, response to cyclic shear has been investigated in order to understand the reversible to irreversible transition, *i.e.* the transition from *absorbing* to diffusive states, as observed in non-Brownian colloidal suspensions, glasses, related systems and models thereof [123,251–255] Memory formation in models of suspensions and glasses have also been a subject of considerable interest [135,256,257]. In many of these works, particularly when related to yielding the cyclic deformations considered have been *symmetric*, i.e. the applied strain of the system is varied through a cycle as $0 \to \gamma_{\max} \to 0 \to -\gamma_{\max} \to 0$, where $\gamma_{\max}$ is the amplitude of shear. Given that significant structural change is observed below yielding for poorly annealed cases but not for well annealed cases, one may expect that the choice of range from $\gamma_{\min}$ to $\gamma_{\max}$ over which the strain is varied cyclically may significantly influence the plasticity and yielding behaviour. Indeed, such dependence is of practical importance in determining the characteristics of fatigue and fatigue failure [258], which in turn dictate the scope and limits of operability of such materials in real-life applications. With the aim of investigating the dependence of the nature of plasticity and yielding on particular cyclic deformation protocols, here we consider the response totally asymmetric cycles of shear, $0 \to \gamma^1_{\max} \to 0 \to \gamma^1_{\max} \ldots$. We simulate a model glass employing the athermal quasistatic (AQS) shear procedure for a wide range of annealing and amplitudes of strain, in order to investigate the nature of plasticity and yielding. The observed behaviour is found to be markedly different from the case of *symmetric* cyclic shear, as we describe below.

For the well-annealed samples, for the smaller system sizes considered, we find an *intermediate* range of $\gamma^1_{\max}$ values over which the stress decreases from the maximum value attained, *i.e. beyond* the stress peak, but no diffusive behavior is present. The onset of diffusive behavior, at a larger $\gamma^1_{\max}$ value, is identified with yielding [26, 129, 130, 245] We investigate the dependence on system size N, and find that the intermediate window of $\gamma^1_{\max}$ narrows with system size for well annealed case. Our results suggest, but cannot conclusively demonstrate, that the intermediate strain window will vanish as $N \to \infty$, but the narrowing itself leads to a remarkable conclusion: Under asymmetric shear, well annealed glasses will yield at smaller strain amplitudes than poorly annealed glasses, reversing the trend observed in the case of symmetric shear protocols.

In order to better understand our results, we analyse the possibility of shear induced anisotropy of the structures obtained through the AQS simulations. Remarkably, despite of the asymmetric shear protocol employed, we find that the structures are highly isotropic, resembling those obtained under symmetric cyclic shear [256].

7.2 Simulations details

We perform AQS simulations of a model glass former, the 80 : 20 Kob-Andersen binary Lennard-Jones mixture (KA-BMLJ), in which particles interact with a Lennard-Jones potential, employing a quadratic cutoff that ensures that the energy and force go smoothly to zero at the cutoff distance. Further details of the model are given in chapter 2. The results presented here were obtained from the simulations of 3d samples with $N = 4000$ particles. In order to to investigate finite size effects, we also consider systems with $N = 200$, 400, 800, 4000, 8000, 32000 and 64000 particles. With V being the sample volume, we equilibrate the system at fixed density $\rho = N/V = 1.2$ in the liquid state at reduced temperatures $T = 1.0, 0.60, 0.466, 0.40, 0.37$ *via* a constant temperature molecular dynamics simulation. Subsequently, equilibrated configurations are subjected to energy minimization to obtain local energy minimum (inherent structure) configurations that have average energies per particle $E_{\text{init}} = -6.89, -6.92, -6.98, -7.03, -7.05$ respectively for the temperatures stated above. The results shown are averaged over 15 independent samples. Energy minimization is performed using the conjugate gradient algorithm. The molecular dynamics and AQS simulations are performed using LAMMPS [259].

Shear deformation Protocol.

The inherent structures, or glasses, are then subjected to cyclic shear deformation in the xz plane using the Athermal Quasi-Static (AQS) procedure which involves the application of strain by small increments ($d\gamma = 2 \times 10^{-4}$) following by energy minimization. We apply asymmetric shear cycles that follow the sequence: $0 \to \gamma^1_{\text{max}} \to 0$, where γ^1_{max} is the amplitude of deformation. We apply cycles of shear until a steady state is reached, wherein the system either reaches an *absorbing* state such that the same sequences of configurations are visited in a cycle for repeated cycles, or a *diffusive* state is attained in which the properties exhibited from cycle to cycle are statistically similar [129,130]. For symmetric cyclic shear [129,130], the *yield strain amplitude* γ_y^{sym} has been identified as the strain value marking the onset of the *diffusive* state, which also coincides with a discontinuous stress drop from the largest stress value attained just prior yielding [129, 130]. As described below, for asymmetric shear, the location of the stress peak and the onset of diffusion differ in general, and we will therefore distinguish these strain values as γ_{peak} and γ_{diff}, respectively. Note that both for symmetric and asymmetric shear, significant plastic rearrangements occur before an *absorbing* steady state is established.

7.3 Results

7.3.1 Poorly annealed glass:

We first consider the steady states attained under asymmetric shear for a poorly annealed glass with $E_{\rm init} = -6.89$. In Fig. 7.1 we show the energy and stress through a cycle as a function of γ in the steady state for a single sample. The energy *vs.* strain curves display a minimum at finite strain that increases as $\approx \gamma^1_{\rm max}/2$ for $\gamma^1_{\rm max} \leq 0.15$, and for larger $\gamma^1_{\rm max}$, the energy curves display two well-separated minima. The sample-averaged strain $\gamma_{E_{\rm min}}$ at which the minimum $E_{\rm min}$ of the energy in the limit-cycle is obtained, is observed to vary as $\gamma^1_{\rm max}/2$.

As we have observed that the minimum energy occurs at finite γ, $\gamma_{E_{min}}$, it is important to focus on the minimum energy (E_{min}) as well as $\gamma_{E_{min}}$ to characterize the yielding point in asymmetric shear deformation. In Fig. 7.2, we show the evolution of E_{min} against the number of cycles. We observe that the energy reaches a steady state after a transient. The final state of the energy depends upon the amplitude by which it is deformed; final energy decreases until strain amplitude, $\gamma^1_{max} = 0.150$; beyond $\gamma = 0.150$ it starts increasing, suggesting the yielding point, $\gamma_y \sim 0.160$. In Fig. 7.2 (Top: Middle panel) we have shown the evolution of $\gamma_{E_{min}}$ as a function of number of cycles for different γ^1_{max}. We have observed that the application of shear deformation moves $\gamma_{E_{min}}$ from zero to a finite value as we increase the number of cycles of deformation, and it saturates to a finite value in the steady state, below yielding, and fluctuates around a mean value above the yielding amplitude. We have computed MSD at the steady state and show as a function of number of cycles (Fig. 7.2, Top right). For all strain amplitudes below 0.15 MSD is almost zero, suggesting these states are absorbing state, whereas the system becomes diffusive starting from the strain amplitude, 0.160. This behavior of MSD clearly demonstrates that the yielding amplitude is around $\gamma_y \sim 0.160$.

These observations can be simply rationalised by a shift in what we term the *reference strain*, i.e. the strain at which the stress is zero, to the mid-point of the strain cycle as a result of plastic rearrangements during the initial cycles (transient), as shown in the right panel of Fig. 7.1. As we see from results shown below (Fig. 7.2 (bottom panel), the yielding behaviour for poorly annealed glasses can be quantitatively, mapped to the results for the symmetric case with strain amplitude $\gamma^{\rm sym}_{\rm max}$, by the equivalence $\gamma^{\rm sym}_{\rm max} = \gamma^1_{\rm max}/2$. In particular, the observation of yielding for $\gamma^1_{\rm max} > 0.15$ is consistent with the the observed $\gamma^{\rm sym}_y \approx 0.08$ [26].

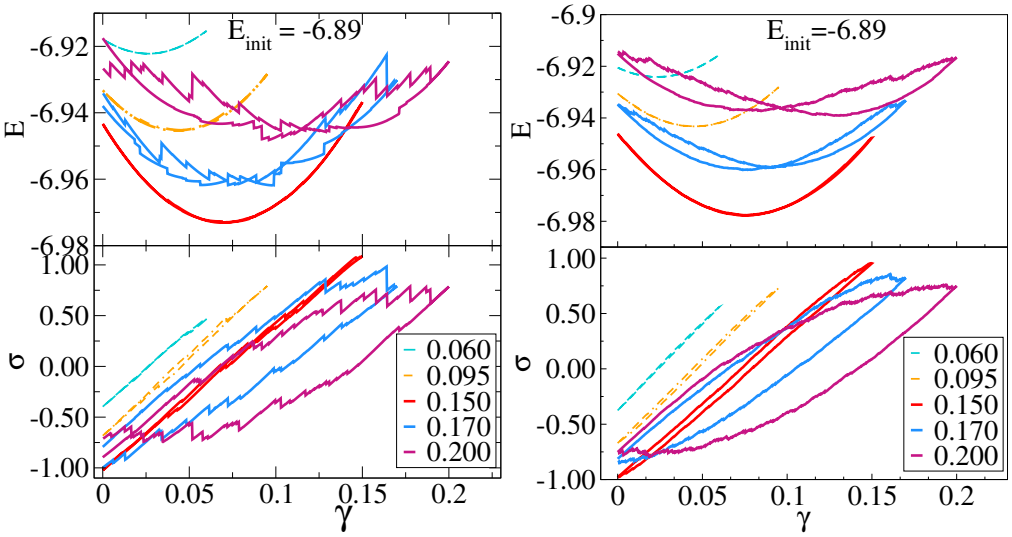

Figure 7.1: Variation of the energy and shear stress through one cycle of strain in the steady state for a glass with initial energy E_{init} is −6.89. Left: Single sample is considered. Bottom: Sample avearged data is shown here. Different curves in each panel correspond to different strain amplitude.

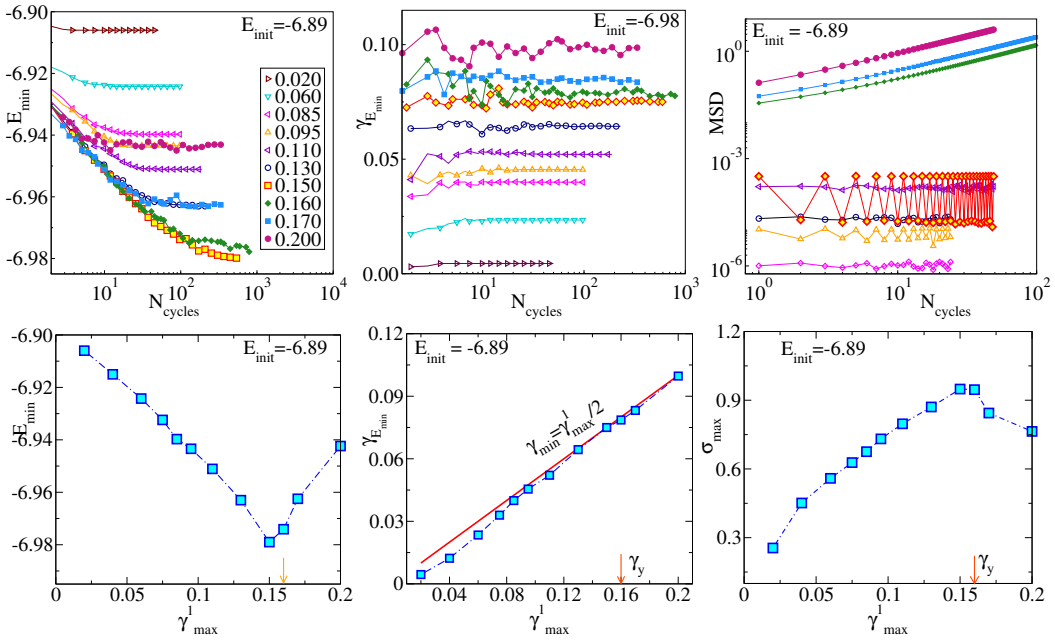

Figure 7.2: The initial energy of this system is $E_{init} = -6.89$. Top left: Evolution of E_{min} is shown as a function of number of shear cycles (N_{cycles}) for different strain amplitude. Top middle: Evolution of $\gamma_{E_{min}}$ is shown as a function of number N_{cycles} for different strain amplitudes. Top right: MSD is plotted as a function of number of cycles for different strain amplitudes. Bottom left: minimum energy (E_{min}) is plotted as a function of γ^1_{max}. Bottom middle: $\gamma_{E_{min}}$ is plotted as a function γ^1_{max}. The red line corresponds to $\gamma_{E_{min}} = 1/2\gamma^1_{max}$. Bottom: σ_{max} is plotted as a function of γ^1_{max}.

7.3.2 Well annealed glass

The picture changes dramatically when we consider well annealed glasses. To show this, we first consider the well annealed case with $E_{\text{init}} = -7.05$. For this case, under symmetric shear [26], no change in energy is observed with $\gamma^{\text{sym}}_{\text{max}}$ whatsoever, until the yield point is reached. In contrast, we see in Fig. 7.3 (a), which shows E_{min} as a function of cycle number N_{cycles} for selected γ^{1}_{max}, that the energy indeed does not change with N_{cycles} for small γ^{1}_{max}, but for $\gamma^{1}_{\text{max}} \geq 0.13$, E_{min} increases with N_{cycles} and saturates at values that grow with γ^{1}_{max}. Interestingly, the strain at which the energy is minimum, $\gamma_{E_{min}}$, reflects the same pattern: $\gamma_{E_{min}}$ remains fixed at 0 for $\gamma^{1}_{\text{max}} < 0.13$, but grows with N_{cycles} as well as γ^{1}_{max} for larger γ^{1}_{max} values. Moreover, the asymptotic $\gamma_{E_{min}} \approx \gamma^{1}_{\text{max}}/2$ is attained only when $\gamma^{1}_{\text{max}} > 0.15$, while for $\gamma^{1}_{\text{max}} = 0.13, 0.15$ intermediate values interpolating between 0 and $\gamma^{1}_{\text{max}}/2$ are observed. Nevertheless, for $\gamma^{1}_{\text{max}} > 0.095$, substantial plastic deformations appear to lead to finite $\gamma_{E_{min}}$ values, even though, as shown in Fig. 7.3 (c), a diffusive, or yielded, state is reached only for $\gamma^{1}_{\text{max}} > 0.15$.

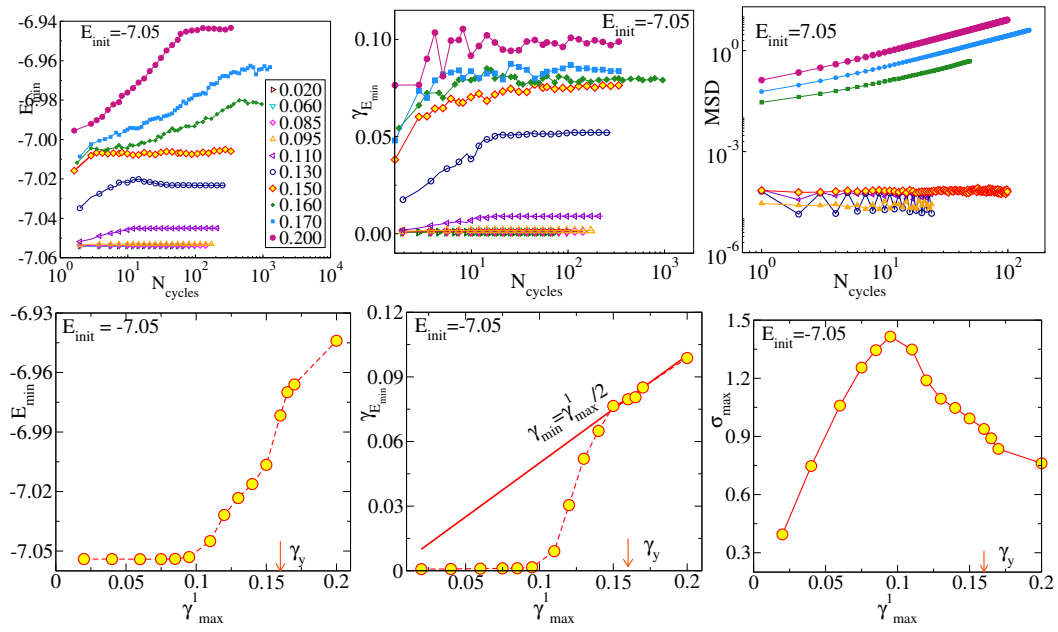

Figure 7.3: The initial energy of this system is $E_{init} = -7.05$. Top left: Evolution of E_{min} is shown as a function of number of cycles for different strain amplitudes. Top middle: Evolution of $\gamma_{E_{min}}$ is shown as a function of number of cycles for different strain amplitudes. Top right: MSD is plotted as a function of number of cycles for different strain amplitudes. Bottom left: The minimum energy (E_{min}) is plotted against γ^{1}_{max}. Bottom middle: $\gamma_{E_{min}}$ is plotted as a function γ^{1}_{max}. The red line corresponds to $\gamma_{E_{min}} = 1/2\gamma^{1}_{max}$. Bottom: σ_{max} is plotted as a function of γ^{1}_{max}.

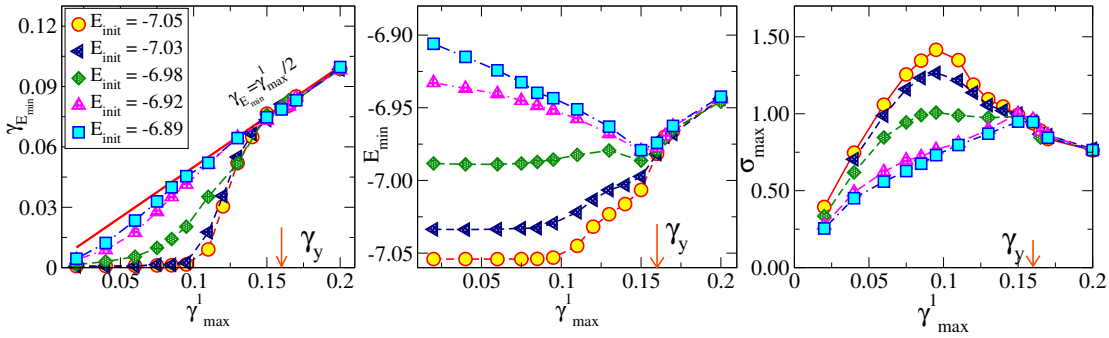

Figure 7.4: Left: $\gamma_{E_{min}}$ as a function of γ^1_{max} for differently annealed samples. Middle: E_{min} as a function of γ^1_{max} for different annealed samples. Right: σ_{max} is plotted as a function of γ^1_{max} for differently annealed samples ($N = 4000$).

7.3.3 Role of annealing

We summaries the results for the full range of annealing of the glasses we consider (with $E_{\text{init}} = -6.89, -6.92, -6.98, -7.03$ and -7.05) in Fig. 7.4. Fig. 7.4 (Left) shows the steady state energies as a function of E_{init} and the strain amplitude γ^1_{max}. For $E_{\text{init}} = -6.89, -6.92$, the variation of the energies is similar to the symmetric case, displaying a non-monotonic change in energy across the yielding amplitude. In sharp contrast, for $E_{\text{init}} = -7.03, -7.05$, the energies remain constant up to values of γ^1_{max} close to the yield amplitudes in the symmetric case ($\gamma y^{\text{sym}} = 0.098, 0.105$ for $E_{\text{init}} = -7.03, -7.05$ respectively [26]), but rise for larger γ^1_{max}, until they reach a value of ≈ -6.985 is reached, which was identified as the *threshold energy* in [26] across which the character of yielding changes in the symmetric case. The intermediate case of $E_{\text{init}} = -6.98$ displays an interesting non-monotonic behaviour. For $\gamma^1_{\text{max}} > 0.15$ the energies for all cases increase along a common curve, and we identify $\gamma^1_y > 0.155 - 0.16$ as the yield value. A rationalisation of these results can be found in the behaviour of the reference strain $\gamma_{E_{min}}$ shown in Fig. 7.3 (Middle). The extent to which $\gamma_{E_{min}} \approx \gamma^1_{\text{max}}/2$ can be seen as indicative of the plastic deformations that that take place before a steady state is reached. Clearly, for $E_{\text{init}} = -7.03, -7.05$, such deformations occur very little until $\gamma^1_{\text{max}} \approx 0.1$, whereas for higher γ^1_{max} the reference strain shifts, along with the energies, until configurations that are stable under the imposed cyclic strain are reached. For higher E_{init}, such reorganizations occur for all γ^1_{max}, to a greater degree for larger E_{init}. Finally, we consider the variation of shear stress σ_{max} evaluated at γ^1_{max}. In Fig. 7.3 (Right) we present the data for σ_{max}. Once again, for $E_{\text{init}} = -6.89, -6.92$, we observe a monotonic increase of σ_{max} before yielding, but for lower E_{init}, we observe a highly unusual *non-monotonic* change of σ_{max}, well before the yield point. The maximum stress values obtained, for $\gamma^1_{\text{max}} \approx 0.1$ are comparable to the yield stress values in the symmetric cyclic shear case [26]. Unlike the symmetric shear case, the location of the stress maximum and the onset of diffusive behaviour do

not coincide for asymmetric shearing of well annealed glasses, as seen in Fig. 7.3(f), (c), with γ_{peak} (location of the stress maximum) < γ_{diff} (onset of the diffusive steady state). These results are surprising in the context of cyclic shear, since previous observations of plasticity before yielding have invariably been associated with annealing (decrease of energy). The new non-trivial ingredient that is brought forth by the asymmetric shear results is dynamics induced by deformation along the *plastic strain* axis.

7.3.4 System size analysis.

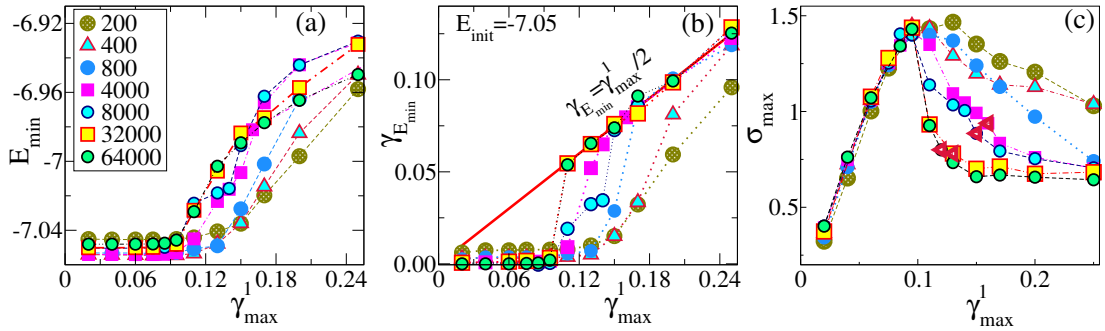

Figure 7.5: System size dependence of E_{min}, $\gamma_{E_{min}}$, σ_{max} for the well annealed system. The red line corresponds to $\gamma_{E_{min}} = 1/2\gamma^1_{max}$.

In order to interrogate better the intermediate regime $\gamma_{\text{peak}} < \gamma^1_{\text{max}} < \gamma_{\text{diff}}$, that emerges for the well-annealed samples, we consider next the effect of system size. In Fig. 7.7 (a) and (b) we plot the behavior of the minimum energy E_{min} and the plastic strain $\gamma_{E_{min}}$ at steady state against γ^1_{max}, for different system sizes, $E_{init} = -7.05$. A strong system size dependence is apparent: the smaller the system size, the larger the strain γ^1_{max} value beyond which $\gamma_{E_{min}} = \gamma^1_{max}/2$. In Fig. 7.7 (c) we show the corresponding evolution for σ_{max}. For system sizes larger than 4000, the stress maximum appears around a common value $\gamma_{\text{peak}} = 0.1$, but the subsequent drop of stress becomes sharper with increasing system size. In Fig. 7.6 we show again the stress at the maximum strain, as a function of the maximum strain γ^1max (Left panel) and the MSD as a function of the number of cycles for different systems sizes of a well-annealed glass with $E_{init} = -7.05$. The left triangle marks the value of the amplitude of asymmetric strain γ_{diff} from which diffusive behavior sets in. The values of γ_{diff} extracted from the MSD vs. N_{cycles} plots are: 0.160, 0.150 0.130 and 0.120 for the system sizes 4000, 8000, 32000 and 64000 respectively. These plots clearly demonstrate that with increasing system sizes the difference between $\gamma_{\text{peak}} = 0.095$ and γ_{diff} decreases. We expect that $\gamma_{\text{diff}} \to \gamma_{\text{peak}}$ as $N \to \infty$. Now we investigate the system size effect of poorly annealed glass. In Fig. 7.7, we show the system size dependence of $\gamma_{E_{min}}$, E_{min}, and σ_{max}, the stress at maximum strain γ^1_{max} for a poorly-annealed glass, $E_{init} = -6.89$, and different system sizes N, indicated in the

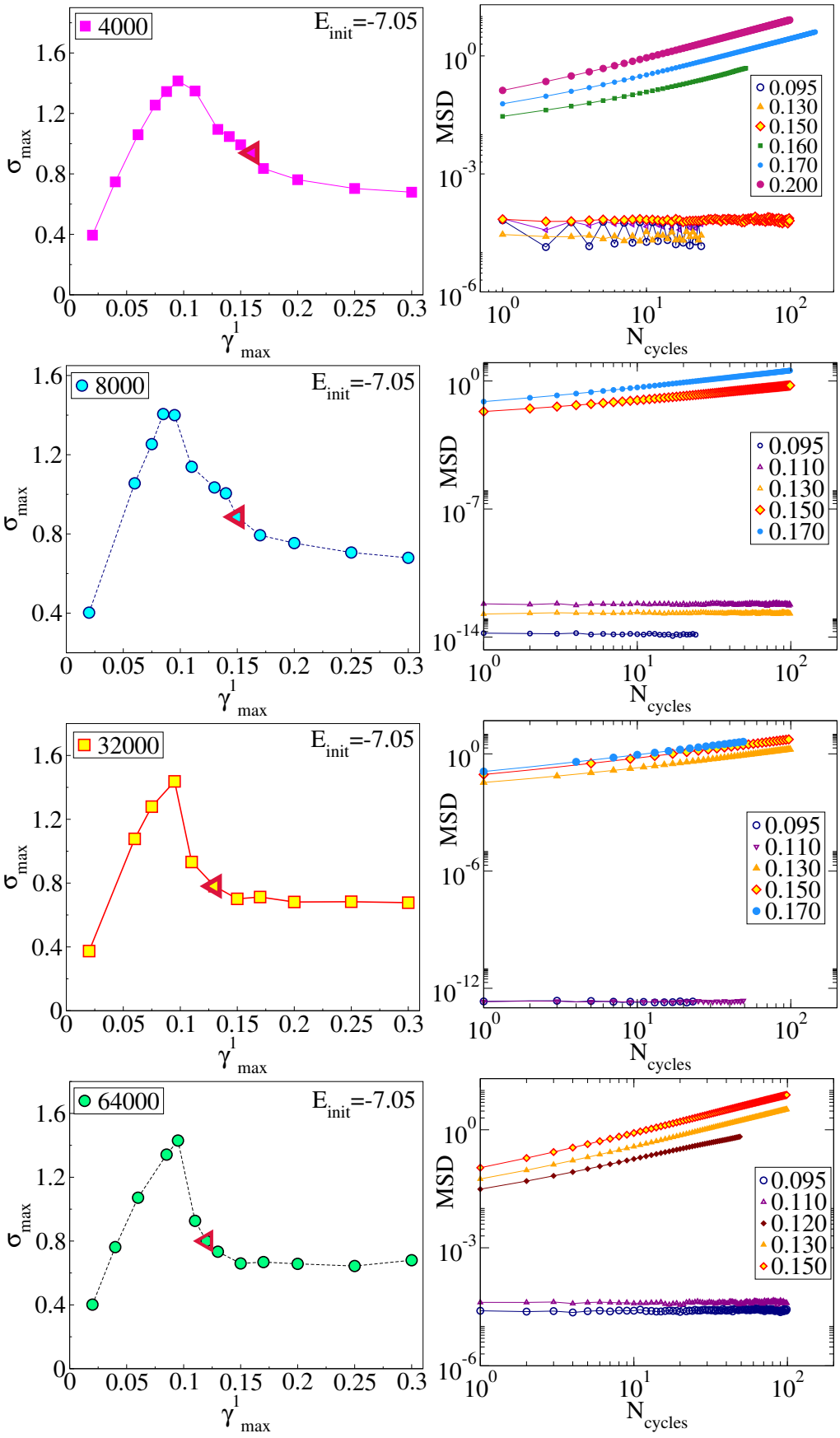

Figure 7.6: Left column: Stress is plotted as a function of γ^1_{max}. Open red triangles correspond to the value of the amplitude of asymmetric strain γ_{diff} beyond which diffusive behavior sets in. Right column: The mean squared displacement (MSD) (at the steady state) is plotted against the number of cycles for different γ^1_{max}.

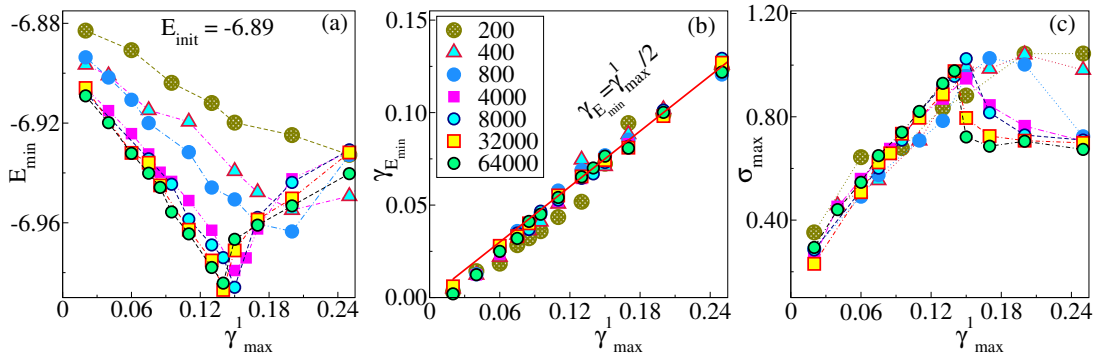

Figure 7.7: (a) - (c): System size dependence of E_{min}, $\gamma_{E_{min}}$, and σ_{max}, for a poorly-annealed system with initial energy $E_{init} = -6.89$. The systems sizes N are indicated in (b). The red line in (b) corresponds to $\gamma_{E_{min}} = \gamma^1_{max}/2$.

legend of (b). (a) For system sizes larger than 4000, $E_{\rm min}$ reaches its lowest value around $\gamma^1_{\rm max} = 0.15$, which we interpret as the yielding amplitude. Note that this is twice the corresponding value for symmetric shear. (b), The behavior of the plastic strain $\gamma_{E_{min}}$ with $\gamma^1_{\rm max}$ has almost no dependence on system size and closely follows the line $\gamma_{E_{\rm min}} = \gamma_{\rm min}/2$. This is in stark contrasting with the response of the well annealed glasses to asymmetric shear shown above. (c) System size dependence of the stress $\sigma_{\rm max}$ at strain $\gamma^1_{\rm max}$. With increasing system size N the strain $\gamma^1_{\rm max}$ at which σ_{max} reaches its maximum moves to $\gamma^1_{\rm max} \approx 0.15$. At the same time, the subsequent stress-drop becomes sharper with increasing N. With increasing system sizes, the yielding amplitude does not change for poorly annealed glass. Whereas there is a significant change for well annealed glass and this leads to the remarkable conclusion that for asymmetric shear, the yield value $\gamma_{\rm diff}$ will be smaller for well annealed glasses compared to poorly annealed glasses, reversing the trend seen for symmetric shear.

7.3.5 Structure of sheared configurations

We next investigate whether the asymmetric nature of the shear protocol has consequences for the anisotropy of structures we generate. A corresponding investigation for symmetric cyclic shear revealed no anisotropies [256]. We compute two dimensional pair correlations functions $g(x,z)$, which are shown in Fig. 7.8 for $E_{\rm init} = -6.89, -7.05$ for $\gamma^1_{\rm max} = 0.13, 0.15$, below the yielding point and for $\gamma^1_{\rm max} = 0.17$ above yielding (shown in Fig. 7.9) . In all cases $g(x,z)$ are found to be symmetric, although the strain protocol is asymmetric.

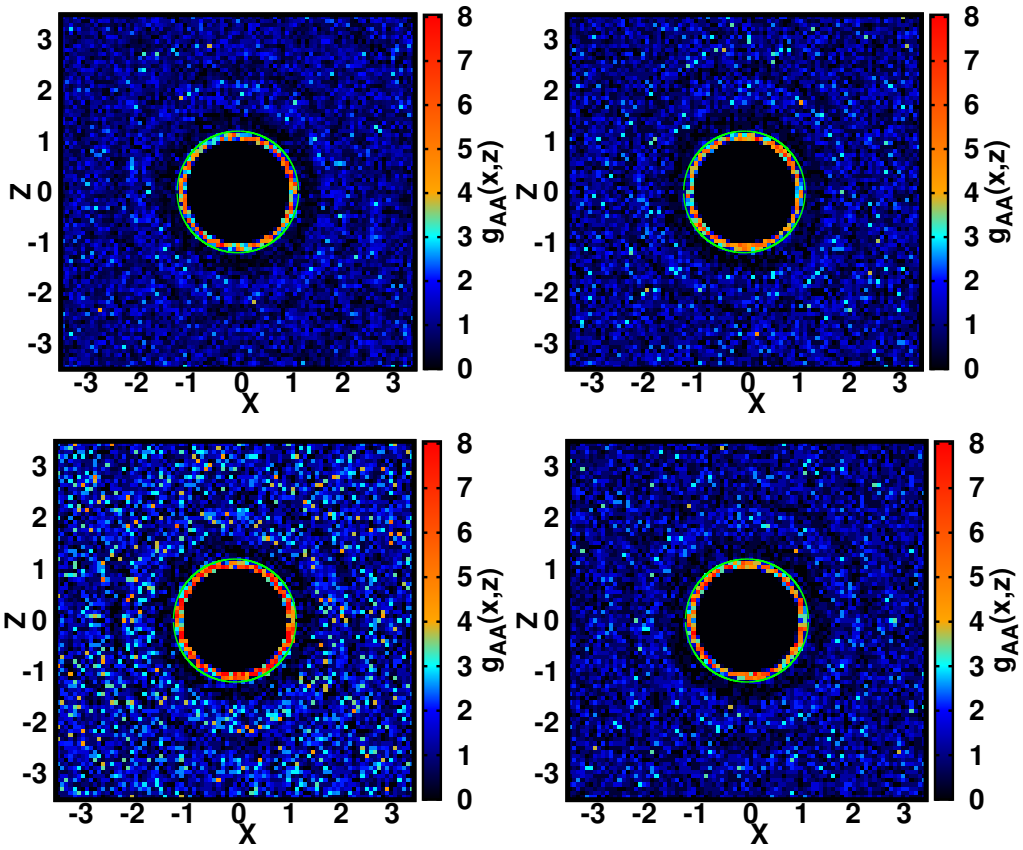

Figure 7.8: The two-dimensional pair correlations (for A particles) $g(x,z)$ for $E_{\text{init}} = -6.89$ (Top panels) and $E_{\text{init}} = -7.05$ (Bottom panels) for different strain amplitudes $\gamma^1_{\text{max}} = 0.13$(left) and 0.15(right).

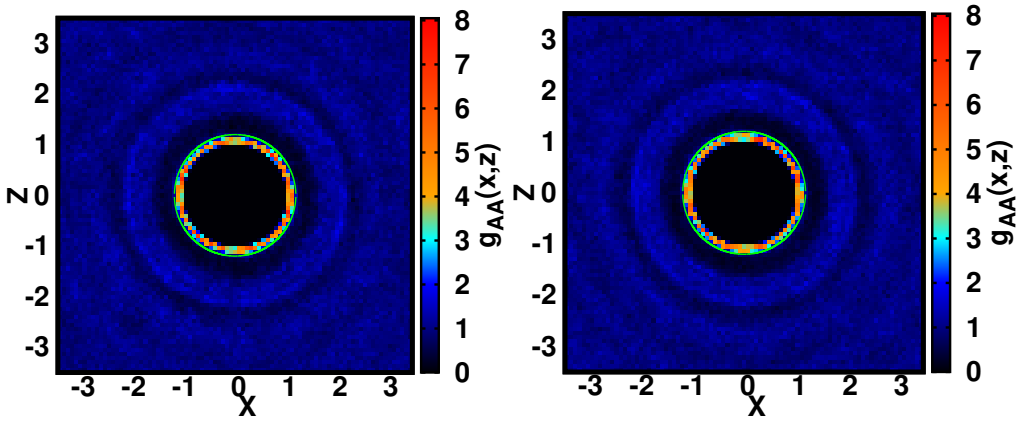

Figure 7.9: The two-dimensional pair correlations (for A particles) $g(x,z)$ for $E_{\text{init}} = -6.89$ (left panel) and -7.05 (right panel), for $\gamma^1_{\text{max}} = 0.17$.

7.4 Discussion

In summary, we have investigated the yielding behaviour of a model amorphous solid under asymmetric cyclic shear deformation. We show that the response of poorly annealed glasses under asymmetric shear deformation is very similar to symmetric shear deformation with yielding amplitude of asymmetric shear deformation is twice of symmetric deformation. However, yielding behaviour for well annealed glasses displays striking new features not observed for symmetric cyclic shear, including the emergence of an intermediate window of strain amplitudes dominated by significant plastic rearrangements and accompanied by a decrease of stress. Such a window is expected to vanish for $N \to \infty$, as our system size results indicate. Nevertheless, our results reveal the central role played by the non-trivial evolution of *plastic strain* in the case of asymmetric cyclic shear, in addition to the evolution of energy, in determining plastic response, which provides insight into the behaviour of deformed glasses in general. Investigating finite size effects leads to the remarkable conclusion that for asymmetric shear, the yield strain amplitude is smaller for well annealed glasses, in a reversal of observations for symmetric shear. Interestingly, the structure of the shear-deformed configurations is isotropic though the nature of the deformation is asymmetric.

Chapter 8

Conclusions

This chapter summarises the main results of this thesis and discusses the questions the work in this thesis raises, which merit further investigations.

The first part of the thesis has been devoted to studying glass formation in spatial dimension $3-8$. In the second part, the mechanical behaviour of glasses, particularly yielding and memory formation, is investigated under cyclic shear deformation.

In chapter 3, we have investigated the dimensional dependence of the glass transition density and the jamming density by studying sphere assemblies as model glass formers in spatial dimensions $3-8$. At low temperatures, the dynamics undergo a crossover from a sub-Arrhenius relaxation process at low density to super-Arrhenius behaviour at higher densities in all the dimensions we considered. Relaxation times are analysed through a scaling function developed by Berthier and Witten to obtain two distinct scaling collapse across ϕ_0, the crossover density. This cross over density, ϕ_0 corresponds to the ideal glass transition density of the hard-sphere. Though this scaling function produces a nice data collapse, it fails to capture the behaviour at ϕ_0 which should be purely Arrhenius. We introduce a new scaling function which makes sure the dynamics is Arrhenius around ϕ_0 and, using the scaling function ϕ_0 is estimated in spatial dimensions $3-8$. Next, the jamming density is estimated with an independent method for spatial dimension $3-8$. ϕ_0 and ϕ_J are close to each other in 3 and 4 dimensions; however, their difference systematically increases for $d > 4$. Remarkably, our estimated ϕ_0 qualitatively matches with the theoretical prediction where finite dimensions were considered [94]. However, ϕ_J underestimates the theoretical predictions of [94]. But recent improved theoretical calculations show that ϕ_J values computed in [94] can not produce the correct value, and our result also confirms that observation. Thus, our results provide a crucial benchmark for the future development of quantitative theories of the glass and jamming transitions.

In an attempt to understand what the density ϕ_0 corresponds to, we have computed ϕ_{nr}, the density at which the fraction of rattler goes to zero. However, we find that ϕ_{nr}

is much larger than ϕ_0. In the future, it will be interesting to find out any structural measures to distinguish the sub-Arrhenius regime from the super Arrhenius regime, which will help to clarify the special nature of the density, ϕ_0. It could also be interesting to check whether this crossover of dynamics can be captured in Mode coupling theory.

In chapter 4, we have investigated the relationship between the heterogeneity in the dynamics, the breakdown of the Stokes-Einstein relation and fragility in higher spatial dimensions. So far, glasses are studied in higher spatial dimensions using hard particles as a model glass where density is the control parameter. However, for a large number of liquids, the temperature is the control parameter to obtain glass. Thus, we study soft sphere assemblies as a model glass former which permits both density and temperature as a control parameter. Our main finding is that at a fixed scaled density, the degree of heterogeneity, fragility and the degree of breakdown of Stokes-Einstein relation decreases with increasing dimension. We show that fragilities decrease with density at all spatial dimensions, approaching Arrhenius behaviour close to the jamming density. This result helps us to resolve the apparent contradiction with previous results where it was found that fragility increases with heterogeneity [64]. In chapter 5, we have investigated the relationship, between different components, of the diffusivity and the relaxation time for the same model glass former. Our results show that for $3d$ the diffusivity or the relaxation time of different components shows a single power law relation. However, for 4d or higher spatial dimensions, two different power law regimes are observed with different exponents for different temperature ranges. For all the dimensions, the exponents in the higher temperature regime are always smaller than the exponents in the lower temperature regime. Both the exponents (for the high temperature and the low temperature ranges) increase with increasing dimensions. We have also investigated the Adam-Gibbs relation for spatial dimension $3-8$, and our initial results show that the Adam-Gibbs relation is not valid at 4d or higher spatial dimensions. However, one caveat is that the vibrational entropy has been computed using the harmonic approximation, which needs to be justified to reach any definite conclusions regarding the validity of the AG relation.

Investigating the cause of the observed violation of the single power law relation between the component diffusivities, and its implication to the Adam-Gibbs relation, could be an interesting direction of future study. In particular, a theoretical understanding of the violation of the single power law will be useful.

In chapter 6, we have performed numerical investigations of memory behaviour in two model systems, the Kob-Andersen binary mixture (BMLJ) and a soft sphere mixture. In the former case, our results extend the earlier observations of encoding and retrieving the memory of an amplitude of deformation by considering different read protocols and measurements. Our results show that single and multiple memories can

be robustly retrieved through these different protocols. We also show that shear deformation by a larger amplitude always erases the stored memories. For the soft sphere model, we identify a regime where the signatures of memory encoding are similar to the model glass, even when transitions between local energy minima are absent. Thus, our results offer a detailed characterisation of memory effects observed in different model systems.

We have studied memory behaviour using Athermal Quasi-Static (AQS) shear. Thus it would be interesting to check the robustness of this memory at finite temperature and finite shear rate. Understanding the observed memory behaviour through representations as mesoscopic models will be an exciting question to answer in the future.

In chapter 7, we have investigated the yielding behaviour of the Kob-Andersen binary mixture (BMLJ) under the asymmetric shear deformation protocol wherein the applied strain is cyclically varied between 0 and a maximum value γ_{max}. Recent studies have shown that yielding behaviour is very different for well annealed glasses compared to poorly annealed glass. For well annealed glass, the energy of the system does not change with deformation amplitude under symmetric cyclic shear until the yielding amplitude is reached and thus, there is no change of structure, whereas poorly annealed glasses display significant mechanically induced annealing below the yielding amplitude and thus show a significant change of structure. Therefore, one could ask that the choice of γ_{min} and γ_{max} over which cyclic shear deformation is applied can change the plasticity and, consequently, the yielding behaviour? With this question in mind, we study yielding behaviour under asymmetric cyclic shear and investigate what role annealing plays in this kind of protocol. We have observed that depending on the degree of annealing of the initial glass, two strikingly different regimes of behaviour similar to that in the case of symmetric shear deformation emerge. However, in an intermediate strain window, substantial plasticity emerges before yielding for well annealed glasses. These results thus reveal the central role of the *reference strain* that evolves with applied strain amplitudes in a non-trivial way in the regime below yielding. However, finite-size analysis shows that this intermediate window decreases with increasing system size and thus leads to a remarkable conclusion that for asymmetric shear, the yield strain amplitude is smaller for well annealed glasses, in a reversal of observations for symmetric shear.

We have studied here fragile glass former; however other studies on strong glass former also show similar behavior of yielding when symmetric cyclic shear deformation is applied. But does fragility play any role for yielding behavior that is not very clear? Thus, the role of fragility in yielding behavior is an interesting question which could be investigated carefully in future.

List of publications

1. Memory formation in cyclically deformed amorphous solids and sphere assemblies, Monoj Adhikari and Srikanth Sastry, The European Physical Journal E 41, 9 (2018), 105.

2. Spatial Dimensionality Dependence of Heterogeneity, Breakdown of the Stokes-Einstein Relation and Fragility of a Model Glass-Forming Liquid,Monoj Adhikari, Smarajit Karmakar, and Srikanth Sastry, Submitted to JPCB

3. Relationship between glass transition and jamming densities of sphere assemblies across spatial dimensions, Monoj Adhikari, Smarajit Karmakar, and Srikanth Sastry, under revision

4. Yielding behavior of glasses under asymmetric cyclic deformation, Monoj Adhikari,Muhittin Mungan and Srikanth Sastry, under revision

Bibliography

[1] R. J. Brook, *Concise encyclopedia of advanced ceramic materials*. Elsevier, 2012.

[2] K. Müller, M. Takashige, and J. Bednorz, "Flux trapping and superconductive glass state in la 2 cuo 4- y: Ba," *Physical review letters*, vol. 58, no. 11, p. 1143, 1987.

[3] M. Mézard, G. Parisi, and M. A. Virasoro, *Spin glass theory and beyond: An Introduction to the Replica Method and Its Applications*, vol. 9. World Scientific Publishing Company, 1987.

[4] A. P. Young, *Spin glasses and random fields*, vol. 12. World Scientific, 1998.

[5] P. N. Pusey and W. Van Megen, "Phase behaviour of concentrated suspensions of nearly hard colloidal spheres," *Nature*, vol. 320, no. 6060, pp. 340–342, 1986.

[6] H. M. Jaeger, S. R. Nagel, and R. P. Behringer, "Granular solids, liquids, and gases," *Reviews of modern physics*, vol. 68, no. 4, p. 1259, 1996.

[7] J. Goyon, A. Colin, G. Ovarlez, A. Ajdari, and L. Bocquet, "Spatial cooperativity in soft glassy flows," *Nature*, vol. 454, no. 7200, pp. 84–87, 2008.

[8] I. Iben, D. Braunstein, W. Doster, H. Frauenfelder, M. Hong, J. Johnson, S. Luck, P. Ormos, A. Schulte, P. Steinbach, *et al.*, "Glassy behavior of a protein," *Physical review letters*, vol. 62, no. 16, p. 1916, 1989.

[9] R. Zallen, *The physics of amorphous solids*. John Wiley & Sons, 2008.

[10] E. Le Bourhis, *Glass: mechanics and technology*. John Wiley & Sons, 2014.

[11] J. Schroers, "Bulk metallic glasses," *Physics today*, vol. 66, no. 2, p. 32, 2013.

[12] A. Feltz, *Amorphous inorganic materials and glasses*. VCH, 1993.

[13] P. Lundquist, R. Wortmann, C. Geletneky, R. Twieg, M. Jurich, V. Lee, C. Moylan, and D. Burland, "Organic glasses: a new class of photorefractive materials," *Science*, vol. 274, no. 5290, pp. 1182–1185, 1996.

[14] C. A. Angell, "Formation of glasses from liquids and biopolymers," *Science*, vol. 267, no. 5206, pp. 1924–1935, 1995.

[15] D. Turnbull, "Under what conditions can a glass be formed?," *Contemporary physics*, vol. 10, no. 5, pp. 473–488, 1969.

[16] J. C. Dyre, "Colloquium: The glass transition and elastic models of glass-forming liquids," *Reviews of modern physics*, vol. 78, no. 3, p. 953, 2006.

[17] G. Tarjus, D. Kivelson, S. Mossa, and C. Alba-Simionesco, "Disentangling density and temperature effects in the viscous slowing down of glassforming liquids," *The Journal of chemical physics*, vol. 120, no. 13, pp. 6135–6141, 2004.

[18] G. Floudas, K. Mpoukouvalas, and P. Papadopoulos, "The role of temperature and density on the glass-transition dynamics of glass formers," *The Journal of chemical physics*, vol. 124, no. 7, p. 074905, 2006.

[19] C. A. Angell, "Structural instability and relaxation in liquid and glassy phases near the fragile liquid limit," *Journal of non-crystalline solids*, vol. 102, no. 1-3, pp. 205–221, 1988.

[20] A. Cavagna, "Supercooled liquids for pedestrians," *Physics Reports*, vol. 476, no. 4-6, pp. 51–124, 2009.

[21] S. F. Swallen, K. L. Kearns, M. K. Mapes, Y. S. Kim, R. J. McMahon, M. D. Ediger, T. Wu, L. Yu, and S. Satija, "Organic glasses with exceptional thermodynamic and kinetic stability," *Science*, vol. 315, no. 5810, pp. 353–356, 2007.

[22] M. D. Ediger, "Perspective: Highly stable vapor-deposited glasses," *The Journal of chemical physics*, vol. 147, no. 21, p. 210901, 2017.

[23] L. Zhu, C. Brian, S. Swallen, P. Straus, M. Ediger, and L. Yu, "Surface self-diffusion of an organic glass," *Physical Review Letters*, vol. 106, no. 25, p. 256103, 2011.

[24] S. Mirigian and K. S. Schweizer, "Theory of activated glassy relaxation, mobility gradients, surface diffusion, and vitrification in free standing thin films," *The Journal of chemical physics*, vol. 143, no. 24, p. 244705, 2015.

[25] W.-T. Yeh, M. Ozawa, K. Miyazaki, T. Kawasaki, and L. Berthier, "Glass stability changes the nature of yielding under oscillatory shear," *Physical review letters*, vol. 124, no. 22, p. 225502, 2020.

[26] H. Bhaumik, G. Foffi, and S. Sastry, "The role of annealing in determining the yielding behavior of glasses under cyclic shear deformation," *Proceedings of the National Academy of Sciences*, vol. 118, no. 16, 2021.

[27] T. S. Grigera and G. Parisi, "Fast monte carlo algorithm for supercooled soft spheres," *Physical Review E*, vol. 63, no. 4, p. 045102, 2001.

[28] L. Berthier, P. Charbonneau, and J. Kundu, "Bypassing sluggishness: Swap algorithm and glassiness in high dimensions," *Physical Review E*, vol. 99, no. 3, p. 031301, 2019.

[29] A. D. Parmar, M. Ozawa, and L. Berthier, "Ultrastable metallic glasses in silico," *Physical Review Letters*, vol. 125, no. 8, p. 085505, 2020.

[30] P. G. Debenedetti and F. H. Stillinger, "Supercooled liquids and the glass transition," *Nature*, vol. 410, no. 6825, pp. 259–267, 2001.

[31] J. Phillips, "Stretched exponential relaxation in molecular and electronic glasses," *Reports on Progress in Physics*, vol. 59, no. 9, p. 1133, 1996.

[32] F. Alvarez, A. Alegra, and J. Colmenero, "Relationship between the time-domain kohlrausch-williams-watts and frequency-domain havriliak-negami relaxation functions," *Physical Review B*, vol. 44, no. 14, p. 7306, 1991.

[33] L. Pardo, P. Lunkenheimer, and A. Loidl, "Dielectric spectroscopy in benzophenone: The β relaxation and its relation to the mode-coupling cole-cole peak," *Physical Review E*, vol. 76, no. 3, p. 030502, 2007.

[34] H. Vogel, "Das temperaturabhaЀĺngigkeitsgesetz der viskositaЀĺt von fluЀĺssigkeiten," *Phys. Z.*, vol. 22, pp. 645–646, 1921.

[35] G. Tammann and W. Hesse, "Die abhängigkeit der viscosität von der temperatur bie unterkühlten flüssigkeiten," *Zeitschrift für anorganische und allgemeine Chemie*, vol. 156, no. 1, pp. 245–257, 1926.

[36] F. Stickel, E. W. Fischer, and R. Richert, "Dynamics of glass-forming liquids. i. temperature-derivative analysis of dielectric relaxation data," *The Journal of chemical physics*, vol. 102, no. 15, pp. 6251–6257, 1995.

[37] D. Kivelson, G. Tarjus, X. Zhao, and S. A. Kivelson, "Fitting of viscosity: Distinguishing the temperature dependences predicted by various models of supercooled liquids," *Physical Review E*, vol. 53, no. 1, p. 751, 1996.

[38] W. Laughlin and D. R. Uhlmann, "Viscous flow in simple organic liquids," *The Journal of Physical Chemistry*, vol. 76, no. 16, pp. 2317–2325, 1972.

[39] S. Sastry, "The relationship between fragility, configurational entropy and the potential energy landscape of glass-forming liquids," *Nature*, vol. 409, no. 6817, p. 164, 2001.

[40] L.-M. Martinez and C. Angell, "A thermodynamic connection to the fragility of glass-forming liquids," *Nature*, vol. 410, no. 6829, pp. 663–667, 2001.

[41] V. Novikov, Y. Ding, and A. Sokolov, "Correlation of fragility of supercooled liquids with elastic properties of glasses," *Physical Review E*, vol. 71, no. 6, p. 061501, 2005.

[42] M. D. Ediger, "Spatially heterogeneous dynamics in supercooled liquids," *Annual review of physical chemistry*, vol. 51, no. 1, pp. 99–128, 2000.

[43] L. Berthier, G. Biroli, J.-P. Bouchaud, L. Cipelletti, and W. van Saarloos, *Dynamical heterogeneities in glasses, colloids, and granular media*, vol. 150. OUP Oxford, 2011.

[44] C. Dasgupta, A. Indrani, S. Ramaswamy, and M. Phani, "Is there a growing correlation length near the glass transition?," *EPL (Europhysics Letters)*, vol. 15, no. 3, p. 307, 1991.

[45] S. Capaccioli, G. Ruocco, and F. Zamponi, "Dynamically correlated regions and configurational entropy in supercooled liquids," *The Journal of Physical Chemistry B*, vol. 112, no. 34, pp. 10652–10658, 2008.

[46] S. Karmakar, C. Dasgupta, and S. Sastry, "Growing length and time scales in glass-forming liquids," *Proceedings of the National Academy of Sciences*, vol. 106, no. 10, pp. 3675–3679, 2009.

[47] S. Karmakar, C. Dasgupta, and S. Sastry, "Growing length scales and their relation to timescales in glass-forming liquids," *Annu. Rev. Condens. Matter Phys.*, vol. 5, no. 1, pp. 255–284, 2014.

[48] W. Kob, C. Donati, S. J. Plimpton, P. H. Poole, and S. C. Glotzer, "Dynamical heterogeneities in a supercooled lennard-jones liquid," *Physical review letters*, vol. 79, no. 15, p. 2827, 1997.

[49] P. Chaudhuri, L. Berthier, and W. Kob, "Universal nature of particle displacements close to glass and jamming transitions," *Physical review letters*, vol. 99, no. 6, p. 060604, 2007.

[50] R. Böhmer, K. Ngai, C. A. Angell, and D. Plazek, "Nonexponential relaxations in strong and fragile glass formers," *The Journal of chemical physics*, vol. 99, no. 5, pp. 4201–4209, 1993.

[51] A. Heuer, "Exploring the potential energy landscape of glass-forming systems: from inherent structures via metabasins to macroscopic transport," *Journal of Physics: Condensed Matter*, vol. 20, no. 37, p. 373101, 2008.

[52] J. C. Dyre, "Ten themes of viscous liquid dynamics," *Journal of Physics: Condensed Matter*, vol. 19, no. 20, p. 205105, 2007.

[53] L. Wang, N. Xu, W. Wang, and P. Guan, "Revealing the link between structural relaxation and dynamic heterogeneity in glass-forming liquids," *Physical review letters*, vol. 120, no. 12, p. 125502, 2018.

[54] D. Pan and Z.-Y. Sun, "Influence of chain stiffness on the dynamical heterogeneity and fragility of polymer melts," *The Journal of chemical physics*, vol. 149, no. 23, p. 234904, 2018.

[55] E. R. Weeks, J. C. Crocker, A. C. Levitt, A. Schofield, and D. A. Weitz, "Three-dimensional direct imaging of structural relaxation near the colloidal glass transition," *Science*, vol. 287, no. 5453, pp. 627–631, 2000.

[56] L. Berthier and G. Biroli, "Theoretical perspective on the glass transition and amorphous materials," *Reviews of Modern Physics*, vol. 83, no. 2, p. 587, 2011.

[57] I. Gartshore, "Fluid mechanics: second english edition (vol. 6 of the course of theoretical physics by the same authors.) ld landau and em lifshitz pergamon press, 1987," 1989.

[58] J. A. Hodgdon and F. H. Stillinger, "Stokes-einstein violation in glass-forming liquids," *Physical Review E*, vol. 48, no. 1, p. 207, 1993.

[59] M. T. Cicerone and M. D. Ediger, "Enhanced translation of probe molecules in supercooled o-terphenyl: Signature of spatially heterogeneous dynamics?," *The Journal of chemical physics*, vol. 104, no. 18, pp. 7210–7218, 1996.

[60] I. Chang and H. Sillescu, "Heterogeneity at the glass transition: Translational and rotational self-diffusion," *The Journal of Physical Chemistry B*, vol. 101, no. 43, pp. 8794–8801, 1997.

[61] T. R. Kirkpatrick and D. Thirumalai, "Comparison between dynamical theories and metastable states in regular and glassy mean-field spin models with underlying first-order-like phase transitions," *Physical Review A*, vol. 37, no. 11, p. 4439, 1988.

[62] S. C. Glotzer, V. N. Novikov, and T. B. Schrøder, "Time-dependent, four-point density correlation function description of dynamical heterogeneity and decoupling in supercooled liquids," *The Journal of Chemical Physics*, vol. 112, no. 2, pp. 509–512, 2000.

[63] T. Kawasaki and H. Tanaka, "Apparent violation of the fluctuation-dissipation theorem due to dynamic heterogeneity in a model glass-forming liquid," *Physical review letters*, vol. 102, no. 18, p. 185701, 2009.

[64] S. Sengupta, S. Karmakar, C. Dasgupta, and S. Sastry, "Breakdown of the stokes-einstein relation in two, three, and four dimensions," *The Journal of chemical physics*, vol. 138, no. 12, p. 12A548, 2013.

[65] S. K. Kumar, G. Szamel, and J. F. Douglas, "Nature of the breakdown in the stokes-einstein relationship in a hard sphere fluid," *The Journal of chemical physics*, vol. 124, no. 21, p. 214501, 2006.

[66] S. Sengupta and S. Karmakar, "Distribution of diffusion constants and stokes-einstein violation in supercooled liquids," *The Journal of chemical physics*, vol. 140, no. 22, p. 224505, 2014.

[67] R. Pastore, A. Coniglio, and M. P. Ciamarra, "Dynamic phase coexistence in glass–forming liquids," *Scientific reports*, vol. 5, no. 1, pp. 1–10, 2015.

[68] S. R. Becker, P. H. Poole, and F. W. Starr, "Fractional stokes-einstein and debye-stokes-einstein relations in a network-forming liquid," *Physical review letters*, vol. 97, no. 5, p. 055901, 2006.

[69] S. Pan, Z. Wu, W. Wang, M. Li, and L. Xu, "Structural origin of fractional stokes-einstein relation in glass-forming liquids," *Scientific reports*, vol. 7, no. 1, pp. 1–9, 2017.

[70] B. Charbonneau, P. Charbonneau, Y. Jin, G. Parisi, and F. Zamponi, "Dimensional dependence of the stokes–einstein relation and its violation," *The Journal of chemical physics*, vol. 139, no. 16, p. 164502, 2013.

[71] T. B. Schrøder, S. Sastry, J. C. Dyre, and S. C. Glotzer, "Crossover to potential energy landscape dominated dynamics in a model glass-forming liquid," *The Journal of Chemical Physics*, vol. 112, no. 22, pp. 9834–9840, 2000.

[72] A. Banerjee, S. Sengupta, S. Sastry, and S. M. Bhattacharyya, "Role of structure and entropy in determining differences in dynamics for glass formers with different interaction potentials," *Phys. Rev. Lett.*, vol. 113, p. 225701, Nov 2014.

[73] W. Kauzmann, "The nature of the glassy state and the behavior of liquids at low temperatures.," *Chemical reviews*, vol. 43, no. 2, pp. 219–256, 1948.

[74] C. Cammarota and G. Biroli, "Ideal glass transitions by random pinning," *Proceedings of the National Academy of Sciences*, vol. 109, no. 23, pp. 8850–8855, 2012.

[75] W. Kob and L. Berthier, "Probing a liquid to glass transition in equilibrium," *Physical review letters*, vol. 110, no. 24, p. 245702, 2013.

[76] M. Ozawa, W. Kob, A. Ikeda, and K. Miyazaki, "Equilibrium phase diagram of a randomly pinned glass-former," *Proceedings of the National Academy of Sciences*, vol. 112, no. 22, pp. 6914–6919, 2015.

[77] M. Ozawa, A. Ikeda, K. Miyazaki, and W. Kob, "Ideal glass states are not purely vibrational: Insight from randomly pinned glasses," *Physical review letters*, vol. 121, no. 20, p. 205501, 2018.

[78] S. Chakrabarty, S. Karmakar, and C. Dasgupta, "Dynamics of glass forming liquids with randomly pinned particles," *Scientific reports*, vol. 5, no. 1, pp. 1–10, 2015.

[79] G. Adam and J. H. Gibbs, "On the temperature dependence of cooperative relaxation properties in glass-forming liquids," *The journal of chemical physics*, vol. 43, no. 1, pp. 139–146, 1965.

[80] J. H. Gibbs and E. A. DiMarzio, "Nature of the glass transition and the glassy state," *The Journal of Chemical Physics*, vol. 28, no. 3, pp. 373–383, 1958.

[81] S. Sastry, "Evaluation of the configurational entropy of a model liquid from computer simulations," *Journal of Physics: Condensed Matter*, vol. 12, no. 29, p. 6515, 2000.

[82] M. Goldstein, "Viscous liquids and the glass transition: a potential energy barrier picture," *The Journal of Chemical Physics*, vol. 51, no. 9, pp. 3728–3739, 1969.

[83] F. H. Stillinger and T. A. Weber, "Hidden structure in liquids," *Physical Review A*, vol. 25, no. 2, p. 978, 1982.

[84] R. Richert and C. Angell, "Dynamics of glass-forming liquids. v. on the link between molecular dynamics and configurational entropy," *The Journal of chemical physics*, vol. 108, no. 21, pp. 9016–9026, 1998.

[85] J. C. Dyre, T. Hechsher, and K. Niss, "A brief critique of the adam–gibbs entropy model," *Journal of Non-Crystalline Solids*, vol. 355, no. 10-12, pp. 624–627, 2009.

[86] A. Ikeda and K. Miyazaki, "Mode-coupling theory as a mean-field description of the glass transition," *Physical review letters*, vol. 104, no. 25, p. 255704, 2010.

[87] B. Schmid and R. Schilling, "Glass transition of hard spheres in high dimensions," *Physical Review E*, vol. 81, no. 4, p. 041502, 2010.

[88] C. Rainone, P. Urbani, H. Yoshino, and F. Zamponi, "Following the evolution of hard sphere glasses in infinite dimensions under external perturbations: Compression and shear strain," *Physical review letters*, vol. 114, no. 1, p. 015701, 2015.

[89] C. Rainone and P. Urbani, "Following the evolution of glassy states under external perturbations: The full replica symmetry breaking solution," *Journal of Statistical Mechanics: Theory and Experiment*, vol. 2016, no. 5, p. 053302, 2016.

[90] T. Maimbourg, J. Kurchan, and F. Zamponi, "Solution of the dynamics of liquids in the large-dimensional limit," *Physical review letters*, vol. 116, no. 1, p. 015902, 2016.

[91] P. Charbonneau, J. Kurchan, G. Parisi, P. Urbani, and F. Zamponi, "Fractal free energy landscapes in structural glasses," *Nature communications*, vol. 5, p. 3725, 2014.

[92] P. Charbonneau, J. Kurchan, G. Parisi, P. Urbani, and F. Zamponi, "Glass and jamming transitions: From exact results to finite-dimensional descriptions," *Annual Review of Condensed Matter Physics*, vol. 8, pp. 265–288, 2017.

[93] L. Berthier, P. Charbonneau, Y. Jin, G. Parisi, B. Seoane, and F. Zamponi, "Growing timescales and lengthscales characterizing vibrations of amorphous solids," *Proceedings of the National Academy of Sciences*, vol. 113, no. 30, pp. 8397–8401, 2016.

[94] M. Mangeat and F. Zamponi, "Quantitative approximation schemes for glasses," *Physical Review E*, vol. 93, no. 1, p. 012609, 2016.

[95] J. D. Bernal, "A geometrical approach to the structure of liquids," *Nature*, vol. 183, no. 4655, pp. 141–147, 1959.

[96] A. J. Liu and S. R. Nagel, "The jamming transition and the marginally jammed solid," *Annu. Rev. Condens. Matter Phys.*, vol. 1, no. 1, pp. 347–369, 2010.

[97] P. Chaudhuri, L. Berthier, and S. Sastry, "Jamming transitions in amorphous packings of frictionless spheres occur over a continuous range of volume fractions," *Physical review letters*, vol. 104, no. 16, p. 165701, 2010.

[98] D. Bonn, M. M. Denn, L. Berthier, T. Divoux, and S. Manneville, "Yield stress materials in soft condensed matter," *Reviews of Modern Physics*, vol. 89, no. 3, p. 035005, 2017.

[99] F. Krzakala and J. Kurchan, "Landscape analysis of constraint satisfaction problems," *Physical Review E*, vol. 76, no. 2, p. 021122, 2007.

[100] H. Jacquin, L. Berthier, and F. Zamponi, "Microscopic mean-field theory of the jamming transition," *Physical review letters*, vol. 106, no. 13, p. 135702, 2011.

[101] M. Dinkgreve, M. Michels, T. Mason, and D. Bonn, "Crossover between athermal jamming and the thermal glass transition of suspensions," *Physical review letters*, vol. 121, no. 22, p. 228001, 2018.

[102] A. Ikeda, L. Berthier, and P. Sollich, "Unified study of glass and jamming rheology in soft particle systems," *Physical review letters*, vol. 109, no. 1, p. 018301, 2012.

[103] A. Ikeda, L. Berthier, and P. Sollich, "Disentangling glass and jamming physics in the rheology of soft materials," *Soft Matter*, vol. 9, no. 32, pp. 7669–7683, 2013.

[104] L. Berthier, D. Coslovich, A. Ninarello, and M. Ozawa, "Equilibrium sampling of hard spheres up to the jamming density and beyond," *Physical review letters*, vol. 116, no. 23, p. 238002, 2016.

[105] R. Mari, F. Krzakala, and J. Kurchan, "Jamming versus glass transitions," *Physical review letters*, vol. 103, no. 2, p. 025701, 2009.

[106] M. P. Ciamarra, M. Nicodemi, and A. Coniglio, "Recent results on the jamming phase diagram," *Soft Matter*, vol. 6, no. 13, pp. 2871–2874, 2010.

[107] J. Kurchan, G. Parisi, P. Urbani, and F. Zamponi, "Exact theory of dense amorphous hard spheres in high dimension. ii. the high density regime and the gardner transition," *The Journal of Physical Chemistry B*, vol. 117, no. 42, pp. 12979–12994, 2013.

[108] A. Coniglio, M. P. Ciamarra, and T. Aste, "Universal behaviour of the glass and the jamming transitions in finite dimensions for hard spheres," *Soft matter*, vol. 13, no. 46, pp. 8766–8771, 2017.

[109] W. Kob and J.-L. Barrat, "Aging effects in a lennard-jones glass," *Physical review letters*, vol. 78, no. 24, p. 4581, 1997.

[110] N. C. Keim, J. D. Paulsen, Z. Zeravcic, S. Sastry, and S. R. Nagel, "Memory formation in matter," *Reviews of Modern Physics*, vol. 91, no. 3, p. 035002, 2019.

[111] M. P. Lilly, P. T. Finley, and R. B. Hallock, "Memory, congruence, and avalanche events in hysteretic capillary condensation," *Phys. Rev. Lett.*, vol. 71, pp. 4186–4189, Dec 1993.

[112] K. Bhattacharya, *Microstructure of martensite: why it forms and how it gives rise to the shape-memory effect*, vol. 2. Oxford University Press, 2003.

[113] I. Gilbert, G.-W. Chern, B. Fore, Y. Lao, S. Zhang, C. Nisoli, and P. Schiffer, "Direct visualization of memory effects in artificial spin ice," *Phys. Rev. B*, vol. 92, p. 104417, Sep 2015.

[114] M. Dobroka, Y. Kawamura, K. Ienaga, S. Kaneko, and S. Okuma, "Memory formation and evolution of the vortex configuration associated with random organization," *New Journal of Physics*, vol. 19, no. 5, p. 053023, 2017.

[115] Y. Lahini, O. Gottesman, A. Amir, and S. M. Rubinstein, "Nonmonotonic aging and memory retention in disordered mechanical systems," *Phys. Rev. Lett.*, vol. 118, p. 085501, Feb 2017.

[116] J. Gill, "Transient non-linear phenomena and metastable states of charge-density waves in niobium triselenide," *Solid State Communications*, vol. 39, no. 11, pp. 1203–1208, 1981.

[117] R. Fleming and L. Schneemeyer, "Transient electrical response of k 0.30 mo o 3," *Physical Review B*, vol. 28, no. 12, p. 6996, 1983.

[118] A. J. Kovacs, "Transition vitreuse dans les polymères amorphes. etude phénoménologique," in *Fortschritte der hochpolymeren-forschung*, pp. 394–507, Springer, 1964.

[119] S. Mossa and F. Sciortino, "Crossover (or kovacs) effect in an aging molecular liquid," *Physical review letters*, vol. 92, no. 4, p. 045504, 2004.

[120] J. P. Sethna, K. Dahmen, S. Kartha, J. A. Krumhansl, B. W. Roberts, and J. D. Shore, "Hysteresis and hierarchies: Dynamics of disorder-driven first-order phase transformations," *Phys. Rev. Lett.*, vol. 70, pp. 3347–3350, May 1993.

[121] J. M. Deutsch, A. Dhar, and O. Narayan, "Return to return point memory," *Phys. Rev. Lett.*, vol. 92, p. 227203, Jun 2004.

[122] A. A. Middleton, "Asymptotic uniqueness of the sliding state for charge-density waves," *Phys. Rev. Lett.*, vol. 68, pp. 670–673, Feb 1992.

[123] L. Corte, P. M. Chaikin, J. P. Gollub, and D. J. Pine, "Random organization in periodically driven systems," *Nature Physics*, vol. 4, no. 5, pp. 420–424, 2008.

[124] N. C. Keim and S. R. Nagel, "Generic transient memory formation in disordered systems with noise," *Phys. Rev. Lett.*, vol. 107, p. 010603, Jun 2011.

[125] N. C. Keim, J. D. Paulsen, and S. R. Nagel, "Multiple transient memories in sheared suspensions: Robustness, structure, and routes to plasticity," *Phys. Rev. E*, vol. 88, p. 032306, Sep 2013.

[126] J. D. Paulsen, N. C. Keim, and S. R. Nagel, "Multiple transient memories in experiments on sheared non-brownian suspensions," *Phys. Rev. Lett.*, vol. 113, p. 068301, Aug 2014.

[127] M. L. Falk and J. S. Langer, "Deformation and failure of amorphous, solidlike materials," *Annu. Rev. Condens. Matter Phys.*, vol. 2, no. 1, pp. 353–373, 2011.

[128] A. D. Parmar and S. Sastry, "Mechanical behaviour of glasses and amorphous materials," in *Advances in the Chemistry and Physics of Materials: Overview of Selected Topics*, pp. 503–527, World Scientific, 2020.

[129] D. Fiocco, G. Foffi, and S. Sastry, "Oscillatory athermal quasistatic deformation of a model glass," *Physical Review E*, vol. 88, no. 2, p. 020301, 2013.

[130] P. Leishangthem, A. D. Parmar, and S. Sastry, "The yielding transition in amorphous solids under oscillatory shear deformation," *Nature communications*, vol. 8, no. 1, pp. 1–8, 2017.

[131] D. Fiocco, G. Foffi, and S. Sastry, "Encoding of memory in sheared amorphous solids," *Phys. Rev. Lett.*, vol. 112, p. 025702, Jan 2014.

[132] S. Mukherji, N. Kandula, A. Sood, and R. Ganapathy, "Strength of mechanical memories is maximal at the yield point of a soft glass," *Physical Review Letters*, vol. 122, no. 15, p. 158001, 2019.

[133] N. C. Keim, J. Hass, B. Kroger, and D. Wieker, "Global memory from local hysteresis in an amorphous solid," *Physical Review Research*, vol. 2, no. 1, p. 012004, 2020.

[134] F. Preisach, "Über die magnetische nachwirkung," *Zeitschrift für physik*, vol. 94, no. 5-6, pp. 277–302, 1935.

[135] M. Mungan, S. Sastry, K. Dahmen, and I. Regev, "Networks and hierarchies: How amorphous materials learn to remember," *Physical review letters*, vol. 123, no. 17, p. 178002, 2019.

[136] M. Mungan and M. M. Terzi, "The structure of state transition graphs in systems with return point memory: I. general theory," in *Annales Henri Poincaré*, vol. 20, pp. 2819–2872, Springer, 2019.

[137] J. P. Sethna, K. Dahmen, S. Kartha, J. A. Krumhansl, B. W. Roberts, and J. D. Shore, "Hysteresis and hierarchies: Dynamics of disorder-driven first-order phase transformations," *Physical Review Letters*, vol. 70, no. 21, p. 3347, 1993.

[138] C. Donati, S. Franz, S. C. Glotzer, and G. Parisi, "Theory of non-linear susceptibility and correlation length in glasses and liquids," *Journal of non-crystalline solids*, vol. 307, pp. 215–224, 2002.

[139] W. G. Hoover, *Computational statistical mechanics*. Elsevier, 2012.

[140] D. Brown and J. Clarke, "A comparison of constant energy, constant temperature and constant pressure ensembles in molecular dynamics simulations of atomic liquids," *Molecular Physics*, vol. 51, no. 5, pp. 1243–1252, 1984.

[141] M. P. Allen and D. J. Tildesley, *Computer simulation of liquids*. Oxford university press, 2017.

[142] D. Frenkel and B. Smit, *Understanding molecular simulation: from algorithms to applications*, vol. 1. Elsevier, 2001.

[143] Y. Rosenfeld and P. Tarazona, "Density functional theory and the asymptotic high density expansion of the free energy of classical solids and fluids," *Molecular Physics*, vol. 95, no. 2, pp. 141–150, 1998.

[144] S. Sastry, "Liquid limits: Glass transition and liquid-gas spinodal boundaries of metastable liquids," *Physical Review Letters*, vol. 85, no. 3, p. 590, 2000.

[145] F. Sciortino, "Potential energy landscape description of supercooled liquids and glasses," *Journal of Statistical Mechanics: Theory and Experiment*, vol. 2005, no. 05, p. P05015, 2005.

[146] C. S. O'Hern, L. E. Silbert, A. J. Liu, and S. R. Nagel, "Jamming at zero temperature and zero applied stress: The epitome of disorder," *Phys. Rev. E*, vol. 68, p. 011306, Jul 2003.

[147] W. Kob and H. C. Andersen, "Testing mode-coupling theory for a supercooled binary lennard-jones mixture. ii. intermediate scattering function and dynamic susceptibility," *Phys. Rev. E*, vol. 52, pp. 4134–4153, Oct 1995.

[148] C. S. O'Hern, S. A. Langer, A. J. Liu, and S. R. Nagel, "Random packings of frictionless particles," *Phys. Rev. Lett.*, vol. 88, p. 075507, Jan 2002.

[149] K. Binder and W. Kob, *Glassy materials and disordered solids: An introduction to their statistical mechanics*. World scientific, 2011.

[150] C. P. Royall, F. Turci, S. Tatsumi, J. Russo, and J. Robinson, "The race to the bottom: approaching the ideal glass?," *Journal of Physics: Condensed Matter*, vol. 30, no. 36, p. 363001, 2018.

[151] S. Torquato and F. H. Stillinger, "Publisher's note: Jammed hard-particle packings: From kepler to bernal and beyond [rev. mod. phys. 82, 2633 (2010)]," *Rev. Mod. Phys.*, vol. 82, pp. 3197–3197, Dec 2010.

[152] R. P. Behringer and B. Chakraborty, "The physics of jamming for granular materials: a review," *Reports on Progress in Physics*, vol. 82, no. 1, p. 012601, 2018.

[153] T. R. Kirkpatrick and D. Thirumalai, "Dynamics of the structural glass transition and the p-spinâĂŤinteraction spin-glass model," *Physical review letters*, vol. 58, no. 20, p. 2091, 1987.

[154] T. R. Kirkpatrick, D. Thirumalai, and P. G. Wolynes, "Scaling concepts for the dynamics of viscous liquids near an ideal glassy state," *Physical Review A*, vol. 40, no. 2, p. 1045, 1989.

[155] G. Parisi, P. Urbani, and F. Zamponi, *Theory of Simple Glasses: Exact Solutions in Infinite Dimensions*. Cambridge University Press, 2020.

[156] P. Charbonneau, A. Ikeda, G. Parisi, and F. Zamponi, "Glass transition and random close packing above three dimensions," *Physical review letters*, vol. 107, no. 18, p. 185702, 2011.

[157] P. Charbonneau, A. Ikeda, G. Parisi, and F. Zamponi, "Dimensional study of the caging order parameter at the glass transition," *Proceedings of the National Academy of Sciences*, vol. 109, no. 35, pp. 13939–13943, 2012.

[158] L. Berthier, P. Charbonneau, and J. Kundu, "Finite dimensional vestige of spinodal criticality above the dynamical glass transition," *Phys. Rev. Lett.*, vol. 125, p. 108001, Aug 2020.

[159] P. Charbonneau and P. K. Morse, "Memory formation in jammed hard spheres," *Physical review letters*, vol. 126, no. 8, p. 088001, 2021.

[160] J. D. Eaves and D. R. Reichman, "Spatial dimension and the dynamics of supercooled liquids," *Proceedings of the National Academy of Sciences*, vol. 106, no. 36, pp. 15171–15175, 2009.

[161] S. Sengupta, S. Karmakar, C. Dasgupta, and S. Sastry, "Adam-gibbs relation for glass-forming liquids in two, three, and four dimensions," *Physical review letters*, vol. 109, no. 9, p. 095705, 2012.

[162] W.-S. Xu, J. F. Douglas, and K. F. Freed, "Entropy theory of polymer glass-formation in variable spatial dimension," *Adv. Chem. Phys*, vol. 161, pp. 443–497, 2016.

[163] M. Adhikari, S. Karmakar, and S. Sastry, "Spatial dimensionality dependence of heterogeneity, breakdown of the stokes-einstein relation and fragility of a model glass-forming liquid," *(Preprint)*, 2021.

[164] R. J. Speedy, "Random jammed packings of hard discs and spheres," *Journal of Physics: Condensed Matter*, vol. 10, no. 19, p. 4185, 1998.

[165] R. J. Speedy and P. G. Debenedetti, "The distribution of tetravalent network glasses," *Molecular Physics*, vol. 88, no. 5, pp. 1293–1316, 1996.

[166] M. Hermes and M. Dijkstra, "Jamming of polydisperse hard spheres: The effect of kinetic arrest," *EPL*, vol. 89, p. 38005, 2010.

[167] M. Ciamarra, A. Coniglio, and A. D. Candia, "Disordered jammed packings of frictionless spheres," *Soft Matter*, vol. 6, pp. 2975–2981, 2010.

[168] M. Ozawa, T. Kuroiwa, A. Ikeda, and K. Miyazaki, "Jamming transition and inherent structures of hard spheres and disks," *Physical review letters*, vol. 109, no. 20, p. 205701, 2012.

[169] L. Berthier and T. A. Witten, "Compressing nearly hard sphere fluids increases glass fragility," *EPL (Europhysics Letters)*, vol. 86, no. 1, p. 10001, 2009.

[170] L. Berthier and T. A. Witten, "Glass transition of dense fluids of hard and compressible spheres," *Physical Review E*, vol. 80, no. 2, p. 021502, 2009.

[171] M. H. Cohen and D. Turnbull, "Molecular transport in liquids and glasses," *The Journal of Chemical Physics*, vol. 31, no. 5, pp. 1164–1169, 1959.

[172] D. J. Durian, "Foam mechanics at the bubble scale," *Physical review letters*, vol. 75, no. 26, p. 4780, 1995.

[173] R. W. Hall and P. G. Wolynes, "The aperiodic crystal picture and free energy barriers in glasses," *The Journal of chemical physics*, vol. 86, no. 5, pp. 2943–2948, 1987.

[174] G. Brambilla, D. El Masri, M. Pierno, L. Berthier, L. Cipelletti, G. Petekidis, and A. B. Schofield, "Probing the equilibrium dynamics of colloidal hard spheres above the mode-coupling glass transition," *Physical review letters*, vol. 102, no. 8, p. 085703, 2009.

[175] V. Baranau and U. Tallarek, "Relaxation times, jamming densities, and ideal glass transition densities for hard spheres in a wide range of polydispersities," *AIP Advances*, vol. 10, no. 3, p. 035212, 2020.

[176] M. Maiti and M. Schmiedeberg, "Temperature dependence of the transition packing fraction of thermal jamming in a harmonic soft sphere system," *Journal of Physics: Condensed Matter*, vol. 31, no. 16, p. 165101, 2019.

[177] J. A. Barker and D. Henderson, "Perturbation theory and equation of state for fluids. ii. a successful theory of liquids," *The Journal of chemical physics*, vol. 47, no. 11, pp. 4714–4721, 1967.

[178] P. K. Morse and E. I. Corwin, "Geometric signatures of jamming in the mechanical vacuum," *Phys. Rev. Lett.*, vol. 112, p. 115701, Mar 2014.

[179] A. Manacorda and F. Zamponi, "Gradient descent dynamics and the jamming transition in infinite dimensions," *arXiv preprint arXiv:2201.01161*, 2022.

[180] H. Sillescu, "Heterogeneity at the glass transition: a review," *Journal of Non-Crystalline Solids*, vol. 243, no. 2-3, pp. 81–108, 1999.

[181] D. N. Perera and P. Harrowell, "Origin of the difference in the temperature dependences of diffusion and structural relaxation in a supercooled liquid," *Physical review letters*, vol. 81, no. 1, p. 120, 1998.

[182] R. Yamamoto and A. Onuki, "Heterogeneous diffusion in highly supercooled liquids," *Physical review letters*, vol. 81, no. 22, p. 4915, 1998.

[183] E. Flenner, H. Staley, and G. Szamel, "Universal features of dynamic heterogeneity in supercooled liquids," *Physical review letters*, vol. 112, no. 9, p. 097801, 2014.

[184] S. Karmakar, C. Dasgupta, and S. Sastry, "Length scales in glass-forming liquids and related systems: a review," *Reports on Progress in Physics*, vol. 79, no. 1, p. 016601, 2016.

[185] E. Rössler, "Indications for a change of diffusion mechanism in supercooled liquids," *Phys. Rev. Lett.*, vol. 65, pp. 1595–1598, Sep 1990.

[186] F. Fujara, B. Geil, H. Sillescu, and G. Fleischer, "Translational and rotational diffusion in supercooled orthoterphenyl close to the glass transition," *Zeitschrift für Physik B Condensed Matter*, vol. 88, no. 2, pp. 195–204, 1992.

[187] D. Thirumalai and R. D. Mountain, "Activated dynamics, loss of ergodicity, and transport in supercooled liquids," *Physical Review E*, vol. 47, no. 1, p. 479, 1993.

[188] F. H. Stillinger and J. A. Hodgdon, "Translation-rotation paradox for diffusion in fragile glass-forming liquids," *Physical review E*, vol. 50, no. 3, p. 2064, 1994.

[189] G. Tarjus and D. Kivelson, "Breakdown of the stokes–einstein relation in supercooled liquids," *The Journal of chemical physics*, vol. 103, no. 8, pp. 3071–3073, 1995.

[190] L. Berthier, D. Chandler, and J. P. Garrahan, "Length scale for the onset of fickian diffusion in supercooled liquids," *EPL (Europhysics Letters)*, vol. 69, no. 3, p. 320, 2004.

[191] L. Berthier, "Time and length scales in supercooled liquids," *Physical Review E*, vol. 69, no. 2, p. 020201, 2004.

[192] Y. Jung, J. P. Garrahan, and D. Chandler, "Excitation lines and the breakdown of stokes-einstein relations in supercooled liquids," *Phys. Rev. E*, vol. 69, p. 061205, Jun 2004.

[193] J. Kim and T. Keyes, "On the breakdown of the stokes- einstein law in supercooled liquids," *The Journal of Physical Chemistry B*, vol. 109, no. 45, pp. 21445–21448, 2005.

[194] S. K. Kumar, G. Szamel, and J. F. Douglas, "Nature of the breakdown in the stokes-einstein relationship in a hard sphere fluid," *The Journal of chemical physics*, vol. 124, no. 21, p. 214501, 2006.

[195] S.-H. Chong, "Connections of activated hopping processes with the breakdown of the stokes-einstein relation and with aspects of dynamical heterogeneities," *Physical Review E*, vol. 78, no. 4, p. 041501, 2008.

[196] S.-H. Chong and W. Kob, "Coupling and decoupling between translational and rotational dynamics in a supercooled molecular liquid," *Physical review letters*, vol. 102, no. 2, p. 025702, 2009.

[197] P. Charbonneau, Y. Jin, G. Parisi, and F. Zamponi, "Hopping and the stokes–einstein relation breakdown in simple glass formers," *Proceedings of the National Academy of Sciences*, vol. 111, no. 42, pp. 15025–15030, 2014.

[198] A. D. Parmar, S. Sengupta, and S. Sastry, "Length-scale dependence of the stokes-einstein and adam-gibbs relations in model glass formers," *Physical review letters*, vol. 119, no. 5, p. 056001, 2017.

[199] M. K. Nandi and S. M. Bhattacharyya, "Continuous time random walk concepts applied to extended mode coupling theory: a study of the stokes–einstein breakdown," *Journal of Physics: Condensed Matter*, vol. 32, no. 6, p. 064001, 2019.

[200] C. Angell, "Relaxation in liquids, polymers and plastic crystalsâĂŤstrong/fragile patterns and problems," *Journal of Non-Crystalline Solids*, vol. 131, pp. 13–31, 1991.

[201] A. I. Nielsen, T. Christensen, B. Jakobsen, K. Niss, N. B. Olsen, R. Richert, and J. C. Dyre, "Prevalence of approximate t relaxation for the dielectric α process in viscous organic liquids," *The Journal of chemical physics*, vol. 130, no. 15, p. 154508, 2009.

[202] J. F. Douglas, J. Dudowicz, and K. F. Freed, "Does equilibrium polymerization describe the dynamic heterogeneity of glass-forming liquids?," *The Journal of chemical physics*, vol. 125, no. 14, p. 144907, 2006.

[203] J. Dudowicz, K. F. Freed, and J. F. Douglas, *Generalized Entropy Theory of Polymer Glass Formation*, ch. 3, pp. 125–222. John Wiley & Sons, Ltd, 2007.

[204] F. W. Starr, J. F. Douglas, and S. Sastry, "The relationship of dynamical heterogeneity to the adam-gibbs and random first-order transition theories of glass formation," *The Journal of chemical physics*, vol. 138, no. 12, p. 12A541, 2013.

[205] B. A. P. Betancourt, J. F. Douglas, and F. W. Starr, "Fragility and cooperative motion in a glass-forming polymer–nanoparticle composite," *Soft Matter*, vol. 9, no. 1, pp. 241–254, 2013.

[206] G. Biroli, J.-P. Bouchaud, K. Miyazaki, and D. R. Reichman, "Inhomogeneous mode-coupling theory and growing dynamic length in supercooled liquids," *Physical review letters*, vol. 97, no. 19, p. 195701, 2006.

[207] A. Manacorda, G. Schehr, and F. Zamponi, "Numerical solution of the dynamical mean field theory of infinite-dimensional equilibrium liquids," *The Journal of Chemical Physics*, vol. 152, no. 16, p. 164506, 2020.

[208] G. Biroli and J.-P. Bouchaud, "Critical fluctuations and breakdown of the stokes–einstein relation in the mode-coupling theory of glasses," *Journal of Physics: Condensed Matter*, vol. 19, p. 205101, apr 2007.

[209] S. Franz, H. Jacquin, G. Parisi, P. Urbani, and F. Zamponi, "Quantitative field theory of the glass transition," *Proceedings of the National Academy of Sciences*, vol. 109, no. 46, pp. 18725–18730, 2012.

[210] E. Flenner and G. Szamel, "Dynamic heterogeneity in a glass forming fluid: Susceptibility, structure factor, and correlation length," *Physical review letters*, vol. 105, no. 21, p. 217801, 2010.

[211] N. Lačević, F. W. Starr, T. Schrøder, and S. Glotzer, "Spatially heterogeneous dynamics investigated via a time-dependent four-point density correlation function," *The Journal of chemical physics*, vol. 119, no. 14, pp. 7372–7387, 2003.

[212] W.-S. Xu, J. F. Douglas, and X. Xu, "Molecular dynamics study of glass formation in polymer melts with varying chain stiffness," *Macromolecules*, vol. 53, no. 12, pp. 4796–4809, 2020.

[213] U. K. Nandi, W. Kob, and S. Maitra Bhattacharyya, "Connecting real glasses to mean-field models," *The Journal of Chemical Physics*, vol. 154, no. 9, p. 094506, 2021.

[214] W.-S. Xu, J. F. Douglas, and K. F. Freed, "Influence of cohesive energy on relaxation in a model glass-forming polymer melt," *Macromolecules*, vol. 49, no. 21, pp. 8355–8370, 2016.

[215] X. Wang, W.-S. Xu, H. Zhang, and J. F. Douglas, "Universal nature of dynamic heterogeneity in glass-forming liquids: A comparative study of metallic and polymeric glass-forming liquids," *The Journal of chemical physics*, vol. 151, no. 18, p. 184503, 2019.

[216] H. Zhang, X. Wang, A. Chremos, and J. F. Douglas, "Superionic uo2: A model anharmonic crystalline material," *The Journal of chemical physics*, vol. 150, no. 17, p. 174506, 2019.

[217] H. Zhang, X. Wang, H.-B. Yu, and J. F. Douglas, "Dynamic heterogeneity, cooperative motion, and johari–goldstei-relaxation in a metallic glass-forming material exhibiting a fragile-to-strong transition," *The European Physical Journal E*, vol. 44, no. 4, pp. 1–30, 2021.

[218] S. Sastry, "Liquid limits: Glass transition and liquid-gas spinodal boundaries of metastable liquids," *Physical Review Letters*, vol. 85, no. 3, p. 590, 2000.

[219] R. Greet and D. Turnbull, "Test of adamâĂŤgibbs liquid viscosity model with o-terphenyl specific-heat data," *The Journal of Chemical Physics*, vol. 47, no. 6, pp. 2185–2190, 1967.

[220] R. J. Speedy, "The hard sphere glass transition," *Molecular Physics*, vol. 95, no. 2, pp. 169–178, 1998.

[221] G. Johari, "A resolution for the enigma of a liquidâĂŹs configurational entropy-molecular kinetics relation," *The Journal of Chemical Physics*, vol. 112, no. 20, pp. 8958–8969, 2000.

[222] A. Scala, F. W. Starr, E. La Nave, F. Sciortino, and H. E. Stanley, "Configurational entropy and diffusivity of supercooled water," *Nature*, vol. 406, no. 6792, pp. 166–169, 2000.

[223] S. Mossa, E. La Nave, H. Stanley, C. Donati, F. Sciortino, and P. Tartaglia, "Dynamics and configurational entropy in the lewis-wahnström model for supercooled orthoterphenyl," *Physical Review E*, vol. 65, no. 4, p. 041205, 2002.

[224] C. Roland, S. Capaccioli, M. Lucchesi, and R. Casalini, "Adam–gibbs model for the supercooled dynamics in the ortho-terphenyl ortho-phenylphenol mixture," *The Journal of chemical physics*, vol. 120, no. 22, pp. 10640–10646, 2004.

[225] M. Ozawa, C. Scalliet, A. Ninarello, and L. Berthier, "Does the adam-gibbs relation hold in simulated supercooled liquids?," *The Journal of chemical physics*, vol. 151, no. 8, p. 084504, 2019.

[226] L. Ortlieb, T. S. Ingebrigtsen, J. E. Hallett, F. Turci, and C. P. Royall, "Relaxation mechanisms in supercooled liquids past the mode–coupling crossover: Cooperatively re–arranging regions vs excitations," *arXiv preprint arXiv:2103.08060*, 2021.

[227] G. Biroli, J.-P. Bouchaud, A. Cavagna, T. S. Grigera, and P. Verrocchio, "Thermodynamic signature of growing amorphous order in glass-forming liquids," *Nature Physics*, vol. 4, no. 10, pp. 771–775, 2008.

[228] C. Cammarota, A. Cavagna, G. Gradenigo, T. S. Grigera, and P. Verrocchio, "Numerical determination of the exponents controlling the relationship between time, length, and temperature in glass-forming liquids," *The Journal of chemical physics*, vol. 131, no. 19, p. 194901, 2009.

[229] S. Karmakar, C. Dasgupta, and S. Sastry, "Length scales in glass-forming liquids and related systems: a review," *Reports on Progress in Physics*, vol. 79, no. 1, p. 016601, 2015.

[230] A. D. Parmar, S. Sengupta, and S. Sastry, "Power law relationship between diffusion coefficients in multi-component glass forming liquids," *The European Physical Journal E*, vol. 41, no. 8, p. 90, 2018.

[231] P. Das and S. Sastry, "Crossover in dynamics in the kob-andersen binary mixture glass-forming liquid," *Journal of Non-Crystalline Solids: X*, p. 100098, 2022.

[232] C. A. Schuh, T. C. Hufnagel, and U. Ramamurty, "Mechanical behavior of amorphous alloys," *Acta Materialia*, vol. 55, no. 12, pp. 4067–4109, 2007.

[233] A. Nicolas, E. E. Ferrero, K. Martens, and J.-L. Barrat, "Deformation and flow of amorphous solids: Insights from elastoplastic models," *Reviews of Modern Physics*, vol. 90, no. 4, p. 045006, 2018.

[234] K. H. Nagamanasa, S. Gokhale, A. Sood, and R. Ganapathy, "Experimental signatures of a nonequilibrium phase transition governing the yielding of a soft glass," *Physical Review E*, vol. 89, no. 6, p. 062308, 2014.

[235] N. C. Keim and P. E. Arratia, "Yielding and microstructure in a 2d jammed material under shear deformation," *Soft Matter*, vol. 9, no. 27, pp. 6222–6225, 2013.

[236] D. V. Denisov, M. T. Dang, B. Struth, A. Zaccone, G. H. Wegdam, and P. Schall, "Sharp symmetry-change marks the mechanical failure transition of glasses," *Scientific Reports*, vol. 5, Sept. 2015.

[237] Y. Shi and M. L. Falk, "Strain localization and percolation of stable structure in amorphous solids," *Physical review letters*, vol. 95, no. 9, p. 095502, 2005.

[238] Y. Shi, M. B. Katz, H. Li, and M. L. Falk, "Evaluation of the disorder temperature and free-volume formalisms via simulations of shear banding in amorphous solids," *Physical review letters*, vol. 98, no. 18, p. 185505, 2007.

[239] A. Wisitsorasak and P. G. Wolynes, "Dynamical theory of shear bands in structural glasses," *Proceedings of the National Academy of Sciences*, vol. 114, no. 6, pp. 1287–1292, 2017.

[240] P. K. Jaiswal, I. Procaccia, C. Rainone, and M. Singh, "Mechanical yield in amorphous solids: A first-order phase transition," *Physical review letters*, vol. 116, no. 8, p. 085501, 2016.

[241] T. Kawasaki and L. Berthier, "Macroscopic yielding in jammed solids is accompanied by a nonequilibrium first-order transition in particle trajectories," *Physical Review E*, vol. 94, no. 2, p. 022615, 2016.

[242] I. Regev, J. Weber, C. Reichhardt, K. A. Dahmen, and T. Lookman, "Reversibility and criticality in amorphous solids," *Nature communications*, vol. 6, no. 1, pp. 1–8, 2015.

[243] Y. Jin, P. Urbani, F. Zamponi, and H. Yoshino, "A stability-reversibility map unifies elasticity, plasticity, yielding, and jamming in hard sphere glasses," *Science advances*, vol. 4, no. 12, p. eaat6387, 2018.

[244] I. Procaccia, C. Rainone, and M. Singh, "Mechanical failure in amorphous solids: Scale-free spinodal criticality," *Physical Review E*, vol. 96, no. 3, p. 032907, 2017.

[245] A. D. Parmar, S. Kumar, and S. Sastry, "Strain localization above the yielding point in cyclically deformed glasses," *Physical Review X*, vol. 9, no. 2, p. 021018, 2019.

[246] A. Barbot, M. Lerbinger, A. Lemaitre, D. Vandembroucq, and S. Patinet, "Rejuvenation and shear banding in model amorphous solids," *Physical Review E*, vol. 101, no. 3, p. 033001, 2020.

[247] G. Parisi, I. Procaccia, C. Rainone, and M. Singh, "Shear bands as manifestation of a criticality in yielding amorphous solids," *Proceedings of the National Academy of Sciences*, vol. 114, no. 22, pp. 5577–5582, 2017.

[248] A. Wisitsorasak and P. G. Wolynes, "On the strength of glasses," *Proceedings of the National Academy of Sciences*, vol. 109, no. 40, pp. 16068–16072, 2012.

[249] K. Khirallah, B. Tyukodi, D. Vandembroucq, and C. E. Maloney, "Yielding in an integer automaton model for amorphous solids under cyclic shear," *Phys. Rev. Lett.*, vol. 126, p. 218005, May 2021.

[250] M. Ozawa, L. Berthier, G. Biroli, A. Rosso, and G. Tarjus, "Random critical point separates brittle and ductile yielding transitions in amorphous materials," *Proceedings of the National Academy of Sciences*, vol. 115, no. 26, pp. 6656–6661, 2018.

[251] D. J. Pine, J. P. Gollub, J. F. Brady, and A. M. Leshansky, "Chaos and threshold for irreversibility in sheared suspensions," *Nature*, vol. 438, no. 7070, pp. 997–1000, 2005.

[252] C. Ness, R. Mari, and M. E. Cates, "Shaken and stirred: Random organization reduces viscosity and dissipation in granular suspensions," *Science advances*, vol. 4, no. 3, p. eaar3296, 2018.

[253] K. Nagasawa, K. Miyazaki, and T. Kawasaki, "Classification of the reversible–irreversible transitions in particle trajectories across the jamming transition point," *Soft matter*, vol. 15, no. 38, pp. 7557–7566, 2019.

[254] S. Martiniani, P. M. Chaikin, and D. Levine, "Quantifying hidden order out of equilibrium," *Physical Review X*, vol. 9, no. 1, p. 011031, 2019.

[255] P. Das, H. Vinutha, and S. Sastry, "Unified phase diagram of reversible–irreversible, jamming, and yielding transitions in cyclically sheared soft-sphere packings," *Proceedings of the National Academy of Sciences*, vol. 117, no. 19, pp. 10203–10209, 2020.

[256] M. Adhikari and S. Sastry, "Memory formation in cyclically deformed amorphous solids and sphere assemblies," *The European Physical Journal E*, vol. 41, no. 9, p. 105, 2018.

[257] D. Fiocco, G. Foffi, and S. Sastry, "Encoding of memory in sheared amorphous solids," *Physical review letters*, vol. 112, no. 2, p. 025702, 2014.

[258] S. Suresh, *Fatigue of materials*. Cambridge University Press, Cambridge, 1998.

[259] S. Plimpton, "Fast parallel algorithms for short-range molecular dynamics," *Journal of computational physics*, vol. 117, no. 1, pp. 1–19, 1995.